Electronic Structure and Spectroscopy of Tetranuclear Mn_4O_4 and $CaMn_3O_4$ Complexes as Models of the Oxygen Evolving Complex in Photosystem II

Thesis by

Heui Beom Lee

In Partial Fulfillment of the Requirements for
the degree of
Doctor of Philosophy

Division of Chemistry and Chemical Engineering
CALIFORNIA INSTITUTE OF TECHNOLOGY
Pasadena, California

2019
(Defended Feb. 27, 2019)

ORCID: 0000-0002-9550-2649

“Do not be anxious about anything, but in everything by prayer and supplication with thanksgiving let your requests be made known to God. And the peace of God, which surpasses all understanding, will guard your hearts and your minds in Christ Jesus”

Philippians 4:6−7

“I have fought the good fight, I have finished the race, I have kept the faith”

2 Timothy 4:7

ACKNOWLEDGEMENTS

"A frog forgets its tadpole days."

Old Korean proverb

I must still be a tadpole. Almost at the end of my graduate career and about to reach one of my greatest academic achievements, I am vividly reminded of my humble beginnings as a scientist, and I am very grateful to all the people who have made this possible. My experience is definitely not unique, and looking back, I can say that graduate school was definitely challenging. There were difficult times; it was character building. However, I am filled with joy and excitement toward what lies ahead, both in science and in life. Briefly, I would like to mention the people who have helped me throughout my career and make the daunting undertaking bearable, enjoyable, surmountable.

First, I would like to thank my advisor, Prof. Theodor Agapie. Theo, thank you for your support with my career, for your patience when I had no results, for your mentorship, enthusiasm, and excitement for my science, and for your encouragement to always give my absolute best. Above all, I benefited most from the highest standard of scholarship that Theo upholds to. Weekly, quarterly, and annual research progress meetings and chemical literature meetings formed much of my intellectual basis for the fundamentals of the discipline, critical thinking process, presentation skills, and a superficial yet holistic view in other areas of chemistry and science. Thank you, Theo, for all those years in the lab! I would also like to thank my supportive thesis committee: Profs. Jonas Peters, Harry Gray, and Garnet Chan. Thank you, Jonas, for teaching me to be rigorously in line with thermodynamics at all times. I also can't forget the time you told me that "hope is not a strategy"; hard work is!

It is not an exaggeration when I say that I wouldn't have completed my thesis without the help of my collaborators. I express my most sincere gratitude to Dr. Paul Oyala at the Caltech EPR facility, David Marchiori and Prof. R. David Britt at the University of California Davis, Drs. Sheraz Gul, Ruchira Chatterjee, and Junko Yano at the Lawrence Berkeley National Laboratory. Paul, your expertise, dedication, and enthusiasm for science and EPR spectroscopy is an example for the entire scientific community! Also thank you for being so flexible in terms of instrument usage. Soon Dr. David Marchiori, thank you for all of your help with D-band spectroscopy! I can only imagine how hard it is to handle those tiny frozen capillary EPR tubes. I am simply glad that I have you as a driven, efficient, and friendly collaborator. I hope that we continue to cross paths in our future scientific endeavors. Thank you Prof. R. Dave Britt for sharing your excitement and expertise in the EPR studies of my compounds. Sheraz, Ruchira, and Junko, thank you for being so reliable and dependable when it comes to XAS spectroscopy. Thanks for accommodating me with one week's notice on some of my samples!

Before my time at Caltech, I had the privilege of doing undergraduate research under the mentorship of Prof. Eric J. Schelter at the University of Pennsylvania. Eric's mentorship has profoundly impacted my decision to pursue a career in chemical research and education. Thank you Eric for your mentorship and friendship and for making science fun all those years! I would also like to thank my undergraduate professors, mentors, and colleagues: Profs. Gary Molander, David Chenoweth, Don Berry, Pat Walsh, Chris Graves, Jerome Robinson, Justin Bogart, and soon Dr. Michael Boreen.

I would like to thank all of my teachers and schoolmates from my formative years in Guatemala. I truly miss the time I spent with my physics teacher ingeniero Rafael Santiago,

chemistry teacher licenciada Mabel Miranda, and computer science teacher Cesar Archila at Suger Montano. I also had the privilege of taking advanced math classes at the Universidad de San Carlos; thank you Sergio Silverio Merida. I would like to thank my English teachers Whitney Elliot and Selena Herranen at Han Al Academy. Los extraño tanto. Que Dios los bendiga y los cuide!

Over the last six years at Caltech, I have had the opportunity to interact with some of the most brilliant minds. All interactions with members of the cluster subgroup are deeply appreciated. Jacob Kanady, thank you for the initial training that you gave me in the lab. Emily Tsui, thank you for putting up with me as a baymate. I know I can be messy sometimes. Davide Lionetti, Kyle Horak, Joshua Buss, Trevor Castillo, and Favier Fajardo, thank you for the scientific discussions inside and outside the lab and for the Saturday morning soccer. Ole! Ole! Chick-fil-a after soccer was always a treat. Guy Edouard, thank you for always putting a smile on my face and for helping me become a real person by buying Paul Kelley's old Jeep. It still runs great! Gyeongshin Choi, thank you for being a synthetic inspiration in the lab and also for introducing me to tennis. Blessings to your family. Graham de Ruiter, in true Dutch fashion, thank you for showing me the value of trading synthetic intermediates towards a greater goal. These last few months have been somewhat stressful, but thank you all current members of the Agapie group for being there and promoting more social activities. Manar Shosani, Gwen Bailey, Christopher Reed, Angela Shiau, and Marcus Low, thank you for sharing your passion for food with me. Angela Shiau, the remaining beacon of hope towards a full dangler model of the OEC, be great and be excellent! To all other Agapie alumni, thank you for being great scientists and friends!

Caltech has been an excellent place to do science. I thank each one of the excellent staff scientists at Caltech: Mona Shahgholi for ESI-MS, Dave Vander Valde for NMR, Mike Takase and Larry Henling for XRD, and Paul Oyala for EPR. Science wouldn't be possible without your dedication and expertise. I also thank the administrative staff at Caltech: Margarita Davis as group admin, Rick Germond and crew at facilities and N_2 delivery, Agnes Tong as CCE admin at the time of my admission, and Laura Flower Kim in the international student office. Thank you Caltech housing for letting me live in the Cats for all five years. Thank you Caltech dining services for the yearly Thanksgiving dinner and the year-round service. Thank you all!

Lastly, I want to thank my supportive family. Mom and dad, thank you for your unconditional love and support! Your instruction will always resonate in my heart. "Plan your life as if you're immortal, live today as if your last day."

RESPECTIVE CONTRIBUTIONS

Much of the work described in this thesis is the result of collaborative efforts. Specific notes are included for compounds not synthesized by the author, and general comments on collaborators are given here.

In Chapter 2, the synthetic procedure for the desymmetrized carboxylate ligand was initially developed by Prof. Emily Y. Tsui. In Chapter 3, the synthetic procedure for the phosphinate-bridged [Mn_4O_4] cubane complexes was developed by Ms. Angela A. Shiau.

X-band and Q-band EPR studies reported in this thesis were performed with Dr. Paul H. Oyala at the California Institute of Technology; all D-band EPR studies were performed by soon Dr. David A. Marchiori and Prof. R. David Britt at the University of California Davis. X-ray spectroscopic studies reported in this thesis were performed by Drs. Sheraz Gul, Ruchira Chatterjee, and Junko Yano at the Lawrence Berkeley National Laboratory. X-ray crystallographic studies reported in this thesis were performed with the assistance of Mr. Lawrence M. Henling and Dr. Michael K. Takase at the California Institute of Technology. SQUID magnetometry studies reported in this thesis were performed with the assistance of Dr. Ignacio B. Martini at the University of California Los Angeles.

ABSTRACT

This thesis describes a series of studies devoted toward the synthesis of model complexes that mimic aspects of structure, redox state, and spectroscopy of the oxygen evolving complex (OEC) of Photosystem II. The OEC is a unique metallocofactor featuring a heteronuclear $CaMn_4$ core that catalyzes water oxidation. While advances in spectroscopic and structural techniques offer an ever more detailed view of the structure of the S-state catalytic intermediates, the precise mechanism of O−O bond formation remains debated. Aspects such as (1) role of Ca^{2+}, (2) the location of the substrate waters, and (3) the (electronic)structure of the S-state intermediates remain unclear. To obtain a better understanding of the OEC, systematic structure−function(property) studies on relevant model complexes may be necessary. Despite significant efforts to prepare tetra- and pentanuclear complexes as models of the OEC, relevant complexes in terms of structure, redox state, spectroscopy, and reactivity are rare, likely due to the synthetic challenges of accessing a series of isolable clusters that are suitable for comparisons.

Chapter 1 presents a survey of tetramanganese model compounds with an emphasis on redox state and electronic structure, as probed by magnetometry and EPR spectroscopy. Structurally characterized model complexes are grouped according to Mn oxidation states and the S-state that they are mirroring. In contrast to the vast number of spectroscopic studies on the OEC, studies that probe the effect of systematic changes in structure on the spectroscopy of model complexes are rare in the literature.

Chapter 2 presents ongoing synthetic efforts to prepare accurate structural models of the OEC. The synthesis of accurate structural models is hampered by the low structural symmetry of the cluster, the presence of two types of metals, and the propensity of oxo

moieties to form extended oligomeric structures. Desymmetrization of the previously reported trinucleating ligand leads to the formation of tetranuclear Mn_4^{II} precursors. Oxidation in the presence of Ca^{2+} leads to a $CaMn_4O_2$ model of the OEC, underscoring the utility of low-symmetry multinucleating ligands in the synthesis of hitherto unobserved oxo-bridged multimetallic core geometries related to the OEC.

Chapter 3 presents a series of $[Mn^{III}Mn_3^{IV}O_4]$ cuboidal complexes as spectroscopic models of the S_2 state of the OEC. Such complexes resemble the oxidation state and EPR spectra of the S_2 state, and the effect of systematic changes in the nature of the bridging ligands on spectroscopy was studied. Results show that the electronic structure of tetranuclear Mn complexes is highly sensitive to even small geometric changes and the nature of the bridging ligands. Model studies suggest that the spectroscopic properties of the OEC may also react very sensitively to small changes in structure; the effect of protonation state and other reorganization processes needs to be carefully assessed.

Chapter 4 presents a series of $[YMn_3O_4]$ complexes as models of the $[CaMn_3O_4]$ subsite of the OEC. The effect of systematic changes in the basicity and chelating properties of the bridging ligands on redox potential was studied. Results show that in the absence of ligand-induced geometric distortions that enforce a contraction of metal-oxo distances, increasing the basicity of the ligands results in a decrease of cluster reduction potential. A small contraction of metal-oxo/metal-metal distances by ~0.1 Å enforced by a chelating ligand results in an increase of cluster reduction potential even in the presence of strong basic donors. Such small, protein-induced changes in Ca-oxo/Ca-Mn distances may have a similar effect in tuning the redox potential of the OEC through entatic states, and may explain the cation size dependence on the progression of the S-state cycle.

Chapter 5 presents a series of $[CaMn_3O_4]$ and $[YMn_3O_4]$ complexes as models of the $[CaMn_3O_4]$ subsite of the OEC. The effect of systematic changes in cluster geometry, heterometal identity, and bridging oxo protonation on cluster spin state structure was studied. Results show that the electronic structure of the Mn_3^{IV} core is highly sensitive to small geometric changes, the nature of the bridging ligands, and the protonation state of the bridging oxos: the spin ground states of essentially isostructural compounds can be $S = 3/2$, 5/2, or 9/2. Interpretation of EPR signals and subsequent structural assignments based on an $S = 9/2$ spin state of the $CaMn_3O_4$ subsite of the OEC must be done very cautiously.

While unfinished, appendices 1 and 2 present other important aspect in OEC model chemistry. Appendix 1 presents the synthesis of ^{17}O-labeled $[Mn^{III}Mn_3^{IV}O_4]$ and $[CaMn_3^{IV}O_4]$ complexes as models of the OEC. Ongoing characterization of μ^3-oxos in such complexes provide valuable benchmarking parameters for future mechanistic studies. Appendix 2 presents the synthesis and characterization of $[Mn_4^{IV}O_4]$ cuboidal complexes as spectroscopic models of the S_3 state of the OEC, the last observable intermediate prior to O−O bond formation at the OEC.

PUBLISHED CONTENT AND CONTRIBUTIONS

Parts of this thesis have been adapted from articles co-written by the author.

"A $CaMn_4O_2$ model of the biological oxygen evolving complex: synthesis via cluster expansion on a low symmetry ligand" Heui Beom Lee, Emily Y. Tsui, and Theodor Agapie. *Chem. Commun.*, **2017**, *53*, 6832-6835. DOI: 10.1039/c7cc02313h
H. B. L. performed experiments, obtained data, and wrote the manuscript.

"Tetranuclear $[Mn^{III}Mn_3^{IV}O_4]$ Complexes as Spectroscopic Models of the S_2 State of the Oxygen Evolving Complex in Photosystem II" Heui Beom Lee, Angela A. Shiau, Paul H. Oyala, David A. Marchiori, Sheraz Gul, Ruchira Chatterjee, Junko Yano, R. David Britt, and Theodor Agapie. *J. Am. Chem. Soc.*, **2018**, *140*, 17175-17187.
DOI: 10.1021/jacs.8b09961
H. B. L. performed synthesis, obtained EPR spectra and magnetometry data, and wrote the majority of the manuscript.

The following articles were reproduced in part with permission from the American Chemical Society:

"Support for a dimer of di-μ-oxo dimers model for the photosystem II manganese aggregate. Synthesis and properties of $[(Mn_2O_2)_2(tphpn)_2](ClO_4)_4$" Michael K. Chan and William H. Armstrong. *J. Am. Chem. Soc.* **1991**, *113*, 5055-5057.
DOI: 10.1021/ja00013a049

"Distorted manganese cubane $[Mn_4O_3Cl]^{6+}$ complexes with arenecarboxylate ligation: crystallographic, magnetochemical, and spectroscopic characterization" Michael W. Wemple, Hui-Lien Tsai, Kirsten Folting, David N. Hendrickson, and George Christou. *Inorg. Chem.* **1993**, *32*, 2025-2031. DOI: 10.1021/ic00062a026

"Aqueous Chemistry of High-Valent Manganese. Structure, Magnetic, and Redox Properties of a New Type of Mn-Oxo Cluster, $[Mn_4^{IV}O_4(bpy)_6]^{4+}$: Relevance to the Oxygen Evolving Center in Plants" Christian Philouze, Genevieve Blondin, Jean-Jacques Girerd, Jean Guilhem, Claudine Pascard, and Doris Lexa. *J. Am. Chem. Soc.* **1994**, *116*, 8557-8565. DOI: 10.1021/ja00098a016

"Modeling the Photosynthetic Water Oxidation Center: Chloride/Bromide Incorporation and Reversible Redox Processes in the Complexes $Mn_4O_3X(OAc)_3(dbm)_3$ (X = Cl, Br) and $(pyH)_3[Mn_4O_3Cl_7(OAc)_3]$" Sheyi Wang, Hui-Lien Tsai, Eduardo Libby, Kirsten Folting, William E. Streib, David N. Hendrickson, and George Christou. *Inorg. Chem.* **1996**, *35*, 7578-7589. DOI: 10.1021/ic9601347

"A Spin Topological Model for the g = 4.1 S_2 State Photosystem II Water Oxidase Manganese Aggregate" Christopher E. Dube, Roberta Sessoli, Michael P. Hendrich, Dante Gatteschi, and William H. Armstrong. *J. Am. Chem. Soc.* **1999**, *121*, 3537-3538. DOI: 10.1021/ja9840910

"Protonation and Dehydration Reactions of the $Mn_4O_4L_6$ Cubane and Synthesis and Crystal Structure of the Oxidized Cubane $[Mn_4O_4L_6]^+$: A Model for the Photosynthetic Water Oxidizing Complex" Wolfgang F. Ruettinger, Douglas M. Ho, and G. Charles Dismukes. *Inorg. Chem.* **1999**, *38*, 1036-1037. DOI: 10.1021/ic981145y

"^{55}Mn ENDOR of the S_2-State Multiline EPR Signal of Photosystem II: Implications on the Structure of the Tetranuclear Mn Cluster" Jeffrey M. Peloquin, Kristy A. Campbell, David W. Randall, Marc A. Evanchik, Vincent L. Pecoraro, William H. Armstrong, and R. David Britt. *J. Am. Chem. Soc.* **2000**, *122*, 10926-10942. DOI: 10.1021/ja002104f

"Tuning Tetranuclear Manganese–Oxo Core Electronic Properties: Adamantane-Shaped Complexes Synthesized by Ligand Exchange" Christopher E. Dube, Sumitra Mukhopadhyay, Peter J. Bonitatebus, Jr., Richard J. Staples, and William H. Armstrong. *Inorg. Chem.* **2005**, *44*, 5161-5175. DOI: 10.1021/ic050183w

"On the Magnetic and Spectroscopic Properties of High-Valent Mn_3CaO_4 Cubanes as Structural Units of Natural and Artificial Water-Oxidizing Catalysts" Vera Krewald, Frank Neese, and Dimitrios A. Pantazis. *J. Am. Chem. Soc.* **2013**, *135*, 5726-5739. DOI: 10.1021/ja312552f

"Tetranuclear $[Mn^{III}Mn_3^{IV}O_4]$ Complexes as Spectroscopic Models of the S_2 State of the Oxygen Evolving Complex in Photosystem II" Heui Beom Lee, Angela A. Shiau, Paul H. Oyala, David A. Marchiori, Sheraz Gul, Ruchira Chatterjee, Junko Yano, R. David Britt, and Theodor Agapie. *J. Am. Chem. Soc.* **2018**, *140*, 17175-17187. DOI: 10.1021/jacs.8b09961

The following articles were reproduced in part with permission from the Royal Society of Chemistry:

"Electron paramagnetic resonance study of the S = 1/2 ground state of a radiolysis-generated manganese(III)–trimanganese(IV) form of $[Mn^{IV}_4O_6(bipy)_6]^{4+}$ (bipy = 2,2′-bipyridine). Comparison with the photosynthetic Oxygen Evolving Complex" Geneviève Blondin, Roman Davydov, Christian Philouze, Marie-France Charlot, tenbjörn Styring, Björn Åkermark, Jean-Jacques Girerd, and Alain Boussac. *J. Chem. Soc., Dalton Trans.* **1997**, 4069-4074. DOI: 10.1039/A703381H

"Role of oxido incorporation and ligand lability in expanding redox accessibility of structurally related Mn_4 clusters" Jacob S. Kanady, Rosalie Tran, Jamie A. Stull, Luo Lu, Troy A. Stich, Michael W. Day, Junko Yano, R. David Britt, and Theodor Agapie. *Chem. Sci.* **2013**, *4*, 3986-3996. DOI:10.1039/C3SC51406D

"$CaMn_4O_2$ Model of the Biological Oxygen Evolving Complex: Synthesis by Cluster Expansion on Low Symmetry Ligand" Heui Beom Lee, Emily Y. Tsui, and Theodor Agapie. *Chem. Commun.* **2017**, *53*, 6832-6835. DOI: 10.1039/c7cc02313h

The following article was reproduced in part with permission from the American Association for the Advancement of Science:

"A synthetic Mn_4Ca-cluster mimicking the oxygen-evolving center of photosynthesis" Chunxi Zhang, Changhui Chen, Hongxing Dong, Jian-Ren Shen, Holger Dau, and Jingquan Zhao. *Science* **2015**, *348*, 690-693. DOI: 10.1126/science.aaa6550

TABLE OF CONTENTS

CHAPTER 1

Synthesis, Electronic Structure, and Spectroscopy of Multinuclear Mn Complexes Relevant to the Oxygen Evolving Complex of Photosystem II

1.1) S-state intermediates in the oxygen evolving complex of Photosystem II

In photosynthetic organisms such as plants and cyanobacteria, water oxidation takes place at the oxygen evolving complex (OEC) of Photosystem II (PSII).[1-3] At 1.9 Å resolution, the active site of the OEC has been characterized crystallographically, revealing a heterometallic [Mn_3CaO_4] cubane motif bearing a pendant Mn via a bridging oxide or hydroxide (Figure 1a).[4] The OEC catalyzes the $4e^-/4H^+$ oxidation of two water molecules to dioxygen; the corresponding cathodic half reaction involves the synthesis of plastoquinol and adenosine triphosphate (ATP), both of which are used for CO_2 fixation in the Calvin cycle. Given broad fundamental interest and potential application in the development of improved synthetic water oxidation catalysts, the structure of the OEC and the mechanism of water oxidation has been the subject of extensive biochemical, spectroscopic, synthetic, and computational studies.[5-23] Despite such efforts, many aspects of the OEC remain debated: (1) the mechanism of cluster assembly and O_2 formation, (2) structural changes in the OEC as it proceeds through the catalytic cycle, (3) electronic structure of the intermediates, and (4) the role of calcium.

Mechanistic studies are performed in the context of the Joliot-Kok cycle of S_n ($n = 0-4$) states.[24-25] Starting from the most reduced S_0 form, light-induced sequential one-electron oxidations lead to progression to higher S_n states, culminating in the formation of the elusive S_4 state, where O_2 formation is proposed to occur (Figure 1b).[26] Importantly, four oxidizing equivalents are stored in the OEC prior to O−O bond formation, precluding the generation and release of harmful products such as peroxide or superoxide.[27] Thus, precise spatial and temporal resolution in the sequence of electron-transport, proton-transport, and substrate binding events is necessary to fully understand the mechanism of biological water

oxidation. Structural determination and spectroscopic characterization of S_n state intermediates heavily influence mechanistic proposals for O−O bond formation.[5, 7, 9, 13, 16, 19, 28-32]

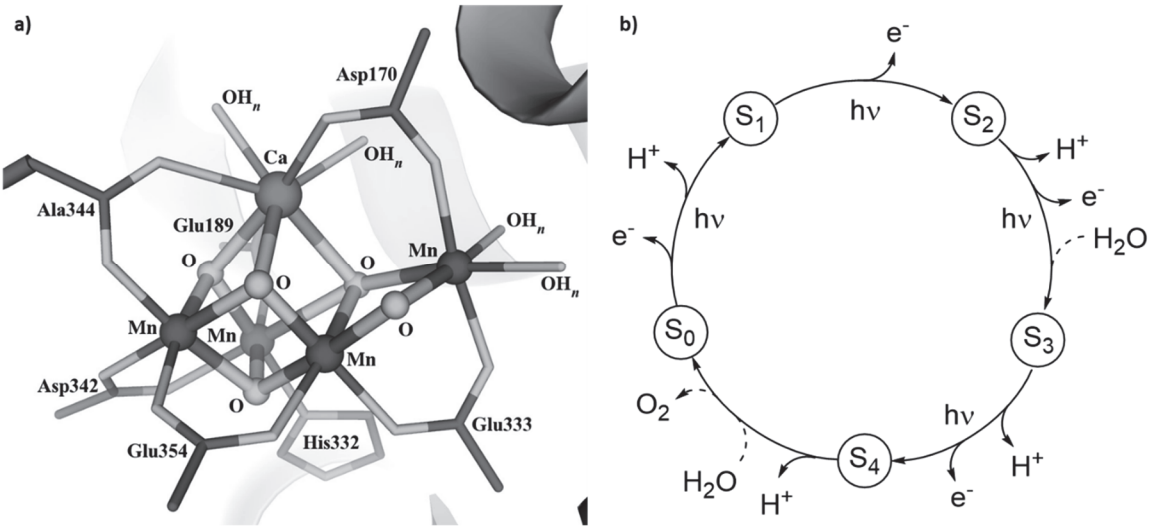

Figure 1. a) The OEC as described by the 1.9 Å resolution structure highlighting the $CaMn_4O_5$ core. b) The Joliot-Kok S-state catalytic cycle.

The dark-stable, resting S_1 state of the OEC has been the primary target of structural methods such as X-ray absorption spectroscopy and protein crystallography.[33-35] The 1.9 Å, atomic resolution model indicates that the structure of the OEC consists of a $CaMn_3$ subsite with a pendant Mn center, with bridging oxo moieties (Figure 1a).[4] It has been subsequently shown that X-ray induced Mn reduction resulted in a structural model that must be considered as a spatially averaged representation of physiological and non-physiological states.[36] This problem can be mitigated by using X-ray free electron laser (XFEL) pulses.[37-41] Although issues with S-state heterogeneity and resolution need to be addressed, XFEL studies offer the possibility of observing structural and spectroscopic changes in the OEC under dynamic conditions.[42]

A significant level of insight derived from EPR spectroscopy and related magnetic resonance techniques has been obtained for the S_2 state, which features two characteristic

EPR signals at $g = 2$ and $g = 4.1$.[5, 7-8, 30] The relative intensity of the two signals is condition-dependent, and each signal is proposed to originate from different structures (Figure 2): an open-cubane structure with a low-spin (LS) $S = 1/2$ ground state and a closed-cubane structure with a high-spin (HS) $S = 5/2$ ground state.[6, 12, 15, 43] The interconvertibility of the two EPR signals suggests a small energy difference between these two structures, which effectively differ only by the relative position of the bridging O(5) oxygen, a proposed substrate oxygen.[44-45] EXAFS studies support structural differences between the species responsible for the $g = 2$ and the $g = 4.1$ signal, but further atomistic details are unknown.[20, 46]

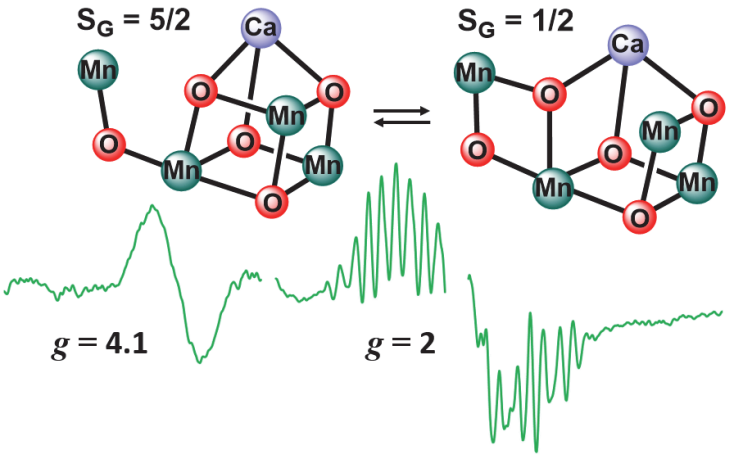

Figure 2. Proposed closed-cubane ($S = 5/2$) and open-cubane ($S = 1/2$) isomers of the S_2 state, giving rise to X-band EPR signals at $g = 4.1$ and $g = 2$, respectively.

Chemical changes such as Ca^{2+} removal or treatment with NH_3 or F^- inhibit the $S_2 \rightarrow S_3$ transition specifically, highlighting opportunities for mechanistic insight, but also the need for benchmarking with well characterized synthetic models to address the effect of structure on electronic structure and spectroscopy.[19, 47] Growing experimental data support that conversion from the LS form of the S_2 state to its HS form is an intermediate step in the $S_2 \rightarrow S_3$ transition.[17] pH dependence studies indicate that deprotonation of the LS form leads to the HS form.[21] Structural changes following deprotonation are unknown, but

computational studies suggest that the electronic structure of the OEC is highly sensitive to small changes in structure as reported by EPR spectroscopy.[10] Deprotonation of a Mn-bound water and/or a reorientation of a Glu residue in the S_2 state may perturb the spin state from LS to HS, indicating that spectroscopic properties may react very sensitively to small geometric changes that do not affect significantly the total energy of the cluster.

Synthetic cluster models have been targeted to benchmark the spectroscopy and to mimic the reactivity of the OEC. In general, systematic studies that probe the effect of small structural changes on the spectroscopic and magnetic properties of S-state model clusters are very rare, likely due to the synthetic challenges of accessing a series of isolable clusters that are suitable for comparisons.[48-49] Indeed, despite significant efforts to prepare tetra- and penta-nuclear clusters that are relevant to the S-state intermediates in terms of structure, reactivity, redox state, or spectroscopy, accurate models for benchmarking against the biological system are rare.[22, 50-54] In the following sections, structurally characterized tetranuclear Mn complexes with oxidation states relevant to S_0–S_3 states ($Mn_3^{III}Mn^{IV}$–Mn_4^{IV}) are surveyed, primarily focusing on aspects of electronic structure and EPR spectroscopy. In Chapter 3, a series of structurally related $[Mn^{III}Mn_3^{IV}O_4]$ cuboidal complexes as spectroscopic models of the S_2 state are highlighted.[22]

1.2) Mixed-valent $Mn^{III}Mn^{IV}$ dinuclear systems

Although structurally not related to the OEC, oxo-bridged, mixed-valent $[Mn^{III}Mn^{IV}O_2]^{3+}$ complexes feature EPR spectra that are highly reminiscent of the multiline signal observed in the S_2 state.[15, 55-58] The nature of the exchange coupling interaction in such complexes is typically antiferromagnetic, ranging from $J = -100$ to -400 cm^{-1}.[59] Accordingly, the ground state in these systems is $S = 1/2$, and broad EPR transitions

centered at $g = 2$ featuring Mn hyperfine interactions are observed (Figure 3). Analysis of the ENDOR spectra of $[Mn_2O_2(bpy)_4]^{3+}$ allowed the unambiguous assignment of ^{55}Mn nuclear spin transitions of both the Mn^{III} and Mn^{IV} ions.[56] Parameters found for the dimeric species failed to simulate the ^{55}Mn ENDOR spectrum of the S_2 state, easily ruling out the dimeric origin of the multiline signal in the S_2 state. The deduction of a "3+1" arrangement of Mn ions in the OEC by ENDOR spectroscopy prior to the advent of atomic resolution crystal structures is a landmark assignment from EPR spectroscopy.[8] The interaction of ligand nuclei (e.g. ^{1}H, ^{2}H, ^{13}C, ^{14}N, ^{15}N, ^{17}O) with the electron spin of the Mn centers has been studied by pulsed EPR techniques to obtain structural information and determine plausible sites of substrate water binding.[13, 19] Pulse-EPR data for ^{17}O-labelled dinuclear complexes have provided a magnetic fingerprint for bridging oxo ligands similar to those found in the OEC.[57] In the following sections, a selective survey of structurally characterized tetranuclear Mn complexes will be presented, with an emphasis on electronic structure as probed by magnetic susceptibility and EPR studies.

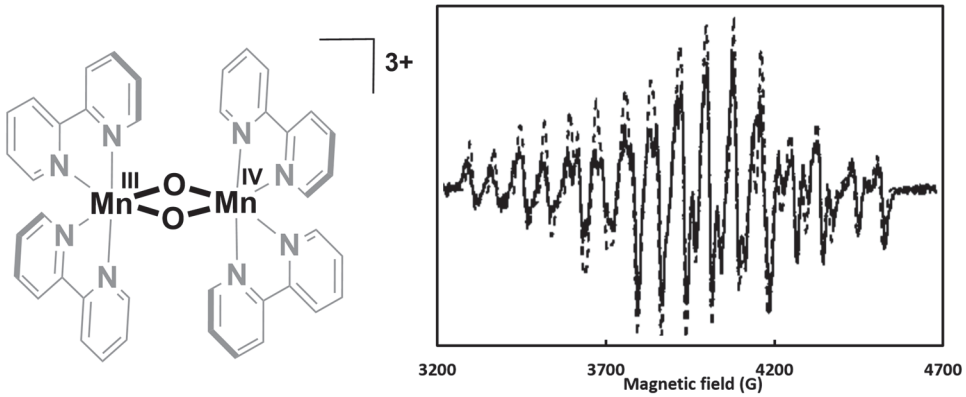

Figure 3. Structure of $[Mn_2O_2(bpy)_4]^{3+}$ and its X-band EPR spectrum.

1.3) $Mn_3^{III}Mn^{IV}$ complexes as models of the S_0 state of the OEC

A class of carboxylate-bridged $Mn_3^{III}Mn^{IV}$ complexes with a general $[Mn_4O_3X]^{6+}$ core ($X^- = F^-$, Cl^-, Br^-, NO_3^-, OH^-, OCH_3^-, OPh^-, OAc^-, OBz^-, N_3^-, or NCO^-) has been

described.[60-69] Single crystal X-ray crystal structures reveal a *pseudo*-C_3 symmetric core with the μ^3–X ligand bridging the three Mn^{III} centers (Figure 4). Each metal center is 6-coordinate, with the coordination sphere of the Mn^{IV} center occupied by three carboxylates and three oxo ligands. Monodentate ligands such as Cl^- or heterocycles such as pyridine or imidazole bind in a *cis* fashion to complete the coordination sphere of each Mn^{III} center. Clusters with bidentate ligands such as dibenzoylmethane (dbm) have also been reported (Figure 4).

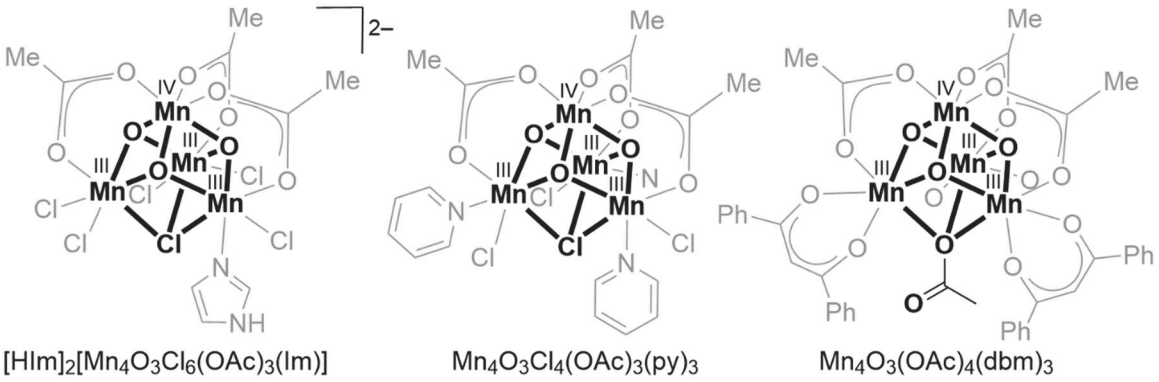

Figure 4. Examples of carboxylate bridged $Mn_3^{III}Mn^{IV}$ complexes with a $[Mn_4O_3X]^{6+}$ core.

Magnetic susceptibility studies are consistent with a well-isolated $S = 9/2$ ground state, consistent with the Curie behavior observed between 5−50 K (Figure 5). The sudden decrease in the effective magnetic moment below 5 K was attributed in part to the presence of zero field splitting. From reduced magnetization data, a positive axial zero-field splitting parameter in the range of the X-band EPR quanta (c.a. 0.3 cm^{-1}) has been estimated (Figure 5). To fit the susceptibility data, an exchange coupling model with two coupling constants $J(Mn^{III}–Mn^{IV})$ and $J(Mn^{III}–Mn^{III})$ has been employed. Invariably, for the series of compounds with different X^-, bridging carboxylate, and terminal ligands, the $J(Mn^{III}–Mn^{IV})$ coupling was found to be antiferromagnetic, with values in the range of −30 to −20 cm^{-1}; the $J(Mn^{III}–Mn^{III})$ coupling was found to be ferromagnetic, with values in the range +2 to

+11 cm^{-1}. The first excited state $S = 7/2$ was estimated to lie c.a. 200 cm^{-1} above the $S = 9/2$ ground state. Accordingly, the variable temperature EPR spectra of these complexes do not show significant population of spin excited states; aside from line broadening, the spectrum at 5 K is nearly identical to that at 78 K (Figure 6).[69] The transitions occurring within the $|\pm 1/2\rangle$ Kramers doublet were observed at $g = 8.2$ and $g = 2$. The feature at $g = 5.2$ was tentatively assigned to the $|-1/2\rangle \rightarrow |-3/2\rangle$ transition.[64] In contrast to the electronic structure of $[Mn_4O_3X]^{6+}$ complexes, the ground state of the S_0 state of the OEC has been shown to be $S = 1/2$, with a broad multiline EPR signal centered at $g = 2$.[70] Although not structurally characterized, in situ one electron reduction of $[(Mn_2O_2)_2(tphpn)_2]^{4+}$ (*vide infra*) leads to a species with an EPR spectrum reminiscent of the S_0 state.[71]

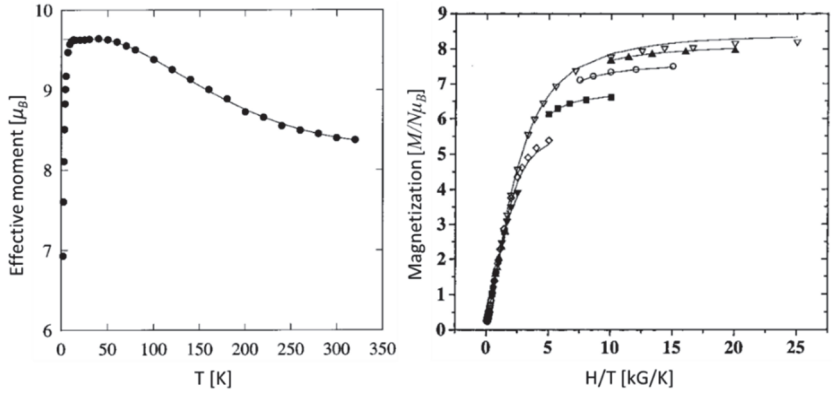

Figure 5. Temperature dependence of the effective moment (left) and reduced magnetization plot (right) of $Mn_4O_3(OAc)_4(dbm)_3$.

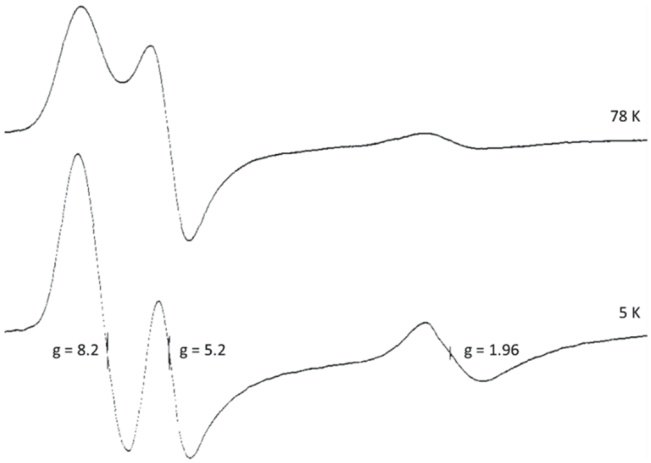

Figure 6. X-band EPR spectra of $Mn_4O_3Cl_4(OBz)_3(py)_3$.

1.4) $Mn_2^{III}Mn_2^{IV}$ complexes as models of the S_1 state of the OEC

Three classes of $Mn_2^{III}Mn_2^{IV}$ complexes have been described: (1) cubane complexes with a $[Mn_4O_4]^{6+}$ core,[51, 72] (2) square complexes that can be described as an alkoxide bridged dimer of two $[Mn_2O_2]^{3+}$ units,[73] and (3) a unique $[CaMn_4O_4]^{8+}$ complex highly reminiscent of the OEC featuring a $[CaMn_3O_4]$ subsite with a dangling Mn ion (Figure 7).[54] Thus far, magnetic susceptibility studies of these complexes have not been reported. The parallel mode X-band EPR of $[(Mn_2O_2)_2(tphpn)_2]^{4+}$ shows a broad signal at $g = 6$; the EPR spectrum of the $[CaMn_4O_4]^{8+}$ complex shows a broad signal at $g = 12$ (Figure 7).

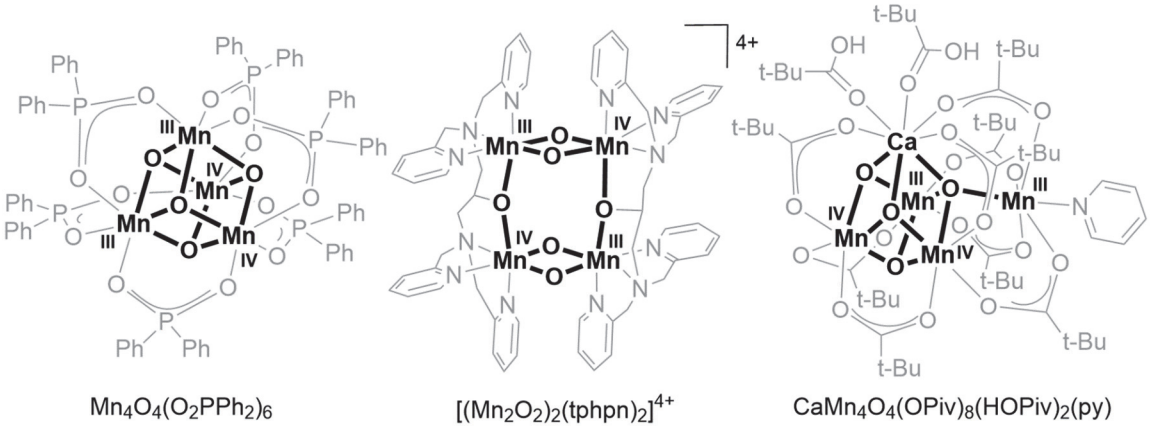

Figure 7. Examples of $Mn_2^{III}Mn_2^{IV}$ complexes.

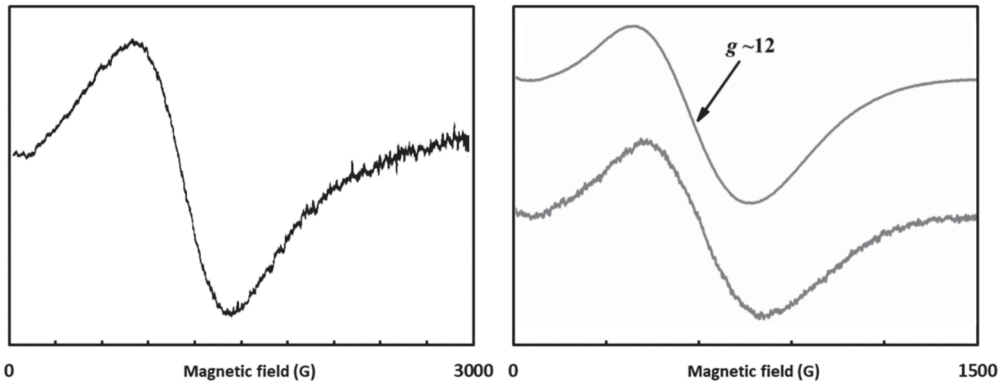

Figure 8. Parallel mode X-band EPR of $[(Mn_2O_2)_2(tphpn)_2]^{4+}$ (left) and $CaMn_4O_4(OPiv)_8$ (right).

For the S_1 state, parallel mode signals at $g = 4.9$ and $g = 12$ have been observed.[74-76] Temperature dependence studies on the S_1 state indicate that these two signals arise from

spin excited states $S = 1$ and $S = 2$, respectively, and that the S_1 state has a diamagnetic ground state.[76] Magnetic studies of the cubane cluster $LMn_2^{III}Mn_2^{IV}O_4(OAc)_3$ reported by our group indicate an $S = 1$ ground state, consistent with the observed χT value of 0.9 emu K mol^{-1} at 5 K.[77] The perpendicular EPR spectrum shows a broad signal centered at $g = 2$, and was rationalized as coming from the $S = 1$ ground state with a small zero field splitting (Figure 9).[78]

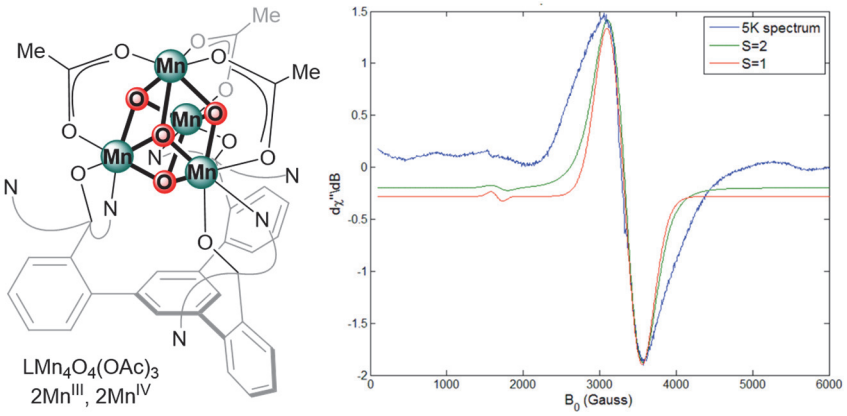

Figure 9. Perpendicular mode X-band EPR of $LMn_4O_4(OAc)_3$.

1.5) $Mn^{III}Mn_3^{IV}$ complexes as models of the S_2 state of the OEC

In addition to the extensive spectroscopic studies performed on the native S_2 state of the OEC, non-native, MeOH or NH_3 modified S_2 states have also been studied.[16, 19, 23, 31, 79] In contrast, structural and spectroscopic studies of $Mn^{III}Mn_3^{IV}$ model complexes remain rare. Three classes of synthetic $Mn^{III}Mn_3^{IV}$ complexes have been described: (1) cubane complexes with a $[Mn_4O_4]^{7+}$ core,[80] (2) adamantane-shaped complexes with a $[Mn_4O_6]^{3+}$ core,[81-82] and (3) linear-chain complexes with a $[Mn_4O_6]^{3+}$ core (Figure 10).[83] The phosphinate-bridged, cuboidal complex $[Mn_4O_4(Ph_2PO_2)_6]^+$ shows a broad EPR spectrum with transitions consistent with an $S \geq 3/2$ ground state (Figure 11).[80] Complementary susceptibility studies have not been provided. The EPR spectrum of the adamantane-shaped complex $[Mn_4O_6(bpea)_4]^{3+}$ features a broad signal at $g = 4.1$ that has been assigned

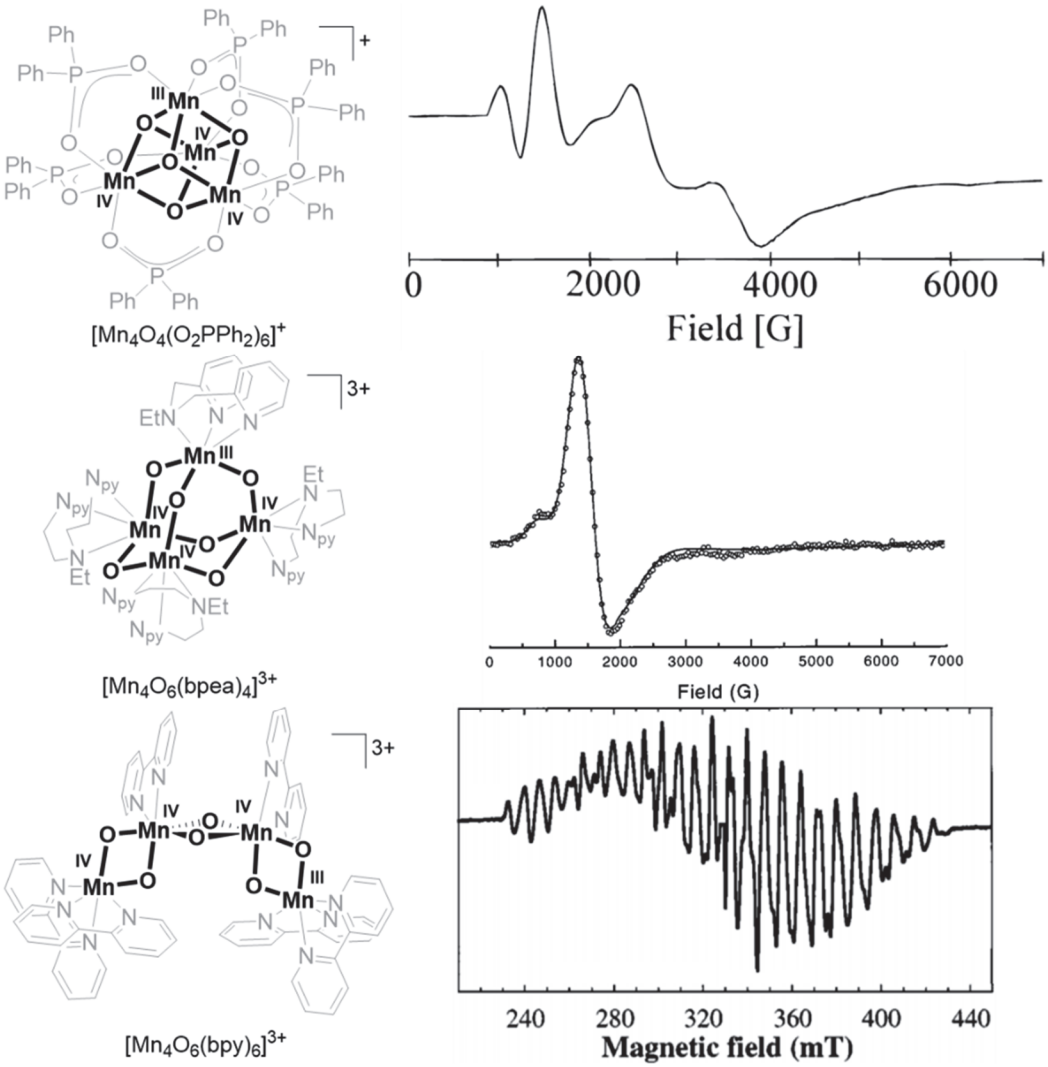

Figure 10. Examples of $Mn^{III}Mn_3^{IV}$ complexes and their corresponding X-band EPR spectra.

to the transition within the first excited $|\pm 3/2\rangle$ Kramers doublet of an $S = 5/2$ ground state determined from magnetization data.[81] This $g = 4.1$ signal is highly reminiscent of the high-spin form of the S_2 state. Starting from a structurally characterized linear-chain $[Mn_4O_6(bpy)_6]^{4+}$ precursor, a putative $[Mn_4O_6(bpy)_6]^{3+}$ complex was generated by radiolysis in a frozen matrix and its EPR spectrum features a multiline signal centered at $g = 2$ consistent with an $S = 1/2$ ground state.[83] In situ oxidation of a close OEC structural model complex, $CaMn_4O_4(OPiv)_8$ (*vide supra*, section 1.4.), gives rise to two EPR signals

at g = 4.9 and g = 2, attributed to different spin states of the cluster corresponding to a $[CaMn_4O_4(OPiv)_8]^+$ species, although further structural, spectroscopic, and magnetic data have not been provided.[54] Follow-up computational studies disagree on the assignment of the two signals, one of them suggesting that the two signals must be due to structurally very different clusters.[84-85]

In general, systematic studies akin to those performed on the S_2 state that probe the effect of small structural changes on the spectroscopic and magnetic properties of S_2 model clusters are uncommon, likely due to the synthetic challenges of accessing a series of isolable clusters that are suitable for comparisons. A series of cuboidal complexes in the relevant $Mn^{III}Mn_3^{IV}$ redox state, with systematic variation of bridging ligands, has recently been reported and provides useful insight into structure-property relationships (Chapter 3).[22]

1.6) Mn_4^{IV} complexes as models of the S_3 state of the OEC

EPR spectroscopic studies show all Mn ions to be present as Mn(IV) in the S_3 state.[26] Similar to the S_2 state, the S_3 state is spectroscopically heterogeneous, with an EPR observable species having an S = 3 ground state.[1] The $S_2 \rightarrow S_3$ transition is highly debated, with the details of substrate water incorporation and deprotonation being largely unknown. Broadly, two general classes of synthetic tetranuclear Mn_4^{IV} complexes have been described related to S_3: linear complexes featuring $[Mn_4O_5]^{6+}$ and $[Mn_4O_6]^{4+}$ cores, and adamantane-shaped complexes with $[Mn_4O_6]^{4+}$ cores (Figure 11).[86-88]

For the linear complexes, strong pair-wise antiferromagnetic exchange coupling interactions lead to a diamagnetic ground state. An EPR spectrum has been reported at 140 K from the population of thermally accessible spin excited states, but further

characterization has not been provided.[88] Magnetic susceptibility studies of a series of adamantane-shaped $[Mn_4O_6]^{4+}$ complexes indicate overall ferromagnetic exchange coupling interactions giving rise to an $S = 6$ ground state (Figure 12).[89] EPR studies for the adamantane-shaped complexes have not been reported. Upon protonation of a bridging oxo, the overall ferromagnetic interaction in the adamantane-shaped $[Mn_4O_6]^{4+}$ complex was found to switch to antiferromagnetic, but spectroscopic studies have not been reported.[90] A unique cuboidal $[Mn_4^{IV}O_4]$ cluster mirroring the spin state of the S_3 state has been reported (Appendix 2).

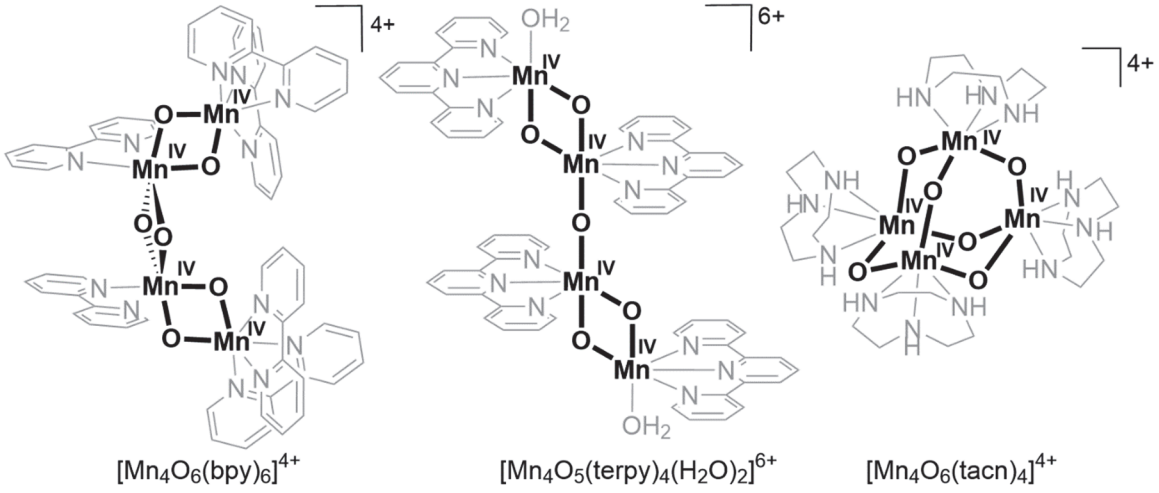

Figure 11. Examples of Mn_4^{IV} complexes.

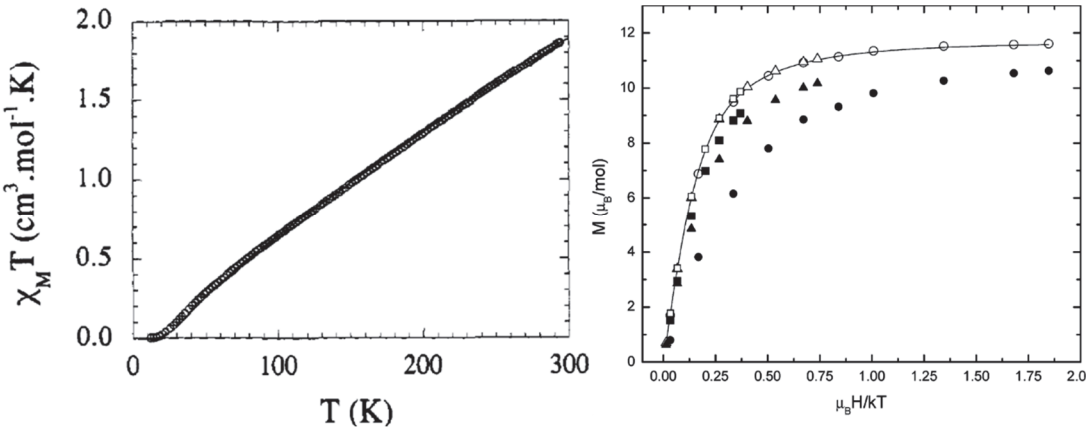

Figure 12. (Left) χT vs. T plot of the linear $[Mn_4O_6(bpy)_6]^{4+}$ complex showing a diamagnetic ground state. (Right) Reduced magnetization plot of the adamantane-shaped $[Mn_4O_6(tacn)_4]^{4+}$ complex showing a high-spin $S = 6$ ground state.

1.7) Structurally related Mn_4 clusters on a rigid multinucleating scaffold

Toward developing a methodology to access Mn clusters related to the OEC that can be systematically changed to provide rational access to different metal arrangement, oxo content, and heterometal content, a geometrically restricted, multinucleating ligand was employed. Stepwise protocols toward the synthesis of tetra- and pentanuclear complexes have been described.[22, 50-51, 53, 77-78, 91-96] For the series of tetranuclear Mn complexes relevant to the OEC, initial metalation of H_3L with $Mn(OAc)_2$ leads to the trinuclear complex $LMn_3(OAc)_3$.[97] Oxidation of $LMn_3(OAc)_3$ with KO_2 in the presence of $Ca(OTf)_2$ leads to the formation of the Ca cubane complex $LCaMn_3O_4(OAc)_3(THF)$ (Figure 13).[51] Substitution of Ca^{2+} with Mn^{2+} leads to the formation of $LMn_2^{III}Mn_2^{IV}O_4(OAc)_3$. From this complex, oxygen-atom transfer reactivity has been studied, with addition of PMe_3 resulting in the formation of $LMn_4^{III}O_3(OAc)_3$.[77] Reoxidation in the presence of labelled water has been demonstrated and computational studies suggest oxide bridge movements reminiscent of the proposal for O(5) in the OEC. Depending on the synthetic procedure, lower oxidation state tetranuclear complexes with cores $[Mn_3^{II}Mn^{III}O]^{7+}$, $[Mn_2^{II}Mn_2^{III}O]^{8+}$, and

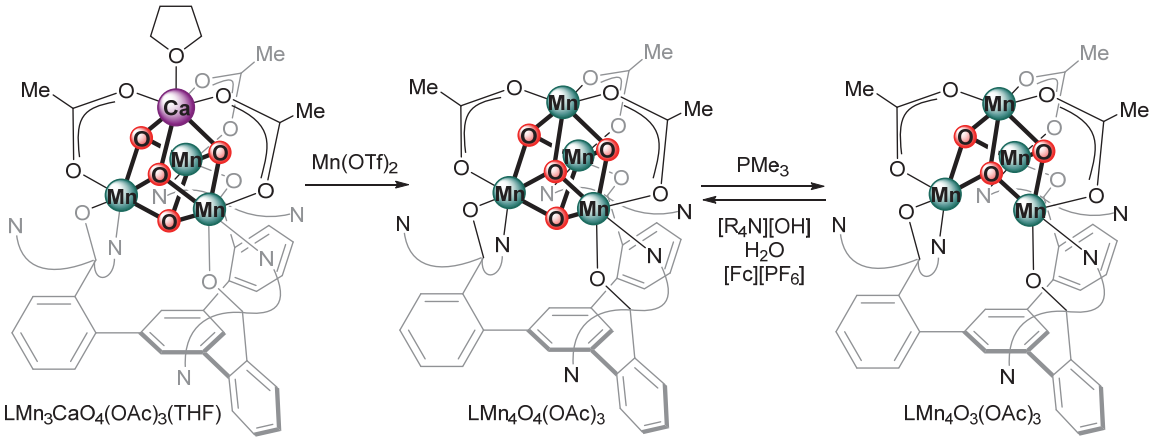

Figure 13. Synthesis of tetranuclear Mn complexes supported by a geometrically rigid multinucleating ligand.

$[Mn_2^{II}Mn_2^{III}O_2]^{6+}$ have been obtained, underscoring the flexibility of the ligand scaffold in stabilizing tetranuclear Mn complexes of different oxidation states.[78]

1.8) Concluding remarks

In the absence of direct and unambiguous structural data, proposals for the mechanism of water oxidation have relied heavily on the spectroscopic characterization of S-state intermediates. Spectroscopic features were interpreted in terms of structural implications, but studies that probe the effect of structural changes on the electronic structure and spectroscopy of relevant tetranuclear Mn complexes remain rare. In this chapter, tetranuclear Mn complexes with oxidation states corresponding to the S_0−S_3 states have been surveyed. With the exception of a special $[CaMn_4O_4(OPiv)_8]$ case, most tetranuclear complexes fall within a small number of structure types: cuboidal, square, linear, or adamantane-shaped. Although magnetic susceptibility and spectroscopic studies indicate that the spin ground state correlates with the cluster geometry, with linear clusters generally having low-spin ground states while cuboidal and adamantane clusters having higher spin ground states, systematic studies within a series of structurally related complexes are rare. A versatile ligand platform that can support a variety of oxidation states and allow systematic changes to the nature of bridging and terminal ligands had been developed in our laboratories. While trends in redox potential and oxygen atom transfer reactivity have been studied, systematic structure−electronic structure studies on $[CaMn_3O_4]$ and $[Mn_4O_4]$ cuboidal complexes had not been performed. Given that spectroscopic studies have been invaluable for gaining insight into the nature of intermediates in the catalytic cycle of water oxidation by the OEC, benchmarking with synthetic clusters that are thoroughly

characterized structurally and spectroscopically is imperative to further inform the interpretation of such spectroscopic studies.

Given progress over recent years, goals such as the synthesis of more accurate structural models of the OEC and systematic structure−electronic structures studies may be within reach. Spectroscopic characterization of Mn_4 complexes in oxidation states relevant to S_2−S_4 will prove valuable for benchmarking against the biological system. Additionally, the influence of protonation state on electronic structure and ^{17}O labelling and spectroscopic characterization will provide further mechanistic insight. The following chapters detail efforts toward (1) the synthesis of pentanuclear $CaMn_4$ models of the OEC (Chapter 2), (2) electronic structure studies on $[Mn_4O_4]$ complexes as spectroscopic models of S_2 and S_3 states (Chapter 3 and Appendix 2), (3) effects of protonation and cluster desymmetrization on the electronic structure of $[CaMn_3O_4]$ complexes (Chapter 5), and (4) ^{17}O labelling and pulsed-EPR studies (Appendix 1). Importantly, geometrical changes much smaller than the ones proposed for the OEC with respect to the metal oxo/hydroxo motifs could have substantial effects on the EPR signals. Therefore, the deduction of the geometry of OEC S-state intermediates based on EPR spectroscopic features need to be complemented with appropriate structural determination, and further synthetic and spectroscopic studies on relevant OEC model complexes are encouraged.

1.9) References

(1) Pantazis, D. A., *ACS Catal.* **2018**, 9477.
(2) Shen, J.-R., *Annu. Rev. Plant Biol.* **2015,** *66*, 23.
(3) Yano, J.; Yachandra, V., *Chem. Rev.* **2014,** *114*, 4175.
(4) Umena, Y.; Kawakami, K.; Shen, J.-R.; Kamiya, N., *Nature* **2011,** *473*, 55.
(5) Boussac, A.; Un, S.; Horner, O.; Rutherford, A. W., *Biochemistry* **1998,** *37*, 4001.
(6) Horner, O.; Rivière, E.; Blondin, G.; Un, S.; Rutherford, A. W.; Girerd, J.-J.; Boussac, A., *J. Am. Chem. Soc.* **1998,** *120*, 7924.
(7) Boussac, A.; Rutherford, A. W., *Biochim. Biophys. Acta* **2000,** *1457*, 145.

(8) Peloquin, J. M.; Campbell, K. A.; Randall, D. W.; Evanchik, M. A.; Pecoraro, V. L.; Armstrong, W. H.; Britt, R. D., *J. Am. Chem. Soc.* **2000,** *122*, 10926.
(9) Haddy, A.; Lakshmi, K. V.; Brudvig, G. W.; Frank, H. A., *Biophys. J.* **2004,** *87*, 2885.
(10) Ames, W.; Pantazis, D. A.; Krewald, V.; Cox, N.; Messinger, J.; Lubitz, W.; Neese, F., *J. Am. Chem. Soc.* **2011,** *133*, 19743.
(11) Cox, N.; Rapatskiy, L.; Su, J.-H.; Pantazis, D. A.; Sugiura, M.; Kulik, L.; Dorlet, P.; Rutherford, A. W.; Neese, F.; Boussac, A.; Lubitz, W.; Messinger, J., *J. Am. Chem. Soc.* **2011,** *133*, 3635.
(12) Pantazis, D. A.; Ames, W.; Cox, N.; Lubitz, W.; Neese, F., *Angew. Chem. Int. Ed.* **2012,** *51*, 9935.
(13) Rapatskiy, L.; Cox, N.; Savitsky, A.; Ames, W. M.; Sander, J.; Nowaczyk, M. M.; Rögner, M.; Boussac, A.; Neese, F.; Messinger, J.; Lubitz, W., *J. Am. Chem. Soc.* **2012,** *134*, 16619.
(14) Cox, N.; Pantazis, D. A.; Neese, F.; Lubitz, W., *Acc. Chem. Res.* **2013,** *46*, 1588.
(15) Lohmiller, T.; Ames, W.; Lubitz, W.; Cox, N.; Misra, S. K., *Appl. Magn. Reson.* **2013,** *44*, 691.
(16) Oyala, P. H.; Stich, T. A.; Stull, J. A.; Yu, F.; Pecoraro, V. L.; Britt, R. D., *Biochemistry* **2014,** *53*, 7914.
(17) Boussac, A.; Rutherford, A. W.; Sugiura, M., *Biochim. Biophys. Acta - Bioenergetics* **2015,** *1847*, 576.
(18) Gupta, R.; Taguchi, T.; Lassalle-Kaiser, B.; Bominaar, E. L.; Yano, J.; Hendrich, M. P.; Borovik, A. S., *Proc. Nat. Acad. Sci.* **2015,** *112*, 5319.
(19) Oyala, P. H.; Stich, T. A.; Debus, R. J.; Britt, R. D., *J. Am. Chem. Soc.* **2015,** *137*, 8829.
(20) Chatterjee, R.; Han, G.; Kern, J.; Gul, S.; Fuller, F. D.; Garachtchenko, A.; Young, I. D.; Weng, T.-C.; Nordlund, D.; Alonso-Mori, R.; Bergmann, U.; Sokaras, D.; Hatakeyama, M.; Yachandra, V. K.; Yano, J., *Chem. Sci.* **2016,** *7*, 5236.
(21) Boussac, A.; Ugur, I.; Marion, A.; Sugiura, M.; Kaila, V. R. I.; Rutherford, A. W., *Biochim. Biophys. Acta - Bioenergetics* **2018,** *1859*, 342.
(22) Lee, H. B.; Shiau, A. A.; Oyala, P. H.; Marchiori, D. A.; Gul, S.; Chatterjee, R.; Yano, J.; Britt, R. D.; Agapie, T., *J. Am. Chem. Soc.* **2018,** *140*, 17175.
(23) Marchiori, D. A.; Oyala, P. H.; Debus, R. J.; Stich, T. A.; Britt, R. D., *J. Phys. Chem. B* **2018,** *122*, 1588.
(24) Joliot, P., *Biochim. Biophys. Acta* **1965,** *102*, 116.
(25) Kok, B.; Forbush, B.; McGloin, M., *Photochem. Photobiol.* **1970,** *11*, 457.
(26) Cox, N.; Retegan, M.; Neese, F.; Pantazis, D. A.; Boussac, A.; Lubitz, W., *Science* **2014,** *345*, 804.
(27) Rutherford, A. W.; Osyczka, A.; Rappaport, F., *FEBS Lett.* **2012,** *586*, 603.
(28) Britt, R. D.; Lorigan, G. A.; Sauer, K.; Klein, M. P.; Zimmermann, J.-L., *Biochim. Biophys. Acta - Bioenergetics* **1992,** *1140*, 95.
(29) Dismukes, G. C.; Siderer, Y., *Proc. Nat. Acad. Sci.* **1981,** *78*, 274.
(30) Kim, D. H.; Britt, R. D.; Klein, M. P.; Sauer, K., *Biochemistry* **1992,** *31*, 541.
(31) Pérez Navarro, M.; Ames, W. M.; Nilsson, H.; Lohmiller, T.; Pantazis, D. A.; Rapatskiy, L.; Nowaczyk, M. M.; Neese, F.; Boussac, A.; Messinger, J.; Lubitz, W.; Cox, N., *Proc. Nat. Acad. Sci.* **2013,** *110*, 15561.
(32) Siegbahn, P. E. M., *Acc. Chem. Res.* **2009,** *42*, 1871.

(33) Ferreira, K. N.; Iverson, T. M.; Maghlaoui, K.; Barber, J.; Iwata, S., *Science* **2004,** *303*, 1831.
(34) Kamiya, N.; Shen, J.-R., *Proc. Nat. Acad. Sci.* **2003,** *100*, 98.
(35) Zouni, A.; Witt, H.-T.; Kern, J.; Fromme, P.; Krauss, N.; Saenger, W.; Orth, P., *Nature* **2001,** *409*, 739.
(36) Yano, J.; Kern, J.; Irrgang, K.-D.; Latimer, M. J.; Bergmann, U.; Glatzel, P.; Pushkar, Y.; Biesiadka, J.; Loll, B.; Sauer, K.; Messinger, J.; Zouni, A.; Yachandra, V. K., *Proc. Nat. Acad. Sci* **2005,** *102*, 12047.
(37) Kern, J.; Alonso-Mori, R.; Tran, R.; Hattne, J.; Gildea, R. J.; Echols, N.; Glöckner, C.; Hellmich, J.; Laksmono, H.; Sierra, R. G.; Lassalle-Kaiser, B.; Koroidov, S.; Lampe, A.; Han, G.; Gul, S.; DiFiore, D.; Milathianaki, D.; Fry, A. R.; Miahnahri, A.; Schafer, D. W.; Messerschmidt, M.; Seibert, M. M.; Koglin, J. E.; Sokaras, D.; Weng, T.-C.; Sellberg, J.; Latimer, M. J.; Grosse-Kunstleve, R. W.; Zwart, P. H.; White, W. E.; Glatzel, P.; Adams, P. D.; Bogan, M. J.; Williams, G. J.; Boutet, S.; Messinger, J.; Zouni, A.; Sauter, N. K.; Yachandra, V. K.; Bergmann, U.; Yano, J., *Science* **2013,** *340*, 491.
(38) Kern, J.; Tran, R.; Alonso-Mori, R.; Koroidov, S.; Echols, N.; Hattne, J.; Ibrahim, M.; Gul, S.; Laksmono, H.; Sierra, R. G.; Gildea, R. J.; Han, G.; Hellmich, J.; Lassalle-Kaiser, B.; Chatterjee, R.; Brewster, A. S.; Stan, C. A.; Glöckner, C.; Lampe, A.; DiFiore, D.; Milathianaki, D.; Fry, A. R.; Seibert, M. M.; Koglin, J. E.; Gallo, E.; Uhlig, J.; Sokaras, D.; Weng, T.-C.; Zwart, P. H.; Skinner, D. E.; Bogan, M. J.; Messerschmidt, M.; Glatzel, P.; Williams, G. J.; Boutet, S.; Adams, P. D.; Zouni, A.; Messinger, J.; Sauter, N. K.; Bergmann, U.; Yano, J.; Yachandra, V. K., *Nat. Commun.* **2014,** *5*, 4371.
(39) Kupitz, C.; Basu, S.; Grotjohann, I.; Fromme, R.; Zatsepin, N. A.; Rendek, K. N.; Hunter, M. S.; Shoeman, R. L.; White, T. A.; Wang, D.; James, D.; Yang, J.-H.; Cobb, D. E.; Reeder, B.; Sierra, R. G.; Liu, H.; Barty, A.; Aquila, A. L.; Deponte, D.; Kirian, R. A.; Bari, S.; Bergkamp, J. J.; Beyerlein, K. R.; Bogan, M. J.; Caleman, C.; Chao, T.-C.; Conrad, C. E.; Davis, K. M.; Fleckenstein, H.; Galli, L.; Hau-Riege, S. P.; Kassemeyer, S.; Laksmono, H.; Liang, M.; Lomb, L.; Marchesini, S.; Martin, A. V.; Messerschmidt, M.; Milathianaki, D.; Nass, K.; Ros, A.; Roy-Chowdhury, S.; Schmidt, K.; Seibert, M.; Steinbrener, J.; Stellato, F.; Yan, L.; Yoon, C.; Moore, T. A.; Moore, A. L.; Pushkar, Y.; Williams, G. J.; Boutet, S.; Doak, R. B.; Weierstall, U.; Frank, M.; Chapman, H. N.; Spence, J. C. H.; Fromme, P., *Nature* **2014,** *513*, 261.
(40) Suga, M.; Akita, F.; Hirata, K.; Ueno, G.; Murakami, H.; Nakajima, Y.; Shimizu, T.; Yamashita, K.; Yamamoto, M.; Ago, H.; Shen, J.-R., *Nature* **2014,** *517*, 99.
(41) Young, I. D.; Ibrahim, M.; Chatterjee, R.; Gul, S.; Fuller, F. D.; Koroidov, S.; Brewster, A. S.; Tran, R.; Alonso-Mori, R.; Kroll, T.; Michels-Clark, T.; Laksmono, H.; Sierra, R. G.; Stan, C. A.; Hussein, R.; Zhang, M.; Douthit, L.; Kubin, M.; de Lichtenberg, C.; Vo Pham, L.; Nilsson, H.; Cheah, M. H.; Shevela, D.; Saracini, C.; Bean, M. A.; Seuffert, I.; Sokaras, D.; Weng, T.-C.; Pastor, E.; Weninger, C.; Fransson, T.; Lassalle, L.; Bräuer, P.; Aller, P.; Docker, P. T.; Andi, B.; Orville, A. M.; Glownia, J. M.; Nelson, S.; Sikorski, M.; Zhu, D.; Hunter, M. S.; Lane, T. J.; Aquila, A.; Koglin, J. E.; Robinson, J.; Liang, M.; Boutet, S.; Lyubimov, A. Y.; Uervirojnangkoorn, M.; Moriarty, N. W.; Liebschner, D.; Afonine, P. V.; Waterman, D. G.; Evans, G.; Wernet, P.; Dobbek, H.; Weis, W. I.; Brunger, A. T.; Zwart, P. H.; Adams, P. D.; Zouni, A.; Messinger, J.; Bergmann, U.; Sauter, N. K.; Kern, J.; Yachandra, V. K.; Yano, J., *Nature* **2016,** *540*, 453.

(42) Sauter, N. K.; Echols, N.; Adams, P. D.; Zwart, P. H.; Kern, J.; Brewster, A. S.; Koroidov, S.; Alonso-Mori, R.; Zouni, A.; Messinger, J.; Bergmann, U.; Yano, J.; Yachandra, V. K., *Nature* **2016,** *533*, E1.

(43) Lohmiller, T.; Krewald, V.; Navarro, M. P.; Retegan, M.; Rapatskiy, L.; Nowaczyk, M. M.; Boussac, A.; Neese, F.; Lubitz, W.; Pantazis, D. A.; Cox, N., *Phys. Chem. Chem. Phys.* **2014,** *16*, 11877.

(44) Bovi, D.; Narzi, D.; Guidoni, L., *Angew. Chem. Int. Ed.* **2013,** *52*, 11744.

(45) Vinyard, D. J.; Khan, S.; Askerka, M.; Batista, V. S.; Brudvig, G. W., *J. Phys. Chem. B* **2017,** *121*, 1020.

(46) Liang, W.; Latimer, M. J.; Dau, H.; Roelofs, T. A.; Yachandra, V. K.; Sauer, K.; Klein, M. P., *Biochemistry* **1994,** *33*, 4923.

(47) DeRose, V. J.; Latimer, M. J.; Zimmermann, J.-L.; Mukerji, I.; Yachandra, V. K.; Sauer, K.; Klein, M. P., *Chem. Phys.* **1995,** *194*, 443.

(48) Mukhopadhyay, S.; Mandal, S. K.; Bhaduri, S.; Armstrong, W. H., *Chem. Rev.* **2004,** *104*, 3981.

(49) Mullins, C. S.; Pecoraro, V. L., *Coord. Chem. Rev.* **2008,** *252*, 416.

(50) Han, Z.; Horak, K. T.; Lee, H. B.; Agapie, T., *J. Am. Chem. Soc.* **2017,** *139*, 9108.

(51) Kanady, J. S.; Tsui, E. Y.; Day, M. W.; Agapie, T., *Science* **2011,** *333*, 733.

(52) Mukherjee, S.; Stull, J. A.; Yano, J.; Stamatatos, T. C.; Pringouri, K.; Stich, T. A.; Abboud, K. A.; Britt, R. D.; Yachandra, V. K.; Christou, G., *Proc. Nat. Acad. Sci.* **2012,** *109*, 2257.

(53) Reed, C. J.; Agapie, T., *J. Am. Chem. Soc.* **2018,** *140*, 10900.

(54) Zhang, C.; Chen, C.; Dong, H.; Shen, J.-R.; Dau, H.; Zhao, J., *Science* **2015,** *348*, 690.

(55) Randall, D. W.; Gelasco, A.; Caudle, M. T.; Pecoraro, V. L.; Britt, R. D., *J. Am. Chem. Soc.* **1997,** *119*, 4481.

(56) Randall, D. W.; Sturgeon, B. E.; Ball, J. A.; Lorigan, G. A.; Chan, M. K.; Klein, M. P.; Armstrong, W. H.; Britt, R. D., *J. Am. Chem. Soc.* **1995,** *117*, 11780.

(57) Rapatskiy, L.; Ames, W. M.; Pérez-Navarro, M.; Savitsky, A.; Griese, J. J.; Weyhermüller, T.; Shafaat, H. S.; Högbom, M.; Neese, F.; Pantazis, D. A.; Cox, N., *J. Phys. Chem. B* **2015,** *119*, 13904.

(58) Schäfer, K.-O.; Bittl, R.; Zweygart, W.; Lendzian, F.; Haselhorst, G.; Weyhermüller, T.; Wieghardt, K.; Lubitz, W., *J. Am. Chem. Soc.* **1998,** *120*, 13104.

(59) Pecoraro, V. L., *Photochem. Photobiol.* **1988,** *48*, 249.

(60) Andres, H.; Basler, R.; Güdel, H.-U.; Aromí, G.; Christou, G.; Büttner, H.; Rufflé, B., *J. Am. Chem. Soc.* **2000,** *122*, 12469.

(61) Aromí, G.; Wemple, M. W.; Aubin, S. J.; Folting, K.; Hendrickson, D. N.; Christou, G., *J. Am. Chem. Soc.* **1998,** *120*, 5850.

(62) Aubin, S. M. J.; Wemple, M. W.; Adams, D. M.; Tsai, H.-L.; Christou, G.; Hendrickson, D. N., *J. Am. Chem. Soc.* **1996,** *118*, 7746.

(63) Cinco, R. M.; Rompel, A.; Visser, H.; Aromí, G.; Christou, G.; Sauer, K.; Klein, M. P.; Yachandra, V. K., *Inorg. Chem.* **1999,** *38*, 5988.

(64) Hendrickson, D. N.; Christou, G.; Schmitt, E. A.; Libby, E.; Bashkin, J. S.; Wang, S.; Tsai, H. L.; Vincent, J. B.; Boyd, P. D. W., *J. Am. Chem. Soc.* **1992,** *114*, 2455.

(65) Wang, S.; Tsai, H.-L.; Hagen, K. S.; Hendrickson, D. N.; Christou, G., *J. Am. Chem. Soc.* **1994,** *116*, 8376.

(66) Wang, S.; Tsai, H.-L.; Libby, E.; Folting, K.; Streib, W. E.; Hendrickson, D. N.; Christou, G., *Inorg. Chem.* **1996,** *35*, 7578.
(67) Wang, S.; Wemple, M. S.; Yoo, J.; Folting, K.; Huffman, J. C.; Hagen, K. S.; Hendrickson, D. N.; Christou, G., *Inorg. Chem.* **2000,** *39*, 1501.
(68) Wemple, M. W.; Adams, D. M.; Folting, K.; Hendrickson, D. N.; Christou, G., *J. Am. Chem. Soc.* **1995,** *117*, 7275.
(69) Wemple, M. W.; Tsai, H. L.; Folting, K.; Hendrickson, D. N.; Christou, G., *Inorg. Chem.* **1993,** *32*, 2025.
(70) Kulik, L. V.; Epel, B.; Lubitz, W.; Messinger, J., *J. Am. Chem. Soc.* **2007,** *129*, 13421.
(71) Mukhopadhyay, S.; Mok, H. J.; Staples, R. J.; Armstrong, W. H., *J. Am. Chem. Soc.* **2004,** *126*, 9202.
(72) Ruettinger, W. F.; Campana, C.; Dismukes, G. C., *J. Am. Chem. Soc.* **1997,** *119*, 6670.
(73) Chan, M. K.; Armstrong, W. H., *J. Am. Chem. Soc.* **1991,** *113*, 5055.
(74) Campbell, K. A.; Peloquin, J. M.; Pham, D. P.; Debus, R. J.; Britt, R. D., *J. Am. Chem. Soc.* **1998,** *120*, 447.
(75) Dexheimer, S. L.; Klein, M. P., *J. Am. Chem. Soc.* **1992,** *114*, 2821.
(76) Yamauchi, T.; Mino, H.; Matsukawa, T.; Kawamori, A.; Ono, T.-a., *Biochemistry* **1997,** *36*, 7520.
(77) Kanady, J. S.; Mendoza-Cortes, J. L.; Tsui, E. Y.; Nielsen, R. J.; Goddard, W. A.; Agapie, T., *J. Am. Chem. Soc.* **2013,** *135*, 1073.
(78) Kanady, J. S.; Tran, R.; Stull, J. A.; Lu, L.; Stich, T. A.; Day, M. W.; Yano, J.; Britt, R. D.; Agapie, T., *Chem. Sci.* **2013,** *4*, 3986.
(79) Su, J.-H.; Cox, N.; Ames, W.; Pantazis, D. A.; Rapatskiy, L.; Lohmiller, T.; Kulik, L. V.; Dorlet, P.; Rutherford, A. W.; Neese, F.; Boussac, A.; Lubitz, W.; Messinger, J., *Biochim. Biophys. Acta - Bioenergetics* **2011,** *1807*, 829.
(80) Ruettinger, W. F.; Ho, D. M.; Dismukes, G. C., *Inorg. Chem.* **1999,** *38*, 1036.
(81) Dubé, C. E.; Sessoli, R.; Hendrich, M. P.; Gatteschi, D.; Armstrong, W. H., *J. Am. Chem. Soc.* **1999,** *121*, 3537.
(82) Dubé, C. E.; Wright, D. W.; Pal, S.; Bonitatebus, P. J.; Armstrong, W. H., *J. Am. Chem. Soc.* **1998,** *120*, 3704.
(83) Blondin, G.; Davydov, R.; Philouze, C.; Charlot, M.-F.; Styring, t.; Akermark, B.; Girerd, J.-J.; Boussac, A., *J. Chem. Soc. Dalton Trans.* **1997**, 4069.
(84) Paul, S.; Cox, N.; Pantazis, D. A., *Inorg. Chem.* **2017,** *56*, 3875.
(85) Shoji, M.; Isobe, H.; Shen, J.-R.; Yamaguchi, K., *Phys. Chem. Chem. Phys.* **2016,** *18*, 11330.
(86) Chen; Collomb, M.-N.; Duboc, C.; Blondin, G.; Rivière, E.; Faller, J. W.; Crabtree, R. H.; Brudvig, G. W., *Inorg. Chem.* **2005,** *44*, 9567.
(87) Chen, H.; Faller, J. W.; Crabtree, R. H.; Brudvig, G. W., *J. Am. Chem. Soc.* **2004,** *126*, 7345.
(88) Philouze, C.; Blondin, G.; Girerd, J.-J.; Guilhem, J.; Pascard, C.; Lexa, D., *J. Am. Chem. Soc.* **1994,** *116*, 8557.
(89) Dubé, C. E.; Mukhopadhyay, S.; Bonitatebus, P. J.; Staples, R. J.; Armstrong, W. H., *Inorg. Chem.* **2005,** *44*, 5161.
(90) Hagen, K. S.; Westmoreland, T. D.; Scott, M. J.; Armstrong, W. H., *J. Am. Chem. Soc.* **1989,** *111*, 1907.

(91) Kanady, J. S.; Lin, P.-H.; Carsch, K. M.; Nielsen, R. J.; Takase, M. K.; Goddard, W. A.; Agapie, T., *J. Am. Chem. Soc.* **2014,** *136*, 14373.
(92) Lee, H. B.; Tsui, E. Y.; Agapie, T., *Chem. Commun.* **2017,** *53*, 6832.
(93) Lin, P.-H.; Tsui, E. Y.; Habib, F.; Murugesu, M.; Agapie, T., *Inorg. Chem.* **2016,** *55*, 6095.
(94) Tsui, E. Y.; Agapie, T., *Proc. Nat. Acad. Sci.* **2013,** *110*, 10084.
(95) Tsui, E. Y.; Kanady, J. S.; Agapie, T., *Inorg. Chem.* **2013,** *52*, 13833.
(96) Tsui, E. Y.; Tran, R.; Yano, J.; Agapie, T., *Nat. Chem.* **2013,** *5*, 293.
(97) Tsui, E. Y.; Kanady, J. S.; Day, M. W.; Agapie, T., *Chem. Commun.* **2011,** *47*, 4189.

CHAPTER 2

$CaMn_4O_2$ Model of the Biological Oxygen Evolving Complex: Synthesis by Cluster Expansion on Low Symmetry Ligand

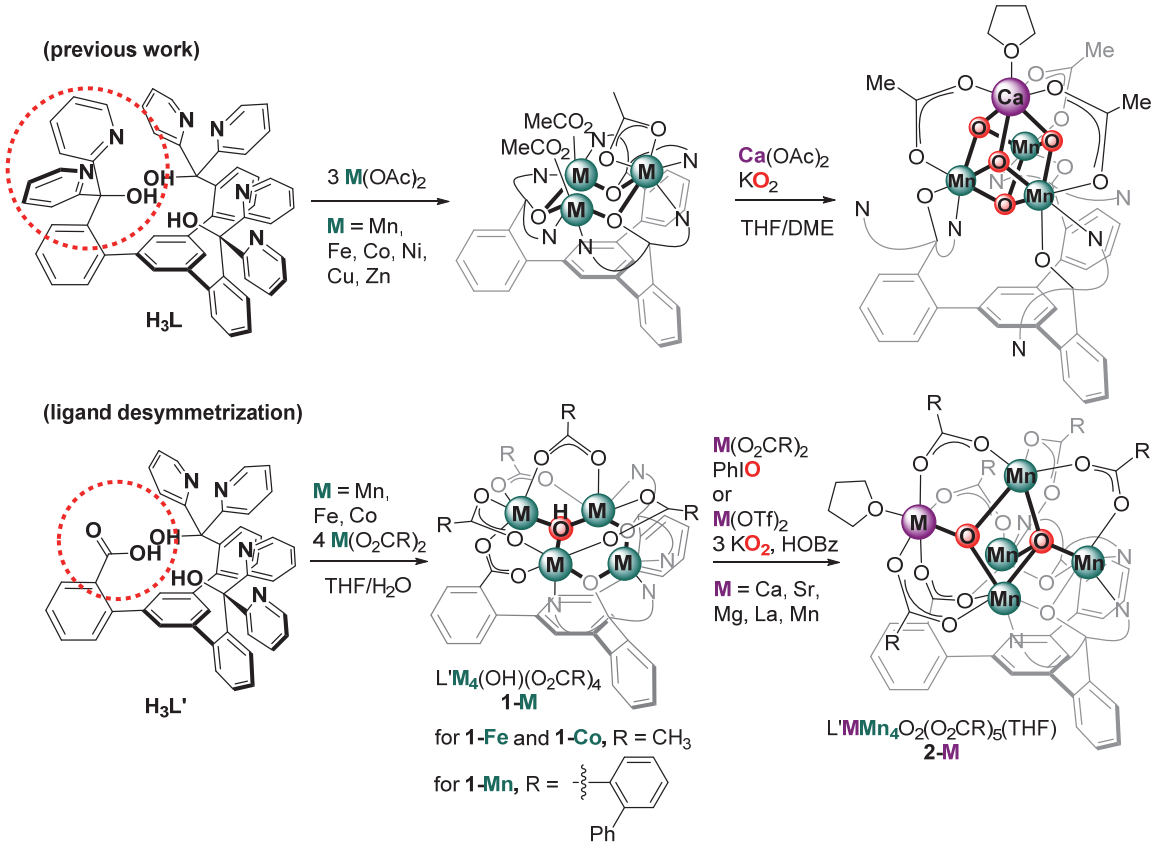

The text for this chapter was reproduced in part from:

Lee, H. B.; Tsui, E. Y.; Agapie, T. *Chem. Commun.*, **2017**, *53*, 6832−6835. DOI: 10.1039/c7cc02313h

Abstract

Using a new multinucleating ligand **H_3L'** featuring two dipyridylalkoxide and a carboxylate moiety, low symmetry tetranuclear complexes **1-M** featuring a [$M_3^{II}(\mu^3$-OH)M^{II}] core (M = Mn, Fe, and Co) have been synthesized. Complex **1-Mn** was used as precursor for the synthesis of a pentanuclear [$CaMn_2^{II}Mn_2^{III}O_2$] cluster (**2-Ca**) with the same metal stoichiometry as the biological oxygen evolving complex (OEC), underscoring the importance of cluster desymmetrization strategies such as **H_3L'** in the synthesis of hitherto unobserved oxo-bridged multimetallic core geometries related to the OEC.

2.1) Introduction

Access to model complexes that mimic the structure and function of the oxygen evolving complex (OEC) in Photosystem II facilitates understanding of the mechanism of biological water oxidation.[1-5] The inorganic [$CaMn_4O_5$] core of the OEC consists of a cuboidal [$CaMn_3O_4$] subsite bound to a dangling fourth Mn through a bridging μ^2-oxo or hydroxo moiety (Figure 1a).[1-2] The synthesis of accurate structural models is hampered by the low structural symmetry of the cluster, the presence of two types of metals, and the propensity of oxo moieties to form extended oligomeric structures.[4, 6-7] The nuclearity and geometry of heterometallic oxo-bridged clusters is therefore often hard to control.[7-17] More recently, models of discrete [Mn_3CaO_n] cores have been prepared using a methodology that allows for systematic structure-function studies.[18-21] Pentanuclear clusters, [$CaMMn_3O_4$] (M = Ca,[13] Ag,[22] Mn[23]) with structures closely mimicking the OEC, have been accessed by both self-assembly as well as rational, stepwise approaches (Figure 1b). Particularly notable is the report of a [$CaMn_4O_4$] synthetic cluster.[23] Despite these advances, general methodologies that allow investigations on the effects of cluster structure on its properties remain very rare.

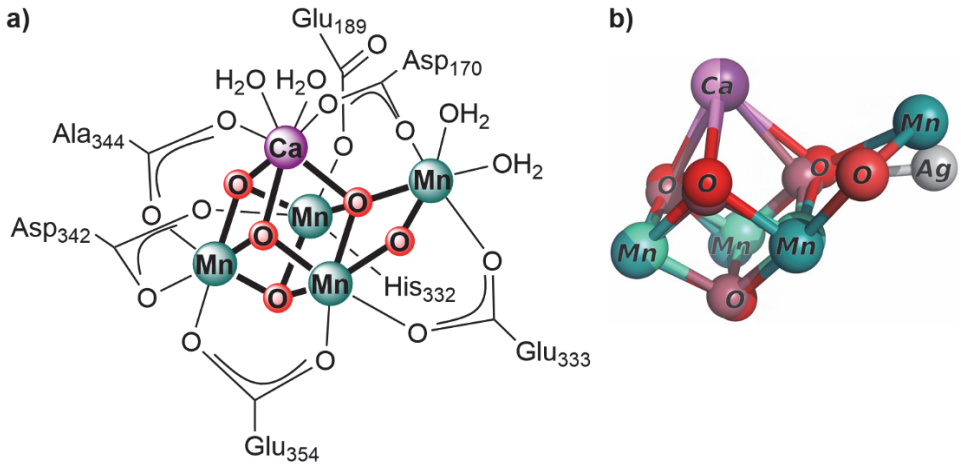

Figure 1. a) Representation of the [$CaMn_4O_5$] core of the OEC, and b) overlay of the OEC with a synthetic [$CaAgMn_3O_4$] cluster core.

Toward rational methodologies for model complex preparation, a cluster with the complexity of the OEC requires careful consideration of synthetic strategy. We have previously established a methodology that involves the synthesis of trinuclear precursors [Mn_3^{II}] (**A**, Figure 2) on a suitable supporting ligand. Oxygenation in the presence of a fourth equivalent of metal results in [$MMn_3^{IV}O_n$] clusters, with cubane (n = 4) highlighted (**B**) in Figure 2. Further synthetic steps have been demonstrated to provide access to [$CaAgMn_3^{IV}O_4$] (**C**), and hold promise for other cluster compositions. An alternative approach targeted in this study involves a ligand framework that can directly support a [Mn_4^{II}] (**D**) in a low symmetry cluster. From this tetranuclear precursor, oxygenation in the presence of a fifth equivalent of metal can provide model [MMn_4O_5] (**E**). We report herein new desymmetrized ligands that afford access to tetranuclear clusters that can be further elaborated to more oxidized pentanuclear clusters, including a heterometallic [$CaMn_2^{II}Mn_2^{III}O_2$] complex with the same metal stoichiometry as the OEC.

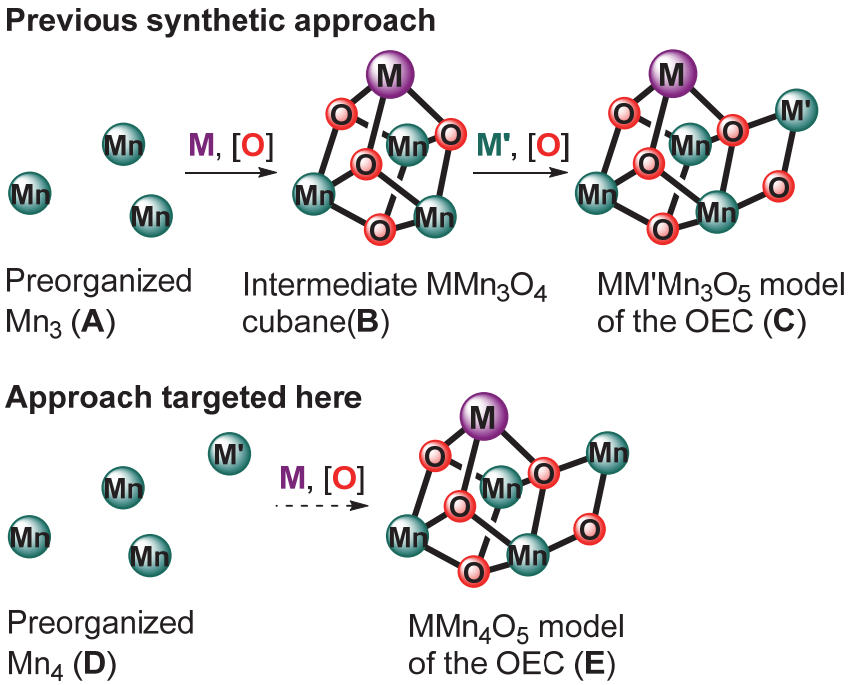

Figure 2. Previously reported synthetic strategy to OEC models and a new approach targeted in this study.

The nuclearity and geometry of multinuclear metal-oxo complexes can be controlled through careful ligand design. For approach 1, a series of trinuclear complexes was accessed using a pseudo−C_3 symmetric ligand based on a 1,3,5-triarylbenzene framework functionalized with three dipyridyl alkoxide moieties.[24] These precursors (**A**, Figure 2) allowed the synthesis of tetranuclear species with a variety of oxo content (for example, **B**).[18-22, 25-26] Given the low symmetry of the OEC, pseudo−C_3 symmetric $CaMn_3O_4$ complex (**B**) was desymmetrized via ligand substitution, which facilitated binding of Ag(I) to a specific oxo moiety to generate a $CaAgMn_3O_4$ cluster (**C**).[22] A desymmetrized version of the supporting ligand was targeted as an alternate approach, with the goals of preparing a tetranuclear, rather than trinuclear, precursor and to obtain a low-symmetry Mn_4 core. Changing one of the three dipyridyl alkoxide moieties of the pseudo−C_3 symmetric ligand for a carboxylate or a phosphinate group provides a more sterically open ligand precursor, **H_3L'** or **H_2LiL^P**, with lower symmetry.

2.2) Ligand synthesis

Two variations of the symmetric ligand **H_3L** featuring three dipyridyl alkoxide moieties were envisioned. Substitution of one of the dipyridyl alkoxide moieties with a carboxylate (**H_3L'**) or a phenylphosphinate (**H_2LiL^P**) moiety was targeted (Figures 3 and 4). The targeted proligand **H_3L'** was synthesized in four steps from 1,3,5-tris(2-bromophenyl)benzene (Figure 3), previously used for the synthesis of the pseudo−C_3 symmetric ligand.[24] Lithium-halogen exchange using 1 equiv of *n*-BuLi followed by addition of DMF gives the monoaldehyde-dibromide **L1** as a major product. **L1** was separated from minor amounts of starting material as well as the dialdehyde species via silica flash column chromatography. The aldehyde moiety in **L1** was then protected by

conversion to an acetal upon condensation with ethylene glycol, giving **L2**. The conversion to **L2** is quantitative and the product can be used without further purification. Treatment of **L2** with 4 equiv of *t*-BuLi followed by addition of 2 equiv of di(2-pyridyl)ketone gives the aldehyde precursor **L3** upon acidic workup. Conversion of the aldehyde moiety in **L3** to the carboxylic acid was achieved via Pinnick oxidation using $NaClO_2$.[27] Without optimization, $\mathbf{H_3L}$ can be obtained on multigram scale (> 20 g) in 46% overall yield from the tribromide precursor.

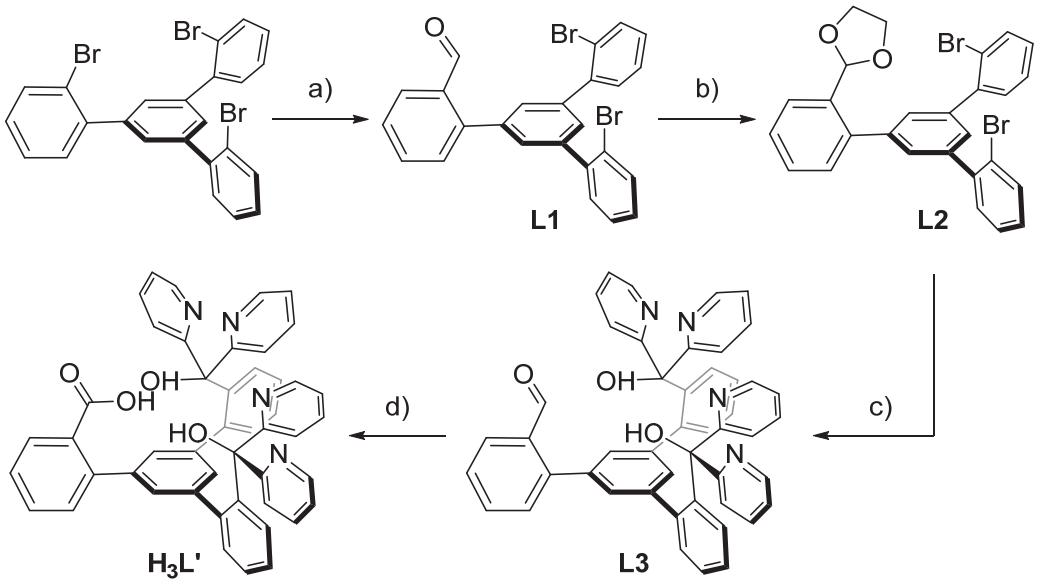

Figure 3. Synthesis of proligand $\mathbf{H_3L'}$. a) 1.1 equiv *n*-BuLi, 2 equiv DMF, THF; b) ethylene glycol, 10 mol% TsOH, C_6H_6; c) 4.1 equiv *t*-BuLi, 2 equiv di(2-pyridyl)ketone, THF; d) 3 equiv $NaClO_2$, 3 equiv NaH_2PO_4, THF/H_2O/DMSO.

The synthesis of the analogous lithium phosphinate proligand $\mathbf{H_2LiL^P}$ was achieved in three steps from the same tribromide precursor (Figure 4). Lithium-halogen exchange using 1 equiv of *n*-BuLi followed by addition to a cold solution of $PhPCl_2$ gives the phosphine oxide-dibromide **L4** as a major product upon aqueous workup. **L4** was separated from minor amounts of starting material as well as the diphosphine-bromide species via silica flash column chromatography. Oxidation of the phosphpine oxide moiety to the phosphinic

acid was achieved via treatment with H_2O_2/NaOH in refluxing MeOH. The protonated phosphinic acid **L5** was isolated upon acidic workup with aqueous HCl. Treatment of **L5** with 1 equiv of $LiN(SiMe_3)_2$ affords the Li-phosphinate dibromide intermediate; this is then treated with 4 equiv of *t*-BuLi followed by addition of 2 equiv of di(2-pyridyl)ketone to afford the desired pro-ligand $\mathbf{H_2LiL^P}$ upon acidic workup with aqueous NH_4Cl. Note that the phosphinate moiety stays deprotonated at this stage. Based on ESI-MS, the lithium-phosphinate formulation is proposed: reliable NMR data has not been obtained due to its very low solubility.

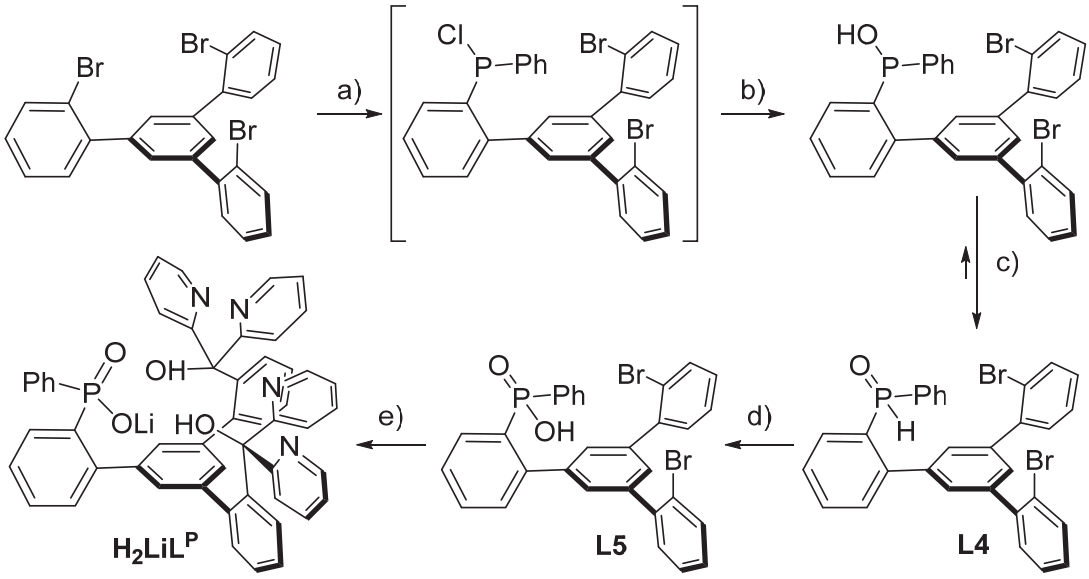

Figure 4. Synthesis of proligand $\mathbf{H_2LiL^P}$. a) 1.1 equiv *n*-BuLi, 1 equiv $PhPCl_2$, THF, −78 °C; b) NaOH (aq.); c) rearrangement of hydroxyphosphine to the phosphine oxide; d) 2 equiv NaOH, 10 equiv H_2O_2, MeOH, reflux, then acidic workup; e) 1.1 equiv $LiN(SiMe_3)_2$, 4.2 equiv. *t*-BuLi, 2 equiv di(2-pyridyl)ketone, THF. Aqueous workup with NH_4Cl (aq.) affords the Li-phosphinate ligand.

2.3) Complexes supported by the desymmetrized carboxylate ligand

Metalation reactions were performed with Mn(II) (Figure 5). Treatment of $\mathbf{H_3L'}$ with $Mn(OAc)_2$ in THF/H_2O results in the formation of a tetranuclear complex as indicated by a prominent peak at m/z = 1128 in the ESI-MS corresponding to the mass of

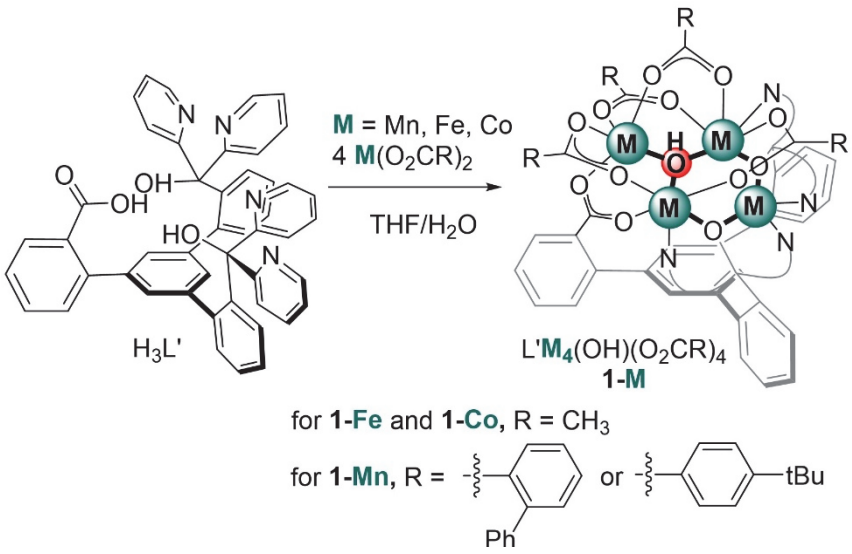

Figure 5. Synthesis of complexes **1-M** (M = Mn, Fe, Co) supported by **H_3L'**.

$[L'Mn_4O(OAc)_3]^+$. Single crystals suitable for X-ray diffraction could not be obtained to date. Treatment of **H_3L'** with different Mn(II) benzoate precursors (benzoate, OBz^-) gives rise to ESI-MS peaks at *m/z* = 1543 and 1724, corresponding to the masses of $[LMn_4O(OBz)_3]^+$ and $[LMn_4(OBz)_4]^+$, respectively, for OBz^- = 2-phenylbenzoate. Colorless single crystals of **1-Mn** were obtained from DCM/Et_2O vapor diffusion (Figure 6a). Structural parameters and charge balance are consistent with the $LMn_4^{II}(OH)(OBz)_4$ formulation. For OBz^- = 4-*t*-Bu-benzoate, single crystals consistent with the $LMn_4^{II}(OH)(OBz)_4(HOBz)$ formulation were obtained (Figure 6b). Both alkoxide moieties of **H_3L'** serve as bridging ligands between Mn(1) and Mn(2) through O(1), and between Mn(1) and Mn(3) through O(2). The binding mode of the dipyridyl alkoxide moieties in **1-Mn** is identical to that in the trimetallic complex.[24] In contrast, a fourth Mn center is incorporated in **1-Mn** supported by the carboxylate moiety of **H_3L**, bridging Mn(3) and Mn(4), and by a water derived μ^3-O(3) ligand bridging Mn(2), Mn(3), and Mn(4). Notably, the μ^3-O(3) ligand occupies the position that an alkoxide moiety occupies in the trimetallic complex geometrically and in terms of bridging two metals that are also coordinated by alkoxides.

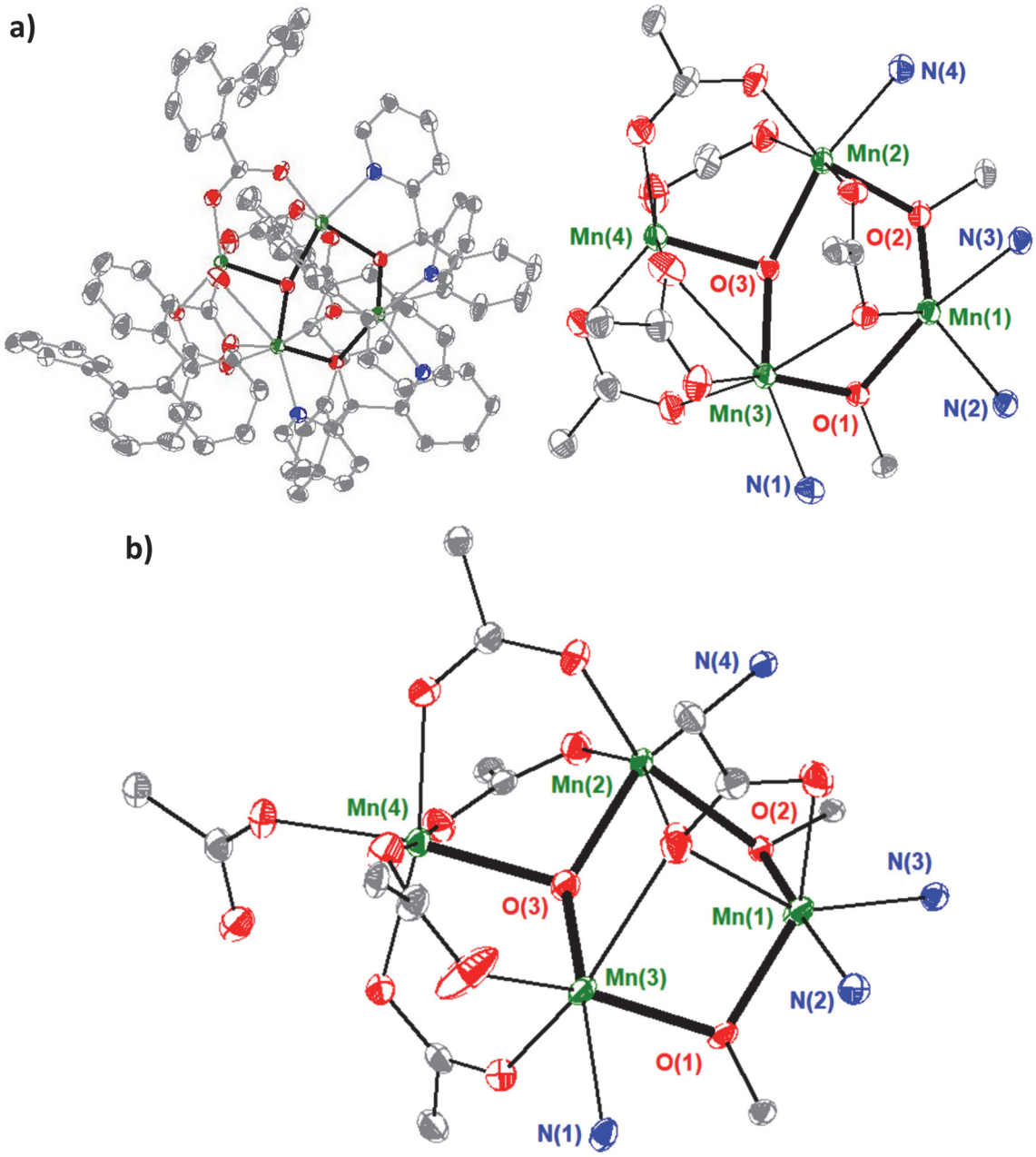

Figure 6. a) Crystal structure of **1-Mn** and the truncated Mn_4 core. Bolded bonds highlight metal-hydroxide and metal-alkoxide bonds. b) Truncated core of the 4-*t*-Bu-benzoate analogue.

Although the trinuclear [$Mn_3(\mu^3$-OH)] subsite in **1-Mn** is reminiscent of the numerous examples of carboxylate bridged $[Mn_3O]^{6+/7+}$ complexes, comparison of Mn-O(3) bond distances in **1-Mn** suggests that O(3) is a hydroxide.[28-29] Bond metrics within the [$Mn^{II}_3(\mu^3$-OH)] core are consistent with known Mn(II) complexes.[30-31]

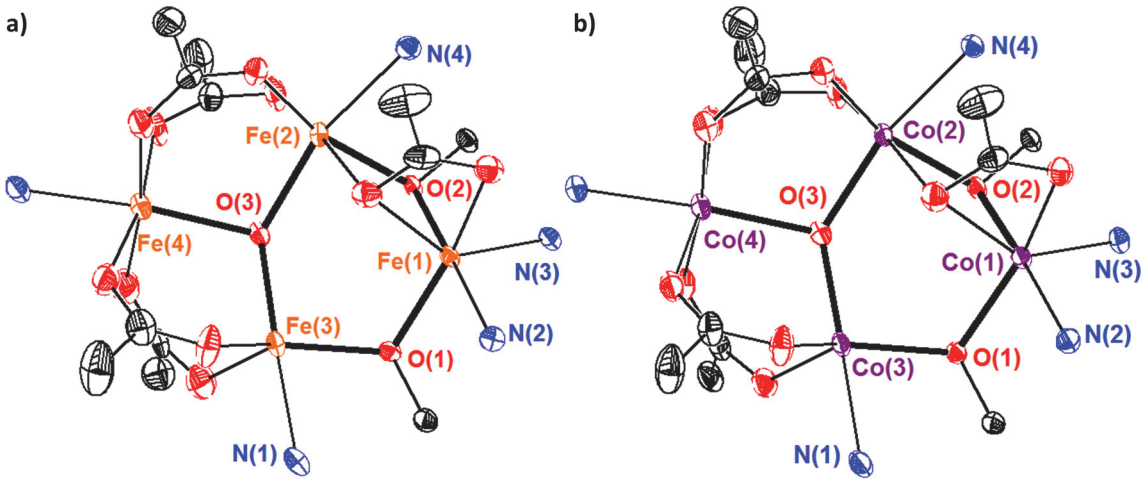

Figure 7. Truncated crystal structures of a) **1-Fe** and b) **1-Co**. Bolded bonds highlight metal-hydroxide and metal-alkoxide bonds.

To test the versatility of $\mathbf{L}^{3-}$ in supporting tetranuclear clusters, other first row transition metals were tested. Fe and Co complexes structurally analogous to **1-Mn** were targeted. Treatment of **H_3L** with $Fe(OAc)_2$ or $Co(OAc)_2$ in the presence of organic bases such as Et_3N or py leads to the formation of tetranuclear complexes **1-Fe** and **1-Co**, respectively. For both compounds, single crystals suitable for X-ray crystallography were obtained from py/Et_2O vapor diffusion (Figure 7). The structures are consistent with the $LM_4(OH)(OAc)_4(py)$ formulation. **1-Fe** and **1-Co** are isostructural, and the binding mode of **H_3L** is essentially analogous to **1-Mn**. Bond metrics within the $[M^{II}_3(\mu^3\text{-OH})]$ core are consistent with known Fe and Co complexes.[32-34] A pyridine molecule is bound to the six-coordinate Fe(4) and Co(4) centers, in contrast to the five-coordinate Mn(4) center in **1-Mn**. Such difference in coordination geometry is accompanied by structural changes in the $[M_3(\mu^3\text{-OH})]$ core. Mn(2)−Mn(4) and Mn(3)−Mn(4) distances are shorter than the corresponding Fe−Fe and Co−Co distances, whereas the Mn(2)−Mn(3) distance is longer. Mn(2)−O(3)−Mn(4) and Mn(3)−O(3)−Mn(4) angles are more acute than the corresponding Fe−O(3)−Fe and Co−O(3)−Co angles, whereas the Mn(2)−O(3)−Mn(3) angle is more

obtuse. Aside from these differences, the overall topology of the three **1-M** complexes is highly analogous.

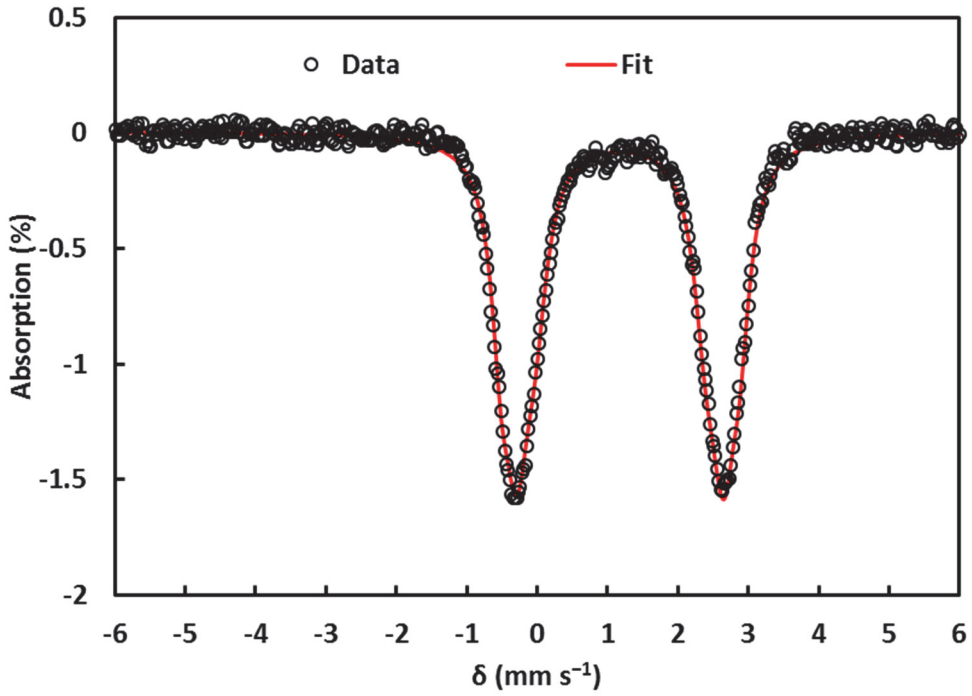

Figure 8. Zero-field Mössbauer spectrum of **1−Fe** at 80 K with simulated parameters: δ = 1.18 mm/s, $|\Delta E_Q|$ = 2.95 mm/s.

The zero-field Mössbauer spectrum of **1-Fe** shows a broad quadrupole doublet with δ = 1.18 mm/s and $|\Delta E_Q|$ = 2.95 mm/s (Figure 8). These values are consistent with known carboxylate bridged high-spin Fe(II) centers.[35-36] Mössbauer parameters for the diiron(II) μ^2–hydroxo species supported by bridging acetate ligands (δ = 1.16 mm/s, $|\Delta E_Q|$ = 2.83 mm/s) are in excellent agreement with the values observed for **1-Fe**.[37-38]

To obtain insight into the magnetic exchange coupling interactions between the M(II) centers, magnetic susceptibility measurements were performed on powdered crystalline samples of **1-Mn**, **1-Fe**, and **1-Co** in the temperature range 2 K−270 K at a non-saturating field of 0.1 T. For **1-Mn**, the χT value of 10.8 emu K mol^{-1} at 270 K indicates antiferromagnetic coupling between the Mn(II) centers, deviating from the expected spin-

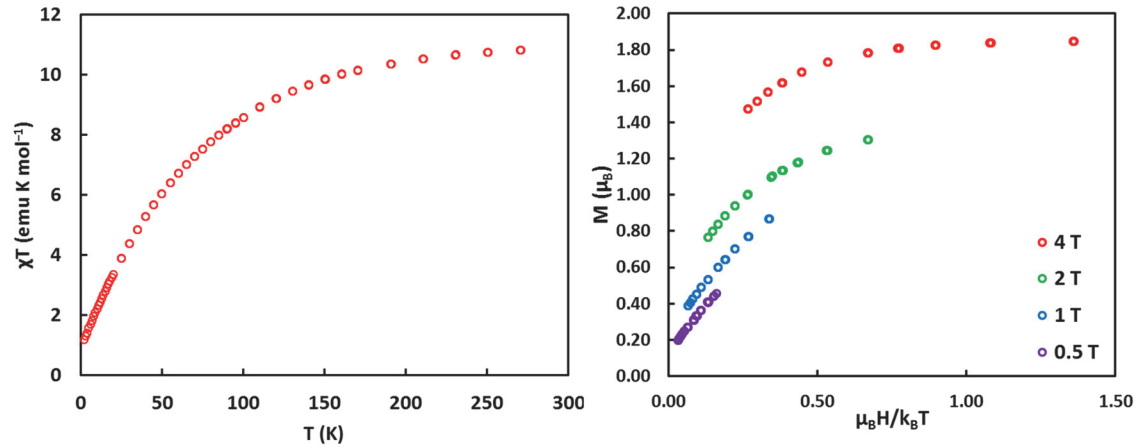

Figure 9. χT vs T and reduced magnetization plot of **1-Mn**.

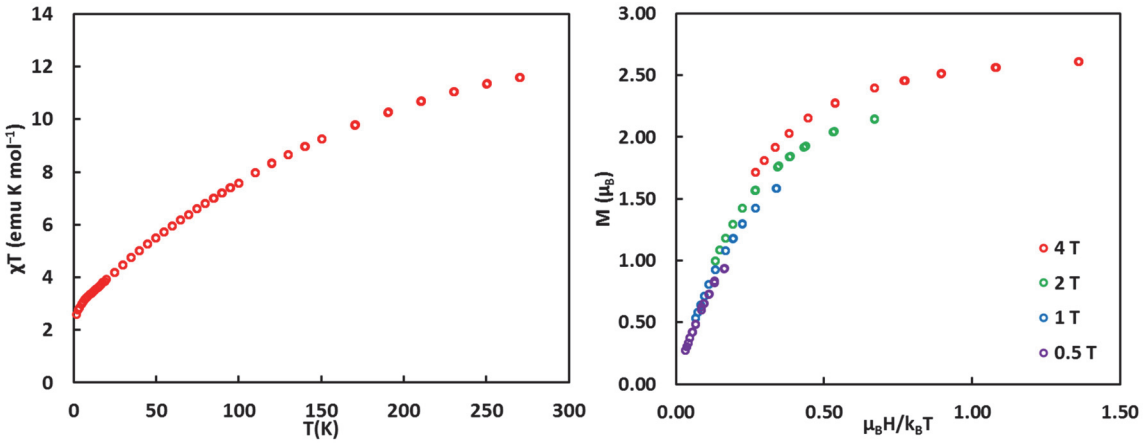

Figure 10. χT vs T and reduced magnetization plot of **1-Fe**.

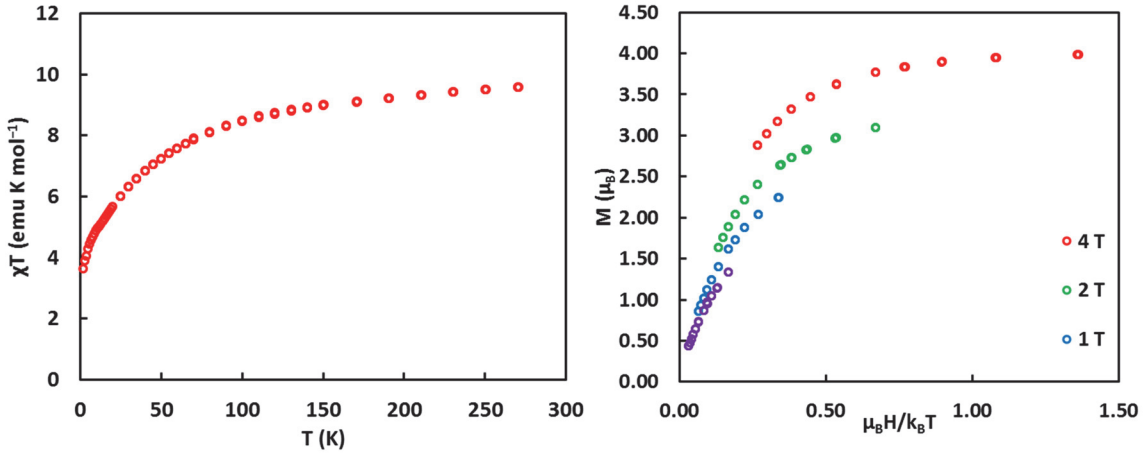

Figure 11. χT vs T and reduced magnetization plot of **1-Co**.

only value of 17.5 emu K mol^{-1} (g = 2) for four uncoupled Mn^{II} (S = 5/2) centers (Figure 9). χT decreases monotonically with temperature, reaching a value of 1.18 emu K mol^{-1} at

2 K, in good agreement with the expected χT value of 1.0 emu K mol^{-1} for an $S = 1$ ($g = 2$) ground state. Accordingly, the reduced magnetization reaches a maximum value of 1.84 $\mu_B N_A$ for the 4 T isofield curve, deviating slightly from the expected value of 2.0 for an $S = 1$ ($g = 2$) ground state. The lower reduced magnetization value can be attributed to zero-field splitting effects. For **1-Fe**, the χT value of 11.6 emu K mol^{-1} at 270 K is in good agreement with the spin only value of 12.0 emu K mol^{-1} ($g = 2$) for four uncoupled Fe^{II} ($S = 2$) centers (Figure 10). Therefore, the magnitude of the magnetic exchange coupling in **1-Fe** is expected to be very small. Consistent with antiferromagnetic interactions, χT decreases monotonically with temperature, reaching a value of 2.57 emu K mol^{-1} at 2 K. This value is intermediate between the expected values of 1.0 emu K mol^{-1} for an $S = 1$ ($g = 2$) and 3.0 emu K mol^{-1} for an $S = 2$ ($g = 2$) ground state. A small separation between the $S = 1$ ground state and the $S = 2$ first excited state is expected. Accordingly, the reduced magnetization reaches a maximum value of 2.61 $\mu_B N_A$ for the 4 T isofield curve, deviating from the expected value of 2.0 for an $S = 1$ ($g = 2$) ground state. The higher reduced magnetization value can be attributed to the contribution from the $S = 2$ excited state. For **1-Co**, the χT value of 9.57 emu K mol^{-1} at 270 K deviates from the spin only value of 7.5 emu K mol^{-1} ($g = 2$) for four uncoupled Co^{II} ($S = 3/2$) centers (Figure 11). The larger value of 9.57 emu K mol^{-1} can be attributed to the unquenched orbital angular momentum of the Co^{II} centers. χT decreases monotonically with temperature, reaching a value of 3.6 emu K mol^{-1} at 2 K, in good agreement with the expected χT value of 3.0 emu K mol^{-1} for an $S = 2$ ($g = 2$) ground state. Accordingly, the reduced magnetization reaches a maximum value of 3.98 $\mu_B N_A$ for the 4 T isofield curve, in excellent agreement with the expected value of 4.0 for an $S = 2$ ($g = 2$) ground state.

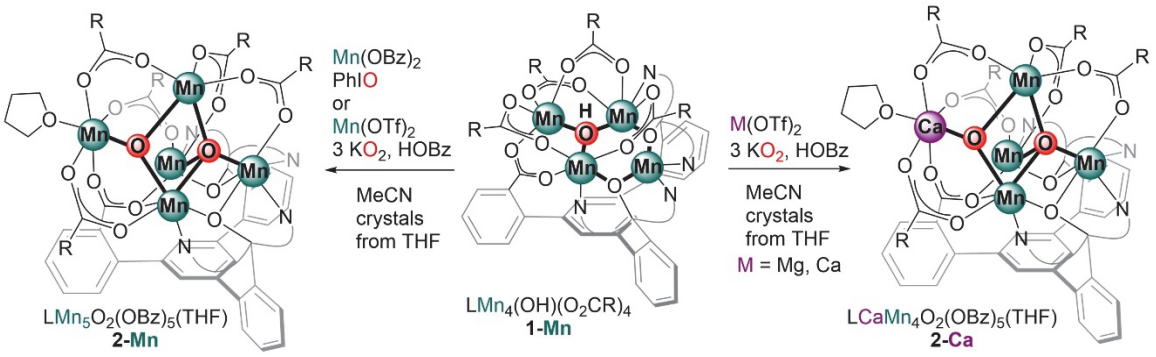

Figure 12. Synthesis of pentanuclear complexes **2-Mn**, **2-Ca**, and **2-Mg** from **1-Mn**.

Tetranuclear Mn clusters with varying oxo content have been obtained from the higher symmetry trinuclear analogs of **1-Mn**.[26] For instance, treatment of $LMn_3(OAc)_3$ with $Mn(OAc)_2$ and KO_2 results in the formation of a Mn_4O_2 cluster featuring μ^4–O and μ^2–O moieties. Similar incorporation of an additional metal center is observed upon treatment of **1-Mn** with $Mn(O_2CR)_2$ and PhIO or $Mn(OTf)_2$, KO_2, and 2-phenylbenzoic acid (Figure 12), as indicated by a prominent ESI-MS peak at 1810 that corresponds to the mass of $[LMn_5O_2(OBz)_4]^+$. The solid-state structure of product **2** is consistent with the $LMn_5O_2(OBz)_5(THF)$ formulation (Figure 13a). While the binding mode of the dipyridyl alkoxide moieties remains unchanged compared to the higher symmetry ligand, the incorporation of a carboxylate moiety in **L** facilitates binding of Mn(5). Based on Mn−oxo distances, the oxidation states of Mn(1), Mn(2), and Mn(5) are assigned to Mn(II), and those of Mn(3) and Mn(4) to Mn(III). The $[Mn_5O_2]^{8+}$ core of **2-Mn** is reminiscent of an incomplete $[Mn_6(\mu^4\text{-}O)_2]^{10+}$ core of pseudo-D_{3h} symmetric $[Mn_6(\mu^4\text{-}O)_2(OAc)_{10}]$ complexes, missing one of the metal centers.[29]

Toward the synthesis of a Ca-Mn cluster, treatment of **1-Mn** with $Ca(OTf)_2$, KO_2, and 2-phenylbenzoic acid (Figure 12) results instead in the formation of product **2-Ca** consistent with the $LCaMn_4O_2(OBz)_5(THF)$ formulation. The structure of **2-Ca** (Figure

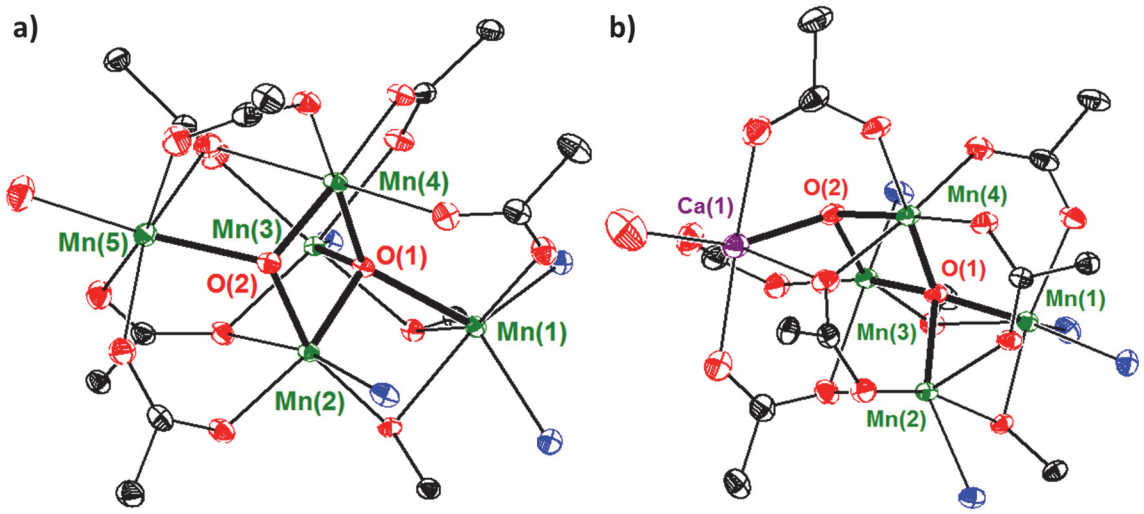

Figure 13. Truncated crystal structures of a) **2-Mn** and b) **2-Ca**. Bolded bonds highlight metal-oxo bonds.

13b) is analogous to **2** and shows a $CaMn_4O_2$ cluster with the same metal stoichiometry as the OEC. Based on Mn−oxo distances, the oxidation states of Mn(1) and Mn(2) are assigned to Mn(II), and those of Mn(3) and Mn(4) to Mn(III). Among reported discrete $CaMn_4$ clusters,[3c, 3h, 6, 13] there are only two reports of clusters that display oxo bridges $CaMn_4O_x$ (x = 1 or 4).[3c, 6] To our knowledge, the $[Mn_5(\mu^4\text{-}O)(\mu^3\text{-}O)]^{8+}$ and $[CaMn_4(\mu^4\text{-}O)(\mu^3\text{-}O)]^{8+}$ clusters have not been described, underscoring the utility of low-symmetry multinucleating ligands such as **H_3L'** in the synthesis of hitherto unobserved oxo-bridged multimetallic core geometries related to the OEC. Furthermore, addition of $Mn(OTf)_2$ to **2-Ca** results in the formation of **2-Mn**, providing a modular approach to the synthesis of other pentametallic complexes.

2.4) Complexes supported by the desymmetrized phosphinate ligand

Metalation reactions with **H_2LiL^P** were performed with several Mn carboxylate precursors (Figure 14). Treatment of **H_2LiL^P** with $Mn(OAc)_2$ in DMF/H_2O results in the formation of a hexanuclear species despite careful addition of only 4 equiv of Mn(II). Colorless single crystals of **3-Mn** were obtained from DMF/Et_2O vapor diffusion (Figure

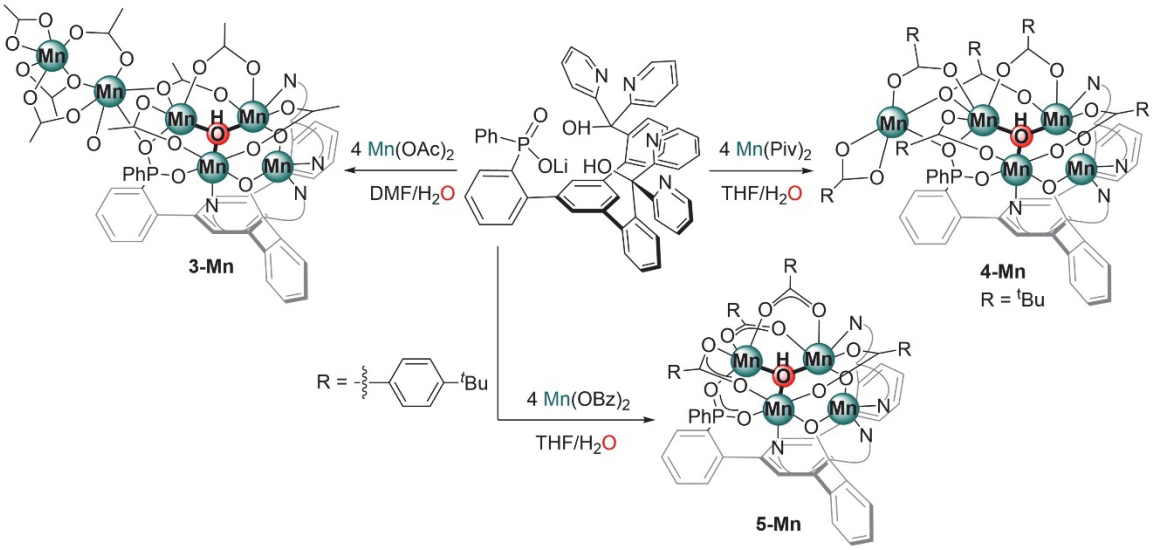

Figure 14. Synthesis of hexanuclear (**3-Mn**), pentanuclear (**4-Mn**), and tetranuclear (**5-Mn**) complexes supported by $\mathbf{H_2LiL^P}$.

15a). The structure is consistent with the $LMn_6(OH)(OAc)_8$ formulation. Both of the dipyridyl alkoxide moieties of serve as bridging ligands between Mn(1) and Mn(2) through O(1), and between Mn(1) and Mn(3) through O(2). The phosphinate moiety bridges Mn(2) and Mn(4), and a water derived hydroxide μ^3-OH(3) ligand bridges Mn(2), Mn(3), and Mn(4). The $[Mn^{II}_3(\mu^3\text{-OH})]$ subsite of **3-Mn** is reminiscent of the tetrametallic complexes **1-M** isolated from $\mathbf{H_3L'}$ (Figure 5). Interestingly, the phosphinate moiety also bridges Mn(4) and Mn(5) through O(5), which we initially attributed to the superiority of the phosphinate moiety as a bridging ligand compared to the carboxylate moiety. Further binding of a sixth Mn(6) center was observed through bridging acetate moieties. To prevent formation of **3-Mn,** a bulkier Mn pivalate precursor was used for metalation. We found $Mn_2(H_2O)(Piv)_4(bpy)_2$ to be an adequate precursor readily accessible from $Mn(OAc)_2$ and HPiv. We reasoned that binding of bpy to Mn(4) could also prevent binding of additional Mn centers through the phosphinate O(5). Despite careful addition of only 4 equiv of Mn(II), colorless single crystals of **4-Mn** were obtained from DCM/Et_2O vapor diffusion

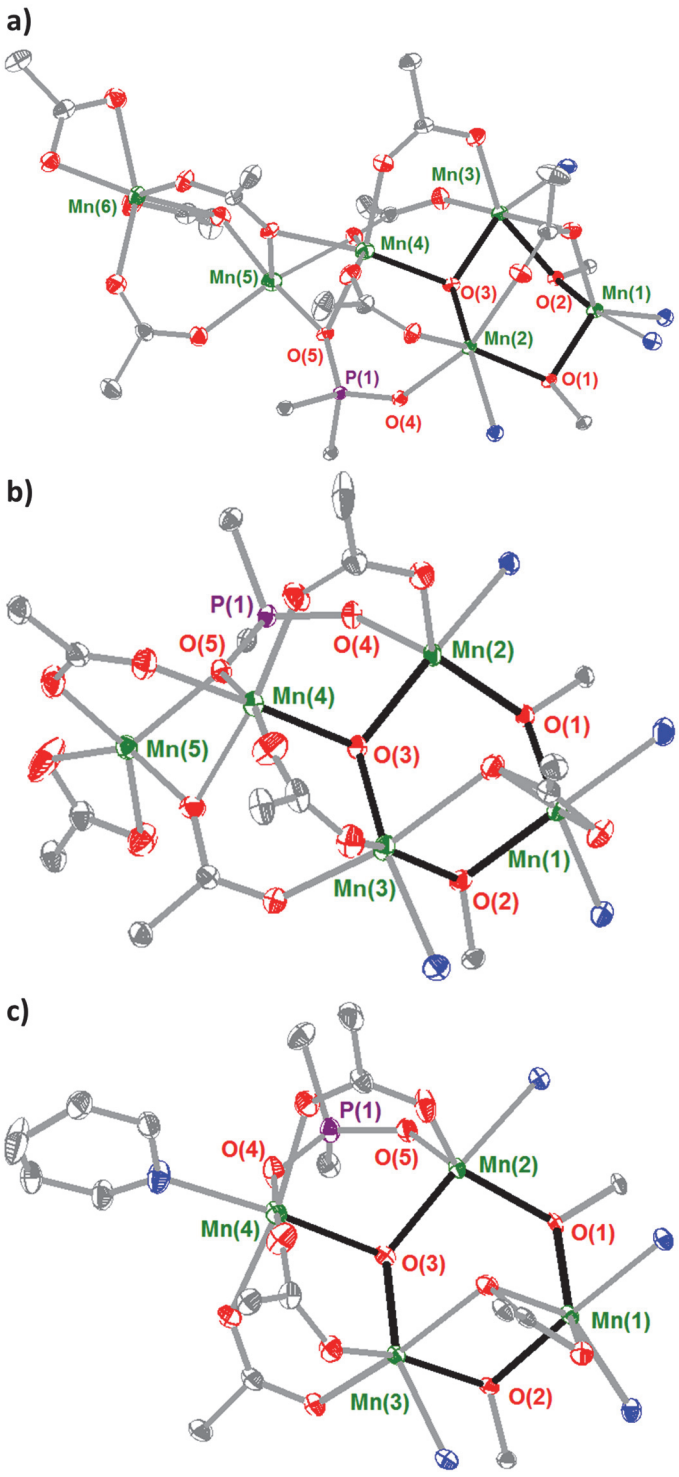

Figure 15. Synthesis of hexanuclear (**3-Mn**), pentanuclear (**4-Mn**), and tetranuclear (**5-Mn**) complexes supported by $\mathbf{H_2LiL^P}$.

(Figure 15b). The structure is consistent with the $LMn_5(OH)(Piv)_6$ formulation. Interestingly, the major peak in ESI-MS corresponds to the mass of $[LMn4(OH)(Piv)_3]^+$

and no peaks consistent with the pentanuclear species was observed. The overall topology of **4-Mn** is highly analogous to **3-Mn**: formation of the [$Mn^{II}_3(\mu^3$-OH)] subsite is again observed and the phosphinate moiety bridges Mn(4) and Mn(5) through O(5). A capping pivalate moiety prevents further binding of a sixth Mn. Notably, bpy was found to be ineffective in preventing binding of a fifth metal. Gratifyingly, when Mn(*p-tert*-Bu-benzoate)$_2$ [abbreviated as Mn(OBz]$_2$] was used for metalation, clean formation of the desired tetranuclear complex **5-Mn** was obtained. Single crystals were obtained from py/Et_2O vapor diffusion (Figure 15c). The structure is consistent with the $LMn_4(OH)(OBz)_4(py)$ formulation. The reduced basicity of the benzoate moieties and binding of a pyridine molecule to Mn(4) may preclude further binding of a fifth Mn. Starting from 5-Mn, further oxidation in the presence of a fifth metal have not been explored in detail thus far.

2.5) Discussion

In summary, low symmetry tetranuclear complexes **1-M** (M = Mn, Fe, Co) have been synthesized and structurally characterized. The feasibility of using **1-Mn** as a precursor for the synthesis of novel pentanuclear clusters has been demonstrated with the synthesis of **2-Mn** and **2-Ca** featuring more oxidized $[Mn_5O_2]^{8+}$ and $[CaMn_4O_2]^{8+}$ cores. Compound **2-Ca** is notable as a rare example of cluster of same metal composition, with oxo bridges, as the OEC. Synthesis of pentanuclear complexes with higher oxo content toward more accurate models of the OEC is currently being pursued.

2.6) Experimental section

Synthesis of **L1**: A 500-mL Schlenk flask equipped with a stir bar was charged with tris(2-bromophenyl)benzene (34.5 g, 63 mmol, 1 equiv). Anhydrous THF (300 mL) was

added via cannula, and the flask was cooled to −78 °C. A solution of *n*-butyllithium in hexane (2.5 M, 30 mL, 75 mmol, 1.2 equiv) was added slowly via syringe and stirred for an additional hour at −78 °C. Anhydrous, degassed DMF (9.8 g, 134 mmol, 2.1 equiv) was added via syringe, and the mixture was stirred at ambient temperature for 12 h. The reaction mixture was quenched with a saturated aqueous solution of NH_4Cl, and the organic phase was separated. The aqueous phase was extracted three times with EtOAc, and the combined organic fraction was washed repeatedly with brine to remove excess DMF, dried over anhydrous $MgSO_4$, filtered, and concentrated under reduced pressure. The residue was purified by flash column chromatography on silica using 5:1 hexanes/CH_2Cl_2 (R_f = 0.4), then dried under reduced pressure to yield **L1** as a white foamy solid (21.4 g, 69%). ^{1}H NMR ($CDCl_3$, 300 MHz): δ 10.23 (s, 1H, C<u>H</u>O), 8.08 (dd, *J* = 7.8, 1.5 Hz, 1H, *o*-CHO), 7.71 (dd, *J* = 8.2, 1.5 Hz, 2H), 7.68 (td, *J* = 7.5, 1.5, 1H), 7.59 (d, *J* = 8.5 Hz, 1H), 7.55 (t, *J* = 1.5 Hz, 1H), 7.53 (t, *J* = 7.5 Hz, 1H), 7.50 (d, *J* = 1.5 Hz, 2H), 7.46 (dd, *J* = 7.8, 1.5 Hz, 2H), 7.40 (td, *J* = 7.5, 1.5 Hz, 2H), 7.25 (td, *J* = 7.8, 2.0 Hz, 2H) ppm. ^{13}C NMR ($CDCl_3$, 75 MHz): 192.6, 145.5, 141.6, 141.2, 137.3, 134.0, 133.8, 133.4, 131.5, 131.1, 130.4, 130.3, 129.3, 128.2, 127.8, 127.7, 122.8 ppm. HRMS (FAB+): calculated for $C_{25}H_{17}OBr^{18}Br$: 492.9626; found: 492.9645 [M+H].

Synthesis of **L2**: A 500-mL round-bottom flask equipped with a stir bar was charged with a solution of **L1** (21.4 g, 43.5 mmol) in benzene (200mL), ethylene glycol (25 mL), and *p*-toluenesulfonic acid monohydrate (0.5 g, 2.6 mmol, 0.06 equiv). A Dean-Stark apparatus was connected to the flask, and the mixture was refluxed for 15 h under N_2. The mixture was cooled to ambient temperature and quenched with a saturated aqueous solution of $NaHCO_3$. The organic fraction was separated, washed with brine, dried over anhydrous

$MgSO_4$, filtered, and dried under reduced pressure to yield **L2** as a white foamy solid (22.1 g, 95%). The resulting material was used without further purification. ^{1}H NMR ($CDCl_3$, 300 MHz): δ 7.78–7.74 (m, 1H), 7.70 (dd, J = 8.0, 1.2 Hz, 2H), 7.54 (d, J = 1.7 Hz, 2H), 7.48−7.43 (m, 6H), 7.40−7.35 (overlapping ddd and s, 3H), 7.22 (ddd, J = 8.0, 7.3, 1.9 Hz, 2H), 5.92 (s, 1H), 4.18 (m, 2H), 3.98 (m, 2H) ppm. ^{13}C NMR ($CDCl_3$, 75 MHz): δ 142.20, 141.63, 140.61, 139.41, 134.79, 133.28, 131.60, 130.39, 130.01, 129.36, 129.28, 129.04, 127.98, 127.56, 127.02, 122.83, 101.48, 65.73 ppm. HRMS (FAB+): calculated for $C_{27}H_{20}O_2Br^{18}Br$: 535.9810; found: 535.9816 [M+H].

Synthesis of **L3**: A 500-mL Schlenk flask equipped with a stir bar was charged with **L2** (22.1 g, 41 mmol, 1 equiv) under N_2 counter-flow. Anhydrous THF (250 mL) was added via cannula, and the flask was cooled to −78 °C. A solution of *t*-butyllithium in pentane (1.7 M, 100 mL, 170 mmol, 4.1 equiv) was added slowly via cannula, and the resulting red solution was stirred at −78 °C for 1 hr. A solution of di(2-pyridyl)ketone (15.2 g, 82 mmol, 2 equiv) in anhydrous THF (100 mL) was added via cannula, and the resulting mixture was stirred at ambient temperature for 15 hrs. The reaction mixture was quenched with 1M hydrochloric acid to pH 1 and stirred for 2 hrs. After neutralizing the acid with a saturated aqueous solution of $NaHCO_3$, the mixture was concentrated under reduced pressure to remove excess THF. The product was extracted with CH_2Cl_2, washed with brine, dried over anhydrous $MgSO_4$, filtered, and dried under reduced pressure. **L3** is obtained as a white foamy solid and used without further purification. ^{1}H NMR (CDCl3, 300 MHz): δ 9.82 (s, 1H, C<u>H</u>O), 8.33 (d, *J* = 5.1 Hz, 4 H), 8.01 (d, *J* = 7.8 Hz, 1 H), 7.66 (d, *J* = 8.1 Hz, 4 H), 7.61 (d, *J* = 7.5 Hz, 1 H), 7.46 (t, *J* = 7.5 Hz, 6 H), 7.36 (t, *J* = 7.5 Hz, 2 H), 7.21 (t, *J* = 7.5 Hz, 2 H), 7.13 (d, *J* = 7.5 Hz, 2 H), 7.07 (s, 1 H), 6.97 (m, 6 H), 6.81 (s, 2 H), 6.75

(d, *J* = 8.1 Hz, 2 H) ppm. HRMS (FAB+): calculated for $C_{47}H_{35}N_4O_3$: 703.2709; found: 703.2697 [M+H].

Synthesis of **H_3L'**: A 1 L round-bottom flask equipped with a stir bar was charged with crude **L3** (obtained from 22.1 g of **L2**) and THF (50 mL). DMSO (450 mL) was added as an HClO scavenger. A saturated aqueous solution of NaH_2PO_4•$2H_2O$ (3.5g, 22.4 mmol, 5 equiv) was added via a dropping funnel. Subsequently, a saturated aqueous solution of $NaClO_2$ (1.2 g, 13.27 mmol, 3 equiv) was added via a dropping funnel and the resulting mixture was stirred for 18 hrs at ambient temperature. The reaction mixture was eluted with EtOAc (500 mL) and washed repeatedly with brine to remove excess DMSO, dried over anhydrous $MgSO_4$, filtered, and concentrated under reduced pressure. The residue was dissolved in minimum acetone and precipitated from Et_2O to afford **H_3L** as a white powder (20.9 g, 46% overall yield in 4 steps). ^{1}H NMR (300 MHz, $CDCl_3$): δ 8.32 (d, *J* = 4.8 Hz, 4H), 7.65 (m, *5*H), 7.47 (t, *J* = 7.2 Hz, 4H), 7.27 (m, *2*H), 7.14 (t, *J* = 7.8 Hz, 2H), 7.02 (d, *J* = 7.5 Hz, 2H), 6.96 (m, *5*H), 6.86 (s, *2*H), 6.73 (d, *J* = 7.8 Hz, 2H), 6.63 (s, 1H) ppm. ^{13}C NMR (75 MHz, $CDCl_3$): 162.88, 146.86, 144.07, 143.23, 142.00, 140.35, 137.36, 136.36, 133.00, 130.93, 130.81, 130.74, 129.96, 129.02, 128.65, 127.21, 127.16, 126.68, 126.46, 123.46, 122.04 ppm. HRMS (ES+): calculated for $C_{47}H_{35}N_4O_4$: 719.2658; found: 719.2677 [M+H].

Synthesis of manganese benzoate precursors: An example for the 2-phenylbenzoate analogue is presented here. Under strictly anaerobic conditions, an aqueous suspension of 2-phenylbenzoic acid (0.951 g, 4.8 mmol, 2 equiv) was treated with NaOH (0.192 g, 4.8 mmol, 2 equiv). The mixture was gently warmed to 60 ºC, resulting in a slightly yellow solution. An aqueous solution of $MnCl_2$•$4H_2O$ (0.474 g, 2.4 mmol, 1 equiv) was added

dropwise. The total volume of the reaction was 20 mL. The mixture was stirred at 60ºC for 3 h, resulting in the formation of a white precipitate. After cooling to room temperature, the precipitate was collected and washed thoroughly with copious amounts of water and Et_2O, successively. The remaining white solid was dried under reduced pressure. Yield = 1.041 g. Crystallization from DME affords $Mn_3(OBz)_6(DME)_2$.

Synthesis of **1-Mn**: A solution of **H_3L'** (1.708 g, 2.38 mmol, 1 equiv) in THF was added to a stirring suspension of $Mn(OBz)_2•xH_2O$ (4.956 g, 9.5 mmol, 4 equiv) in THF. The reaction mixture was stirred at ambient temperature, becoming homogeneous within 1 hour. After stirring for 18 hours, all volatiles were removed under reduced pressure. The residue was washed with copious amounts of Et_2O, then dissolved in hot benzene and filtered through Celite. All volatiles were removed from the filtrate under reduced pressure. The residue was dissolved in CH_2Cl_2. Clear, colorless crystals of the product were obtained by slow vapor diffusion of Et_2O. Compound **1−Mn** was isolated by filtration and dried under reduced pressure. Yield = 3.87 g, 94 %. Analysis calculated for $LMn_4(OH)(OBz)_4•1/2(CH_2Cl_2)$ [$C_{199}H_{138}Cl_2Mn_8N_8O_{26}$]: C 66.99, H 3.90, N 3.14; found: C 67.03, H 4.08, N 3.02.

Synthesis of **1-Fe**: A solution of **H_3L'** (1.162 g, 1.62 mmol, 1 equiv) in THF (10 mL) was added to a stirring suspension of $Fe(OAc)_2$ (1 g, 5.75 mmol, 3.5 equiv) in THF (5 mL). Water (2 mL) was added and the mixture was stirred until a homogeneous red solution was obtained. Triethylamine (1 mL) was added and the mixture was stirred for 12 hours at ambient temperature, resulting in the formation of an orange precipitate. This precipitate was collected and washed with copious amounts of THF. The solid residue was dissolved in pyridine and filtered through Celite. All volatiles were removed from the filtrate under

reduced pressure. Compound **1-Fe** was isolated as air-sensitive red microcrystals. Yield = 1.67 g, 91 % (based on Fe). Crystals suitable for X-ray crystallography are obtained by slow vapor diffusion of Et_2O into a concentrated solution of **1-Fe** in pyridine. Analysis calculated for $LFe_4(OH)(OAc)_4(py)$•py [$C_{65}H_{54}Fe_4N_6O_{13}$]: C 57.81, H 4.03, N 6.22; found: C 57.91, H 4.29, N 6.49.

Synthesis of **1-Co**: A solution of $Co(OAc)_2$•$4H_2O$ (1.476 g, 5.93 mmol, 3.8 equiv) in MeOH (10 mL) was added to a solution of **H_3L'** (1.120 g, 1.56 mmol, 1 equiv) in MeOH (5 mL). Pyridine (1 mL) was added, and the resulting violet solution was stirred for 12 hours at ambient temperature. All volatiles were then removed under reduced pressure. The residue was washed with copious amounts of Et_2O, THF, and MeCN. The solid residue was dissolved in pyridine and filtered through Celite. All volatiles were removed from the filtrate under reduced pressure. Compound **1-Co** was isolated as air-stable violet microcrystals. Yield = 1.477 g, 79 %. Crystals suitable for X-ray crystallography are obtained by slow vapor diffusion of Et_2O into a concentrated solution of **1-Co** in pyridine. Analysis calculated for $LCo_4(OH)(OAc)_4(py)$•2py [$C_{70}H_{59}Co_4N_7O_{13}$]: C 58.31, H 4.12, N 6.80; found: C 58.40, H 4.29, N 6.40.

Synthesis of **2-Mn**: A solid mixture of **1-Mn** (0.442 g, 0.25 mmol, 1 equiv), $Mn(OTf)_2$ (99 mg, 0.28 mmol, 1.1 equiv), and 2-phenylbenzoic acid (56 mg, 0.28 mmol, 1.1 equiv) was treated with CH_3CN (15 mL) and stirred to a homogeneous yellow solution. KO_2 (55 mg, 0.77 mmol, 3 equiv) was added as a solid and stirred at r.t. for 18 h, resulting in the formation of a brown-red precipitate. The precipitate was collected and washed with copious amounts of CH_3CN. The solid residue was dissolved in THF, filtered through Celite, and concentrated under reduced pressure. Yield = 0.435 g, 82 %. Red crystals

suitable for X-ray crystallography are obtained from a concentrated THF solution by slow vapor diffusion of Et_2O. Analysis calculated for $C_{116}H_{84}Mn_5N_4O_{17}$: C 66.96, H 4.07, N 2.69; found: C 66.15, H 4.35, N 2.98.

Synthesis of **2-Ca**: A solid mixture of **1-Mn** (0.640 g, 0.367 mmol, 1 equiv), $Ca(OTf)_2$ (135 mg, 0.40 mmol, 1.1 equiv), and 2-phenylbenzoic acid (96 mg, 0.48 mmol, 1.3 equiv) was treated with CH_3CN (15 mL) and stirred to a homogeneous yellow solution. KO_2 (65 mg, 0.091 mmol, 2.5 equiv) was added as a solid and stirred at r.t. for 18 h, resulting in the formation of a red-orange precipitate. The precipitate was collected and washed with copious amounts of CH_3CN. The solid residue was dissolved in THF, filtered through Celite, and concentrated under reduced pressure. Yield = 0.421 g, 55 %. Red crystals suitable for X-ray crystallography are obtained from a concentrated THF/CH_2Cl_2 solution by slow vapor diffusion of Et_2O. Analysis calculated for $C_{116}H_{84}CaMn_4N_4O_{17}$: C 67.45, H 4.10, N 2.71; found: C 67.67, H 4.46, N 2.46.

Synthesis of **L4**: A 2 L three-neck, round-bottom flask equipped with a stir bar was charged with tris(2-bromophenyl)benzene (55.3 g, 102 mmol, 1 equiv). THF (500 mL) was added via cannula, and the solution was cooled to −78 °C in a dry ice/acetone bath. A solution of *n*-butyllithium in hexane (2.5 M, 45 mL, 113 mmol, 1.1 equiv) was added over 10 min via syringe, and the resulting orange solution was stirred for 1 hour at −78 °C. A separate 2 L three-neck, round-bottom flask equipped with a stir bar was charged with $PhPCl_2$ (19.2 g, 15 mL, 107 mmol, 1.05 equiv) and THF (500 mL). The solution containing the lithiated species was added to the solution of $PhPCl_2$ via cannula. The mixture was warmed to ambient temperature and stirred for 15 additional hours. The reaction was quenched with a saturated aqueous solution of $NaHCO_3$. The organic phase was separated,

and the aqueous phase was extracted three times with CH_2Cl_2. The combined extract was washed with brine and dried over anhydrous $MgSO_4$, filtered, and dried under reduced pressure. The residue was purified by flash column chromatography on silica using 1:1 hexanes/EtOAc (R_f = 0.3), and then dried under reduced pressure to yield **L4** as a white foamy solid (31.6 g, 53%). ^{31}P NMR ($CDCl_3$): 18.20 ppm. HRMS (FAB+): calculated for $C_{30}H_{22}OPBr^{18}Br$: 588.9754; found: 588.9749 [M+H].

Synthesis of **L5**: A pure sample of **L1** obtained from 36.8 g of tris(2-bromophenyl)benzene was used for this procedure. A 500 mL round-bottom flask equipped with a stir bar was charged with **L1**, KOH (4 g), and MeOH (300 mL). An aqueous solution of H_2O_2 (30 %, 10 mL) was added and the mixture was heated to 80 ºC for 1 hour. The mixture was cooled to room temperature and stirred for 15 additional hours. The reaction was quenched with water (500 mL) and concentrated hydrochloric acid was added dropwise until pH 0. The resulting white precipitate was collected in a fritted funnel and washed with copious amounts of water. The remaining white solid was dissolved in EtOAc, rinsed with brine, dried over anhydrous $MgSO_4$, filtered, and dried under reduced pressure to yield **L2** as a white solid (20.44 g, 50% over two steps). ^{31}P NMR ($CDCl_3$): 32.65 ppm. HRMS (FAB+): calculated for $C_{30}H_{22}O_2PBr^{18}Br$: 604.9704; found: 604.9709 [M+H].

Synthesis of $\mathbf{H_2LiL^P}$: In the glovebox, a 500 mL round-bottom flask equipped with a stir bar was charged with **L2** (19.93 g, 33 mmol, 1 equiv) and THF (200 mL). A solution of $LiN(SiMe3)_2$ (6.12 g, 36 mmol, 1.1 equiv) in THF (100 mL) was added dropwise, and the resulting red solution was stirred for 8 hours at ambient temperature. Subsequently, all volatiles were removed under reduced pressure. The beige residue was washed twice with 100 mL portions of pentane, redissolved in THF, and filtered through a pad of Celite. The

total volume of the red THF filtrate was 300 mL. The filtrate was then transferred to a 1 L Schlenk flask equipped with a stir bar and cooled to −78 ºC in a dry ice/acetone bath. A solution of *n*-butyllithium in hexane (2.5 M, 29 mL, 73 mmol, 2.2 equiv) was added via syringe at −78 °C, and the resulting green solution was stirred for 30 minutes, during which a white precipitate formed. A separate 500 mL Schlenk flask was charged with di(2-pyridyl)ketone (13.44 g, 73 mmol, 2.2 equiv) and THF (150mL). The solution of the ketone was added to the solution of the lithiated species via cannula, resulting in a green solution. Subsequently, the mixture was warmed to ambient temperature and stirred for 40 hours. The reaction was quenched by adding a saturated, aqueous solution of NH_4Cl (300 mL) and EtOAc (300 mL). The organic phase was separated, and the blue aqueous phase was extracted three times with CH_2Cl_2. The combined extract was dried over anhydrous $MgSO_4$, filtered, and dried under reduced pressure. The yellow residue was washed with copious amounts of Et_2O and dried under reduced pressure to yield **$L^{phos}H_2Li$** as a beige powder (23.7 g, 85%). HRMS (ES^-): calculated for $C_{52}H_{38}N_4O_4P$: 813.2631; found: 813.2661 [M^-].

Table 1. Crystal and refinement data for complexes **1−Mn**, **1−Fe**, and **1−Co**.

Compound	**1−Mn**	**1−Fe**	**1−Co**
CCDC	1540537	1540538	1540539
Empirical formula	$C_{102.88}H_{75.05}Cl_{2.56}Mn_4N_4O_{13.65}$	$C_{64}H_{58}Fe_4N_5O_{14}$	$C_{64}H_{58}Co_4N_5O_{14}$
Formula weight	1896.13	1344.55	1356.87
Temperature/K	99.99	100.04	100.03
Crystal system	triclinic	triclinic	triclinic
Space group	P-1	P-1	P-1
a/Å	13.5028(18)	13.7237(14)	13.7817(7)
b/Å	16.598(2)	13.9138(13)	13.8132(7)
c/Å	21.517(3)	17.8609(17)	17.7104(9)
α/°	77.057(3)	75.523(4)	75.742(2)
β/°	82.240(3)	75.229(3)	75.384(2)
γ/°	83.778(3)	65.876(3)	66.637(2)
Volume/Å^3	4641.4(11)	2968.4(5)	2954.1(3)
Z	2	2	2
ρ_{calc}g/cm^3	1.357	1.504	1.525
μ/mm^{-1}	0.671	1.030	1.176
F(000)	1946.0	1386.0	1394.0
Crystal size/mm^3	0.1 × 0.05 × 0.05	0.02 × 0.02 × 0.02	0.2 × 0.1 × 0.1
Radiation	MoKα (λ = 0.71073)	MoKα (λ = 0.71073)	MoKα (λ = 0.71073)
2Θ range for data collection/°	3.802 to 61.494	4.782 to 56.528	4.82 to 61.016
Index ranges	-19 ≤ h ≤ 19, -23 ≤ k ≤ 23, -30 ≤ l ≤ 30	-18 ≤ h ≤ 18, -18 ≤ k ≤ 18, -23 ≤ l ≤ 23	-19 ≤ h ≤ 19, -19 ≤ k ≤ 19, -25 ≤ l ≤ 25
Reflections collected	132477	105521	113132
Independent reflections	28763 [R_{int} = 0.0752, R_{sigma} = 0.0738]	14691 [R_{int} = 0.1863, R_{sigma} = 0.1232]	18006 [R_{int} = 0.0489, R_{sigma} = 0.0335]
Data/restraints/parameters	28763/8/1108	14691/6/765	18006/0/765
Goodness-of-fit on F^2	1.061	1.045	1.054
Final R indexes [I>=2σ (I)]	R_1 = 0.0904, wR_2 = 0.2523	R_1 = 0.0744, wR_2 = 0.1510	R_1 = 0.0448, wR_2 = 0.1262
Final R indexes [all data]	R_1 = 0.1340, wR_2 = 0.2767	R_1 = 0.1521, wR_2 = 0.1771	R_1 = 0.0641, wR_2 = 0.1375
Largest diff. peak/hole / e Å^{-3}	2.22/-1.47	1.67/-1.06	1.84/-1.46

Table 2. Crystal and refinement data for complexes **2-Mn** and **2-Ca**.

Compound	**2-Mn**	**2-Ca**
CCDC	1540540	1540541
Empirical formula	$C_{128}H_{109}Mn_5N_4O_{20}$	$C_{120}H_{92}CaCl_4Mn_4N_4O_{17.5}$
Formula weight	2297.93	2271.61
Temperature/K	100.04	100.0
Crystal system	triclinic	triclinic
Space group	P-1	P-1
a/Å	14.7524(8)	14.8017(4)
b/Å	16.2906(8)	16.3782(5)
c/Å	22.1991(12)	21.9258(6)
α/°	90.350(2)	88.2880(10)
β/°	98.124(2)	81.0900(10)
γ/°	92.207(2)	87.5960(10)
Volume/Å^3	5277.2(5)	5245.1(3)
Z	2	2
ρ_{calc}g/cm^3	1.446	1.438
μ/mm^{-1}	0.658	0.693
F(000)	2380.0	2336.0
Crystal size/mm^3	0.05 × 0.05 × 0.05	0.1 × 0.05 × 0.05
Radiation	MoKα (λ = 0.71073)	MoKα (λ = 0.71073)
2Θ range for data collection/°	4.312 to 61.016	4.408 to 61.046
Index ranges	-21 ≤ h ≤ 21, -23 ≤ k ≤ 23, -31 ≤ l ≤ 31	-21 ≤ h ≤ 21, -23 ≤ k ≤ 23, -31 ≤ l ≤ 31
Reflections collected	130593	161254
Independent reflections	32156 [R_{int} = 0.0384, R_{sigma} = 0.0461]	31911 [R_{int} = 0.0567, R_{sigma} = 0.0615]
Data/restraints/parameters	32156/10/1412	31911/26/1362
Goodness-of-fit on F^2	1.032	1.025
Final R indexes [I>=2σ (I)]	R_1 = 0.0528, wR_2 = 0.1279	R_1 = 0.0745, wR_2 = 0.1886
Final R indexes [all data]	R_1 = 0.0782, wR_2 = 0.1414	R_1 = 0.1157, wR_2 = 0.2124
Largest diff. peak/hole / e Å^{-3}	1.69/-1.10	2.22/-1.84

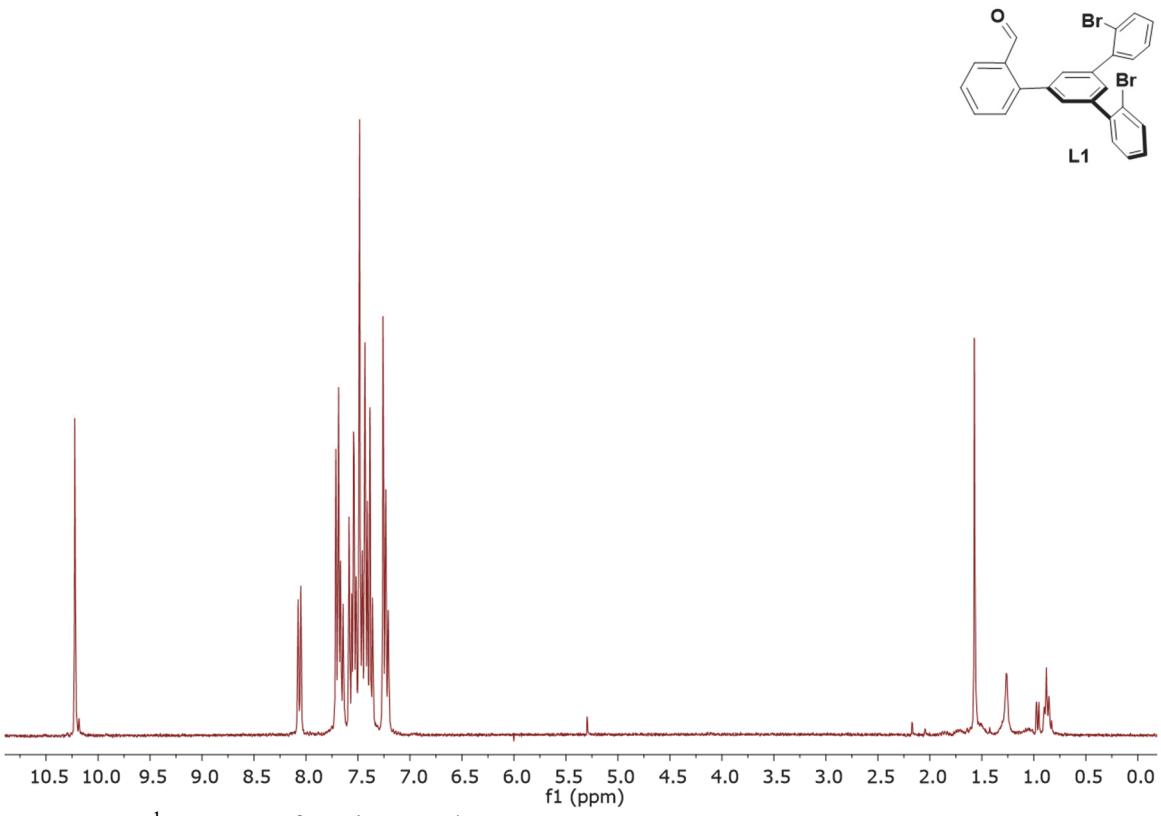

Figure 16. ^{1}H NMR of **L1** in $CDCl_3$.

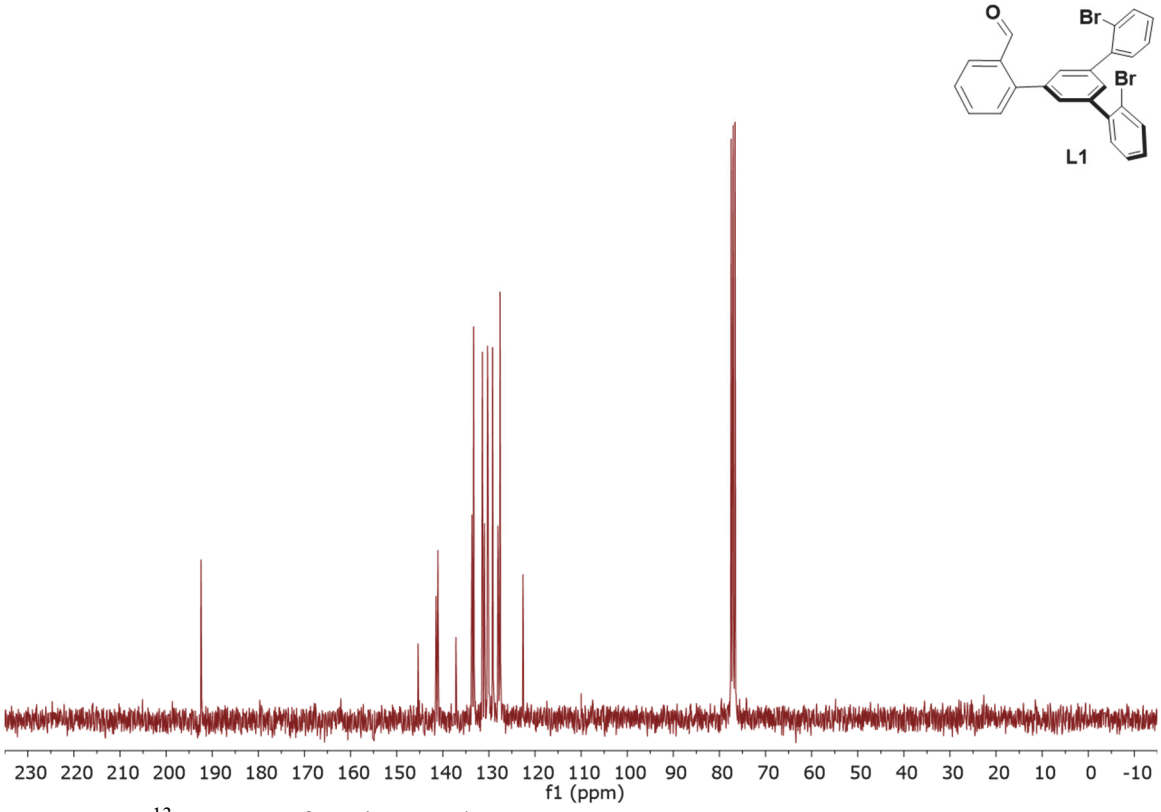

Figure 17. ^{13}C NMR of **L1** in $CDCl_3$.

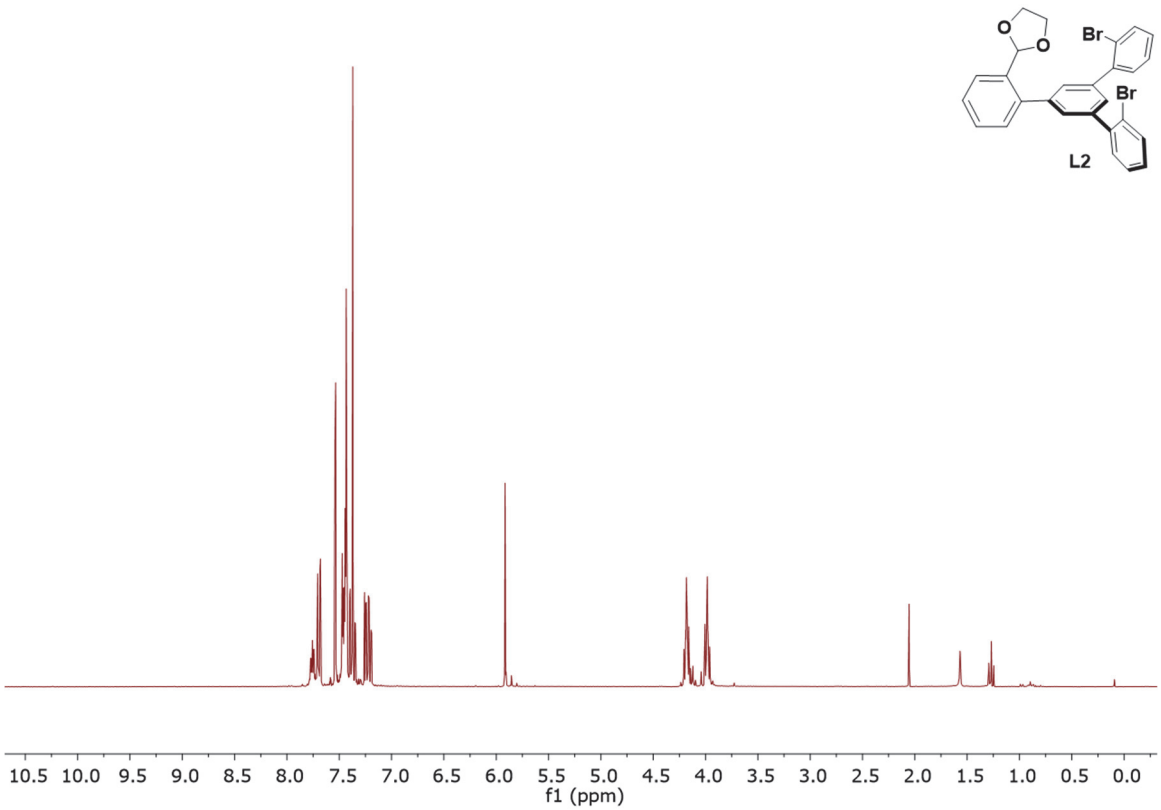

Figure 18. ^{1}H NMR of **L2** in $CDCl_3$.

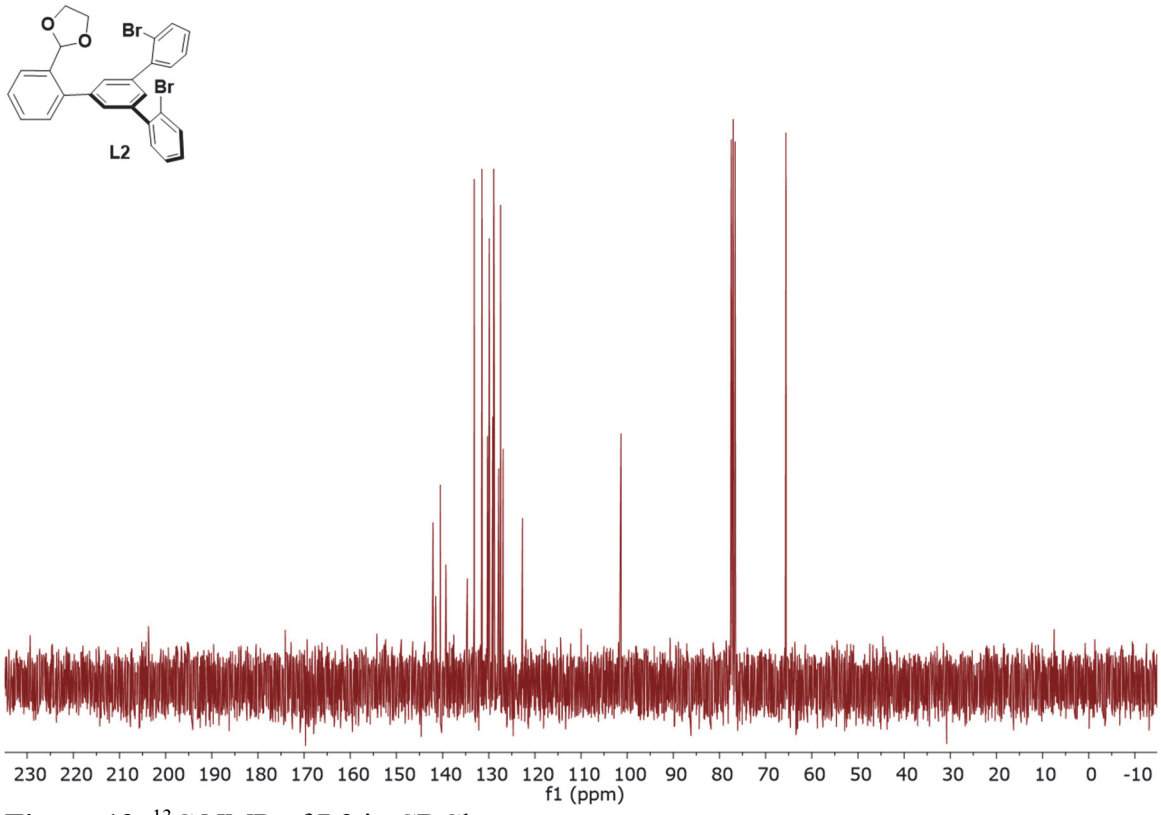

Figure 19. ^{13}C NMR of **L2** in $CDCl_3$.

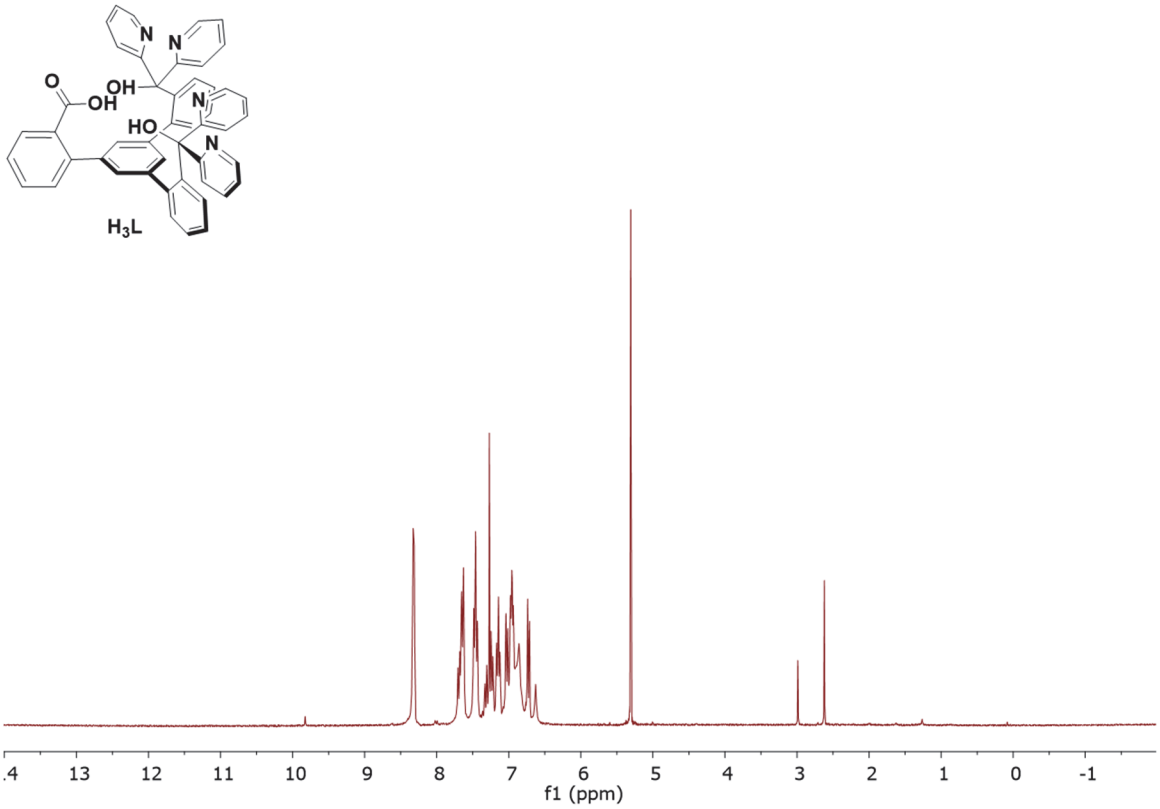

Figure 20. ^{1}H NMR of **H_3L'** in $CDCl_3$.

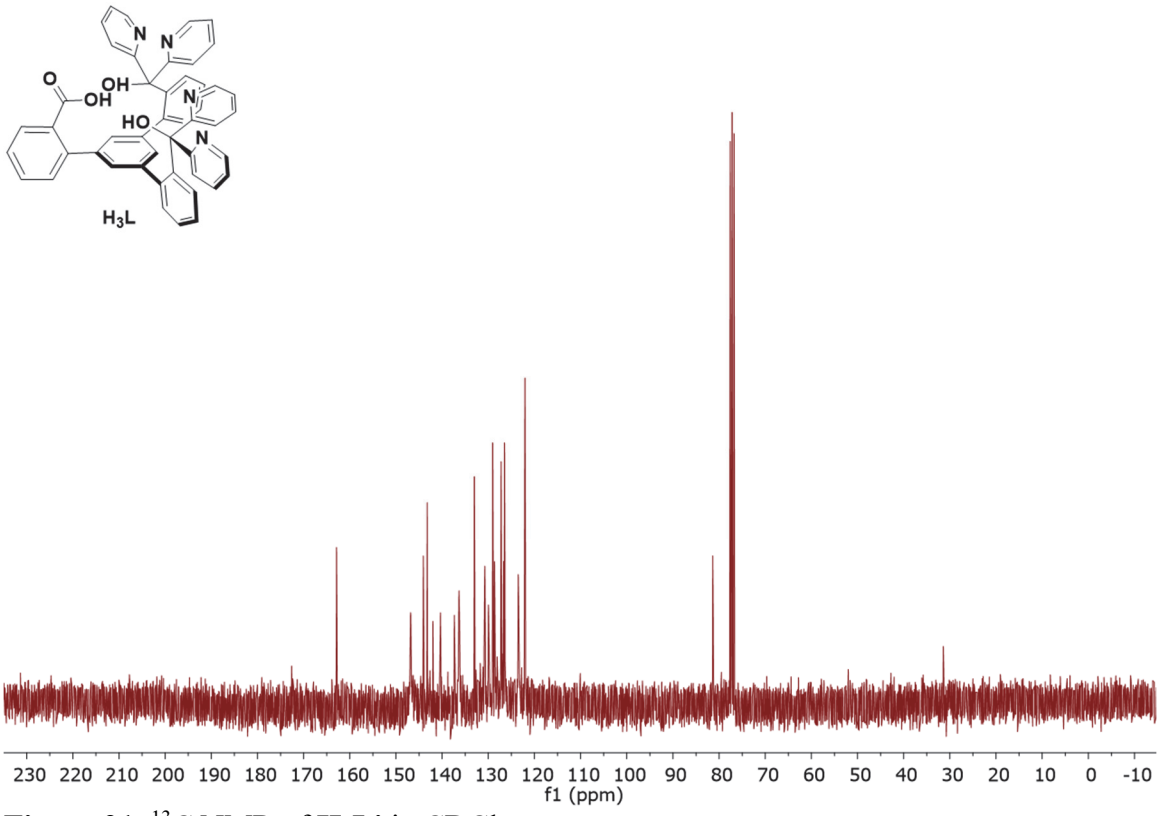

Figure 21. ^{13}C NMR of **H_3L'** in $CDCl_3$.

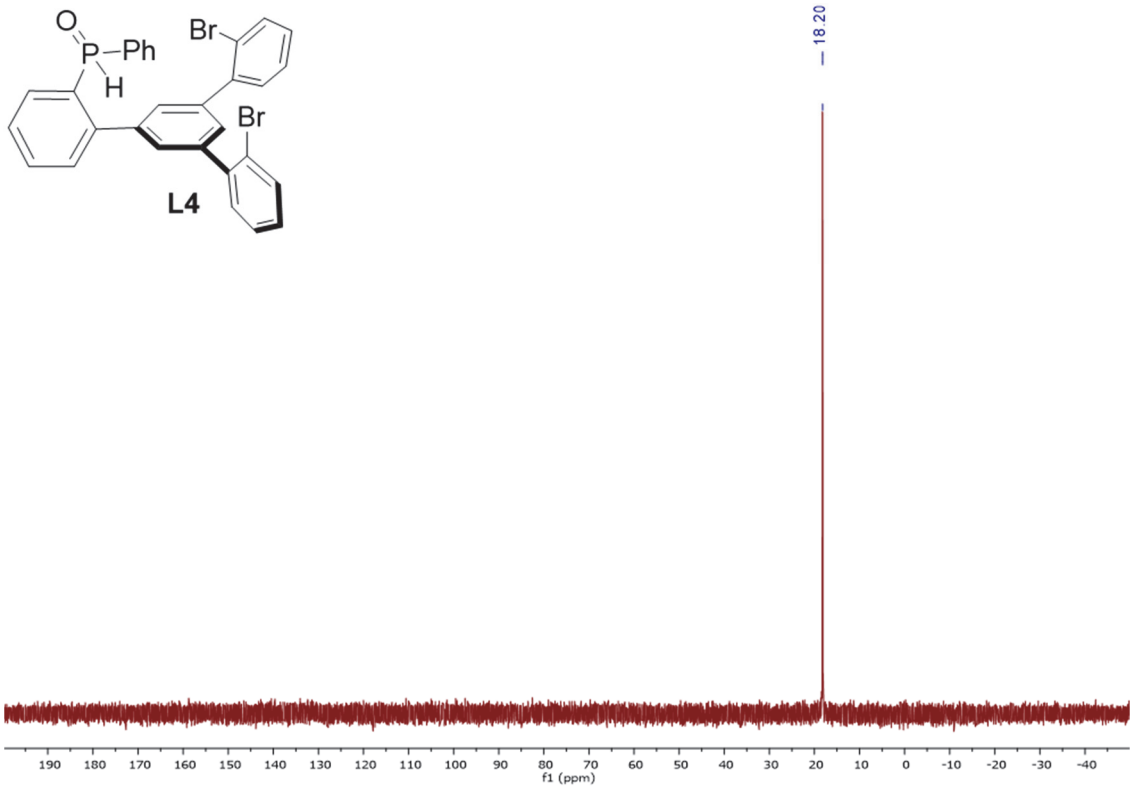

Figure 22. ^{31}P NMR of **L4**.

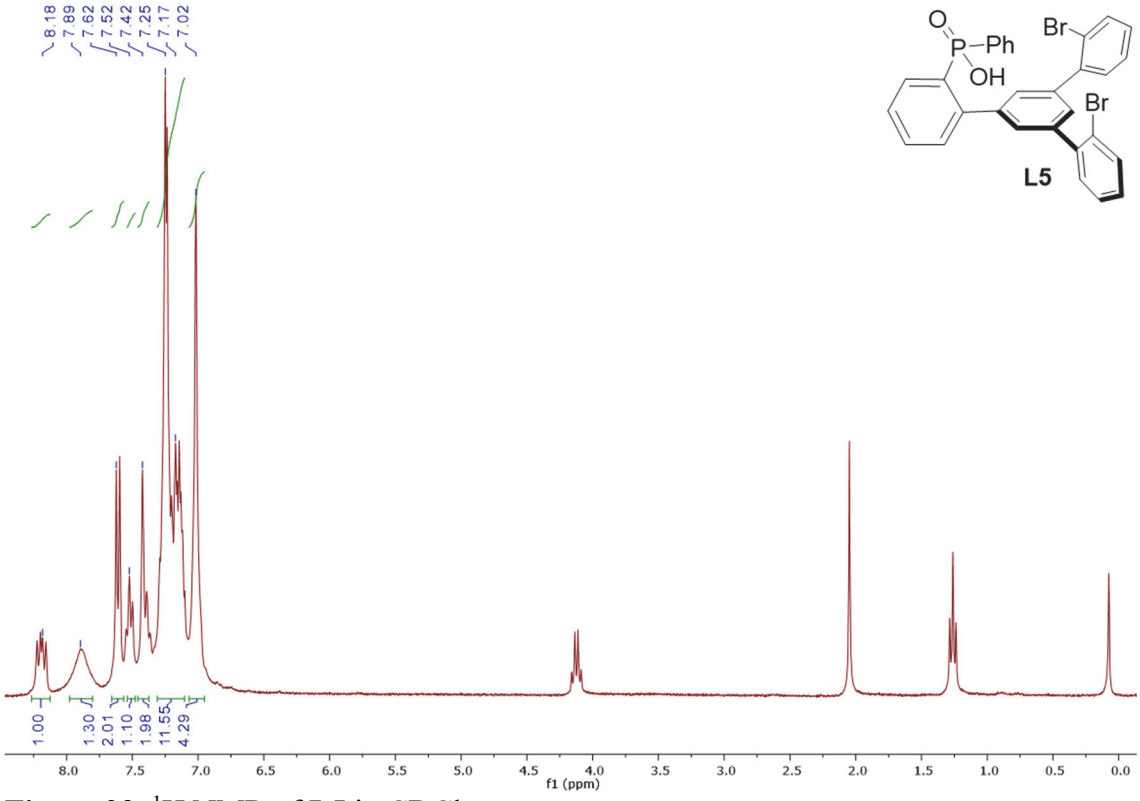

Figure 23. ^{1}H NMR of **L5** in $CDCl_3$.

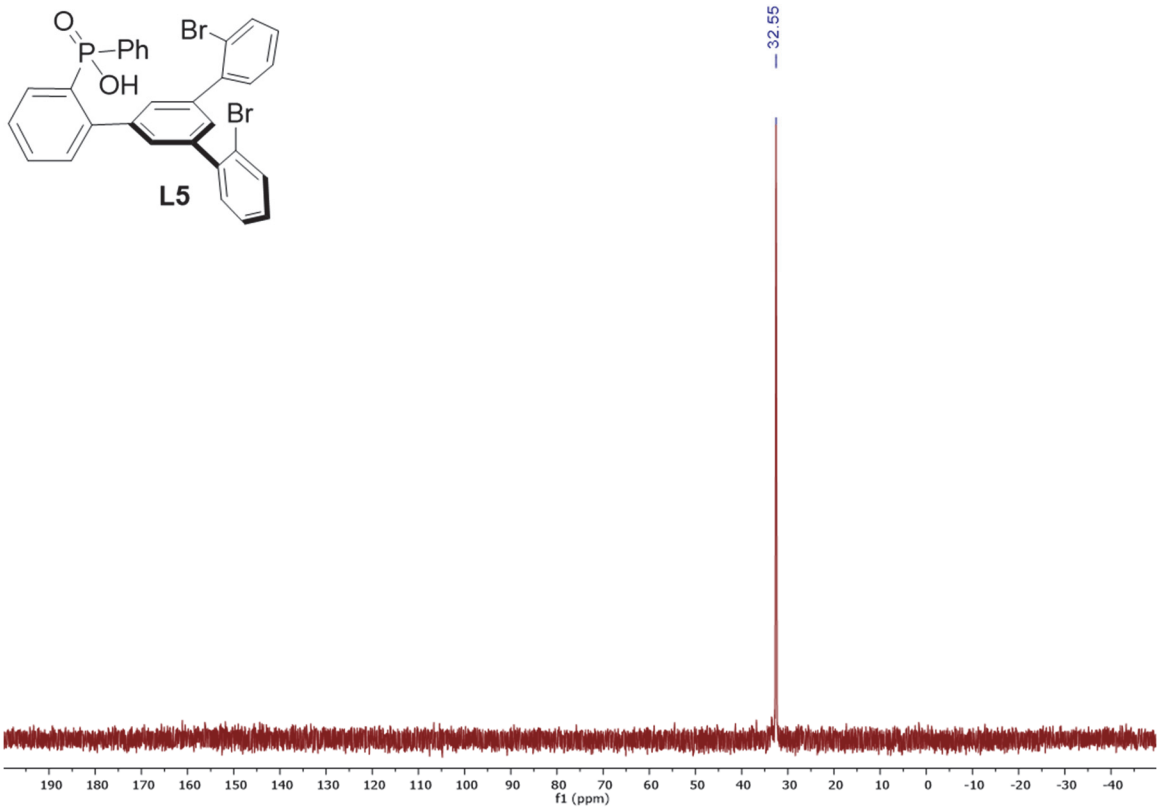

Figure 24. ^{31}P NMR of **L5**.

2.7) References

(1) Yano, J.; Yachandra, V., *Chem. Rev.* **2014**, *114*, 4175.
(2) Shen, J. R., *Annu Rev Plant Biol* **2015**, *66*, 23.
(3) Blakemore, J. D.; Crabtree, R. H.; Brudvig, G. W., *Chem. Rev.* **2015**, *115*, 12974.
(4) Tsui, E. Y.; Kanady, J. S.; Agapie, T., *Inorg. Chem.* **2013**, *52*, 13833.
(5) Dismukes, G. C.; Brimblecombe, R.; Felton, G. A. N.; Pryadun, R. S.; Sheats, J. E.; Spiccia, L.; Swiegers, G. F., *Acc. Chem. Res.* **2009**, *42*, 1935.
(6) Mukhopadhyay, S.; Mandal, S. K.; Bhaduri, S.; Armstrong, W. H., *Chem. Rev.* **2004**, *104*, 3981.
(7) Gerey, B.; Gouré, E.; Fortage, J.; Pécaut, J.; Collomb, M.-N., *Coord. Chem. Rev.* **2016**, *319*, 1.
(8) Mishra, A.; Wernsdorfer, W.; Abboud, K. A.; Christou, G., *Chem. Commun.* **2005**, 54.
(9) Mishra, A.; Yano, J.; Pushkar, Y.; Yachandra, V. K.; Abboud, K. A.; Christou, G., *Chem. Commun.* **2007**, 1538.
(10) Hewitt, I. J.; Tang, J.-K.; Madhu, N. T.; Clerac, R.; Buth, G.; Anson, C. E.; Powell, A. K., *Chem. Commun.* **2006**, 2650.
(11) Nayak, S.; Nayek, H. P.; Dehnen, S.; Powell, A. K.; Reedijk, J., *Dalton Trans.* **2011**, *40*, 2699.
(12) Park, Y. J.; Ziller, J. W.; Borovik, A. S., *J. Am. Chem. Soc.* **2011**, *133*, 9258.

(13) Mukherjee, S.; Stull, J. A.; Yano, J.; Stamatatos, T. C.; Pringouri, K.; Stich, T. A.; Abboud, K. A.; Britt, R. D.; Yachandra, V. K.; Christou, G., *Proc. Nat. Acad. Sci.* **2012**, *109*, 2257.
(14) Park, Y. J.; Cook, S. A.; Sickerman, N. S.; Sano, Y.; Ziller, J. W.; Borovik, A. S., *Chem. Sci.* **2013**, *4*, 717.
(15) Koumousi, E. S.; Mukherjee, S.; Beavers, C. M.; Teat, S. J.; Christou, G.; Stamatatos, T. C., *Chem. Commun.* **2011**, *47*, 11128.
(16) Azar, M. R.; Boron, T. T.; Lutter, J. C.; Daly, C. I.; Zegalia, K. A.; Nimthong, R.; Ferrence, G. M.; Zeller, M.; Kampf, J. W.; Pecoraro, V. L.; Zaleski, C. M., *Inorg. Chem.* **2014**, *53*, 1729.
(17) Gerey, B.; Gennari, M.; Goure, E.; Pecaut, J.; Blackman, A.; Pantazis, D. A.; Neese, F.; Molton, F.; Fortage, J.; Duboc, C.; Collomb, M.-N., *Dalton Trans.* **2015**, *44*, 12757.
(18) Kanady, J. S.; Tsui, E. Y.; Day, M. W.; Agapie, T., *Science* **2011**, *333*, 733.
(19) Tsui, E. Y.; Agapie, T., *Proc. Nat. Acad. Sci.* **2013**, *110*, 10084.
(20) Kanady, J. S.; Mendoza-Cortes, J. L.; Tsui, E. Y.; Nielsen, R. J.; Goddard, W. A.; Agapie, T., *J. Am. Chem. Soc.* **2013**, *135*, 1073.
(21) Tsui, E. Y.; Tran, R.; Yano, J.; Agapie, T., *Nat Chem* **2013**, *5*, 293.
(22) Kanady, J. S.; Lin, P.-H.; Carsch, K. M.; Nielsen, R. J.; Takase, M. K.; Goddard, W. A.; Agapie, T., *J. Am. Chem. Soc.* **2014**, *136*, 14373.
(23) Zhang, C.; Chen, C.; Dong, H.; Shen, J.-R.; Dau, H.; Zhao, J., *Science* **2015**, *348*, 690.
(24) Tsui, E. Y.; Kanady, J. S.; Day, M. W.; Agapie, T., *Chem. Commun.* **2011**, *47*, 4189.
(25) Herbert, D. E.; Lionetti, D.; Rittle, J.; Agapie, T., *J. Am. Chem. Soc.* **2013**, *135*, 19075.
(26) Kanady, J. S.; Tran, R.; Stull, J. A.; Lu, L.; Stich, T. A.; Day, M. W.; Yano, J.; Britt, R. D.; Agapie, T., *Chem. Sci.* **2013**, *4*, 3986.
(27) Bal, B. S.; Childers, W. E.; Pinnick, H. W., *Tetrahedron* **1981**, *37*, 2091.
(28) Vincent, J. B.; Chang, H. R.; Folting, K.; Huffman, J. C.; Christou, G.; Hendrickson, D. N., *J. Am. Chem. Soc.* **1987**, *109*, 5703.
(29) Christou, G., *Acc. Chem. Res.* **1989**, *22*, 328.
(30) Canada-Vilalta, C.; Pink, M.; Christou, G., *Dalton Trans.* **2003**, 1121.
(31) Reynolds, R. A.; Yu, W. O.; Dunham, W. R.; Coucouvanis, D., *Inorg. Chem.* **1996**, *35*, 2721.
(32) Aromí, G.; Batsanov, A. S.; Christian, P.; Helliwell, M.; Parkin, A.; Parsons, S.; Smith, A. A.; Timco, G. A.; Winpenny, R. E. P., *Chem. Eur. J.* **2003**, *9*, 5142.
(33) Kiskin, M. A.; Fomina, I. G.; Aleksandrov, G. G.; Sidorov, A. A.; Novotortsev, V. M.; Shvedenkov, Y. G.; Eremenko, I. L.; Moiseev, I. I., *Inorg. Chem. Commun.* **2004**, *7*, 734.
(34) Lachicotte, R. J.; Hagen, K. S., *Inorg. Chim. Acta* **1997**, *263*, 407.
(35) Mizoguchi, T. J.; Lippard, S. J., *J. Am. Chem. Soc.* **1998**, *120*, 11022.
(36) Mizoguchi, T. J.; Kuzelka, J.; Spingler, B.; DuBois, J. L.; Davydov, R. M.; Hedman, B.; Hodgson, K. O.; Lippard, S. J., *Inorg. Chem.* **2001**, *40*, 4662.
(37) Hartman, J. A. R.; Rardin, R. L.; Chaudhuri, P.; Pohl, K.; Wieghardt, K.; Nuber, B.; Weiss, J.; Papaefthymiou, G. C.; Frankel, R. B.; Lippard, S. J., *J. Am. Chem. Soc.* **1987**, *109*, 7387.
(38) Chaudhury, P.; Wieghardt, K.; Nuber, B.; Weiss, J., *Angew. Chem. Int. Ed.* **1985**, *24*, 778.

CHAPTER 3

Tetranuclear [$Mn^{III}Mn_3^{IV}O_4$] Complexes as Spectroscopic Models of the S_2 State of the Oxygen Evolving Complex in Photosystem II

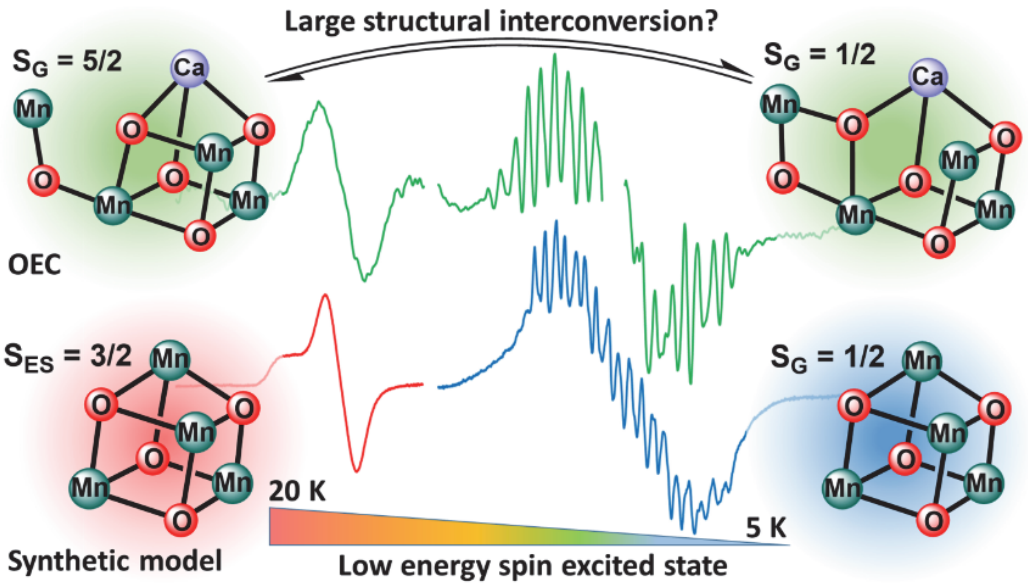

The text for this chapter was reproduced in part from:

Lee, H. B.; Shiau, A. A.; Oyala, P. H.; Marchiori, D. A.; Gul, S.; Chatterjee, R.; Yano, J.; Britt, R. D.; Agapie, T. *J. Am. Chem. Soc.*, **2018**, *140*, 17175-17187
DOI: 10.1021/jacs.8b09961

Abstract

Despite extensive biochemical, spectroscopic, and computational studies, the mechanism of biological water oxidation by the Oxygen Evolving Complex (OEC) of Photosystem II remains a subject of significant debate. Mechanistic proposals are guided by the characterization of reaction intermediates such as the S_2 state, which features two characteristic EPR signals at $g = 2$ and $g = 4.1$. Two nearly isoenergetic structural isomers have been proposed as the source of these distinct signals, but relevant structure−electronic structure studies remain rare. Herein, the synthesis, crystal structure, electrochemistry, XAS, magnetic susceptibility, variable temperature CW-EPR, and pulse EPR data for a series of $[Mn^{III}Mn_3^{IV}O_4]$ cuboidal complexes as spectroscopic models of the S_2 state of the OEC is reported. Resembling the oxidation state and EPR spectra of the S_2 state of the OEC, these model complexes show two EPR signals, a broad low field signal and a multiline signal, that are remarkably similar to the biological system. The effect of systematic changes in the nature of the bridging ligands on spectroscopy were studied. Results show that the electronic structure of tetranuclear Mn complexes is highly sensitive to even small geometric changes and the nature of the bridging ligands. Our model studies suggest that the spectroscopic properties of the OEC may also react very sensitively to small changes in structure; the effect of protonation state and other reorganization processes needs to be carefully assessed.

3.1) Introduction

Structural determination and spectroscopic characterization of intermediates (and derivatives thereof) in the S-state catalytic cycle of the Oxygen Evolving Complex (OEC) of Photosystem II (PSII) heavily influence mechanistic proposals for O−O bond formation.[1-14] The dark-stable S_1 state of the OEC consists of a $CaMn_4O_5$ cluster with Mn oxidation states $Mn^{III}_2Mn^{IV}_2$.[15] Light-induced one electron oxidation of the S_1 state results in the formation of the S_2 state, with two characteristic EPR transitions centered at $g = 2$ and $g = 4.1$.[9, 11, 13, 16] Two additional one electron oxidations lead to the formation of S_3 and S_4 states, respectively, and dioxygen is evolved following formation of the elusive S_4 state.[17] Chemical changes such as Ca^{2+} removal or treatment with NH_3 or F^- inhibit the $S_2 \rightarrow S_3$ transition specifically, highlighting opportunities for mechanistic insight,[4, 18] but also the need for benchmarking with well characterized synthetic models. Constrained by available data from XAS and EPR spectroscopy, the current understanding of the S_2 state structure is based on theoretical studies starting from the high-resolution (1.95 Å), radiation damage-free X-ray structure of the S_1 state.[19-20] Each EPR signal in the S_2 state is proposed to originate from different structures (Figure 1): an "open cubane" structure with a low-spin (LS) $S = 1/2$ ground state and a "closed cubane" structure with a high-spin (HS) $S = 5/2$ ground state.[21-23] The interconvertibility of the two EPR signals suggests a small energy difference between these two structures; IR irradiation of the LS form at 120−150 K results in the formation of the HS form, which can be reverted to the LS form by annealing at 200 K.[11] The two structural isomers effectively differ only by the relative position of the bridging O(5) oxygen, a water derived oxygen, which is proposed to undergo O−O coupling to generate O_2.[24-25] Time-resolved, femtosecond X-ray free electron laser (XFEL)

techniques offer the possibility of observing structural and spectroscopic changes in the OEC under dynamic, catalytically active conditions.[26-31] For such studies, further improvements in resolution and issues with S-state heterogeneity and deconvolution remain to be addressed.[27, 31-32]

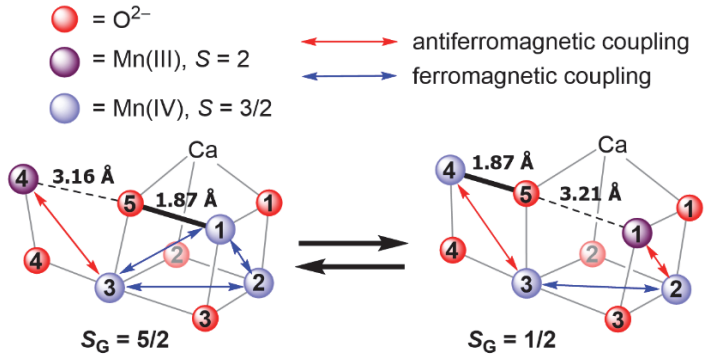

Figure 1. Computed structures for the proposed isomers of the inorganic $CaMn_4O_5$ core of the OEC in the S_2 state. The large structural changes in the Mn-oxo distances have been calculated to lead to different electronic coupling between the Mn centers and a change in the spin ground state (S_G), which explain the two observed EPR signals. Mn(4)−O(5) and Mn(1)−O(5) distances shown with bold and dashed lines. Nature of the computed magnetic exchange coupling initeractions shown in red (antiferromagnetic) and blue (ferromagnetic) arrows.

Growing experimental data support that conversion from the LS form of the S_2 state to its HS form is an intermediate step in the $S_2 \rightarrow S_3$ transition.[33] pH dependence studies indicate that deprotonation of the LS form leads to the HS form.[34] Structural changes following deprotonation are unknown, but computational studies suggest that the electronic structure of the OEC is highly sensitive to small changes in structure as reported by EPR spectroscopy.[35] Deprotonation of a Mn-bound water and/or a reorientation of a Glu residue in the S_2 state may perturb the ground spin state from LS to HS, indicating that spectroscopic properties may react very sensitively to small geometric changes that do not lead to significant changes in the total energy of the cluster.[35] EXAFS studies support structural differences between the species responsible for the $g = 2$ and the $g = 4.1$ signal, but further atomistic details are unknown.[36-37]

In contrast to the extensive studies performed on the S_2 state of the OEC, structural and spectroscopic studies of $Mn^{III}Mn_3^{IV}$ model complexes remain rare[38-40], and can be summarized as follows. The phosphinate-bridged, cuboidal complex $[Mn_4O_4(Ph_2PO_2)_6]^+$ shows a broad EPR spectrum.[41] The g = 4.1 signal of the adamantane-shaped complex $[Mn_4O_6(bpea)_4]^{3+}$ has been assigned to the first excited Kramers doublet of an S = 5/2 ground state determined from magnetization data.[42] Starting from a linear-chain precursor, a putative complex $[Mn_4O_6(bpy)_6]^{3+}$ was generated by radiolysis and features a multiline signal centered at g = 2 consistent with an S = 1/2 ground state.[43] In-situ oxidation of a close OEC structural model complex, $CaMn_4O_4(OPiv)_8$, gives rise to two EPR signals at g = 4.9 and g = 2, attributed to different spin states of the cluster corresponding to a $[CaMn_4O_4(OPiv)_8]^+$ species, although further structural, spectroscopic, and magnetic data have not been provided.[44] Follow-up computational studies disagree on the assignment of the two signals, one of them suggesting that the two signals must be due to structurally very different clusters.[45-46] In general, systematic studies that probe the effect of small structural changes on the spectroscopic and magnetic properties of S_2 model clusters are very rare, likely due to the synthetic challenges of accessing a series of isolable clusters that are suitable for comparisons.[47-48] Indeed, despite significant efforts to prepare tetra- and penta-nuclear clusters that are relevant to the S-state intermediates in terms of structure, redox state, or spectroscopy, accurate models for benchmarking against the biological system are rare.[41, 47, 49-69]

Herein, we report the synthesis, crystal structure, electrochemistry, XAS, SQUID magnetometry, variable temperature CW-EPR, and pulse EPR data for a series of $[Mn^{III}Mn_3^{IV}O_4]$ cuboidal complexes. Results show that the electronic structures of

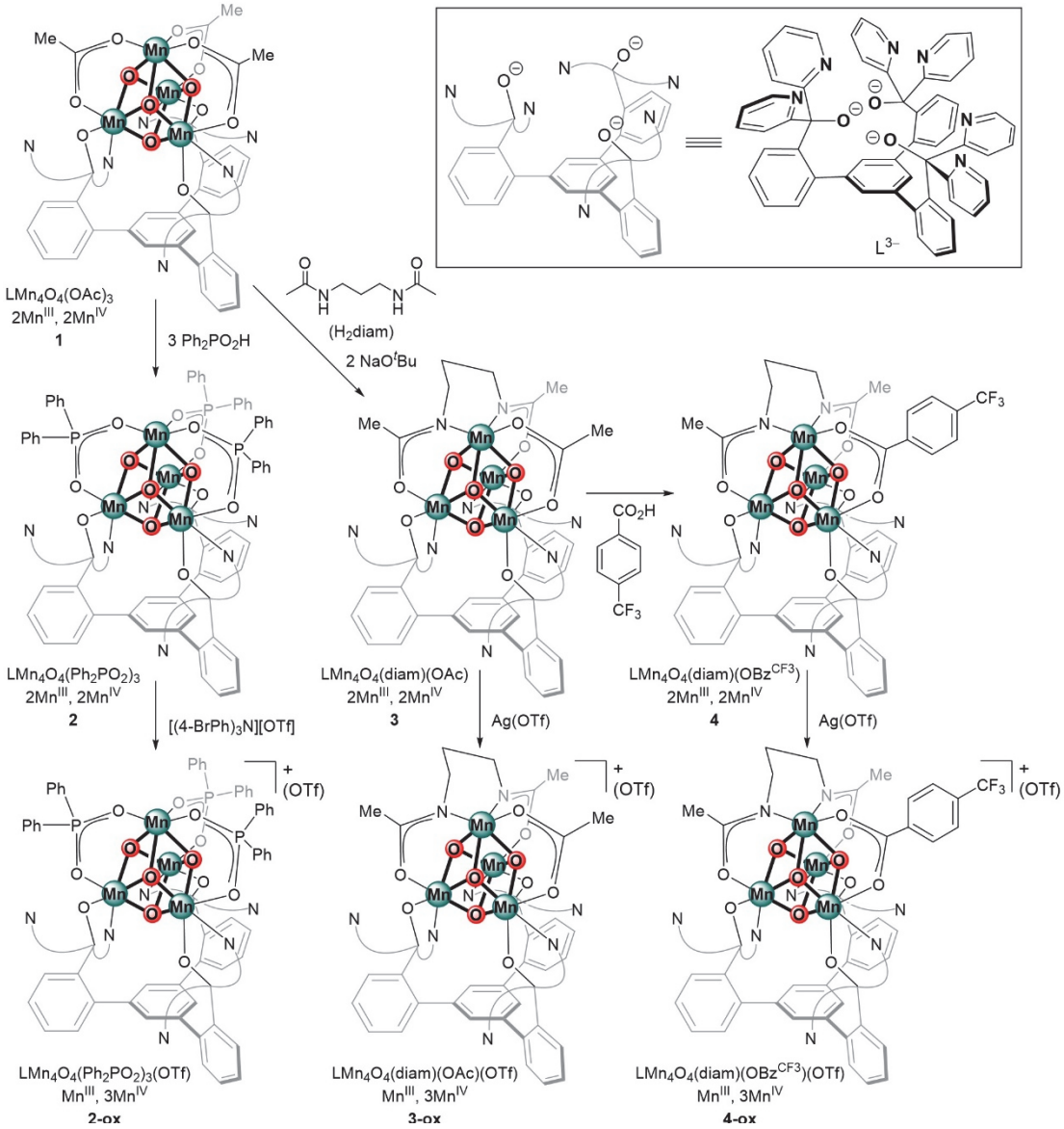

Figure 2. Synthesis of complexes **2**~**4** and their oxidized analogues **2-ox**~**4-ox**.

tetranuclear Mn complexes are highly sensitive to even small geometric changes promoted by the nature of the supporting ligands. Similar to the computational studies performed on the S_2 state, our experimental studies on model clusters suggest that the spectroscopic properties of the OEC may also react very sensitively to small changes in structure.

3.2) Synthesis, crystal structure, and electrochemistry

One electron reduced $[Mn_2^{III}Mn_2^{IV}O_4]$ cuboidal complexes were chosen as precursors for the targeted $[Mn^{III}Mn_3^{IV}O_4]$ complexes. We have previously reported the synthesis of

$LMn_2^{III}Mn_2^{IV}O_4(OAc)_3$ (**1,** Figure 2).[56-57, 70] The cyclic voltammogram (CV) of **1** shows a reversible redox process at +250 mV vs. Fc/Fc^+ assigned to the $(Mn_2^{III}Mn_2^{IV})/(Mn^{III}Mn_3^{IV})$ couple. Treatment of **1** with 1 equiv. of $[(4\text{-}BrPh)_3N][SbCl_6]$ results in the formation of an unstable species, but rapid freeze-quenching of the reaction mixture allowed the observation of an intense EPR spectrum with a broad signal centered at $g = 2$ featuring Mn hyperfine interactions, consistent with an $S = 1/2$ ground state (Figure 3). In contrast, the phosphinate-bridged cuboidal complex $[Mn_4O_4(Ph_2PO_2)_6]^+$ has a higher spin ground state $S \geq 3/2$. The product of oxidation of **1** features other broad EPR signals at $g > 2$ that can be assigned to spin excited states or decomposition products, but further investigation was not pursued.

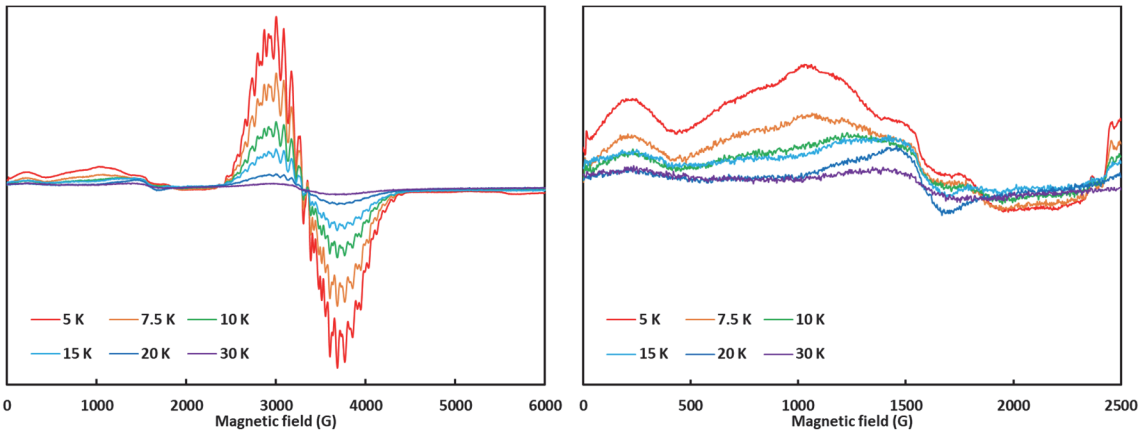

Figure 3. Temperature-dependent X-band CW-EPR spectra of a freeze-quenched reaction mixture of **1** and $[(4\text{-}BrPh)_3N][SbCl_6]$. Data acquisition parameters: frequency = 9.35 MHz, power = 2 mW, conversion time = 20.48 ms, modulation amplitude = 8 G.

Based on the reduction potential of the isolable $[Mn_4O_4(Ph_2PO_2)_6]^+$ complex at +680 mV vs. Fc/Fc^+, we targeted oxidatively stable phosphinate-bridged complexes.[41, 61] Treatment of **1** with 3 equiv. HO_2PPh_2 in THF leads to the formation of **2** via a protonolysis reaction (Figure 2). The ESI-MS peak at m/z = 1792 is consistent with the mass of $[LMn_4O_4(O_2PPh_2)_3]^+$. The X-ray crystal structure of **2** is consistent with the $LMn_4O_4(O_2PPh_2)_3$ formulation (Figure 4). Based on Mn−oxo distances, the oxidation

states of Mn(1) and Mn(2) are assigned to Mn^{IV}, and those of Mn(3) and Mn(4) to Mn^{III}. Axial elongation of Mn^{III}–oxo distances is observed, at 2.177(2) and 2.187(2) Å for Mn(3) and Mn(4), respectively. These are due to population of a dz^2-σ antibonding orbital. Given the heteroleptic coordination around Mn(3), the Jahn-Teller effect is not invoked to describe the observed distortion. The coordination environment around Mn(4) can be viewed as *pseudo-*O_h, in which case the Jahn-Teller elongation can be invoked to remove the degeneracy of the ^5E_g ground state.[71-72] Similar Mn^{III}–oxo elongations were observed for **1**, at 2.201(2) and 2.234(2) Å. The CV of **2** shows a reversible redox process at +190 mV vs. Fc/Fc^+ assigned to the $(Mn_2^{III}Mn_2^{IV})/(Mn^{III}Mn_3^{IV})$ couple (Figure 5). Treatment of **2** with 1 equiv. of $[(4\text{-BrPh})_3N][OTf]$ leads to the formation of the one-electron oxidized species **2-ox**.[73] The ESI-MS and crystal structure of **2-ox** is consistent with the $LMn_4O_4(O_2PPh_2)_3(OTf)$ formulation (Figure 4). Based on Mn–oxo distances, the oxidation state of Mn(4) is assigned as Mn^{III}. The elongated Mn(4)–O(4) distance of 2.241(1) Å is consistent with this assignment.

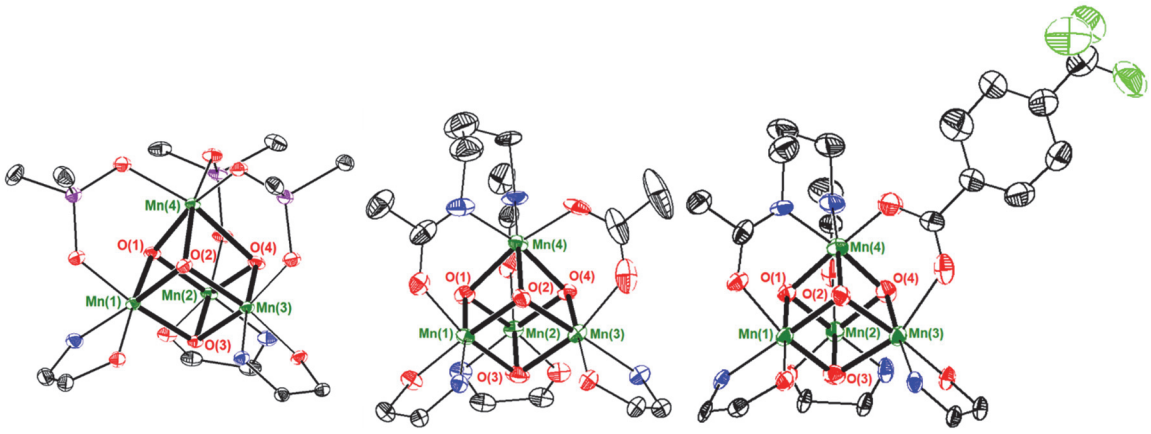

Figure 4. Truncated crystal structures of **2-ox** (left), **3-ox** (middle), and **4-ox** (right). Mn (green), O (red), N (blue), P (purple), C (black), and F (light green). Bolded bonds highlight metal-oxo bonds.

Toward expanding the series of Mn_4 clusters with the same redox state as the S_2 state of the OEC, other supporting ligands were targeted. Based on the precedent that amidate

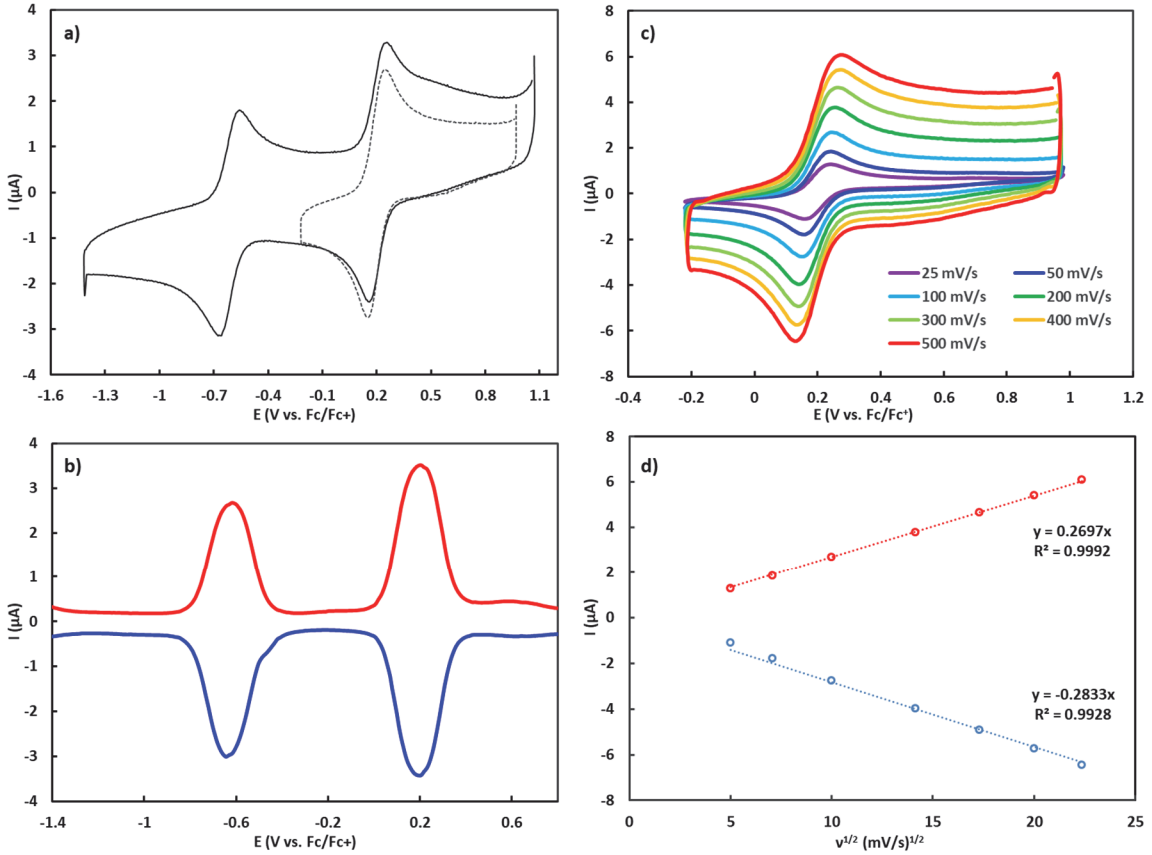

Figure 5. a) CV of **2**. Isolated redox couple shown in dotted lines. E = + 194 mV vs. Fc/Fc^{+}. b) SWV of **2**. c) Isolated redox couple measured at various scan rates. d) Plot of peak current vs. square root of scan rate.

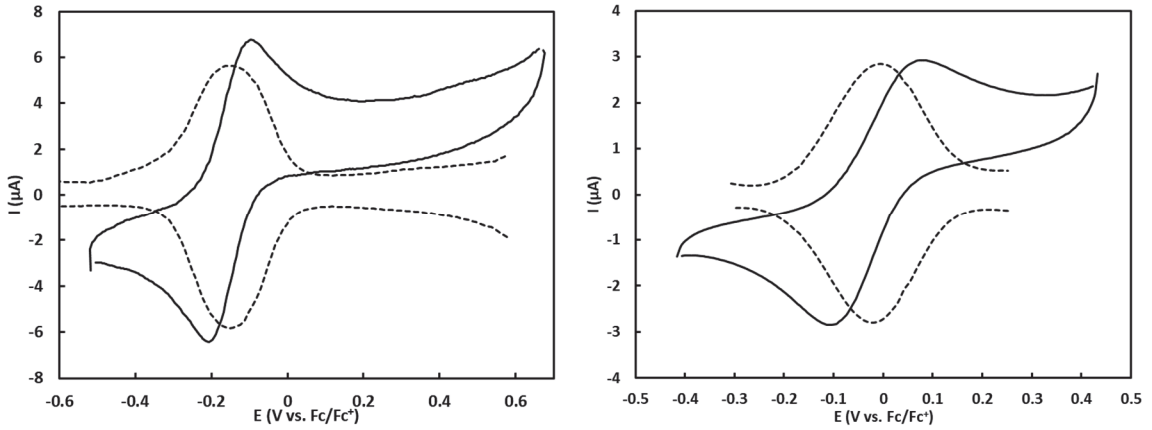

Figure 6. (Left) CV (solid lines) and SVW (dotted lines) of **3** in propylene carbonate. E = −150 mV vs. Fc/Fc^{+}. (Right) CV (solid lines) and SVW (dotted lines) of **4** in propylene carbonate. E = −15 mV vs. Fc/Fc^{+}.

ligands have been employed for the synthesis of a high oxidation state Mn^{V}-oxo complex,[74] we targeted a related class of oxidatively stable amidate-bridged $[Mn_4O_4]$ cuboidal complexes. In contrast to the vast number of carboxylate-bridged high oxidation state

metal-oxo clusters, amidate-bridged metal-oxo clusters are rare.[75-78] We employed an *n*-propyl-linked diacetamide proligand (H_2diam) to replace two acetate moieties. Treatment of **1** with 1 equiv. H_2diam and 2 equiv. NaO^{t}Bu in DMF leads to the formation of **3** (Figure 2). The ESI-MS and crystal structure of **3** are consistent with the LMn_4O_4(diam)(OAc) formulation. A smaller variation of Mn−oxo distances is observed in **3**, ranging from 1.860(2) to 2.087(2) Å. The *n*-propyl-linked diamidate serves as a bridging ligand across two faces of the [Mn_4O_4] cubane moiety, resulting in a *pseudo-C*$_S$ symmetric complex. The reversible ($Mn_2^{III}Mn_2^{IV}$)/($Mn^{III}Mn_3^{IV}$) couple is observed at −150 mV vs. Fc/Fc$^+$ (Figure 6). The diamidate ligand decreases the oxidation potential by 400 mV relative to that of **1**. Treatment of **3** with 1 equiv. Ag(OTf) leads to the formation of the one-electron oxidized species **3-ox**. The ESI-MS and crystal structure of **3-ox** are consistent with the LMn_4O_4(diam)(OAc)(OTf) formulation (Figure 4). The oxidation state of Mn(3) is assigned as Mn^{III} in **3-ox**. With the exception of an elongated Mn(3)−O(3) distance of 2.051(4) Å, all other Mn−oxo distances are in the range 1.893(4)−1.937(4) Å, consistent with the $Mn^{III}Mn_3^{IV}$ oxidation state assignment.

To further investigate the effect of small geometric changes on the electronic structure of the resulting cluster, a diamidate-benzoate complex was targeted.[79] Treatment of **3** with 1 equiv. of p-$CF_3C_6H_4CO_2H$ (^{CF3}BzOH) leads to the formation of **4** via a protonolysis reaction (Figure 2). The ESI-MS peak at m/z = 1485 is consistent with the mass of [LMn_4O_4(diam)(OBz^{CF3})]$^+$. The CV of **4** shows a reversible redox process at −15 mV vs. Fc/Fc$^+$ assigned to the ($Mn_2^{III}Mn_2^{IV}$)/($Mn^{III}Mn_3^{IV}$) couple (Figure 6). The positive shift by 135 mV relative to that of **3** is consistent with the decreased basicity of OBz$^-$ compared to OAc$^-$.[80-81] Treatment of **4** with 1 equiv. Ag(OTf) leads to the formation of the one-electron

oxidized species **4-ox**. The LMn_4O_4(diam)(OBz)(OTf) formulation is consistent with the crystal structure (Figure 4). Similar to **3-ox**, the oxidation state of Mn(3) is assigned as Mn^{III}. An elongated Mn(3)−O(3) distance of 2.143(3) Å is consistent with the $Mn^{III}Mn_3^{IV}$ assignment. Overall, comparing complexes **2-ox**, **3-ox**, and **4-ox**, the elongated Mn^{III}-oxo distance varies from 2.241(1), to 2.051(4), and 2.143(3), while the other Mn-oxo distances are in the range 1.831(1)−1.976(2) Å, 1.893(4)−1.937(4) Å, and 1.873(3)−1.965(3) Å, respectively. For **2-ox**, **3-ox**, and **4-ox**, the redox potential for the reversible $(Mn_2^{III}Mn_2^{IV})/(Mn^{III}Mn_3^{IV})$ couple was measured at +190 mV, −150 mV, and −15 mV vs. Fc/Fc^+, respectively. In comparison, the estimated midpoint redox potential for the (S_1/S_2) couple in the OEC was estimated at +900 mV vs. SHE, which is approximately +250 mV vs. Fc/Fc^+.[82]

3.3) XAS spectroscopy

Solution and solid-state Mn K-edge X-ray absorption near-edge spectroscopy (XANES) and extended X-ray absorption fine structure (EXAFS) were used to further characterize the metal oxidation states and provide evidence of structural integrity in solution (Figures

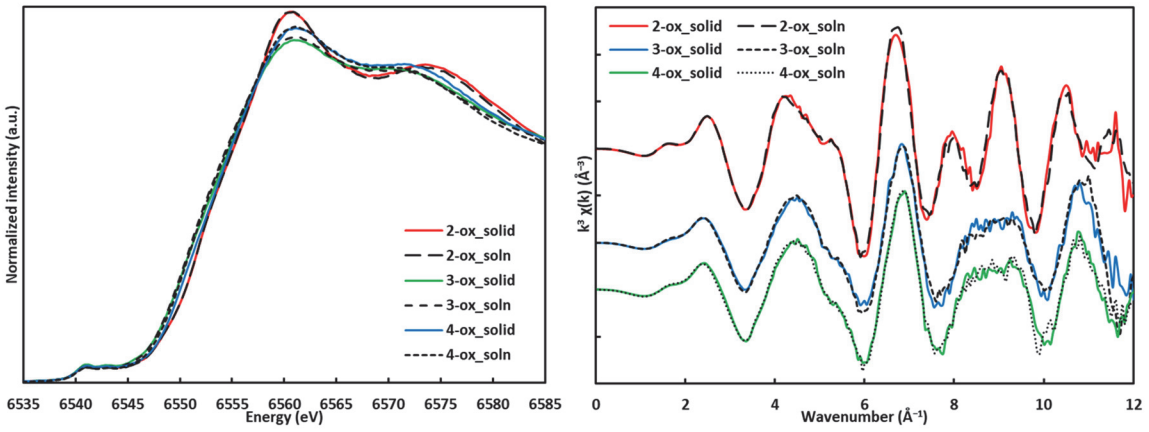

Figure 7. (Left) Normalized XANES data at Mn *K*-edge for complexes **2-ox**, **3-ox**, and **4-ox** in solid and solution phases. (Right) k^3-weighted k-space EXAFS data at Mn K-edge for complexes **2-ox**, **3-ox**, and **4-ox** in solid and solution phases highlighting the integrity of the complexes in solution.

7−8). Absorption edge positions were determined from the second-derivative zero-crossings, giving the following values (eV): 6553.3 (**2-ox**), 6552.8 (**3-ox**), 6553.3 (**4-ox**). These values are comparable to 6553.1 (S_1) and 6554.1 (S_2) from cyanobacteria PSII.[20] Solution EXAFS data for **2-ox**, **3-ox**, and **4-ox** are indistinguishable from the

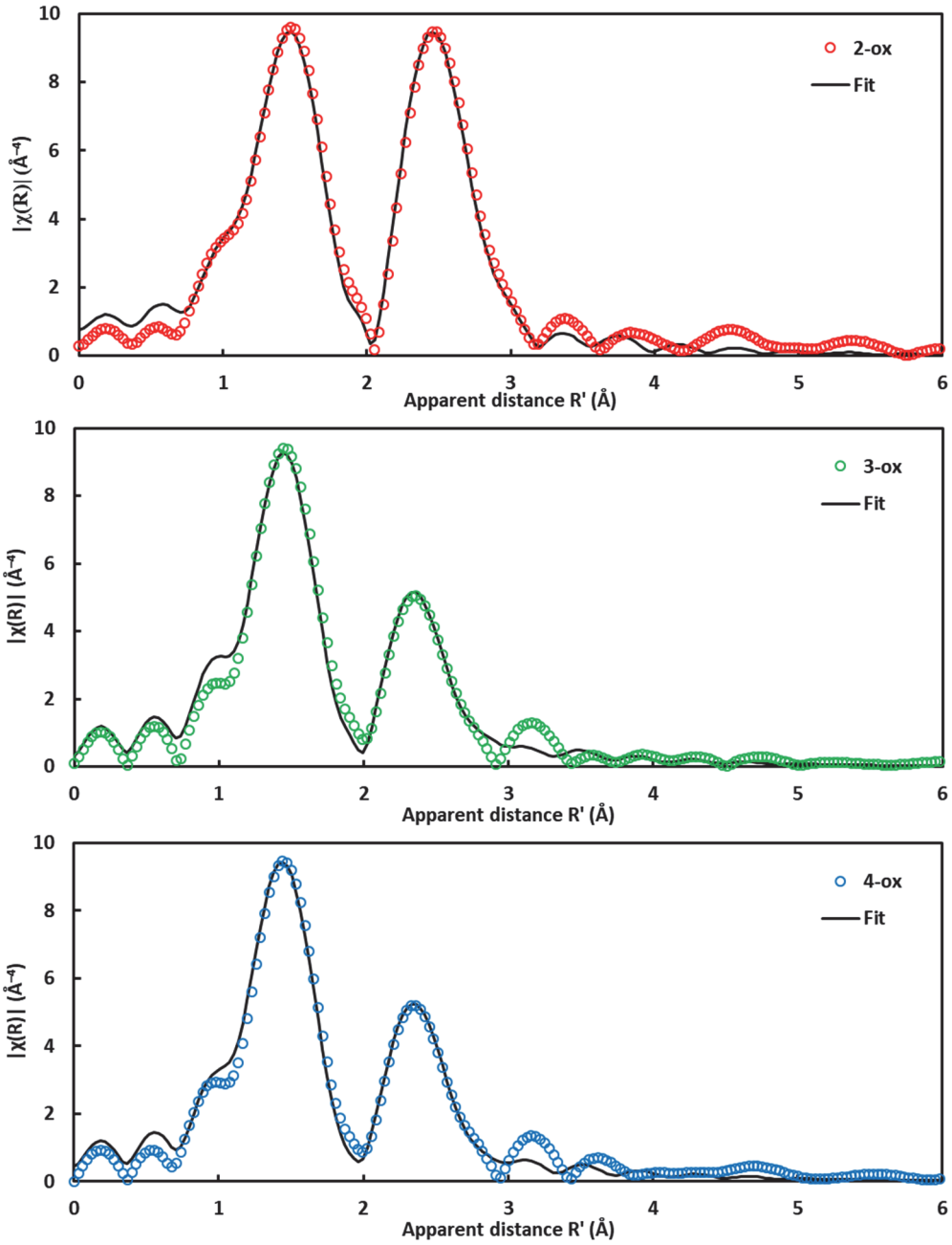

Figure 8. Fourier Transforms of k^3-weighted Mn K-edge EXAFS data (circles) along with the respective best fits (black line) for complexes **2-ox** (a), **3-ox** (b), and **4-ox** (c). The corresponding best fit parameters are presented in Table S3.

corresponding solid-state EXAFS data and are consistent with the solid state structural assignments (Figure 4).

Table 1: Best fit parameters for Mn K-edge EXAFS curve fitting of complexes **2-ox**, **3-ox**, and **4-ox**.[a]

Sample	Path	R (Å)		N	σ^2 (10^{-3} Å^2)	R-factor (%)	ΔE_0 (eV)
		EXAFS	XRD				
2-ox	Mn-O	1.83±0.01	1.83-1.91	3	5.50±1.05	0.80	-0.51±0.94
	Mn-O/N	1.93±0.01	1.92-2.24	3	2.00±0.20		
	Mn-Mn	2.86±0.01	2.85-2.96	3	4.23±0.94		
	Mn-C	2.96±0.01	2.77-3.05	2.25	2.00±0.61		
	Mn-P	3.08±0.01	3.07-3.15	1.50	2.00±0.81		
3-ox	Mn-O	1.81±0.02	1.83-1.92	3	8.00±1.52	1.96	-5.00±3.50
	Mn-O/N	1.91±0.02	1.93-2.06	3	2.00±0.20		
	Mn-Mn	2.79±0.02	2.76-2.96	3	6.15±2.24		
	Mn-C	3.01±0.10	2.79-3.04	4	6.04±6.99		
4-ox	Mn-O	1.82±0.02	1.83-1.92	3	5.01±2.25	1.21	-3.57±2.63
	Mn-O/N	1.92±0.02	1.93-2.08	3	2.00±0.20		
	Mn-Mn	2.79±0.01	2.75-2.99	3	5.58±2.17		
	Mn-C	2.98±0.06	2.79-3.05	4	5.27±5.28		

[a] EXAFS data for complex **2-ox** was fit in the k-range $2.84 \leq k(Å^{-1}) \leq 10.79$ ($1.0 \leq R'(Å) \leq 3.2$). EXAFS data of complex **3-ox** was fit in the k-range $2.79 \leq k(Å^{-1}) \leq 11.30$ ($1.0 \leq R'(Å) \leq 2.9$). EXAFS data for complex **4-ox** was fit in the k-range $2.79 \leq k(Å^{-1}) \leq 11.21$ ($1.0 \leq R'(Å) \leq 2.9$).

Fourier Transforms of k^3-weighted Mn EXAFS data for complexes **2-ox**, **3-ox**, and **4-ox** in solid phase are shown in Figure 7 along with the corresponding best fits. It is important to note that the x-axis represents the non-phase-shift corrected radial distance

(R') which is shorter than the actual scatterer distance by ~0.5 Å originating from the phase shift. The first peak in the FT data corresponds to metal-ligand (Mn-O/N) scattering whereas the second peak includes metal-metal/metal-ligand interactions (Mn-Mn, Mn-C/P). The scattering contribution from relatively heavier P atoms results in greater amplitude of second peak in the EXAFS data of complex **2-ox** as compared to **3-ox** and **4-ox**. For each complex two metal-ligand distances were used for the first peak to get the best fit. In case of complex **2-ox**, one of the Mn atoms has three P second neighbors whereas each of the other three Mn has only one P second neighbor. Therefore, an average coordination number of 1.50 was used to fit the data. Similarly, an average coordination number (2.25) was used for C atoms contributing to the second shell as each of the three Mn atoms with one P in second shell is linked to three C atoms. The best fit parameters obtained are listed in Table 1. The bond distances extracted from fits to the EXAFS data are in good agreement with those determined from XRD data.

3.4) Magnetic susceptibility

To obtain insight into the magnetic exchange coupling interactions between the Mn centers, magnetic susceptibility measurements were performed on powdered crystalline samples of **2-ox**, **3-ox**, and **4-ox** in the temperature range 1.8 K−300 K at a non-saturating field of 0.4 T. For **2-ox**, the χT value of 5.64 emu K mol^{-1} at 300 K indicates antiferromagnetic coupling between the Mn centers, deviating from the expected spin-only value of 8.62 emu K mol^{-1} (g = 2) for uncoupled Mn^{III} (S = 2) and Mn^{IV} (S = 3/2) centers (Figure 9). χT decreases monotonically with temperature, reaching a value of 0.383 emu K mol^{-1} at 1.8 K, in good agreement with the expected χT value of 0.375 emu K mol^{-1} for an S = 1/2 (g = 2) ground state. The near-ideal Curie behavior observed between 1.8−10 K

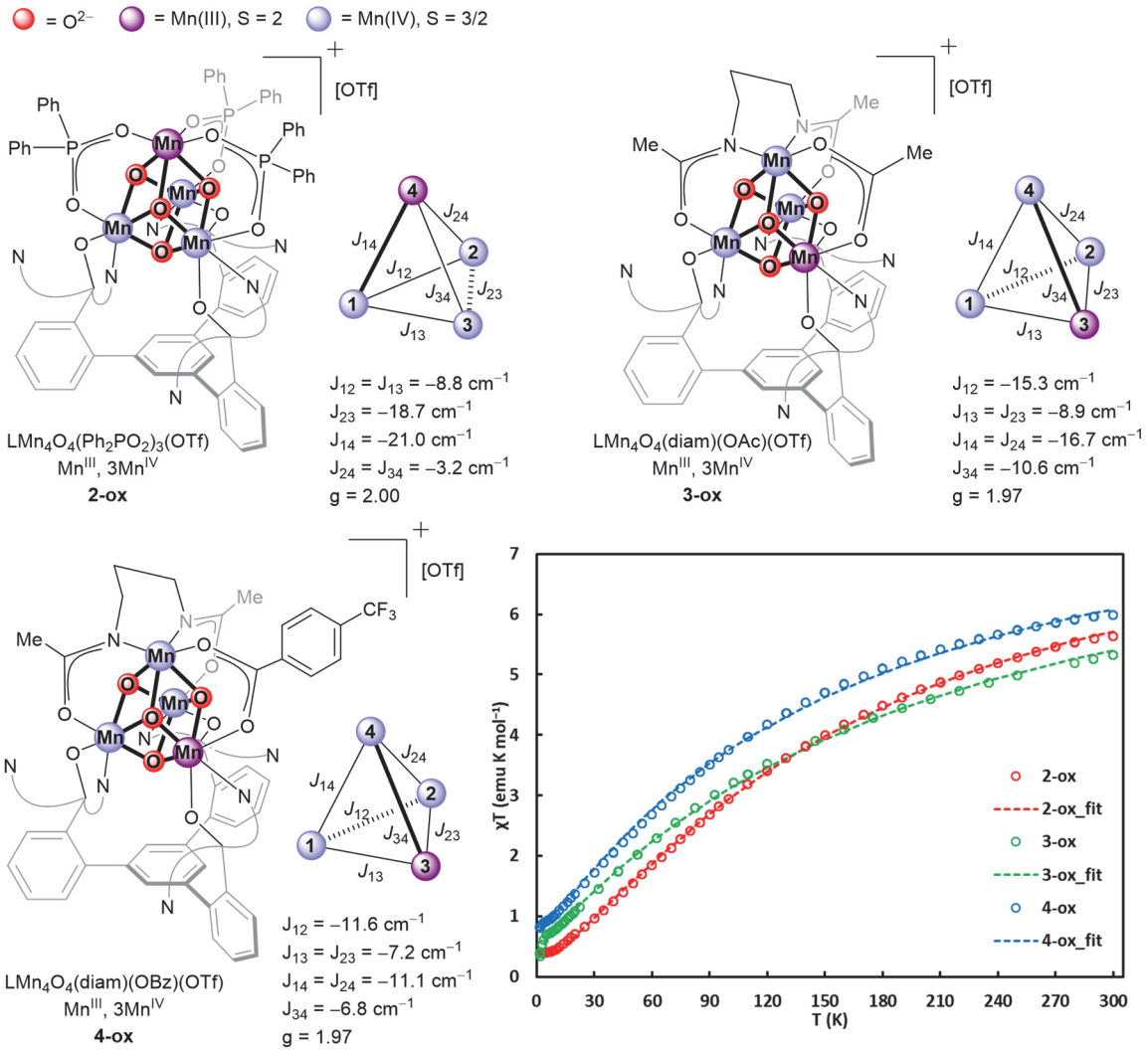

Figure 9. Exchange coupling model, fit parameters, and χT vs. T plot of complexes **2-ox**, **3-ox**, and **4-ox**. For the exchange coupling models, the mirror plane of the *pseudo*-Cs symmetry contains the bold vector and bisects the hashed vector.

can be attributed to the absence of thermally accessible spin excited states $S > 1/2$ in this temperature range. Using software that employs an exact solution to the isotropic spin exchange Hamiltonian (Equation 1)[83], an exchange coupling model that consists of two edge-sharing isosceles triangles with vertices at Mn(1)-Mn(2)-Mn(3) and Mn(2)-Mn(3)-Mn(4) was employed to fit the susceptibility data. This model takes into account the *pseudo*-Cs symmetry of the [Mn_4O_4] core, with the mirror plane containing the Mn(4)-Mn(1) and Mn(4)-O(4) vectors and bisecting the Mn(2)-Mn(3) vector. The following

parameters were used to fit the data: $J_{12} = J_{13} = -8.8$ cm^{-1}, $J_{23} = -18.7$ cm^{-1}, $J_{14} = -21.0$ cm^{-1}, $J_{24} = J_{34} = -3.2$ cm^{-1}, and $g = 2.00$. The smaller $J_{24} = J_{34}$ coupling is expected given the elongated Mn(4)−O(4) distance of 2.241(1) Å. Simulating the susceptibility data assuming single-site zero field splitting parameters $D(\mathrm{Mn^{IV}}) = 0$ cm^{-1} and $D(\mathrm{Mn^{III}}) = 0, -2,$ or -4 cm^{-1} did not result in significant differences in J. Values of $D \approx -0.2$ cm^{-1} and $D \approx -4$ cm^{-1} are typical for 6-coordinate $\mathrm{Mn^{IV}}$ and $\mathrm{Mn^{III}}$, respectively.[17, 84-85] The calculated energy level diagram indicates a quartet excited state *c.a.* 28 cm^{-1} (equivalent temperature of 40 K) above the doublet ground state. This energy separation is comparable to the 25−35 cm^{-1} measured for MeOH-treated OEC poised in the multiline S_2 state.[86]

$$\widehat{H} = -2 \sum_{i \neq j}^{i,j \in N} J_{ij} \widehat{S}_i \cdot \widehat{S}_j \qquad (1)$$

Complex **3-ox** was studied by SQUID magnetometry. Similar to **2-ox**, the χT value of 5.32 emu K mol^{-1} at 300 K indicates antiferromagnetic coupling between the Mn centers (Figure 9). χT decreases monotonically with temperature, reaching a value of 0.85 emu K mol^{-1} at 5 K. The deviation from the expected χT value of 0.38 emu K mol^{-1} ($S = 1/2$, $g = 2$) can be attributed to the presence of thermally accessible spin excited states $S > 1/2$. At 1.8 K, the χT value of 0.383 emu K mol^{-1} is in good agreement with the $S = 1/2$ ($g = 2$) ground state. To fit the susceptibility data, an isotropic exchange coupling model that consists of two edge-sharing isosceles triangles with vertices at Mn(1)-Mn(2)-Mn(3) and Mn(1)-Mn(2)-Mn(4) was employed. This model is different from that employed for **2-ox**, and takes into account the *pseudo*-C_S symmetry of the [Mn_4O_4] core, with different mirror planes that contain the Mn(3)-Mn(4) and Mn(3)-O(3) vector and bisecting the Mn(1)-Mn(2) vector. The following parameters were used to fit the data: $J_{12} = -15.3$ cm^{-1}, $J_{13} = J_{23} =$

−8.9 cm^{-1}, $J_{14} = J_{24} = -16.7$ cm^{-1}, $J_{34} = -10.6$ cm^{-1}, and $g = 1.97$. Compared to **2-ox**, the smaller variation of exchange coupling constants is consistent with the smaller variation of Mn−oxo bond distances in **3-ox**. The calculated energy level diagram indicates the presence of a low-lying quartet excited states at 3−5 cm^{-1} (equivalent temperature of 4.3−7.2 K) above the doublet ground state. Interestingly, an energy separation of 3−6 cm^{-1} has been reported for untreated higher plant OEC in the S_2 state.[86-87]

Complex **4-ox** was studied by SQUID magnetometry. A higher χT value of 6.0 emu K mol^{-1} at 300 K indicates weaker antiferromagnetic coupling in **4-ox** compared to **3-ox**. χT decreases monotonically with temperature, reaching a value of 0.82 emu K mol^{-1} at 1.8 K, deviating significantly from the expected χT value of 0.375 emu K mol^{-1} for an $S = 1/2$ ($g = 2$) ground state. This indicates a further decreased energy separation between the ground and excited states, as expected from the weaker antiferromagnetic coupling between the Mn centers. In fact, **4-ox** does not have a well-isolated spin ground state, *vide infra*. To fit the susceptibility data, a model identical to **3-ox** was employed. The following parameters were used to fit the data: $J_{12} = -11.6$ cm^{-1}, $J_{13} = J_{23} = -7.2$ cm^{-1}, $J_{14} = J_{24} = -11.1$ cm^{-1}, $J_{34} = -6.8$ cm^{-1}, and $g = 1.97$. The calculated energy level diagram indicates that the lowest doublet and quartet states are separated by 0−1 cm^{-1} (equivalent temperature of 1.4 K). Overall, magnetic susceptibility studies indicate that the spin ladder in exchange-coupled tetranuclear Mn complexes is highly sensitive to small changes in structure and nature of the bridging ligands.

3.5) Variable-temperature X-band EPR spectroscopy

EPR studies were conducted in frozen solution samples of **2-ox**, **3-ox** and **4-ox**. At 5 K, the EPR spectrum of **2-ox** features a broad signal centered at $g = 2$ featuring Mn hyperfine

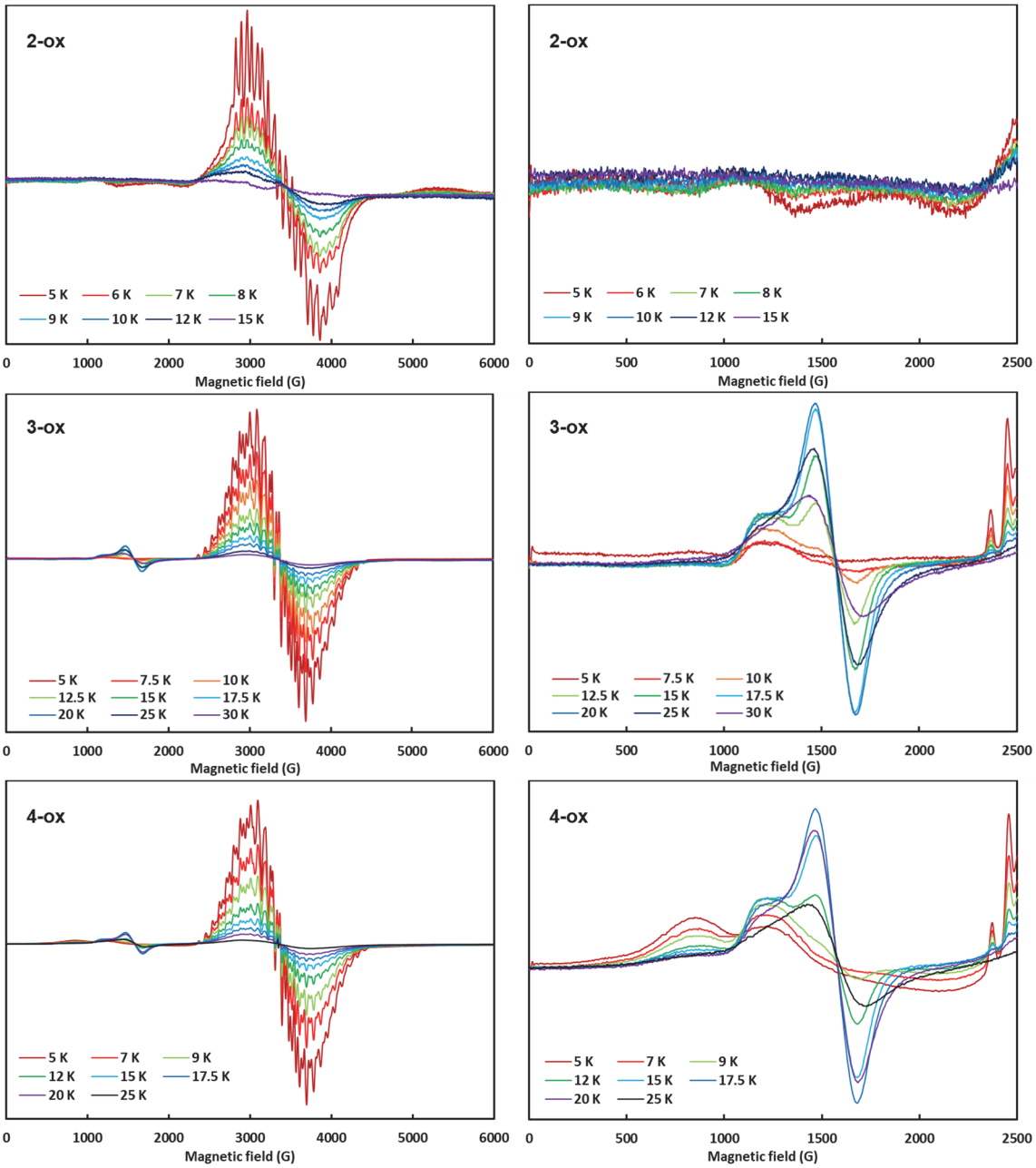

Figure 10. (Left) Variable-temperature X-band continuous-wave EPR spectra of **2-ox**, **3-ox** and **4-ox**. (Right) Expanded view of the low field ($g > 2$) region.

interactions (Figure 10). This is consistent with the $S = 1/2$ ground state determined from susceptibility studies. As the temperature is increased, the $g = 2$ signal loses intensity until no signal is observed above 15 K. Importantly, EPR signals originating from thermally populated spin excited states are not observed, in agreement with the predicted energy

separation of 28 cm^{-1} (40 K) between the ground and excited states. The spectrum can be approximated by g = [2.053, 2.003, 1.952], g_{iso} = 2.00, and the following ^{55}Mn hyperfine interactions A_i, $(A_{iso})_i$: Mn_1 = [434, 434, 313], 394 MHz; Mn_2 = [293, 155, 245], 231 MHz; Mn_3 = [128, 146, 198], 157 MHz; Mn_4 = [134, 133, 72], 113 MHz (Figure 11). The unique, larger Mn hyperfine coupling constant (394 MHz) is consistent with the Mn^{III} center in **2-ox**.[88] The EPR spectrum of **2-ox** is in stark contrast to that of the related $[Mn_4O_4(Ph_2PO_2)_6]^+$ complex with a higher spin ground state $S \geq 3/2$,[41] indicating that the EPR of exchange-coupled tetranuclear Mn complexes are highly sensitive to the Mn coordination environment, even if the core Mn_4O_4 cluster is maintained.

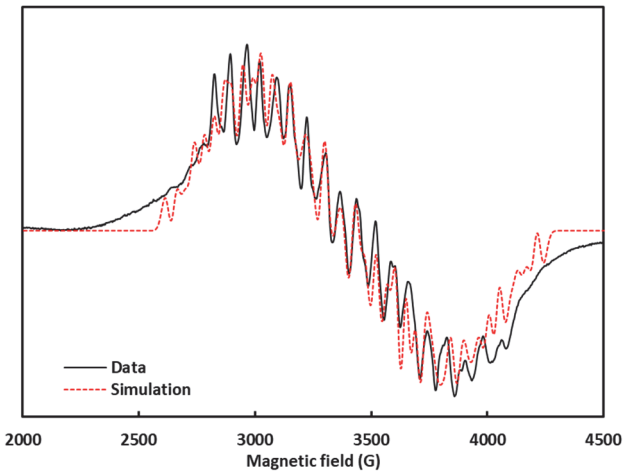

Figure 11. X-band EPR spectrum of **2-ox**. Acquisition parameters: frequency = 9.64 MHz, power = 8 mW, conversion time = 20.48 ms, modulation amplitude = 8 G. See text for simulation parameters.

For the EPR spectrum of **3-ox** at 5 K, only the multiline signal centered at g = 2.0 is discernible. As the sample is warmed, the signal at g = 2 decreases in intensity as a signal centered at g = 4.2 gains intensity (Figure 10). Above 20 K, both signals start to lose intensity due to relaxation. The signal at g = 2 is consistent with the S = 1/2 ground state determined from susceptibility studies. The g = 4.2 signal, assigned to the S = 3/2 excited

state of **3-ox**, is highly reminiscent of the S_2 state in its HS form. The $g = 2$ and the $g = 4.2$ signals of the S_2 state arise from the ground states of structurally distinct species, the relative ratio of which is affected by external chemical stimuli such as pH. As such, both EPR signals can be observed at low temperatures in a ratio that reflects the relative population of the two species.[34] In the case of **3-ox**, the two signals arise from different spin states of a single, structurally static species (Figure 7). The temperature dependence of the EPR spectrum of **3-ox** can be explained in terms of small differences in the Boltzmann distribution of the ground and excited states. At 5 K, only the $S = 1/2$ ground state is significantly populated, and the $g = 2$ signal corresponds to the $|-1/2\rangle \rightarrow |1/2\rangle$ transition. As the temperature is increased, the difference in the population of the $|-1/2\rangle$ and the $|1/2\rangle$ states decrease, resulting in weaker absorption. Concurrently, as the temperature is increased, the $S = 3/2$ spin excited state is populated, and the $g = 4.2$ signal corresponds to the transition within the $|\pm 3/2\rangle$ Kramers doublet. In contrast to **2-ox**, the observation of the $g = 4.2$ signal is consistent with a smaller energy separation between the ground doublet and excited quartet state in **3-ox**, in agreement with the magnetic susceptibility studies. The EPR spectrum of a weakly antiferromagnetically coupled $Mn^{III}Mn^{IV}$ dimer shows a similar temperature dependence: at 20 K, only the $g = 2$ signal is observed, but upon warming to 43 K and to 110 K, a new low-field signal at $g = 5$ gains intensity.[89] This low-field signal has been assigned to the $S = 3/2$ excited state. For more strongly coupled $Mn^{III}Mn^{IV}$ dimeric systems, the quartet excited state is separated from the doublet ground state by hundreds of wavenumbers and the signal corresponding to the $S = 3/2$ excited state was not observed.[39, 90-95]

For the EPR spectrum of **4-ox**, in addition to the signal at $g = 2$, other signals assignable to $S = 3/2$ spin states were observed even at 5 K, at $g = 7.5$ and $g = 5.5$. This indicates a very small energy separation between the doublet and quartet states in **4-ox**, in agreement with the susceptibility studies. As the sample is warmed, the signal at $g = 2$ decreases in intensity. In the low field region, the $g = 7.5$ signal loses intensity upon warming, whereas the $g = 5.5$ and $g = 4.2$ signals gain intensity. At 15 K, the low-field region collapses to the $g = 4.2$ signal observed for **3-ox**. The temperature dependence of the low field region may be explained by the presence of two distinct $S = 3/2$ excited states.

3.6) ^{55}Mn Davies ENDOR spectroscopy

To gain better understanding of the Mn hyperfine interactions (HFI) in **3-ox**, ^{55}Mn Davies ENDOR spectra were collected at Q-band using the pulse sequence π-t_{RF}-π_{RF}-t_{RF}-$\pi/2$-τ-π-τ-echo. Spectra were collected at selected field positions along the electron spin-echo-detected EPR spectrum (ESE-EPR): 1170 mT, 1200 mT, 1240 mT, 1270 mT, and 1300 mT (Figure 12a). By incorporating the ESE-EPR spectrum at D-band (130 GHz) *vide infra*, the g values were constrained to $g = [1.944, 1.964, 2.002]$, $g_{iso} = 1.97$, though it should be noted that there is no significant resolution of any individual g-values in the spectrum, likely due to slight inhomogeneity in the g-values (g-strain = 0.012 for all simulations).[96] This introduces field-dependent broadening that also causes a loss in resolution of the ^{55}Mn hyperfine structure evident in the field swept spectra as the excitation frequency is increased, a phenomenon also observed in multi-frequency EPR spectra of the S_2 state of the $CaMn_4O_5$ cluster of photosystem II.[97] A global fit of the Mn hyperfine interactions incorporating the ENDOR spectra as well as the X-band CW spectrum yields the parameters listed in Table 2. Similar to **2-ox**, the unique, larger Mn

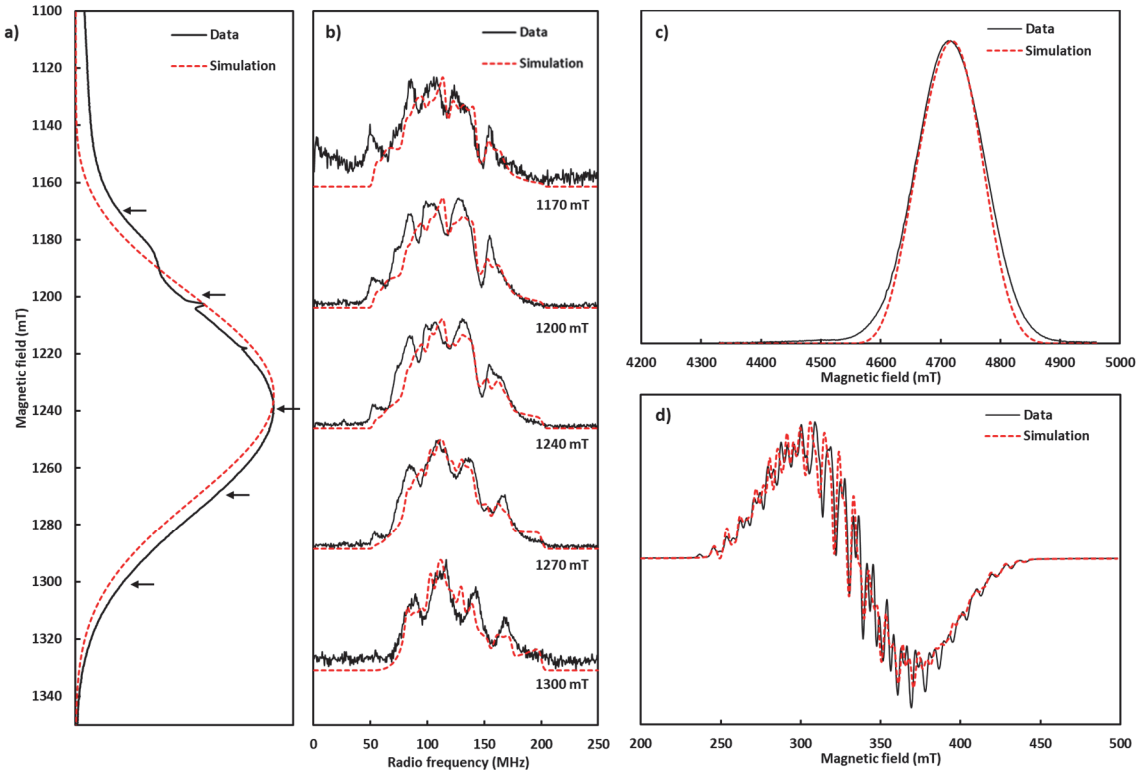

Figure 12. Experimental spectra of **3-ox** (black traces) and simulation (dashed red traces). a) Q-band electron spin echo (ESE) EPR. b) Q-band ^{55}Mn Davies ENDOR recorded at five magnetic field positions indicated in a). Acquisition parameters: Temp. = 3.8 K, MW freq. = 34.115 MHz, π_{MW} = 40 ns, π_{RF} = 3 μs, t_{RF} = 2 μs, τ = 400 ns. c) D-band ESE-EPR. d) X-band CW EPR. Acquisition parameters: Temp. = 5 K, MW freq. = 9.359 MHz, power = 2 mW, modulation amplitude = 4 G. See Table 1 for global fit parameters.

hyperfine coupling constant is consistent with the Mn^{III} center in **3-ox**.[16, 95] The Mn hyperfine coupling constants reported for **3-ox** are similar in magnitude to that of the S_2 state of *T. elongatus*.[16, 86, 97-98] Notably, ^{55}Mn ENDOR spectra for tetranuclear Mn model complexes have been hitherto absent in the literature.

ESE-EPR and electron-electron double resonance-detected NMR (EDNMR) of **3-ox** were recorded at D-band (130 GHz). EDNMR employs a high-turning angle microwave pulse which concurrently excites NMR and EPR transitions rather than an RF pulse to drive NMR transitions as in ENDOR.[99] EDNMR offers some distinctive features compared to ENDOR, including decreased selectivity between magnetic nuclei with very different

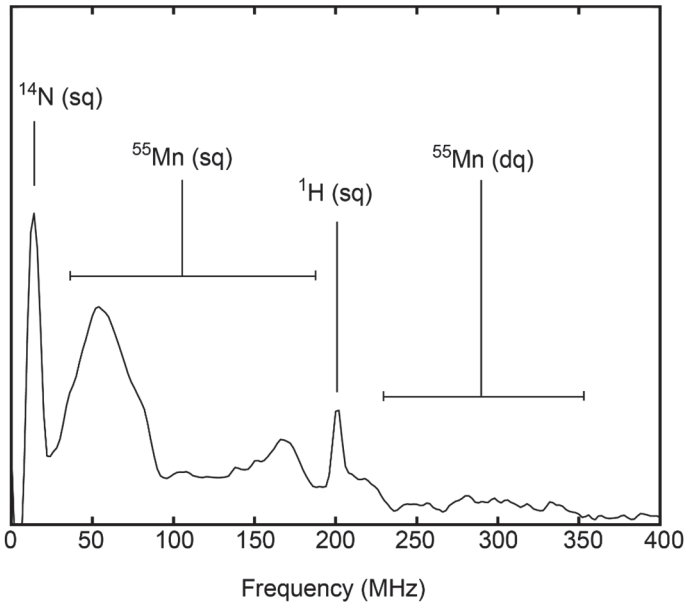

Figure 13. D-band EDNMR of **3-ox** recorded at 4.7 T.

gyromagnetic ratios, decreased dependence on the species of interest to exhibit long spin lattice relaxation times, and vastly enhanced signal intensity for the same amount of acquisition time.[100] However, EDNMR typically suffers from far broader lineshapes in comparison to ENDOR, as well as combination bands and multiple-quantum transitions, which can produce complex, feature-rich spectra.[68, 101] The EDNMR spectrum of **3-ox** at g = 1.97 (4.7 T) is displayed in Figure 13. Features observed at 14 MHz and 200 MHz correspond to single-quantum transitions from ^{14}N and ^{1}H nuclei of the ligand scaffold (^{14}N and ^{1}H Larmor frequencies at 4.7 T are 14.4 MHz and 200 MHz, respectively). A large, broad peak is observed at 50 MHz (FWHM = 48 MHz) as well as peaks at 140 MHz, 150 MHz, and 170 MHz corresponding to ^{55}Mn single-quantum transitions. In the strong coupling limit, these couplings are centered at $A/2$ and split by twice the ^{55}Mn Larmor frequency (*c.a.* 50 MHz at 4.7 T). Based on the observed ^{55}Mn transitions, the ^{55}Mn HFI are estimated in the range 180–240 MHz, in line with the Mn(IV) HFI measured from Q-band ^{55}Mn ENDOR. The spectral signature of the unique Mn(III) ion cannot be

unambiguously assigned from the EDNMR due to multiple overlapping transitions. Nonetheless, the general agreement of the EDNMR and ENDOR data support the hyperfine assignments of **3-ox**. The remaining features appearing from 250–350 MHz are assigned to ^{55}Mn double-quantum transitions.

Table 2. Summary of the effective *g* and ^{55}Mn HFI tensors for **3-ox**, and the S_2 states of *T. elongatus* and spinach PSII.[86, 97] Note: all hyperfine tensor frames are collinear with *g*-tensor frame.

		g	A_i (MHz)			
			A_1	A_2	A_3	A_4
3-ox	x	1.944	376	233	253	193
	y	1.964	297	198	283	222
	z	2.002	272	260	149	131
	iso	1.970	315	230	228	198
T. elongatus	x	1.971	350	249	202	148
	y	1.948	310	227	182	162
	z	1.985	275	278	240	263
	iso	1.968	312	251	208	191
Spinach	x	1.997	310	235	185	170
	y	1.970	310	235	185	170
	z	1.965	275	275	245	240
	iso	1.977	298	248	205	193

The temperature dependence of electron spin-lattice relaxation in **3-ox** was studied using the inversion-recovery sequence ($\pi - t - \pi/2 - \tau - \pi -$ echo) (Figure 14).[102] Data were fit to a bi-exponential function (Equation 2). Subscript *f* denotes the fast relaxing process; *s* denotes the slow process. At 3.8 K, the relaxation time constants for the fast and slow exponential components were 1.3 μs and 6.3 μs, respectively. Over the temperature range studied, both $\ln(1/T_1)$ vs. $1/T$ and $\ln(1/T_1)$ vs. $\ln(T)$ are approximately linear, consistent with either an Orbach or Raman relaxation process.[86] Assuming an Orbach mechanism, an energy separation of 13 cm^{-1} was obtained from the fast relaxing component. This value is slightly larger than the 3−5 cm^{-1} estimated from susceptibility studies but approximately

in the same magnitude. Overall, both electron spin-lattice relaxation and magnetic susceptibility measurements support a small separation between the doublet ground state and the quartet excited state.

$$M_z(T) = M_f\left[1 - 2\exp\left(-\frac{T}{T_{1f}}\right)\right] + M_s\left[1 - 2\exp\left(-\frac{T}{T_{1s}}\right)\right] \qquad (2)$$

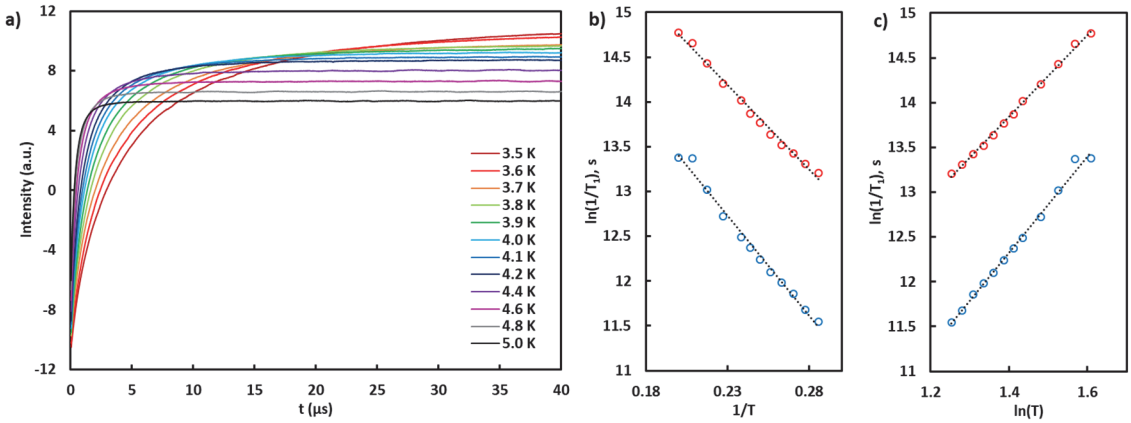

Figure 14. a) Temperature-dependent inversion recovery trace for **3-ox**. b) Plot of ln(1/T_1), T_1 in seconds vs. 1/T (K^{-1}) for the fast and slow exponential components. Slope of the linear fit: 18.9 K (red) and 22.4 K (blue). c) Plot of ln(1/T_1) vs. ln(T) and linear fit to the data. Acquisition parameters: frequency = 34.07 MHz, π_{MW} = 24 ns, τ = 140 ns, srt = 2 ms.

3.7) Discussion

Between the optimized structures of the proposed open- and closed-cubane forms of the S_2 state, Mn(4)−O(5) and Mn(1)−O(5) distances interchange from 1.87 Å to ~3.2 Å, tantamount to a bond breaking-reforming process (Figure 1). This rearrangement process is accompanied by a change in the electronic structure of the S_2 state, as explained from the computed magnetic exchange coupling constants in both open and closed forms. The *g* = 2 and the *g* = 4.2 signals of the S_2 state result from the ground states of clusters that differ significantly in geometry, the relative ratio of which is affected by external chemical stimuli. Our studies indicate that such large structural changes to the inorganic $CaMn_4O_5$ core of the OEC may not be necessary to perturb its electronic structure. Comparisons between the crystal structures of **2-ox**, **3-ox**, and **4-ox** indicate only small variations in

Mn−oxo bond distances, with the longest Mn−oxo bond in each species varying from 2.051(4) Å to 2.241(1) Å. The remaining Mn-O distances are in the range 1.831(1)−1.976(2) Å. Yet such small geometric changes in the $[Mn^{III}Mn_3^{IV}O_4]$ core have a substantial effect in its electronic structure, as is evident from magnetic susceptibility and EPR studies. Assigned to a thermally accessible spin excited state $S = 3/2$, the $g = 4.2$ signal in **3-ox** and **4-ox** is highly reminiscent of the S_2 state in its high-spin form. The absence of such a signal in **2-ox** indicates that spectroscopic properties of tetranuclear Mn complexes are highly dependent on the nature and magnitude of the magnetic exchange coupling interactions, which are finely tuned by the nature of not only bridging ligands but also terminal ligands in the immediate coordination sphere of each Mn ion. While the two signals observed in **3-ox** and **4-ox** are not resulting from ground states of two different isomers, as proposed in PSII, they do correspond to low- and high-spin electronic states. As in PSII, the degrees of population of the two states are affected by different coupling schemes between the Mn centers, which arise from structural differences. Most importantly, large structural distortions are not necessary for the complete disappearance of one of the signals (the HS in this case, for **2-ox**). In a previously reported $Mn^{III}Mn_3^{IV}O_4$ cubane with six phosphinate ligands, the LS signal completely disappears, consistent with a higher $S \geq 3/2$ ground state.[41] Furthermore, the energy separation between the doublet ground state and the first non-doublet excited state can be fine-tuned with small changes in the overall geometry of the cluster, as evidenced by the variable temperature EPR of **3-ox** and **4-ox** (Figure 10). These findings suggest that geometrical changes much smaller than the ones proposed for PSII with respect to the metal and oxo/hydroxo motifs could have substantial effects on the EPR signals. Therefore, the deduction of the geometry of OEC S-state intermediates based

on EPR spectroscopic features need to be complemented with appropriate structural determination. Given that in the present series of compounds, even a change in the nature of a single carboxylate ligand affects the state energies and EPR signals, it is expected that features such as the protonation state of aquo ligands, bridging oxos, and nearby His residues will greatly affect the electronic structure of the OEC.

In conclusion, a series of $Mn^{III}Mn_3^{IV}O_4$ cuboidal complexes has been synthesized and characterized by XRD, electrochemistry, XAS, SQUID magnetometry, variable temperature CW-EPR, and pulsed-EPR. To our knowledge this is the first set of experimental studies that directly addresses the effect of systematic changes of supporting ligands on the EPR behavior of clusters in the redox state of the S_2 state of the OEC. With implications in the interpretation of the OEC spectroscopic properties, our benchmarking results show that the electronic structure of tetranuclear Mn complexes is highly sensitive to small geometric changes and the nature of the bridging ligands. Even in the absence of large oxo movements proposed to account for the HS and LS signals of the OEC, we find that the EPR feature of essentially isostructural compounds can move from LS to a mixture of LS and HS to HS signals. Therefore, interpretation of EPR signals in terms of structural implications must be done very cautiously. Ideally, complementary structural information will be obtained to corroborate spectroscopic assignments.

3.8) Experimental section

Synthesis of propane-1,3-diacetamide (H_2diam): (*Caution! 1,3-diaminopropane fumes in air and is very toxic!*) A round bottom flask equipped with a magnetic stir bar was charged with a solution of 1,3-diaminopropane (19 mL) in MeCN (200 mL) and cooled in an ice bath. Three equivalents of acetic anhydride (65 mL) were added dropwise via an

addition funnel. Immediately, an exothermic reaction ensued. While a white precipitate was observed initially, a homogeneous, colorless solution was obtained as the reaction progressed. Upon complete addition of acetic anhydride, the temperature was raised to 100 ^{o}C and all volatiles were distilled off under partial vacuum, leaving behind a white, crystalline residue. This residue was washed with Et_2O, air-dried, crushed into a fine powder using a mortar and pestle, and washed once again with Et_2O. Propane-1,3-diacetamide was isolated as a white powder. ^{1}H NMR (300 MHz, DMSO−d^6) 7.812 (bs, 2H), 3.01 (td, J = 7.0, 5.6 Hz, 4H), 1.78 (s, 6H), 1.49 (p, J = 7.1 Hz, 2H).

Synthesis of **2-ox**: A solution of $LMn_4O_4(OAc)_3$ (600 mg, 0.46 mmol, 1 equiv) in CH_2Cl_2 (12 mL) was added to a stirring CH_2Cl_2 suspension of diphenylphosphinic acid (330 mg, 1.51 mmol, 3.3 equiv). After stirring the reaction at room temperature for 16 hours, a colorless precipitate formed and was filtered away. All volatiles were removed from the filtrate under reduced pressure. The solid residue was triturated with CH_2Cl_2 (15 mL) and Et_2O (15 mL). The brown powder was then suspended in 15 mL of THF, collected on a pad of Celite, dissolved in CH_2Cl_2, and filtered through Celite. All volatiles were removed from the filtrate under reduced pressure, yielding compound **2** as a red-brown powder. Yield = 462 mg, 57 %. Crystals suitable for X-ray crystallography were grown from slow vapor diffusion of Et_2O into a concentrated solution of **2** in CH_2Cl_2.

To a stirring solution of **2** (150 mg, 84 μmol, 1 equiv) in CH_2Cl_2 (5 mL), a blue CH_2Cl_2 solution (4 mL) of $[(4\text{-}BrPh)_3N][OTf]$ (53 mg, 84 μmol, 1 equiv) was added. After the brown solution was stirred at room temperature for 16 hours, all volatiles were removed under reduced pressure. The residue was washed with Et_2O (4 mL), washed with THF until the filtrate was no longer blue/green, dissolved in CH_2Cl_2, and filtered through Celite.

Volatiles were removed from the filtrate under reduced pressure, yielding **2-ox** as a brown powder (112 mg, 69 %). Crystals suitable for X-ray crystallography were obtained from a slow vapor diffusion of Et_2O into a concentrated solution of **2-ox** in CH_2Cl_2. Analysis calculated for $LMn_4O_4(O_2PPh_2)_3(OTf)$ [$C_{94}H_{69}F_3Mn_4N_6O_{16}P_3S$]: C 58.19, H 3.58, N 4.33; found: C 58.00, H 3.79, N 4.66.

Synthesis of **3-ox**: To a stirred suspension of $LCaMn_3O_4(OAc)_3(THF)$ (660 mg, 0.5 mmol, 1 equiv) in DMF (10 mL) was added $Mn(OTf)_2$•2MeCN (230 mg, 0.53 mmol, 1.06 equiv) and propane-1,3-diacetamide (84 mg, 0.53 mmol, 1.06 equiv). After stirring the reaction mixture at room temperature for 1 hour, sodium *tert*-butoxide (102 mg, 1.06 mmol, 2.1 equiv) was added and additional DMF was added to adjust the volume of the reaction to 20 mL. After stirring at room temperature for 18 hours, the precipitate formed in the reaction mixture was collected on a pad of Celite. The precipitate was rinsed with additional DMF and subsequently with Et_2O. The solid residue was dissolved in CH_2Cl_2 and filtered through Celite. All volatiles were removed from the filtrate under reduced pressure. Compound **3** was isolated as air- and moisture-stable red powder. Yield = 330 mg, 50 %. Crystals suitable for X-ray crystallography were obtained by slow vapor diffusion of Et_2O into a concentrated solution of **3** in CH_2Cl_2. Analysis calculated for $LMn_4O_4(diamidate)(OAc)\cdot\frac{1}{2}CH_2Cl_2\cdot Et_2O$ [$C_{71}H_{65}ClMn_4N_8O_{12}$]: C 57.72, H 4.43, N 7.58; found (duplicate runs): C 57.68, H 4.77, N 7.28; C 57.70, H 4.74, N 7.23.

To a suspension of **3** (70 mg, 52 μmol, 1 equiv) in THF (10 mL), Ag(OTf) (15 mg, 58 μmol, 1.1 equiv) was added as a THF solution. After stirring for 18 hrs, the reaction mixture was filtered through a pad of Celite and concentrated under reduced pressure. The residue was washed with generous amounts of Et_2O, redissolved in CH_2Cl_2, and filtered through a

pad of Celite. All volatiles were removed from the filtrate under reduced pressure. Crystals suitable for X-ray crystallography were obtained by slow vapor diffusion of Et_2O into a concentrated solution of **3-ox** in CH_2Cl_2. Yield = 30 mg, 39 %. Analysis calculated for LMn_4O_4(diamidate)(OAc)(OTf)·CH_2Cl_2 [$C_{68}H_{56}Cl_2F_3Mn_4N_8O_{14}S$]: C 51.40, H 3.55, N 7.05; found (duplicate runs): C 51.26, H 3.49, N 6.73; C 51.24, H 3.61, N 6.87.

Synthesis of **4-ox**: To a stirred solution of **3** (282 mg, 0.21 mmol, 1 equiv) in CH_2Cl_2 (10 mL) was added a solution of *p*-CF_3-benzoic acid (50 mg, 0.26 mmol, 1.25 equiv) in THF (5 mL). After stirring the resulting red solution at room temperature for 6 hours, all volatiles were removed under reduced pressure. To ensure complete substitution, the residue was redissolved in THF, stirred for 1 hour, and all volatiles removed under reduced pressure. This procedure was repeated three times. The solid residue was rinsed with hexanes and subsequently with diethyl ether. The solid residue was dissolved in benzene and filtered through Celite. All volatiles were removed from the filtrate under reduced pressure. The residue was rinsed with MeCN and subsequently with diethyl ether, and dried under reduced pressure. Compound **4** was isolated as a red powder. Yield = 260 mg, 84 %. Crystals suitable for X-ray crystallography could not be obtained.

To a stirred solution of **4** (230 mg, 0.15 μmol, 1 equiv) in CH_2Cl_2 (5 mL), a solution of Ag(OTf) (42 mg, 0.16 μmol, 1.1 equiv) in THF (5 mL) was added. After stirring the resulting mixture at room temperature for 18 hours, the reaction mixture was filtered through a pad of Celite and concentrated under reduced pressure. The residue was washed with a generous amount of Et_2O, redissolved in benzene, and filtered through a pad of Celite. All volatiles were removed from the filtrate under reduced pressure. Crystals suitable for X-ray crystallography were obtained by slow vapor diffusion of Et_2O into a

concentrated solution of **4-ox** in CH_2Cl_2. Yield = 147 mg, 58 %. Analysis calculated for LMn_4O_4(diamidate)(OBz)(OTf)·CH_2Cl_2 [$C_{74}H_{57}Cl_2F_6Mn_4N_8O_{14}S$]: C 51.70, H 3.34, N 6.52; found: C 51.51, H 3.38, N 6.76.

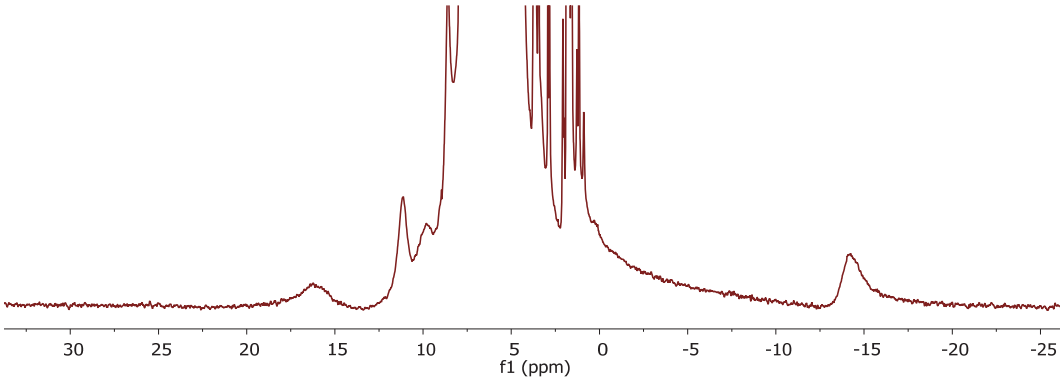

Figure 15. ^{1}H NMR of **2** in CD_2Cl_2.

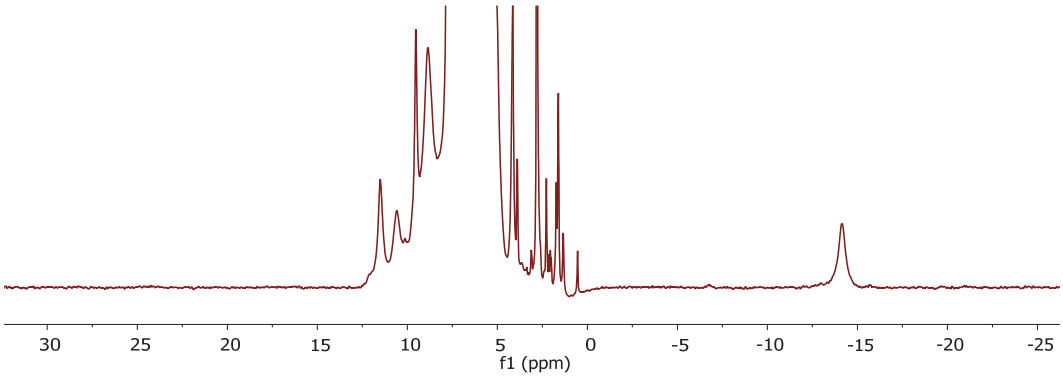

Figure 16. ^{1}H NMR of **2-ox** in CD_2Cl_2.

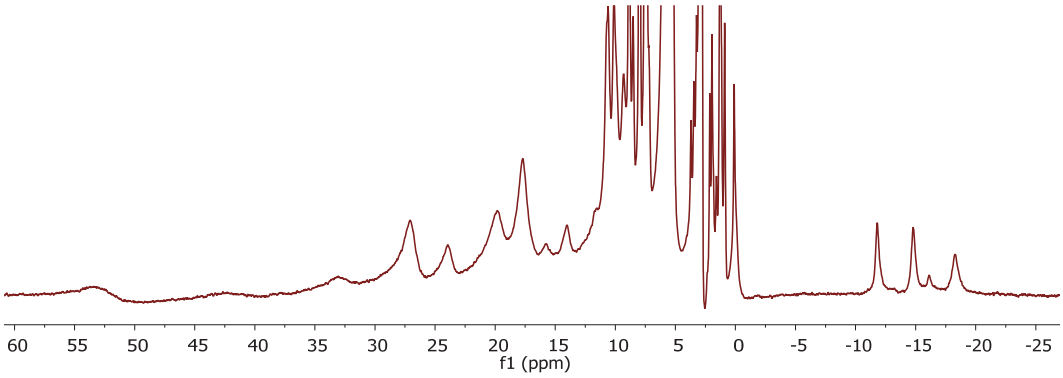

Figure 17. ^{1}H NMR of **3** in CD_2Cl_2.

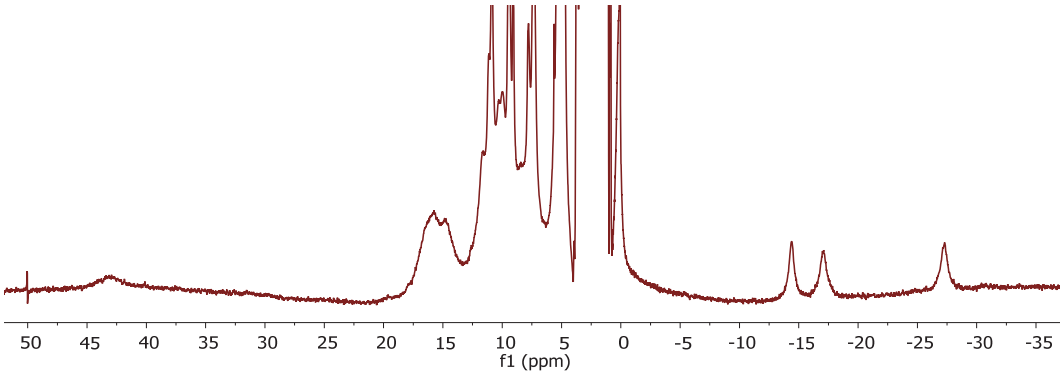

Figure 18. ^{1}H NMR of **3-ox** in CD_2Cl_2.

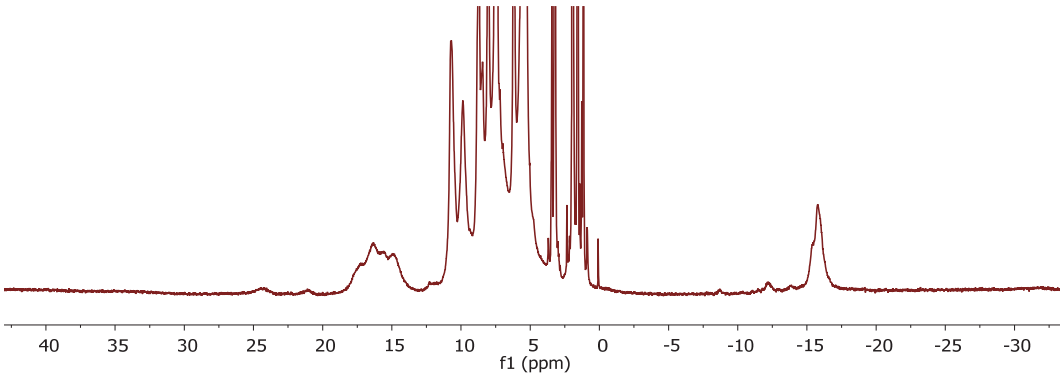

Figure 19. ^{1}H NMR of **4** in CD_2Cl_2.

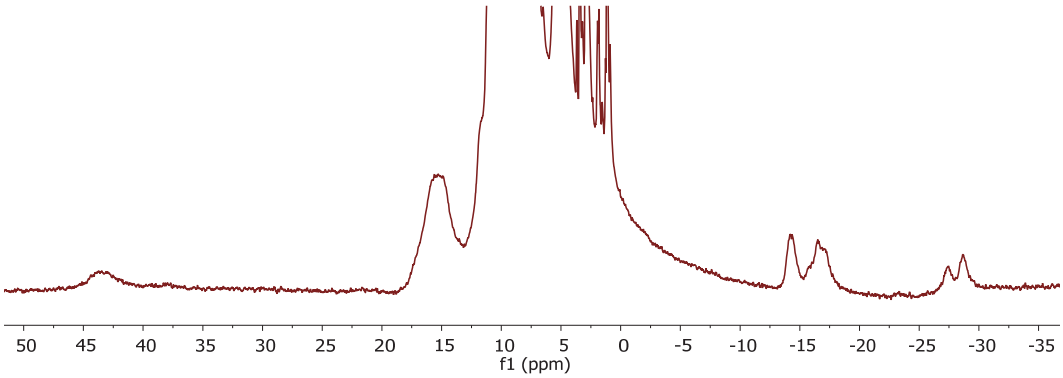

Figure 20. ^{1}H NMR of **4-ox** in CD_2Cl_2.

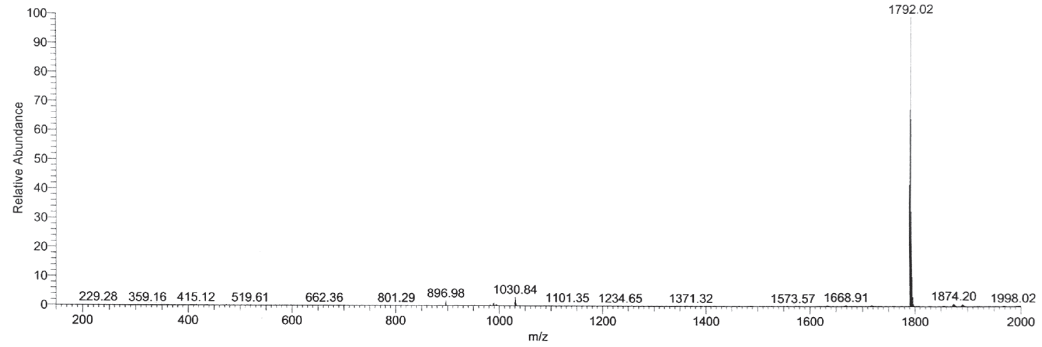

Figure 21. ESI-MS of **2**. m/z = 1792 consistent with $[LMn_4O_4(O_2PPh_2)_3]^+$.

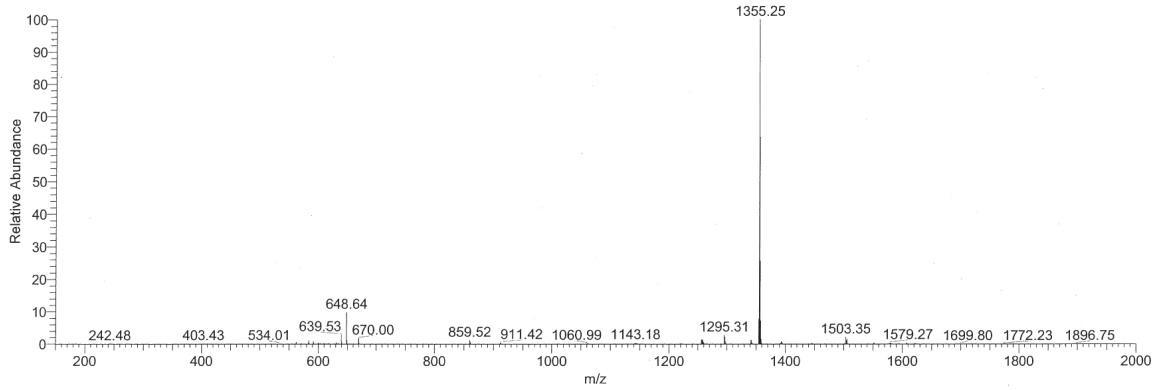

Figure 22. ESI-MS of **3**. *m*/*z* = 1355 consistent with $[LMn_4O_4(diam)(OAc)]^+$.

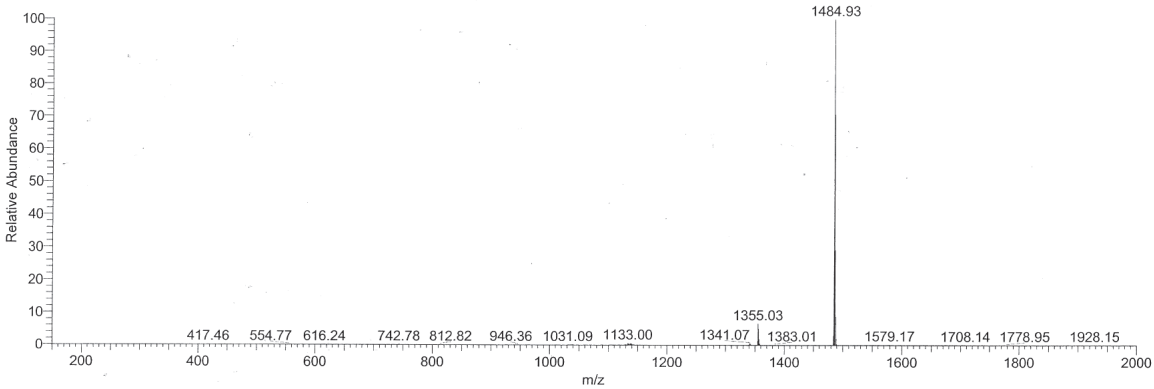

Figure 23. ESI-MS of **4-ox**. *m*/*z* = 1485 consistent with $[LMn_4O_4(diam)(^{CF3}OBz)]^+$.

Magnetometry: Magnetic susceptibility measurements were carried on a Quantum Design MPMS 3 instrument running MPMS Multivu software. Crystalline samples were powdered and suspended in clear plastic straws in polycarbonate capsules. Data were recorded at 0.4 T from 1.8−300 K. Diamagnetic corrections were made as follows: –970, –795, and –860 × 10^{-6} cm^3/mol for **2-ox**, **3-ox**, and **4-ox**, respectively. Fitting simulations were performed using PHI. Fitting simulations were performed assuming an on-site zero field splitting parameter $D(Mn^{IV}) \approx 0$ cm^{-1} and $D(Mn^{III}) = 0$, −2, or −4 cm^{-1}. The average *J* values are reported.

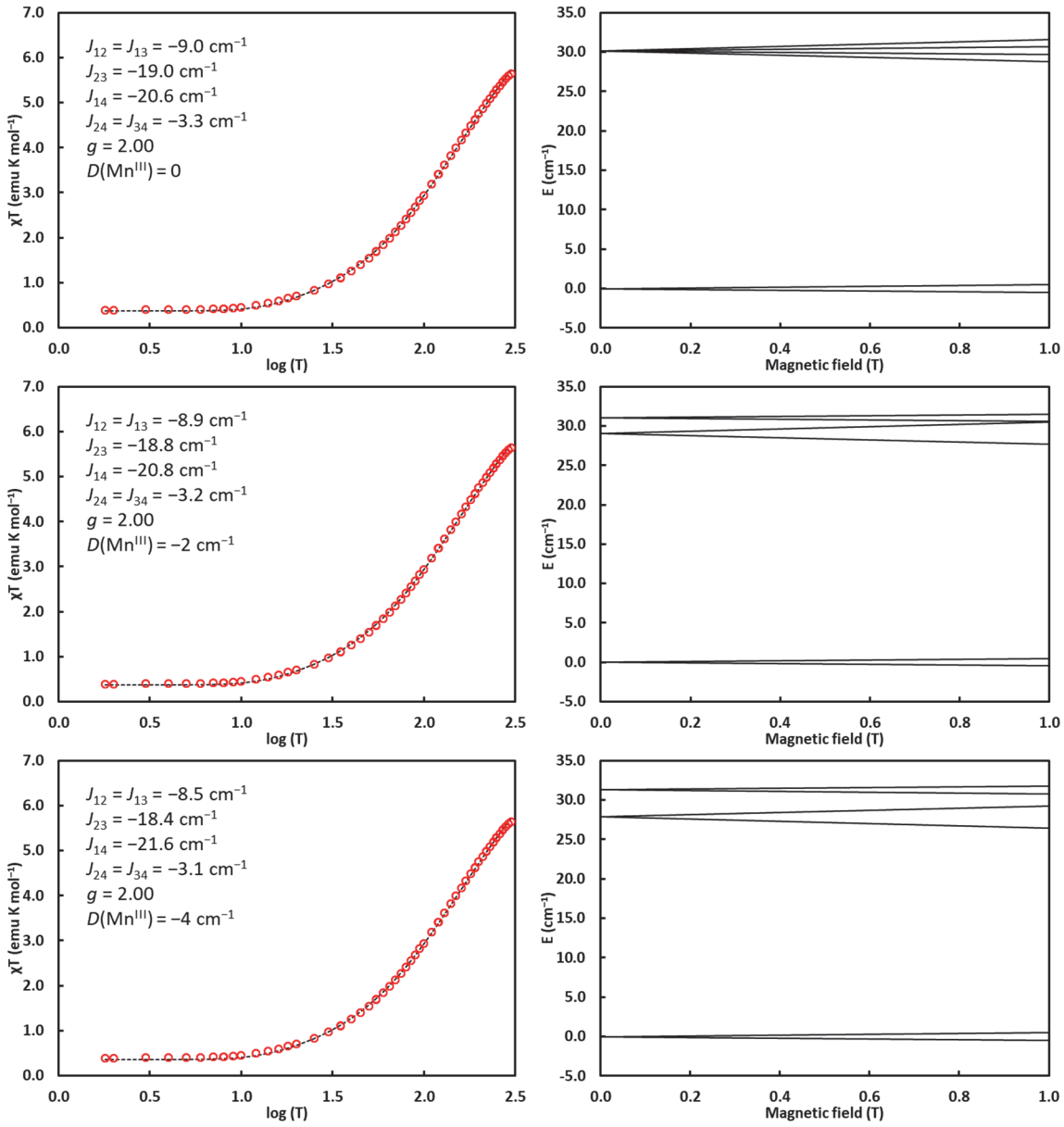

Figure 24. Fit parameters and corresponding χT vs. log(T) plots and Zeeman splitting diagrams for **2-ox**.

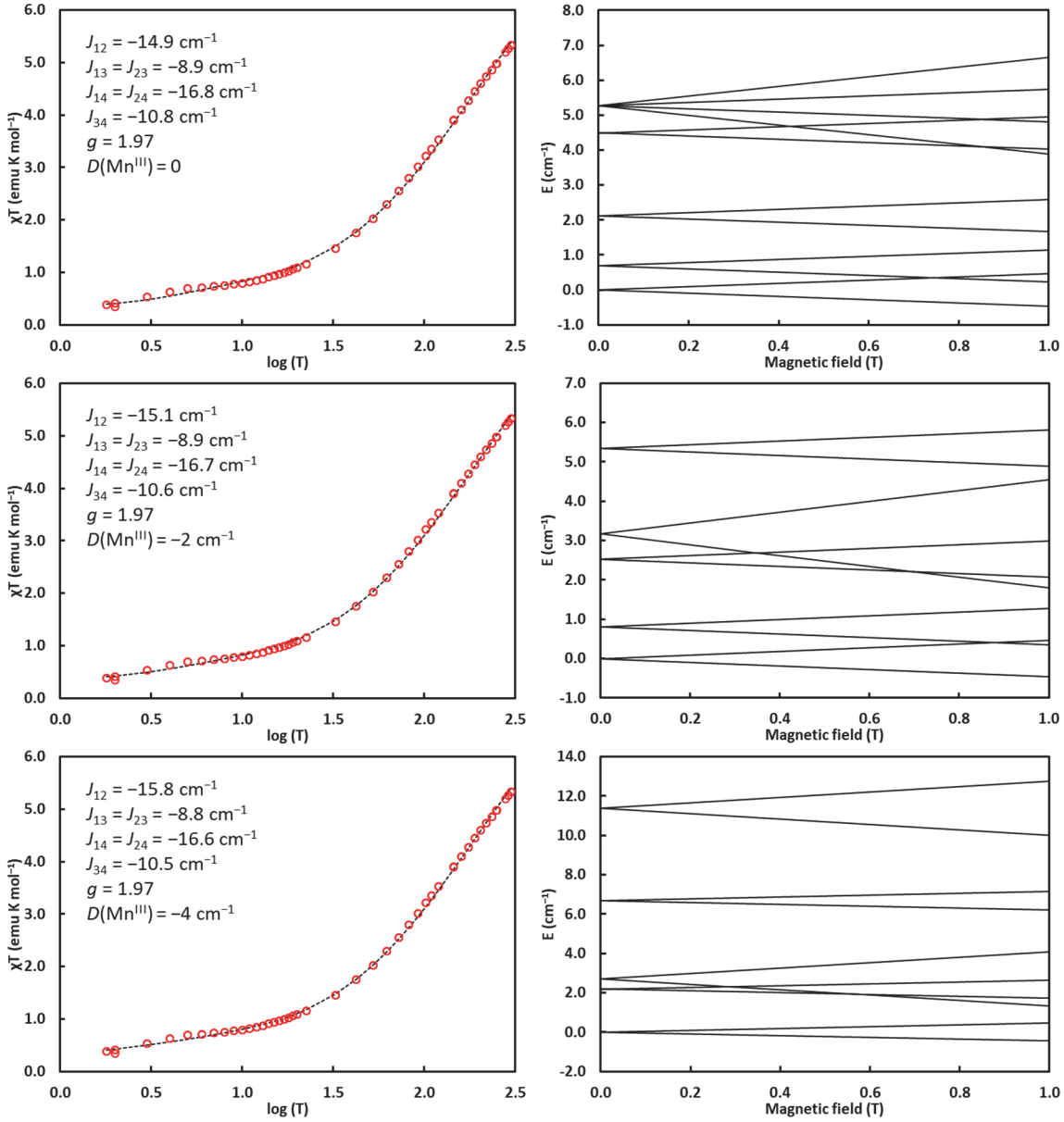

Figure 25. Fit parameters and corresponding χT vs. log(T) plots and Zeeman splitting diagrams for **3-ox**.

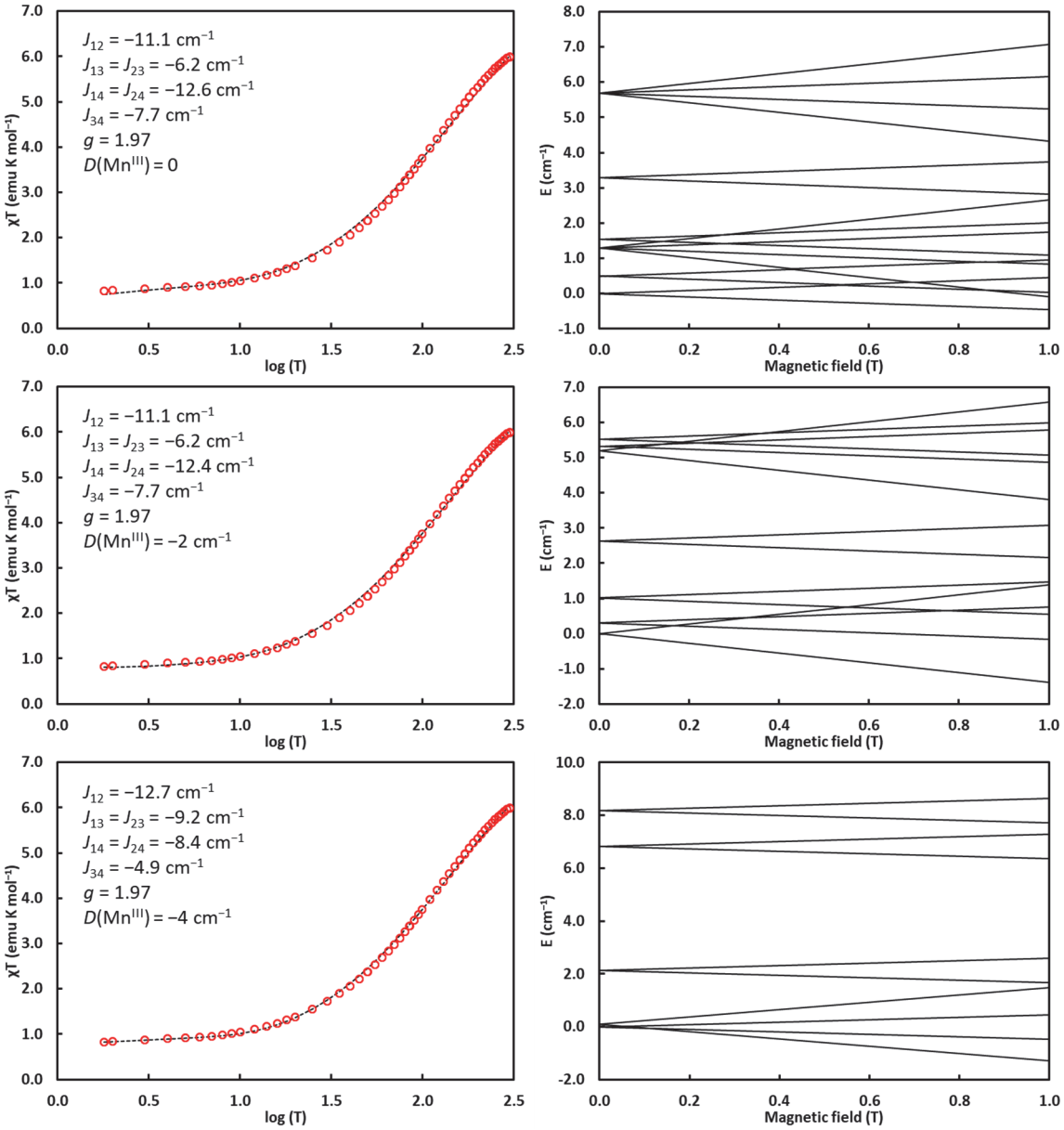

Figure 26. Fit parameters and corresponding χT vs. log(T) plots and Zeeman splitting diagrams for **4-ox**.

Table 3. Crystal and refinement data for complexes **2**, **2-ox**, and **3**.

Compound	**2**	**2-ox**	**3**
CCDC	1863637	1863638	1863639
Empirical formula	$C_{94}H_{71}Cl_2Mn_4N_6O_{13}P_3$	$C_{95}H_{71}Cl_2F_3Mn_4N_6O_{16}P_3S$	$C_{73.55}H_{56}Cl_{2.51}Mn_4N_8O_{12.57}$
Formula weight	1876.13	2025.20	1561.80
Temperature/K	296.15	100.0	100.0
Crystal system	triclinic	monoclinic	triclinic
Space group	P-1	$P2_1/n$	P-1
a/Å	14.2765(10)	14.3608(9)	13.2586(18)
b/Å	14.3034(8)	27.4932(17)	15.443(3)
c/Å	23.7048(18)	23.6617(14)	18.255(3)
α/°	72.614(2)	90	89.004(5)
β/°	87.529(2)	101.255(2)	85.374(5)
γ/°	67.645(2)	90	82.474(5)
Volume/Å^3	4258.6(5)	9162.5(10)	3693.5(10)
Z	2	4	2
ρ_{calc}g/cm^3	1.463	1.468	1.404
μ/mm^{-1}	0.767	0.748	0.825
F(000)	1920.0	4132.0	1593.0
Crystal size/mm^3	0.1 × 0.1 × 0.1	0.1 × 0.05 × 0.03	0.1 × 0.1 × 0.1
Radiation	MoKα (λ = 0.71073)	MoKα (λ = 0.71073)	MoKα (λ = 0.71073)
2Θ range for data collection/°	3.094 to 61.002	4.272 to 72.664	4.992 to 61.126
Index ranges	$-20 \le h \le 19$, $-20 \le k \le 20$, $-33 \le l \le 33$	$-23 \le h \le 23$, $-45 \le k \le 45$, $-39 \le l \le 39$	$-18 \le h \le 18$, $-22 \le k \le 22$, $-26 \le l \le 26$
Reflections collected	163138	470337	130778
Independent reflections	25775 [R_{int} = 0.0594, R_{sigma} = 0.0494]	43739 [R_{int} = 0.0541, R_{sigma} = 0.0346]	22581 [R_{int} = 0.0305, R_{sigma} = 0.0250]
Data/restraints/parameters	25775/0/1099	43739/30/1211	22581/37/935
Goodness-of-fit on F^2	1.012	1.049	1.052
Final R indexes [I>=2σ (I)]	R_1 = 0.0495, wR_2 = 0.1122	R_1 = 0.0590, wR_2 = 0.1539	R_1 = 0.0626, wR_2 = 0.1885
Final R indexes [all data]	R_1 = 0.0780, wR_2 = 0.1244	R_1 = 0.0861, wR_2 = 0.1739	R_1 = 0.0781, wR_2 = 0.2028
Largest diff. peak/hole / e Å^{-3}	0.90/-1.32	2.16/-2.32	2.25/-1.47

Table 4. Crystal and refinement data for complexes **3-ox** and **4-ox**.

Compound	**3-ox**	**4-ox**
CCDC	1863640	1863641
Empirical formula	$C_{68}H_{57}Cl_2F_3Mn_4N_8O_{14}S$	$C_{77}H_{65}F_6Mn_4N_8O_{15}S$
Formula weight	1589.93	1708.19
Temperature/K	100.04	99.99
Crystal system	triclinic	monoclinic
Space group	P-1	C2/c
a/Å	12.925(2)	41.9795(15)
b/Å	15.479(2)	15.5642(8)
c/Å	18.467(3)	26.7105(8)
α/°	81.151(6)	90
β/°	84.367(6)	122.4230(10)
γ/°	66.925(7)	90
Volume/Å^3	3355.5(9)	14731.5(10)
Z	2	8
ρ_{calc}g/cm^3	1.574	1.540
μ/mm^{-1}	7.697	0.787
F(000)	1620.0	6984.0
Crystal size/mm^3	0.02 × 0.02 × 0.02	0.1 × 0.1 × 0.05
Radiation	CuKα (λ = 1.54178)	MoKα (λ = 0.71073)
2Θ range for data collection/°	6.256 to 150.802	4.328 to 61.122
Index ranges	-16 ≤ h ≤ 15, -19 ≤ k ≤ 19, -23 ≤ l ≤ 23	-59 ≤ h ≤ 59, -22 ≤ k ≤ 22, -38 ≤ l ≤ 38
Reflections collected	51382	150607
Independent reflections	13628 [R_{int} = 0.0684, R_{sigma} = 0.0600]	22494 [R_{int} = 0.0436, R_{sigma} = 0.0305]
Data/restraints/parameters	13628/0/914	22494/0/1004
Goodness-of-fit on F^2	1.029	1.051
Final R indexes [I>=2σ (I)]	R_1 = 0.0786, wR_2 = 0.2145	R_1 = 0.0766, wR_2 = 0.2334
Final R indexes [all data]	R_1 = 0.1078, wR_2 = 0.2416	R_1 = 0.0991, wR_2 = 0.2585
Largest diff. peak/hole / e Å^{-3}	3.12/-1.56	2.58/-2.61

3.9) References

(1) Shen, J.-R., *Annu. Rev. Plant Biol.* **2015**, *66*, 23.
(2) Yano, J.; Yachandra, V., *Chem. Rev.* **2014**, *114*, 4175.
(3) Cox, N.; Pantazis, D. A.; Neese, F.; Lubitz, W., *Acc. Chem. Res.* **2013**, *46*, 1588.
(4) Oyala, P. H.; Stich, T. A.; Debus, R. J.; Britt, R. D., *J. Am. Chem. Soc.* **2015**, *137*, 8829.
(5) Siegbahn, P. E. M., *Acc. Chem. Res.* **2009**, *42*, 1871.
(6) Oyala, P. H.; Stich, T. A.; Stull, J. A.; Yu, F.; Pecoraro, V. L.; Britt, R. D., *Biochemistry* **2014**, *53*, 7914.
(7) Pérez Navarro, M.; Ames, W. M.; Nilsson, H.; Lohmiller, T.; Pantazis, D. A.; Rapatskiy, L.; Nowaczyk, M. M.; Neese, F.; Boussac, A.; Messinger, J.; Lubitz, W.; Cox, N., *Proc. Nat. Acad. Sci.* **2013**, *110*, 15561.
(8) Rapatskiy, L.; Cox, N.; Savitsky, A.; Ames, W. M.; Sander, J.; Nowaczyk, M. M.; Rögner, M.; Boussac, A.; Neese, F.; Messinger, J.; Lubitz, W., *J. Am. Chem. Soc.* **2012**, *134*, 16619.
(9) Boussac, A.; Rutherford, A. W., *Biochim. Biophys. Acta* **2000**, *1457*, 145.
(10) Haddy, A.; Lakshmi, K. V.; Brudvig, G. W.; Frank, H. A., *Biophys. J.* **2004**, *87*, 2885.
(11) Boussac, A.; Un, S.; Horner, O.; Rutherford, A. W., *Biochemistry* **1998**, *37*, 4001.
(12) Britt, R. D.; Lorigan, G. A.; Sauer, K.; Klein, M. P.; Zimmermann, J.-L., *Biochim. Biophys. Acta - Bioenergetics* **1992**, *1140*, 95.
(13) Kim, D. H.; Britt, R. D.; Klein, M. P.; Sauer, K., *Biochemistry* **1992**, *31*, 541.
(14) Dismukes, G. C.; Siderer, Y., *Proc. Nat. Acad. Sci.* **1981**, *78*, 274.
(15) Krewald, V.; Retegan, M.; Cox, N.; Messinger, J.; Lubitz, W.; DeBeer, S.; Neese, F.; Pantazis, D. A., *Chem. Sci.* **2015**, *6*, 1676.
(16) Peloquin, J. M.; Campbell, K. A.; Randall, D. W.; Evanchik, M. A.; Pecoraro, V. L.; Armstrong, W. H.; Britt, R. D., *J. Am. Chem. Soc.* **2000**, *122*, 10926.
(17) Cox, N.; Retegan, M.; Neese, F.; Pantazis, D. A.; Boussac, A.; Lubitz, W., *Science* **2014**, *345*, 804.
(18) DeRose, V. J.; Latimer, M. J.; Zimmermann, J.-L.; Mukerji, I.; Yachandra, V. K.; Sauer, K.; Klein, M. P., *Chem. Phys.* **1995**, *194*, 443.
(19) Lohmiller, T.; Krewald, V.; Navarro, M. P.; Retegan, M.; Rapatskiy, L.; Nowaczyk, M. M.; Boussac, A.; Neese, F.; Lubitz, W.; Pantazis, D. A.; Cox, N., *Phys. Chem. Chem. Phys.* **2014**, *16*, 11877.
(20) Glöckner, C.; Kern, J.; Broser, M.; Zouni, A.; Yachandra, V.; Yano, J., *J. Biol. Chem.* **2013**, *288*, 22607.
(21) Lohmiller, T.; Ames, W.; Lubitz, W.; Cox, N.; Misra, S. K., *Appl. Magn. Reson.* **2013**, *44*, 691.
(22) Pantazis, D. A.; Ames, W.; Cox, N.; Lubitz, W.; Neese, F., *Angew. Chem. Int. Ed.* **2012**, *51*, 9935.
(23) Horner, O.; Rivière, E.; Blondin, G.; Un, S.; Rutherford, A. W.; Girerd, J.-J.; Boussac, A., *J. Am. Chem. Soc.* **1998**, *120*, 7924.
(24) Bovi, D.; Narzi, D.; Guidoni, L., *Angew. Chem. Int. Ed.* **2013**, *52*, 11744.
(25) Vinyard, D. J.; Khan, S.; Askerka, M.; Batista, V. S.; Brudvig, G. W., *J. Phys. Chem. B* **2017**, *121*, 1020.

(26) Suga, M.; Akita, F.; Sugahara, M.; Kubo, M.; Nakajima, Y.; Nakane, T.; Yamashita, K.; Umena, Y.; Nakabayashi, M.; Yamane, T.; Nakano, T.; Suzuki, M.; Masuda, T.; Inoue, S.; Kimura, T.; Nomura, T.; Yonekura, S.; Yu, L.-J.; Sakamoto, T.; Motomura, T.; Chen, J.-H.; Kato, Y.; Noguchi, T.; Tono, K.; Joti, Y.; Kameshima, T.; Hatsui, T.; Nango, E.; Tanaka, R.; Naitow, H.; Matsuura, Y.; Yamashita, A.; Yamamoto, M.; Nureki, O.; Yabashi, M.; Ishikawa, T.; Iwata, S.; Shen, J.-R., *Nature* **2017**, *543*, 131.

(27) Young, I. D.; Ibrahim, M.; Chatterjee, R.; Gul, S.; Fuller, F. D.; Koroidov, S.; Brewster, A. S.; Tran, R.; Alonso-Mori, R.; Kroll, T.; Michels-Clark, T.; Laksmono, H.; Sierra, R. G.; Stan, C. A.; Hussein, R.; Zhang, M.; Douthit, L.; Kubin, M.; de Lichtenberg, C.; Vo Pham, L.; Nilsson, H.; Cheah, M. H.; Shevela, D.; Saracini, C.; Bean, M. A.; Seuffert, I.; Sokaras, D.; Weng, T.-C.; Pastor, E.; Weninger, C.; Fransson, T.; Lassalle, L.; Bräuer, P.; Aller, P.; Docker, P. T.; Andi, B.; Orville, A. M.; Glownia, J. M.; Nelson, S.; Sikorski, M.; Zhu, D.; Hunter, M. S.; Lane, T. J.; Aquila, A.; Koglin, J. E.; Robinson, J.; Liang, M.; Boutet, S.; Lyubimov, A. Y.; Uervirojnangkoorn, M.; Moriarty, N. W.; Liebschner, D.; Afonine, P. V.; Waterman, D. G.; Evans, G.; Wernet, P.; Dobbek, H.; Weis, W. I.; Brunger, A. T.; Zwart, P. H.; Adams, P. D.; Zouni, A.; Messinger, J.; Bergmann, U.; Sauter, N. K.; Kern, J.; Yachandra, V. K.; Yano, J., *Nature* **2016**, *540*, 453.

(28) Kern, J.; Tran, R.; Alonso-Mori, R.; Koroidov, S.; Echols, N.; Hattne, J.; Ibrahim, M.; Gul, S.; Laksmono, H.; Sierra, R. G.; Gildea, R. J.; Han, G.; Hellmich, J.; Lassalle-Kaiser, B.; Chatterjee, R.; Brewster, A. S.; Stan, C. A.; Glöckner, C.; Lampe, A.; DiFiore, D.; Milathianaki, D.; Fry, A. R.; Seibert, M. M.; Koglin, J. E.; Gallo, E.; Uhlig, J.; Sokaras, D.; Weng, T.-C.; Zwart, P. H.; Skinner, D. E.; Bogan, M. J.; Messerschmidt, M.; Glatzel, P.; Williams, G. J.; Boutet, S.; Adams, P. D.; Zouni, A.; Messinger, J.; Sauter, N. K.; Bergmann, U.; Yano, J.; Yachandra, V. K., *Nat. Commun.* **2014**, *5*, 4371.

(29) Suga, M.; Akita, F.; Hirata, K.; Ueno, G.; Murakami, H.; Nakajima, Y.; Shimizu, T.; Yamashita, K.; Yamamoto, M.; Ago, H.; Shen, J.-R., *Nature* **2014**, *517*, 99.

(30) Kern, J.; Alonso-Mori, R.; Tran, R.; Hattne, J.; Gildea, R. J.; Echols, N.; Glöckner, C.; Hellmich, J.; Laksmono, H.; Sierra, R. G.; Lassalle-Kaiser, B.; Koroidov, S.; Lampe, A.; Han, G.; Gul, S.; DiFiore, D.; Milathianaki, D.; Fry, A. R.; Miahnahri, A.; Schafer, D. W.; Messerschmidt, M.; Seibert, M. M.; Koglin, J. E.; Sokaras, D.; Weng, T.-C.; Sellberg, J.; Latimer, M. J.; Grosse-Kunstleve, R. W.; Zwart, P. H.; White, W. E.; Glatzel, P.; Adams, P. D.; Bogan, M. J.; Williams, G. J.; Boutet, S.; Messinger, J.; Zouni, A.; Sauter, N. K.; Yachandra, V. K.; Bergmann, U.; Yano, J., *Science* **2013**, *340*, 491.

(31) Kupitz, C.; Basu, S.; Grotjohann, I.; Fromme, R.; Zatsepin, N. A.; Rendek, K. N.; Hunter, M. S.; Shoeman, R. L.; White, T. A.; Wang, D.; James, D.; Yang, J.-H.; Cobb, D. E.; Reeder, B.; Sierra, R. G.; Liu, H.; Barty, A.; Aquila, A. L.; Deponte, D.; Kirian, R. A.; Bari, S.; Bergkamp, J. J.; Beyerlein, K. R.; Bogan, M. J.; Caleman, C.; Chao, T.-C.; Conrad, C. E.; Davis, K. M.; Fleckenstein, H.; Galli, L.; Hau-Riege, S. P.; Kassemeyer, S.; Laksmono, H.; Liang, M.; Lomb, L.; Marchesini, S.; Martin, A. V.; Messerschmidt, M.; Milathianaki, D.; Nass, K.; Ros, A.; Roy-Chowdhury, S.; Schmidt, K.; Seibert, M.; Steinbrener, J.; Stellato, F.; Yan, L.; Yoon, C.; Moore, T. A.; Moore, A. L.; Pushkar, Y.; Williams, G. J.; Boutet, S.; Doak, R. B.; Weierstall, U.; Frank, M.; Chapman, H. N.; Spence, J. C. H.; Fromme, P., *Nature* **2014**, *513*, 261.

(32) Sauter, N. K.; Echols, N.; Adams, P. D.; Zwart, P. H.; Kern, J.; Brewster, A. S.; Koroidov, S.; Alonso-Mori, R.; Zouni, A.; Messinger, J.; Bergmann, U.; Yano, J.; Yachandra, V. K., *Nature* **2016**, *533*, E1.

(33) Boussac, A.; Rutherford, A. W.; Sugiura, M., *Biochim. Biophys. Acta - Bioenergetics* **2015**, *1847*, 576.
(34) Boussac, A.; Ugur, I.; Marion, A.; Sugiura, M.; Kaila, V. R. I.; Rutherford, A. W., *Biochim. Biophys. Acta - Bioenergetics* **2018**, *1859*, 342.
(35) Ames, W.; Pantazis, D. A.; Krewald, V.; Cox, N.; Messinger, J.; Lubitz, W.; Neese, F., *J. Am. Chem. Soc.* **2011**, *133*, 19743.
(36) Liang, W.; Latimer, M. J.; Dau, H.; Roelofs, T. A.; Yachandra, V. K.; Sauer, K.; Klein, M. P., *Biochemistry* **1994**, *33*, 4923.
(37) Chatterjee, R.; Han, G.; Kern, J.; Gul, S.; Fuller, F. D.; Garachtchenko, A.; Young, I. D.; Weng, T.-C.; Nordlund, D.; Alonso-Mori, R.; Bergmann, U.; Sokaras, D.; Hatakeyama, M.; Yachandra, V. K.; Yano, J., *Chem. Sci.* **2016**, *7*, 5236.
(38) Paul, S.; Neese, F.; Pantazis, D. A., *Green Chem.* **2017**, *19*, 2309.
(39) Mukhopadhyay, S.; Mandal, S. K.; Bhaduri, S.; Armstrong, W. H., *Chem. Rev.* **2004**, *104*, 3981.
(40) Mullins, C. S.; Pecoraro, V. L., *Coord. Chem. Rev.* **2008**, *252*, 416.
(41) Ruettinger, W. F.; Ho, D. M.; Dismukes, G. C., *Inorg. Chem.* **1999**, *38*, 1036.
(42) Dubé, C. E.; Sessoli, R.; Hendrich, M. P.; Gatteschi, D.; Armstrong, W. H., *J. Am. Chem. Soc.* **1999**, *121*, 3537.
(43) Blondin, G.; Davydov, R.; Philouze, C.; Charlot, M.-F.; Styring, S.; Akermark, B.; Girerd, J.-J.; Boussac, A., *J. Chem. Soc., Dalton Trans.* **1997**, 4069.
(44) Zhang, C.; Chen, C.; Dong, H.; Shen, J.-R.; Dau, H.; Zhao, J., *Science* **2015**, *348*, 690.
(45) Shoji, M.; Isobe, H.; Shen, J.-R.; Yamaguchi, K., *Phys. Chem. Chem. Phys.* **2016**, *18*, 11330.
(46) Paul, S.; Cox, N.; Pantazis, D. A., *Inorg. Chem.* **2017**, *56*, 3875.
(47) Dubé, C. E.; Mukhopadhyay, S.; Bonitatebus, P. J.; Staples, R. J.; Armstrong, W. H., *Inorg. Chem.* **2005**, *44*, 5161.
(48) Krewald, V.; Neese, F.; Pantazis, D. A., *J. Am. Chem. Soc.* **2013**, *135*, 5726.
(49) Mukherjee, S.; Stull, J. A.; Yano, J.; Stamatatos, T. C.; Pringouri, K.; Stich, T. A.; Abboud, K. A.; Britt, R. D.; Yachandra, V. K.; Christou, G., *Proc. Nat. Acad. Sci.* **2012**, *109*, 2257.
(50) Hendrickson, D. N.; Christou, G.; Schmitt, E. A.; Libby, E.; Bashkin, J. S.; Wang, S.; Tsai, H. L.; Vincent, J. B.; Boyd, P. D. W., *J. Am. Chem. Soc.* **1992**, *114*, 2455.
(51) Hewitt, I. J.; Tang, J.-K.; Madhu, N. T.; Clérac, R.; Buth, G.; Anson, C. E.; Powell, A. K., *Chem. Commun.* **2006**, 2650.
(52) Koumousi, E. S.; Mukherjee, S.; Beavers, C. M.; Teat, S. J.; Christou, G.; Stamatatos, T. C., *Chem. Commun.* **2011**, *47*, 11128.
(53) Tsui, E. Y.; Tran, R.; Yano, J.; Agapie, T., *Nat. Chem.* **2013**, *5*, 293.
(54) Tsui, E. Y.; Agapie, T., *Proc. Nat. Acad. Sci.* **2013**, *110*, 10084.
(55) Kanady, J. S.; Tran, R.; Stull, J. A.; Lu, L.; Stich, T. A.; Day, M. W.; Yano, J.; Britt, R. D.; Agapie, T., *Chem. Sci.* **2013**, *4*, 3986.
(56) Kanady, J. S.; Lin, P.-H.; Carsch, K. M.; Nielsen, R. J.; Takase, M. K.; Goddard, W. A.; Agapie, T., *J. Am. Chem. Soc.* **2014**, *136*, 14373.
(57) Kanady, J. S.; Mendoza-Cortes, J. L.; Tsui, E. Y.; Nielsen, R. J.; Goddard, W. A.; Agapie, T., *J. Am. Chem. Soc.* **2013**, *135*, 1073.

(58) Lin, P.-H.; Tsui, E. Y.; Habib, F.; Murugesu, M.; Agapie, T., *Inorg. Chem.* **2016**, *55*, 6095.
(59) Han, Z.; Horak, K. T.; Lee, H. B.; Agapie, T., *J. Am. Chem. Soc.* **2017**, *139*, 9108.
(60) Lee, H. B.; Tsui, E. Y.; Agapie, T., *Chem. Commun.* **2017**, *53*, 6832.
(61) Ruettinger, W. F.; Campana, C.; Dismukes, G. C., *J. Am. Chem. Soc.* **1997**, *119*, 6670.
(62) Limburg, J.; Vrettos, J. S.; Liable-Sands, L. M.; Rheingold, A. L.; Crabtree, R. H.; Brudvig, G. W., *Science* **1999**, *283*, 1524.
(63) Limburg, J.; Vrettos, J. S.; Chen, H.; de Paula, J. C.; Crabtree, R. H.; Brudvig, G. W., *J. Am. Chem. Soc.* **2001**, *123*, 423.
(64) Chen, H.; Faller, J. W.; Crabtree, R. H.; Brudvig, G. W., *J. Am. Chem. Soc.* **2004**, *126*, 7345.
(65) Chen; Collomb, M.-N.; Duboc, C.; Blondin, G.; Rivière, E.; Faller, J. W.; Crabtree, R. H.; Brudvig, G. W., *Inorg. Chem.* **2005**, *44*, 9567.
(66) Dubé, C. E.; Wright, D. W.; Pal, S.; Bonitatebus, P. J.; Armstrong, W. H., *J. Am. Chem. Soc.* **1998**, *120*, 3704.
(67) Chan, M. K.; Armstrong, W. H., *J. Am. Chem. Soc.* **1990**, *112*, 4985.
(68) Nguyen, A. I.; Suess, D. L. M.; Darago, L. E.; Oyala, P. H.; Levine, D. S.; Ziegler, M. S.; Britt, R. D.; Tilley, T. D., *J. Am. Chem. Soc.* **2017**, *139*, 5579.
(69) Nguyen, A. I.; Darago, L. E.; Balcells, D.; Tilley, T. D., *J. Am. Chem. Soc.* **2018**, *140*, 9030.
(70) Kanady, J. S.; Tsui, E. Y.; Day, M. W.; Agapie, T., *Science* **2011**, *333*, 733.
(71) Carver, G.; Thut, M.; Noble, C.; Tregenna-Piggott, P. L. W., *J. Chem. Theory Comput.* **2008**, *4*, 603.
(72) Tregenna-Piggott, P. L. W.; Weihe, H.; Barra, A.-L., *Inorg. Chem.* **2003**, *42*, 8504.
(73) Reed, C. J.; Agapie, T., *Inorg. Chem.* **2017**, *56*, 13360.
(74) Gupta, R.; Taguchi, T.; Lassalle-Kaiser, B.; Bominaar, E. L.; Yano, J.; Hendrich, M. P.; Borovik, A. S., *Proc. Nat. Acad. Sci.* **2015**, *112*, 5319.
(75) Tsui, E. Y.; Kanady, J. S.; Agapie, T., *Inorg. Chem.* **2013**, *52*, 13833.
(76) Christou, G., *Acc. Chem. Res.* **1989**, *22*, 328.
(77) Thomson, R. K.; Patrick, B. O.; Schafer, L. L., *Can. J. Chem.* **2005**, *83*, 1037.
(78) Xu, J.-Y.; Astner, J.; Walter, O.; Heinemann, F. W.; Schindler, S.; Merkel, M.; Krebs, B., *Eur. J. Inorg. Chem.* **2006**, *2006*, 1601.
(79) Kampert, E.; Janssen, F. F. B. J.; Boukhvalov, D. W.; Russcher, J. C.; Smits, J. M. M.; de Gelder, R.; de Bruin, B.; Christianen, P. C. M.; Zeitler, U.; Katsnelson, M. I.; Maan, J. C.; Rowan, A. E., *Inorg. Chem.* **2009**, *48*, 11903.
(80) Kütt, A.; Leito, I.; Kaljurand, I.; Sooväli, L.; Vlasov, V. M.; Yagupolskii, L. M.; Koppel, I. A., *J. Org. Chem.* **2006**, *71*, 2829.
(81) Nguyen, A. I.; Wang, J.; Levine, D. S.; Ziegler, M. S.; Tilley, T. D., *Chem. Sci.* **2017**, *8*, 4274.
(82) Rappaport, F.; Guergova-Kuras, M.; Nixon, P. J.; Diner, B. A.; Lavergne, J., *Biochemistry* **2002**, *41*, 8518.
(83) Chilton, N. F.; Anderson, R. P.; Turner, L. D.; Soncini, A.; Murray, K. S., *J. Comput. Chem.* **2013**, *34*, 1164.
(84) Krzystek, J.; Ozarowski, A.; Telser, J., *Coord. Chem. Rev.* **2006**, *250*, 2308.

(85) Telser, J.; Ozarowski, A.; Krzystek, J., High-frequency and -field electron paramagnetic resonance of transition metal ion (d block) coordination complexes. In *Electron Paramagnetic Resonance: Volume 23*, The Royal Society of Chemistry: 2013; Vol. 23, pp 209.

(86) Su, J.-H.; Cox, N.; Ames, W.; Pantazis, D. A.; Rapatskiy, L.; Lohmiller, T.; Kulik, L. V.; Dorlet, P.; Rutherford, A. W.; Neese, F.; Boussac, A.; Lubitz, W.; Messinger, J., *Biochim. Biophys. Acta - Bioenergetics* **2011**, *1807*, 829.

(87) Pace, R. J.; Smith, P.; Bramley, R.; Stehlik, D., *Biochim. Biophys. Acta - Bioenergetics* **1991**, *1058*, 161.

(88) Randall, D. W.; Sturgeon, B. E.; Ball, J. A.; Lorigan, G. A.; Chan, M. K.; Klein, M. P.; Armstrong, W. H.; Britt, R. D., *J. Am. Chem. Soc.* **1995**, *117*, 11780.

(89) Larson, E.; Haddy, A.; Kirk, M. L.; Sands, R. H.; Hatfield, W. E.; Pecoraro, V. L., *J. Am. Chem. Soc.* **1992**, *114*, 6263.

(90) Hagen, K. S.; Armstrong, W. H.; Hope, H., *Inorg. Chem.* **1988**, *27*, 967.

(91) Brewer, K. J.; Calvin, M.; Lumpkin, R. S.; Otvos, J. W.; Spreer, L. O., *Inorg. Chem.* **1989**, *28*, 4446.

(92) Pal, S.; Gohdes, J. W.; Wilisch, W. C. A.; Armstrong, W. H., *Inorg. Chem.* **1992**, *31*, 713.

(93) Bashkin, J. S.; Schake, A. R.; Vincent, J. B.; Chang, H. R.; Li, Q.; Huffman, J. C.; Christou, G.; Hendrickson, D. N., *J. Chem. Soc., Chem. Commun.* **1988**, 700.

(94) Wieghardt, K.; Bossek, U.; Zsolnai, L.; Huttner, G.; Blondin, G.; Girerd, J.-J.; Babonneau, F., *J. Chem. Soc., Chem. Commun.* **1987**, 651.

(95) Schäfer, K.-O.; Bittl, R.; Zweygart, W.; Lendzian, F.; Haselhorst, G.; Weyhermüller, T.; Wieghardt, K.; Lubitz, W., *J. Am. Chem. Soc.* **1998**, *120*, 13104.

(96) Stoll, S.; Schweiger, A., *J. Magn. Reson.* **2006**, *178*, 42.

(97) Cox, N.; Rapatskiy, L.; Su, J.-H.; Pantazis, D. A.; Sugiura, M.; Kulik, L.; Dorlet, P.; Rutherford, A. W.; Neese, F.; Boussac, A.; Lubitz, W.; Messinger, J., *J. Am. Chem. Soc.* **2011**, *133*, 3635.

(98) Kulik, L. V.; Epel, B.; Lubitz, W.; Messinger, J., *J. Am. Chem. Soc.* **2007**, *129*, 13421.

(99) Schosseler, P.; Wacker, T.; Schweiger, A., *Chem. Phys. Lett.* **1994**, *224*, 319.

(100) Cox, N.; Lubitz, W.; Savitsky, A., *Mol. Phys.* **2013**, *111*, 2788.

(101) Cox, N.; Nalepa, A.; Lubitz, W.; Savitsky, A., *J. Magn. Reson.* **2017**, *280*, 63.

(102) Lorigan, G. A.; Britt, R. D., *Photosynth. Res.* **2000**, *66*, 189.

CHAPTER 4

Redox Tuning via Ligand-Induced Geometric Distortions at a Cuboidal YMn_3O_4 model of the Biological Oxygen Evolving Complex

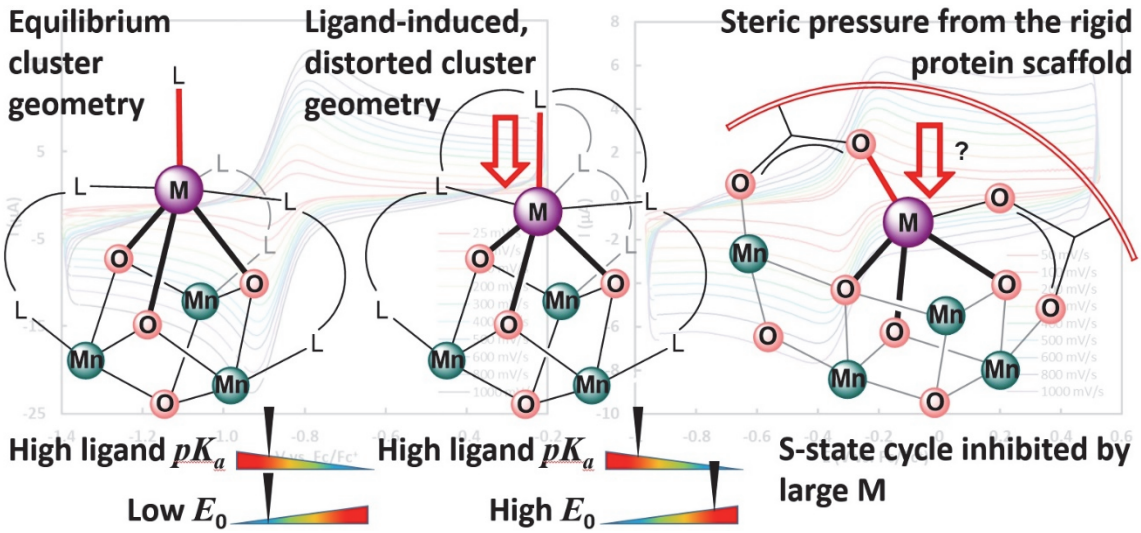

Abstract

The function of proteins involved in electron transfer is dependent on attaining the necessary reduction potential. We establish here a new mode of cluster redox tuning, through steric pressure on a synthetic model related to Photosystem II. Resembling the cuboidal [$CaMn_3O_4$] subsite of the biological oxygen evolving complex (OEC), [Mn_4O_4] and [YMn_3O_4] complexes featuring bridging ligands of different basicity and chelating properties have been synthesized and characterized by cyclic voltammetry. In the absence of ligand-induced geometric distortions that enforce a contraction of metal-oxo distances, increasing the basicity of the ligands results in a decrease of cluster reduction potential. A small contraction of Y-oxo/Y-Mn distances by 0.1/0.15 Å enforced by a chelating ligand results in an increase of cluster reduction potential even in the presence of strong basic donors. Such small, protein-induced changes in Ca-oxo/Ca-Mn distances may have a similar effect in tuning the redox potential of the OEC through entatic states, and may explain the cation size dependence on the progression of the S-state cycle.

4.1) Introduction

In many enzymatic processes such as photosynthesis and respiration, electron transfer (ET) steps play key functional roles.[1-2] Cupredoxins, iron-sulfur clusters, and cytochromes have been studied extensively in the context of biological ET and the structural features responsible for their redox properties.[3-6] In addition to controlling the rate of ET, tuning the redox potential of ET mediators can regulate biological reactions.[7-8] Factors that tune the redox potentials of metallocofactors include: (1) oxidation state and geometry of the metal center(s),[9-12] (2) nature of the ligands in the primary coordination sphere,[13-17] (3) secondary coordination sphere interactions such as hydrogen bonding and polarity of the medium,[18-22] and (4) binding of regulatory molecules.[23]

Featuring a multimetallic [$CaMn_4O_5$] core, the oxygen evolving complex (OEC) of Photosystem II catalyzes the 4 e^-/4 H^+ oxidation of H_2O to O_2.[24-26] The mechanism of O–O

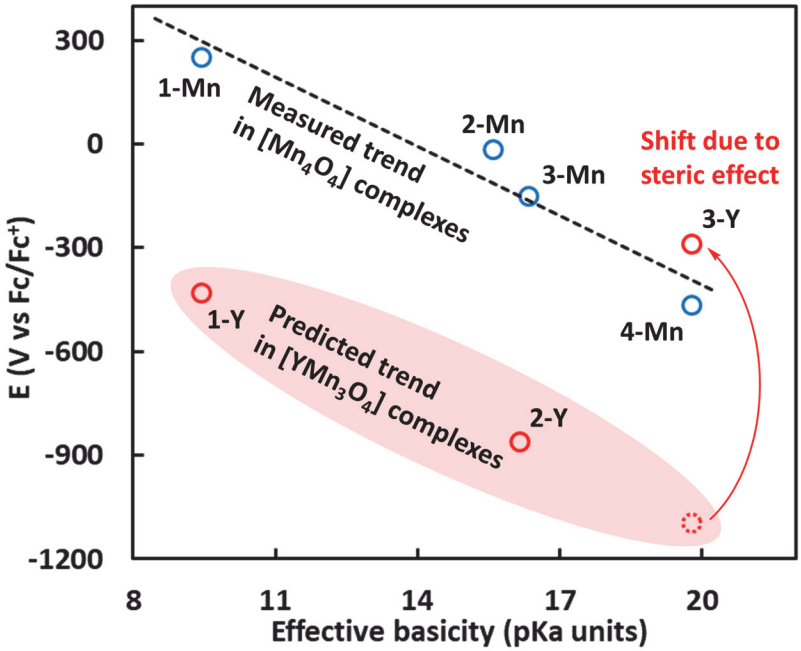

Figure 1. Linear correlation between redox potential and effective ligand basicity in [Mn_4O_4] complexes **1-Mn**~**4-Mn**. Similar trend based on ligand basicity observed for [YMn_3O_4] complexes **1-Y** and **2-Y**. Deviation from the trend in **3-Y** attributed to a steric effect described in this study.

bond formation and the role of the redox-inactive Ca^{2+} ion have been the subject of numerous biochemical, spectroscopic, computational, and synthetic studies, but the role of Ca^{2+} remains unclear.[27-40] Removal of Ca^{2+} has a minimal effect on the $[Mn_4O_5]$ core structure.[31] Incorporation of alkali metals to Ca^{2+}-depleted OEC reveals a cation size dependence in the $S_1 \rightarrow S_2$ one e^- oxidation step: Li^+ and Na^+ supplemented samples show the multiline EPR signal characteristic of the S_2 state, while K^+, Rb^+, and Cs^+ supplemented samples do not show formation of the S_2 state, suggesting that the redox properties of the OEC are affected by the size of the redox-inactive metal.[41] Notably, turnover is inhibited by substitution of Ca^{2+} with other metal ions with the exception of Sr^{2+},[42] providing opportunities for mechanistic insight through systematic structure-function studies on model complexes. Studies on heterometallic complexes featuring acetate-bridged $[MMn_3O_4]$, $[MMn_3O_2]$, and $[MFe_3O(OH)]$ cores with redox-inactive metal ions M = Ca^{2+}, Sr^{2+}, Zn^{2+}, Y^{3+}, Ln^{3+}, and Sc^{3+} have shown that cluster reduction potentials correlate linearly with the pK_a of the metal aqua ion, with the least acidic Ca^{2+}- and Sr^{2+}-containing clusters in the series having the lowest reduction potentials.[43-47] For the series of $[Ln^{3+}Mn_3O_4]$ complexes, redox potential is also found to correlate linearly with the ionic radii of the lanthanides, with the larger, and therefore less acidic lanthanide-containing clusters having lower reduction potentials. Theoretical studies on the cuboidal $[MMn_3O_4]$ model complexes have validated the correlation between redox potential and the Lewis acidity of the redox-inactive metal ion; however, calculations also suggest that such correlation does not hold for the OEC, which is proposed to respond only to the charge of the redox-inactive metal ion.[48] Mononuclear examples have been reported in which metal ions not only influence redox potential, but also modulate the reactivity of bound oxo or

peroxo moieties.[49-52] However, the well-documented correlation between cation acidity and redox potential in model studies fails to address the cation size dependence in the OEC: larger, less acidic alkali metals inhibit the $S_1 \rightarrow S_2$ oxidation, an observation that directly contradicts our current understanding of the effect of redox inactive metals in tuning redox potentials.

Herein, we report the synthesis, crystal structure, and electrochemical characterization of a series of $[Mn_4O_4]$ and $[YMn_3O_4]$ complexes featuring bridging ligands of different basicity and chelating properties (Figure 1). In the absence of ligand-induced geometric distortions that enforce a contraction of metal-oxo distances, increasing the basicity of the ligands results in a decrease of cluster reduction potential. A small contraction of Y-oxo/Y-Mn distances by 0.1/0.15 Å enforced by a chelating ligand results in an increase of cluster reduction potential even in the presence of strong basic donors. We propose that such small changes in Ca-oxo/Ca-Mn distances may have a similar effect in tuning the redox potential of the OEC. A similar effect may explain the cation size dependence in the $S_1 \rightarrow S_2$ oxidation, whereby the rigid cavity surrounding the OEC may enforce shorter, non-equilibrium metal-oxo distances that increase the reduction potential of the OEC.

4.2) Synthesis, crystal structure, and electrochemistry

To investigate the effect of ligand basicity in modulating cluster reduction potential, $[Mn_4O_4]$ complexes featuring carboxylate and amidate bridging ligands were synthesized (Figure 2). Treatment of the previously reported $LMn_4O_4(OAc)_3$ complex **1-Mn** with a tethered diamidate ligand results in the formation of $LMn_4O_4(diam)(OAc)$ (**3-Mn**).[53] Subsequent treatment of **3-Mn** with *p*-CF_3-benzoic acid results in the formation of $LMn_4O_4(diam)(OBz^{CF3})$ (**2-Mn**).[53] For the series of nearly isostructural complexes **1-**

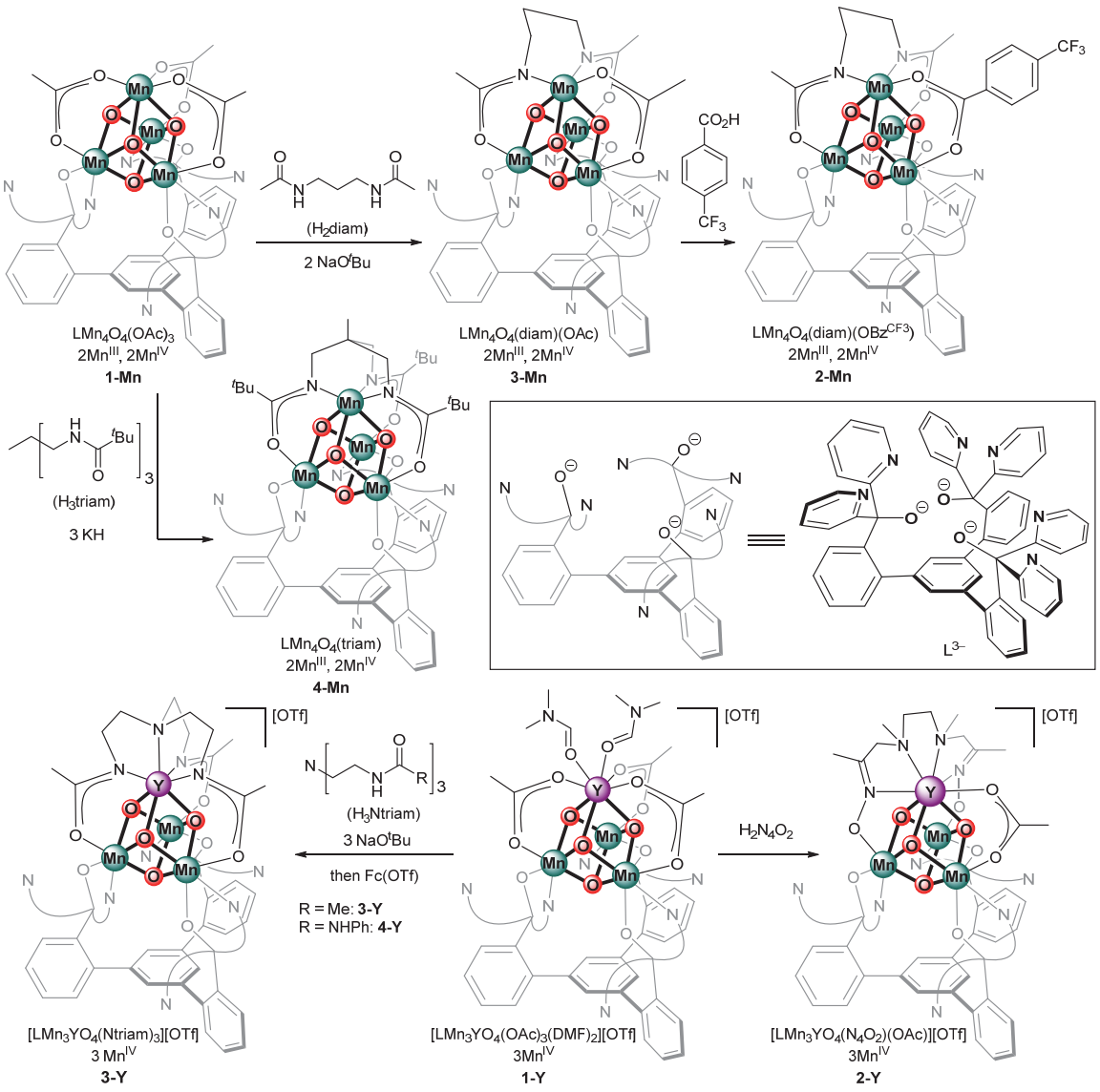

Figure 2. Synthesis of complexes studied in this work.

Mn~3-Mn, electrochemical studies show a redox process assigned to the $[Mn_2^{III}Mn_2^{IV}]/[Mn^{III}Mn_3^{IV}]$ couple at +250, −15, and −150 mV vs Fc/Fc^+, respectively.[44, 53] Toward further decreasing the potential of this redox couple, a triamidate-supported $[Mn_4O_4]$ cluster was targeted. Treatment of 1,1,1-tris(aminomethyl)ethane with pivaloyl chloride results in the formation of the tethered tris-amidate ligand precursor H_3triam (Figure 2). Deprotonation of H_3triam with KH followed by treatment with **1-Mn** results in the formation of LMn_4O_4(triam) (**4-Mn**). The ESI-MS peak at *m*/*z* = 1505 is consistent

with the mass of $[LMn_4O_4(triam)]^+$ (Figure 14). The tethered triamidate serves as a bridging ligand across all three faces of the $[Mn_4O_4]$ cubane, resulting in a pseudo-C_3 symmetric complex (Figure 3). The reversible $[Mn_2^{III}Mn_2^{IV}]/[Mn^{III}Mn_3^{IV}]$ couple is observed at −465 mV vs Fc/Fc^+, representing a shift of 600 mV relative to **1-Mn** (Figure 3). Treatment of **4-Mn** with Ag(OTf) affords the one electron oxidized species $[LMn_4O_4(triam)][OTf]$ (**4-Mn-ox**). In a related series of $[Co_4O_4]$ cuboidal systems, cluster reduction potentials were found to be inversely proportional to the weighted sum of ligand pK_a's (effective basicity) in H_2O.[54] A similar correlation can be obtained for **1-Mn**~**4-Mn** using the pK_a of HOAc (12.6), *p*-CF_3-$C_6H_4CO_2H$ (9.6), and *N*-methylacetamide (25.9) in DMSO, with a slope of −70 mV/pK_a (Figure 1, Table 3), establishing a linear trend between ligand basicity and cluster potential in $[Mn_4O_4]$ complexes.[55-58]

To investigate the effect of ligand basicity in modulating the reduction potential of clusters featuring redox-inactive metals, $[YMn_3O_4]$ complexes supported by different bridging ligands were targeted (Figure 2). Electrochemical studies on $[LYMn_3O_4(OAc)_3]^+$ (**1-Y)** show a redox process at −430 mV vs Fc/Fc^+ assigned to the $[YMn_3^{IV}]/[YMn^{III}Mn_2^{IV}]$

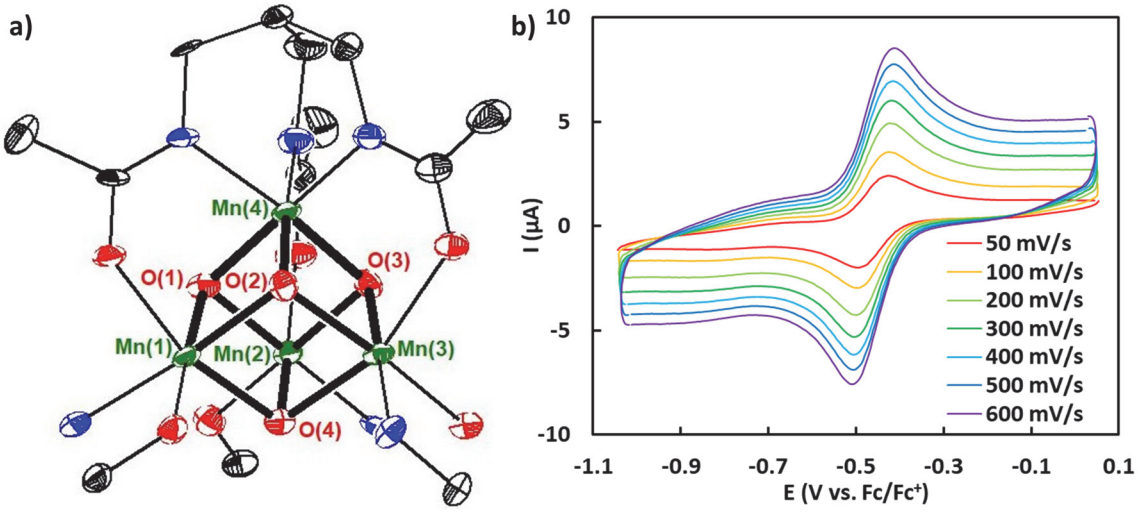

Figure 3. a) Truncated crystal structure of **4-Mn** and b) cyclic voltammogram at various scan rates.

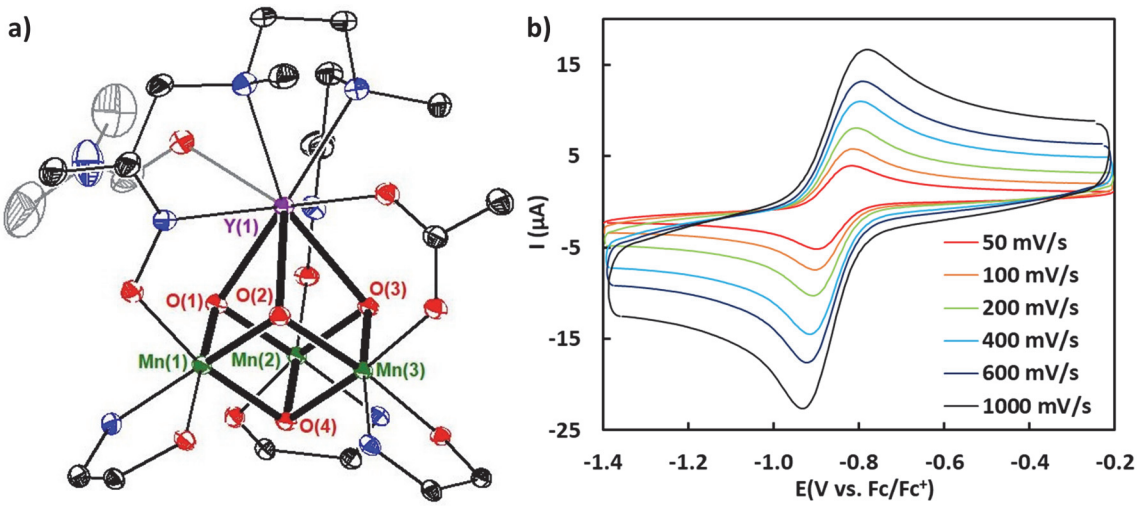

Figure 4. a) Truncated crystal structure of **2-Y** and b) cyclic voltammogram at various scan rates.

couple.[46] Accordingly, treatment of **1-Y** with Cp^*_2Fe results in the formation of the one electron reduced complex **[**$LYMn_3O_4(OAc)_3$**]** (**1-Y-red**).[59] Treatment of **1-Y** with 1 equiv of a chelating bis-oxime proligand ($H_2N_4O_2$) results in the formation of **2-Y** via a protonolysis reaction (Figure 2). The ESI-MS peak at *m*/*z* = 1460 is consistent with the mass of $[LYMn_3O_4(N_4O_2)(OAc)]^+$ (Figure 15), suggesting that two acetate moieties have been substituted by the chelating bis-oximate ligand. The X-ray crystal structure is consistent with the $[LYMn_3O_4(N_4O_2)(OAc)(DMF)][OTf]$ formulation (Figure 4). Despite the pK_a difference of 13 units between acetic acid and acetoxime (pK_a = 25.2)[60] moieties, the reaction is thought to be driven by a kinetic chelate effect. Analogous bis-oximate supported $[CaMn_3O_4]$ and $[GdMn_3O_4]$ complexes have been reported, but their electrochemical properties had not been reported.[61] Electrochemical studies on **2-Y** show a reversible redox process at −860 mV vs Fc/Fc^+ assigned to the $[YMn_3^{IV}]/[YMn^{III}Mn_2^{IV}]$ couple (Figure 4). The bis-oximate ligand decreases the reduction potential of **2-Y** by 430 mV relative to that of **1-Y**, consistent with the increased basicity of the oximate donors compared to acetates. Interestingly, the difference in redox potential between **1-Y** and **2-Y**

is similar to that between **1-Mn** and **3-Mn**, suggesting that a similar trend based on effective ligand basicity may be operative in [YMn_3O_4] complexes.

On the basis of the effective basicity trend, a triamidate-supported [YMn_3O_4] complex was targeted to further decrease the potential of the [YMn_3^{IV}]/[$YMn^{III}Mn_2^{IV}$] couple. Treatment of **1-Y** with 1 equiv of tren-based triacetamide proligand (H_3Ntriam) and 3 equiv of NaO^{t}Bu results in the formation of the amidate-supported, one electron reduced complex **3-Y-red** (Figure 2). The ESI-MS peak at m/z = 1443 is consistent with the mass of [$LYMn_3O_4$(Ntriam)]$^+$ (Figure 16), suggesting that all three acetate moieties have been substituted by the chelating tris-amidate ligand. Through an analogous procedure, treatment of **1-Y** with 1 equiv of tren-based triurea proligand (H_3triurea) results in the formation of the ureate-supported, one electron reduced complex **4-Y-red** (Figure 2). The X-ray crystal structure of **4-Y-red** is consistent with the $LYMn_3O_4$(triurea) formulation. Electrochemical studies on **3-Y-red** show a reversible redox process at −290 mV vs Fc/Fc$^+$ assigned to the [YMn_3^{IV}]/[$YMn^{III}Mn_2^{IV}$] couple (Figure 5). Accordingly, treatment of **3-Y-red** with (Fc)(OTf) leads to the formation of the one electron oxidized complex **3-Y**. The

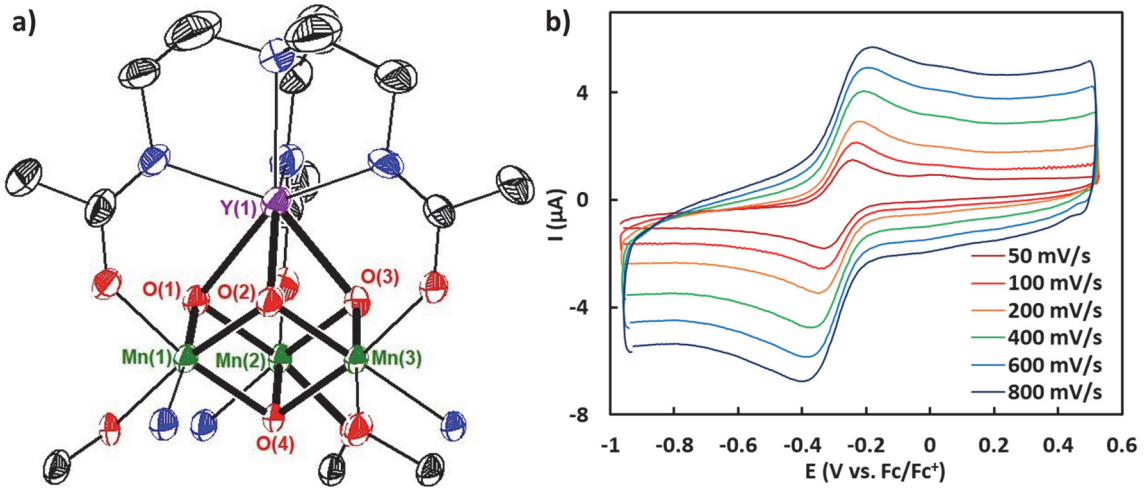

Figure 5. a) Truncated crystal structure of **3-Y** and b) cyclic voltammogram at various scan rates.

X-ray crystal structure of **3-Y** is consistent with the [LYMn$_3$O$_4$(Ntriam)][OTf] formulation (Figure 5). Despite the similarity in pK_a for acetoxime and acetamide moieties, and the increased effective ligand basicity in **3-Y**, the tris-amidate ligand increases the reduction potential of **3-Y** by 140 mV relative to that of **1-Y**, inconsistent with the increased basicity of the amidate donors compared to acetates.

Table 1. Metal-oxo and metal-metal distances (Å) in complexes **1-Y-red**, **1-Y**, **2-Y**, **3-Y**, and **4-Y-red**.

	1-Y-red	**1-Y**	**2-Y**	**3-Y**	**4-Y-red**
Y(1)−O(1)	2.297(3)	2.432(2)	2.308(2)	2.289(4)	2.326(2)
Y(1)−O(2)	2.344(3)	2.335(2)	2.396(2)	2.278(4)	2.273(2)
Y(1)−O(3)	2.306(3)	2.389(2)	2.422(3)	2.289(4)	2.284(2)
Y−O average	2.316(3)	2.385(2)	2.375(2)	2.285(4)	2.294(2)
Y(1)−Mn(1)	3.212(1)	3.239(1)	3.181(1)	3.106(1)	3.123(1)
Y(1)−Mn(2)	3.144(1)	3.298(1)	3.193(1)	3.119(1)	3.137(1)
Y(1)−Mn(3)	3.192(1)	3.213(1)	3.295(1)	3.100(1)	3.133(1)
Y−Mn average	3.183	3.250(1)	3.223(1)	3.108(1)	3.131(1)
Mn(1)−O(1)	1.926(3)	1.840(2)	1.863(3)	1.862(4)	1.843(3)
Mn(1)−O(2)	1.897(3)	1.874(2)	1.882(2)	1.884(4)	1.865(2)
Mn(1)−O(4)	2.205(3)	1.909(2)	1.941(3)	1.926(4)	1.878(2)
Mn(2)−O(1)	1.869(3)	1.875(2)	1.875(3)	1.884(4)	1.876(2)
Mn(2)−O(3)	1.853(3)	1.839(2)	1.849(2)	1.843(4)	1.853(2)
Mn(2)−O(4)	1.854(3)	1.910(2)	1.949(3)	1.923(4)	1.841(3)
Mn(3)−O(2)	1.862(3)	1.844(2)	1.836(3)	1.846(4)	1.919(2)
Mn(3)−O(3)	1.887(3)	1.877(2)	1.869(3)	1.893(4)	1.906(3)
Mn(3)−O(4)	1.857(3)	1.912(2)	1.906(2)	1.921(4)	2.219(2)

To obtain a rationale for the shifts in redox potential observed in complexes **1-Y**~**3-Y**, metal-oxo and metal-metal distances were compared among the series of oxidized and reduced complexes (Table 1). Comparing the reported crystal structures of complexes **1-Y-red** and **1-Y**, a slight contraction of Y-oxo and Y-Mn distances is observed in the reduced analogue.[46, 59] This contraction can be rationalized in terms of the increased basicity of the bridging oxos in the reduced cluster, resulting in the observed Y-oxo/Y-Mn contraction. In addition to charge balance considerations, the unique, elongated Mn(1)−O(4) distance of 2.205(3) Å in **1-Y-red** is consistent with the $Mn^{III}Mn_2^{IV}$ oxidation state assignment.

Comparing the structure of complexes **1-Y** and **2-Y**, the average Y-oxo and Y-Mn distances differ only by about 0.01 Å and 0.03 Å, respectively. The absence of a distinctly elongated Mn-oxo distance in both **1-Y** and **2-Y** is consistent with the Mn_3^{IV} oxidation state assignment. Binding of the bis-oximate ligand does not significantly change the geometry of the $[YMn_3O_4]$ core, and the decrease in reduction potential of **2-Y** relative to that of **1-Y** can be attributed to the increased effective basicity of the ligand framework.

Comparing the structures of complexes **1-Y** and **3-Y**, a more significant contraction in the average Y-oxo and Y-Mn distances is observed in **3-Y**, by about 0.1 Å and 0.15 Å respectively. This contraction in **3-Y** can be attributed to the steric pressure exerted by the chelating tris-amidate ligand framework, resulting in Y-oxo and Y-Mn distances that would otherwise be more comparable to **1-Y** and **2-Y**. Despite the increase in ligand basicity going from acetates to amidates, the closer Y-oxo interactions enforced by the chelating ligand framework increase the reduction potential of **3-Y**, potentially by decreasing the electron density available for the Mn centers at the expense of stronger Y-

oxo interactions. In the series of [Mn_4O_4] complexes **1-Mn**~**4-Mn**, noticeable changes in the [Mn_4O_4] core enforced by the chelating ligand have not been observed.[53] By taking into account only the basicity of the triamidate ligand (N_3triam^{3-}), the reduction potential of **3-Y** would be expected to be in the range of −1000 mV vs Fc/Fc^+, implying that small geometrical changes (0.1/0.15 Å) in the equilibrium Y-oxo/Y-Mn distances may shift the cluster redox potential by ~700 mV. Finally, comparing the structure of the reduced complexes **1-Y-red** and **4-Y-red**, the differences in the average Y-oxo and Y-Mn distances become smaller, to about 0.02 Å and 0.05 Å respectively; the release of steric strain imposed by the chelating ligand framework upon reduction may contribute to the increase in reduction potential.

4.3) Discussion

In summary, a series of [YMn_3O_4] complexes featuring bridging ligands of different basicity and chelating properties have been synthesized and characterized by X-ray crystallography and cyclic voltammetry. In agreement with previous studies, increasing the effective basicity of the ligand framework results in a decrease of cluster reduction potential. A novel mode of tuning cluster reduction potential is reported; ligand-induced distortion of cluster geometry. A small contraction of Y-oxo/Y−Mn distances by 0.1/0.15 Å enforced by the chelating ligand results in an increase of the cluster reduction potential even in the presence of electron donating tris-amidate donors. To the best of our knowledge, such an effect has not been described in heterometallic complexes featuring redox-inactive metals. We propose that within the rigid cavity surrounding the OEC,[31, 62] structural changes that affect Ca-oxo/Ca−Mn distances may have a similar effect in tuning the redox potential of the OEC. Furthermore, our model studies suggest that the cation size

dependence in the $S_1 \rightarrow S_2$ one e^- oxidation in the OEC is the result of redox tuning through a similar steric effect: The rigid cavity surrounding the OEC may enforce shorter, non-equilibrium metal-oxo distances for cations with ionic radii larger than that of Ca^{2+}, resulting in an increase in the reduction potential of the OEC and inhibiting the $S_1 \rightarrow S_2$ transition. While other factors such as the pK_a of the water bound to the redox-inactive metal may affect the slower turnover frequency of the Sr-substituted OEC, a similar size effect may also be in place.[63-64]

4.4) Experimental section

Synthesis of H_3triam: Prepared according to literature[65], the HCl salt of 1,1,1-tris(aminomethyl)ethane (1.5 g, 6.62 mmol, 1 equiv) was suspended in DMF (100 mL) and treated with Et_3N (10 mL). The resulting mixture was cooled to 0 ºC in an ice bath then treated with pivaloyl chloride (5 mL) dropwise. The mixture was warmed to room temperature and stirred for 2 days at room temperature. All volatiles were removed under reduced pressure, and the residue was treated with CH_2Cl_2 and saturated aqueous $NaHCO_3$. The CH_2Cl_2 layer was separated, washed with water, dried over anhydrous $MgSO_4$, and filtered. All volatiles were removed from the filtrate, and the residue was washed with copious amounts of Et_2O. H_3triam was obtained as an off-white powder. Yield: 750 mg, 31 %. ^{1}H NMR (500 MHz, $CDCl_3$): δ 7.09 (t, *J* = 5 Hz, 3H, N*H*), 2.90 (d, *J* = 5 Hz, 6H, C*H*$_2$), 1.24 (s, 27H, −C(C*H*$_3$)$_3$), 0.77 (s, 3H, C*H*$_3$) ppm. ^{13}C NMR (125.7 MHz, $CDCl_3$): 180.12, 42.25, 41.48, 39.04, 27.85, 19.27 ppm. HRMS (FAB+): calculated for $C_{20}H_{40}N_3O_3$: 370.3070; found: 370.3059 [M+H].

Synthesis of **4-Mn**: A solution of H_3triam (265 mg, 0.717 mmol, 1.1 equiv) in THF (200 mL) was treated with KH (300 mg, ~10 equiv) and stirred for 18 hours at room

temperature. Excess KH was removed by filtration, and the filtrate was treated with **1-Mn** (860 mg, 0.653 mmol, 1 equiv). After stirring for 18 hours at room temperature, all volatiles were removed from the crude reaction mixture. The residue was washed with generous amounts of Et_2O and benzene, then redissolved in CH_2Cl_2 and filtered through a pad of Celite. All volatiles were removed from the filtrate. The residue was washed three times with small amounts of MeCN, redissolved in CH_2Cl_2 and filtered through a pad of Celite. Volatiles were removed from the filtrate under reduced pressure, yielding **4-Mn** as a brown powder. Yield: 820 mg, 83 %. Crystals suitable for X-ray crystallography were obtained from slow vapor diffusion of Et_2O into a concentrated solution of **4-Mn** in CH_2Cl_2. ^{1}H NMR (300 MHz, CD_2Cl_2): δ 35.5, 30.0, 17.8, 13.3, 9.7, −5.9 ppm.

Synthesis of **4-Mn-ox**: A solution of **4-Mn** (220 mg, 0.146 mmol, 1 equiv) in THF (10 mL) was treated with a solution of Ag(OTf) (40 mg, 0.155 mmol, 1.05 equiv) in MeCN (3 mL) and stirred for 18 hrs at room temperature. All volatiles were removed from the crude reaction mixture. The residue was washed with generous amounts of Et_2O and ben. The residue was dissolved in CH_2Cl_2 and filtered through a pad of Celite. All volatiles were removed from the filtrate. The residue was washed three times with small amounts of THF, redissolved in CH_2Cl_2 and filtered through a pad of Celite. Volatiles were removed from the filtrate under reduced pressure, yielding **4-Mn-ox** as a brown powder. Yield: 133 mg, 55 %. Crystals suitable for EPR spectroscopy were obtained from slow vapor diffusion of Et_2O into a concentrated solution of **4-Mn-ox** in CH_2Cl_2. ^{1}H NMR (300 MHz, CD_2Cl_2): δ 114.5, 74.6, 13.1, 11.0, −18.5 ppm. Analysis calculated for [LMn_4O_4(triam)](OTf) [$C_{78}H_{75}F_3Mn_4N_9O_{13}S$]: C 56.60, H 4.57, N 7.62; found: C 56.34, H 4.46, N 7.97.

Synthesis of **2-Y**: A solid mixture of **1-Y** (930 mg, 0.565 mmol, 1 equiv) and $H_2N_4O_2$ (143 mg, 0.62 mmol, 1.1 equiv) was treated with THF (18 mL) and stirred at room temperature for 16 hours. The resulting red precipitate was collected, washed with THF until the filtrate was no longer red, dissolved in CH_2Cl_2, and filtered through Celite. Volatiles were removed from the filtrate under reduced pressure, yielding **2-Y** as a red powder. Crystals suitable for X-ray crystallography were obtained from slow vapor diffusion of Et_2O into a concentrated solution of **2-Y** in py (250 mg, 26%). ^{1}H NMR (300 MHz, CD_2Cl_2): δ 68.2, 61.2, 18.6, 17.1, 11.8, 11.0, −17.0, 19.2 ppm. Analysis calculated for [LYMn$_3$O$_4$(N$_4$O$_2$)(OAc)(DMF)](OTf) [$C_{73}H_{69}F_3Mn_3N_{11}O_{15}SY$]: C 52.09, H 4.13, N 9.15; found: C 52.07, H 4.23, N 9.37.

Synthesis of **3-Y-red**: A solid mixture of **1-Y** (420 mg, 0.255 mmol, 1 equiv) and the triacetamide (85 mg, 0.312 mmol, 1.2 equiv) was treated with MeCN (18 mL) and stirred briefly at room temperature. NaO^{t}Bu (81 mg, 0.843 mmol, 3.3 equiv) was added as a solid and the mixture was stirred at room temperature for 16 hours. The resulting orange-brown precipitate was collected, washed with MeCN until the filtrate was no longer brown, dissolved in CH_2Cl_2, and filtered through Celite. Volatiles were removed from the filtrate under reduced pressure, yielding **3-Y-red** as a red powder. (120 mg, 32%). ^{1}H NMR (300 MHz, CD_2Cl_2): δ 24.9, 11.2, 10.2, 9.3, −22.43 ppm.

Synthesis of **3-Y**: A solution of **3-Y-red** (28 mg, 0.019 mmol, 1 equiv) in CH_2Cl_2 (3 mL) was treated with a solution of Fc(OTf) (8 mg, 0.024 mmol, 1.2 equiv) in CH_2Cl_2 (2 mL). The mixture was stirred at room temperature for 16 hours. All volatiles were removed from the resulting red-brown solution, and the residue was washed with Et_2O. The residue was dissolved in cold THF (−30 °C) and filtered through a pad of Celite. Volatiles were

removed from the filtrate under reduced pressure, yielding **3-Y** as a red powder. Yield: 28 mg, 90%. Crystals suitable for X-ray crystallography were obtained from slow vapor diffusion of Et_2O into a concentrated solution of **3-Y** in THF. ^1H NMR (300 MHz, CD_2Cl_2): δ 15.0, 11.5, 9.2, −15.4, −17.2 ppm. Analysis calculated for [$LYMn_3O_4$(Ntriam)](OTf)·CH_2Cl_2 [$C_{71}H_{62}Cl_2F_3Mn_3N_{10}O_{13}SY$]: C 50.85, H 3.73, N 8.35; found: C 50.56, H 4.02, N 8.09.

Synthesis of **4-Y-red**: A solid mixture of **1-Y** (250 mg, 0.152 mmol, 1 equiv) and the triurea (77 mg, 0.168 mmol, 1.1 equiv) was treated with MeCN (18 mL) and stirred briefly at room temperature. NaO^{t}Bu (48 mg, 0.5 mmol, 3.3 equiv) was added as a solid and the mixture was stirred at room temperature for 16 hours. The resulting orange-brown precipitate was collected, washed with MeCN until the filtrate was no longer brown, dissolved in THF, and filtered through Celite. Volatiles were removed from the filtrate under reduced pressure, yielding **4** as a red powder. (100 mg, 39%). Crystals suitable for X-ray crystallography were obtained from slow vapor diffusion of Et_2O into a concentrated solution of **4** in THF. Analysis calculated for [$LYMn_3O_4$(triurea)] [$C_{84}H_{69}Mn_3N_{13}O_{10}Y$]: C 60.26, H 4.15, N 10.88; found: C 60.00, H 4.21, N 10.59.

Table 2. Crystal and refinement data for complexes **4-Mn**, **2-Y**, and **3-Y**.

Compound	**4-Mn**	**2-Y**	**3-Y**
CCDC	1897119	1897117	1897118
Empirical formula	$C_{81}H_{85}Mn_4N_9O_{12}$	$C_{92.48}H_{88.48}F_3Mn_3N_{14.9}O_{15}SY$	$C_{82}H_{60}F_3Mn_3N_{10}O_{16}SY$
Formula weight	1596.33	1991.34	1784.19
Temperature/K	100.0	100.0	99.99
Crystal system	triclinic	triclinic	monoclinic
Space group	P-1	P-1	C2/c
a/Å	12.1663(5)	13.9021(6)	25.8213(17)
b/Å	15.8988(7)	16.1176(7)	17.6106(12)
c/Å	21.2417(10)	21.2112(8)	35.578(2)
α/°	85.786(3)	87.635(3)	90
β/°	85.114(3)	77.947(3)	103.105(2)
γ/°	72.129(2)	83.333(3)	90
Volume/Å^3	3891.5(3)	4615.8(3)	15757.0(18)
Z	2	2	8
ρ_{calc}g/cm^3	1.362	1.433	1.504
μ/mm^{-1}	5.702	4.943	1.307
F(000)	1660.0	2049.0	7256.0
Crystal size/mm^3	0.5 × 0.5 × 0.1	0.1 × 0.1 × 0.05	0.1 × 0.1 × 0.1
Radiation	CuKα (λ = 1.54178)	CuKα (λ = 1.54178)	MoKα (λ = 0.71073)
2Θ range for data collection/°	5.848 to 150.194	7.034 to 149.336	4.412 to 54.95
Index ranges	-15 ≤ h ≤ 15, -19 ≤ k ≤ 19, 0 ≤ l ≤ 26	-17 ≤ h ≤ 17, -20 ≤ k ≤ 20, -26 ≤ l ≤ 26	-33 ≤ h ≤ 33, -22 ≤ k ≤ 22, -46 ≤ l ≤ 45
Reflections collected	13231	101142	125697
Independent reflections	13231 [R_{int} = merged, R_{sigma} = 0.0974]	18768 [R_{int} = 0.0560, R_{sigma} = 0.0428]	18015 [R_{int} = 0.0634, R_{sigma} = 0.0390]
Data/restraints/parameters	13231/2139/943	18768/0/1065	18015/49/942
Goodness-of-fit on F^2	1.072	1.055	1.061
Final R indexes [I>=2σ (I)]	R_1 = 0.1746, wR_2 = 0.4017	R_1 = 0.0624, wR_2 = 0.1781	R_1 = 0.0905, wR_2 = 0.2546
Final R indexes [all data]	R_1 = 0.2030, wR_2 = 0.4246	R_1 = 0.0695, wR_2 = 0.1842	R_1 = 0.1204, wR_2 = 0.2849
Largest diff. peak/hole / e Å^{-3}	3.46/-1.42	1.99/-2.23	3.20/-1.12

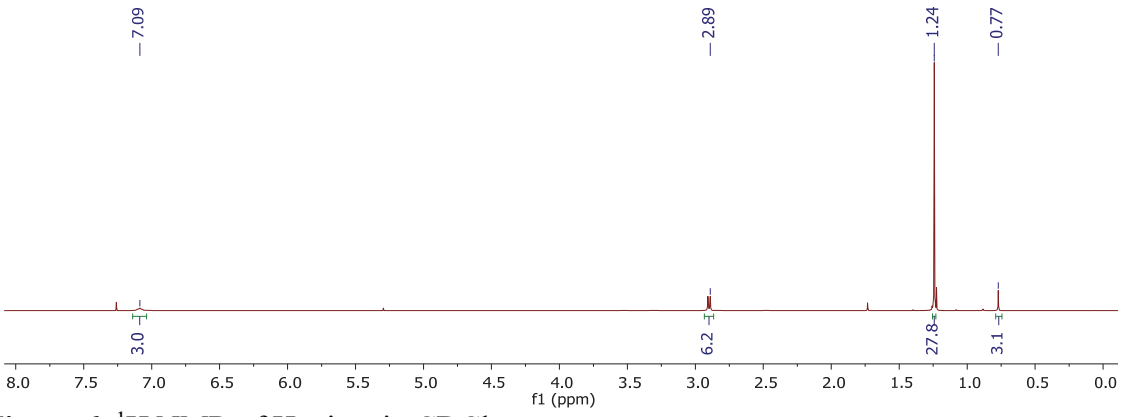

Figure 6. ^{1}H NMR of H_3triam in $CDCl_3$.

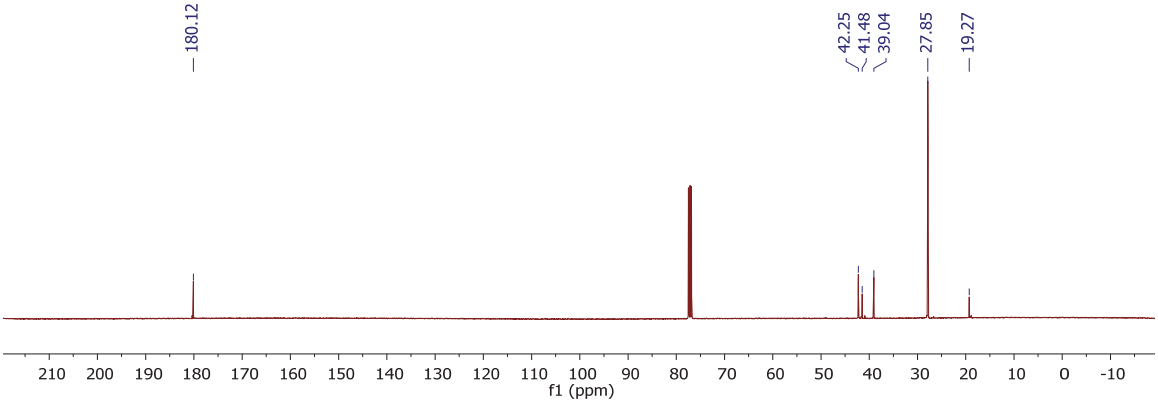

Figure 7. ^{13}C NMR of H_3triam in $CDCl_3$.

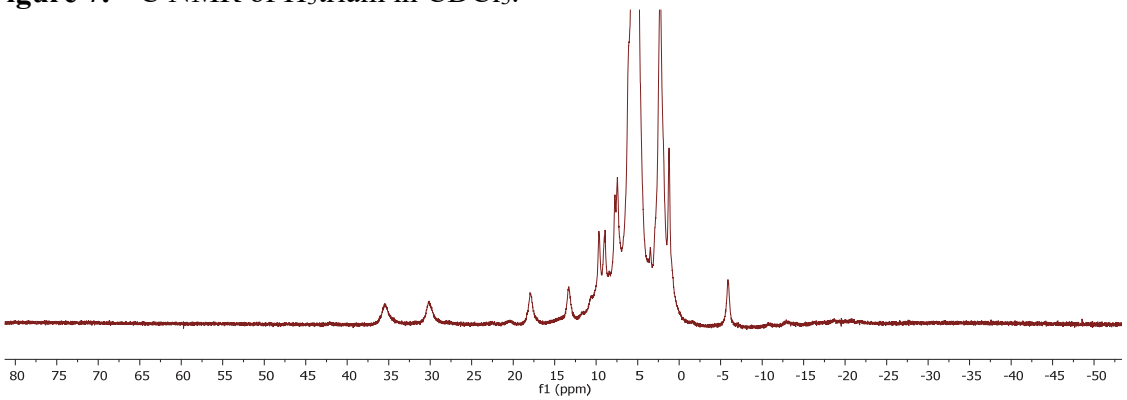

Figure 8. ^{1}H NMR of **4-Mn** in CD_2Cl_2.

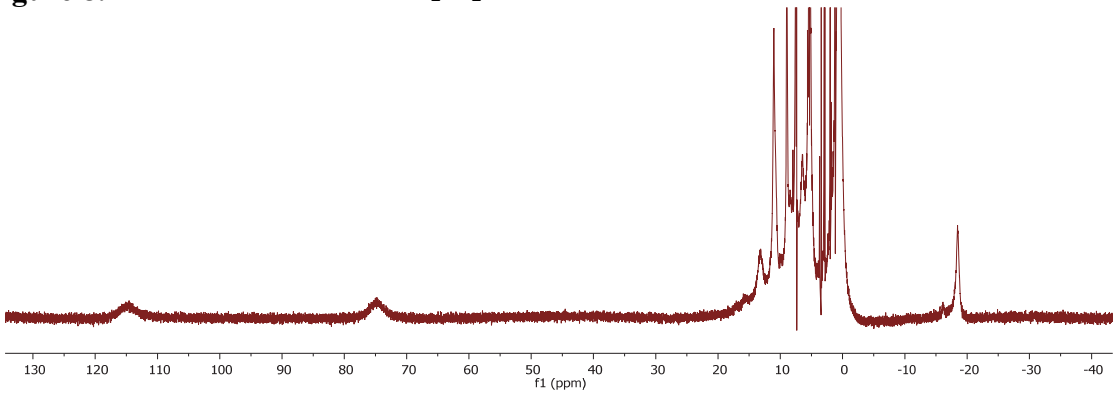

Figure 9. ^{1}H NMR of **4-Mn-ox** in CD_2Cl_2.

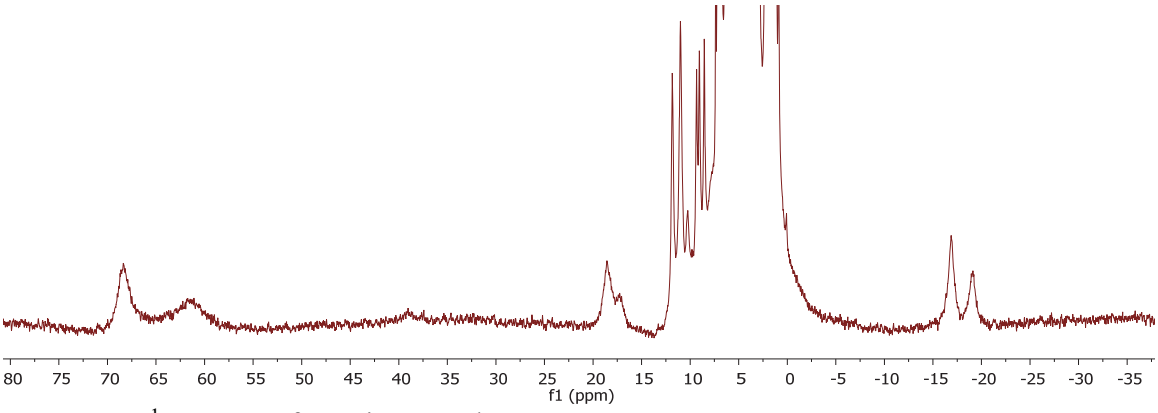

Figure 10. ^{1}H NMR of **2-Y** in CD_2Cl_2.

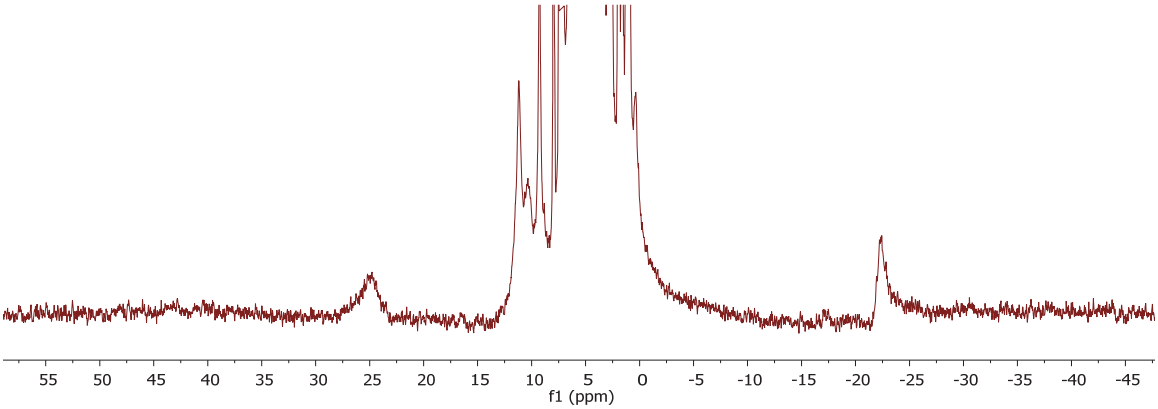

Figure 11. ^{1}H NMR of **3-Y-red** in CD_2Cl_2.

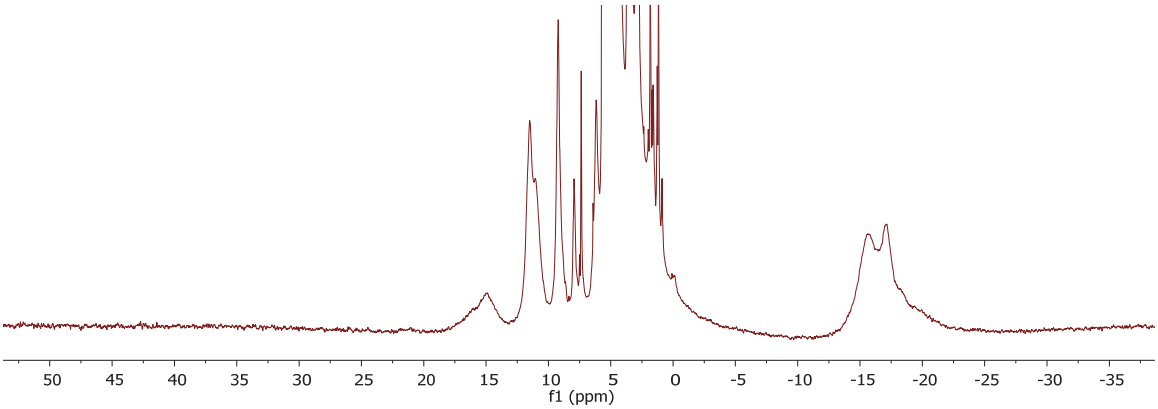

Figure 12. ^{1}H NMR of **3-Y** in CD_2Cl_2.

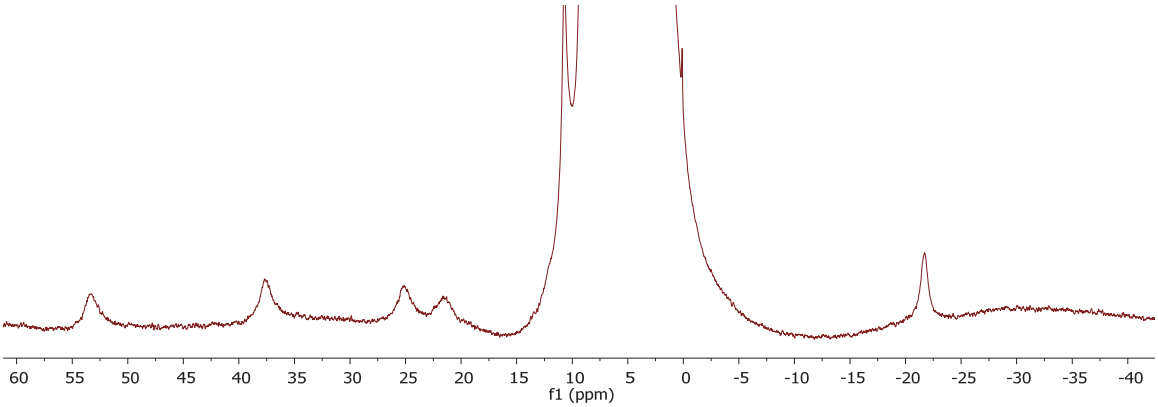

Figure 13. ^{1}H NMR of **4-Y-red** in CD_2Cl_2.

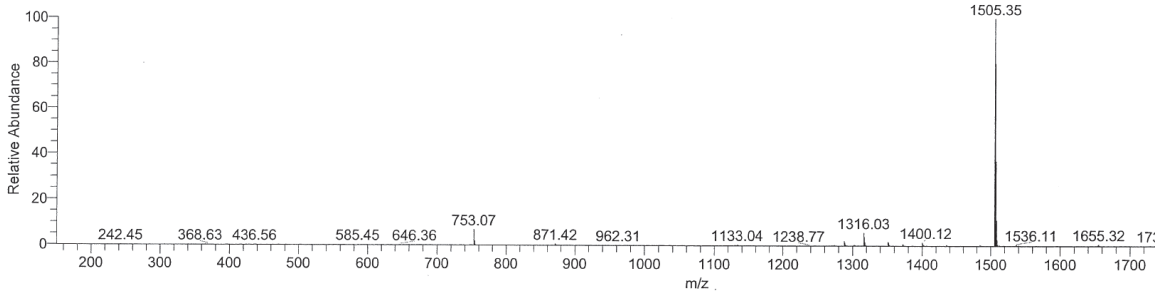

Figure 14. ESI-MS of **4-Mn**. *m*/*z* = 1505 consistent with $[LMn_4O_4(triam)]^+$.

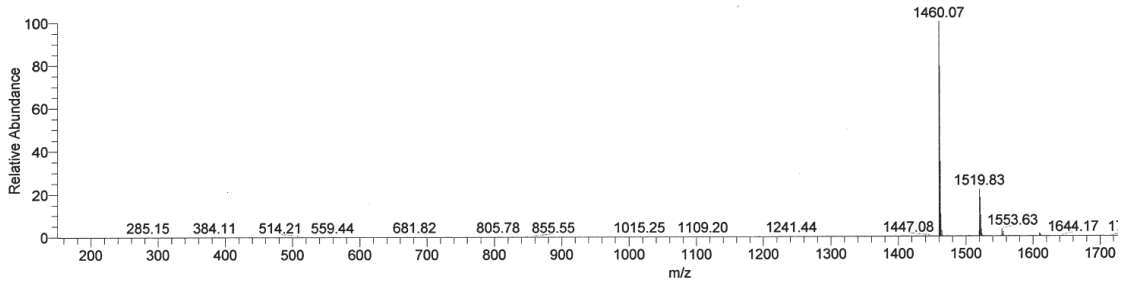

Figure 15. ESI-MS of **2-Y**. *m*/*z* = 1460 consistent with $[LYMn_3O_4(N_4O_2)(OAc)]^+$.

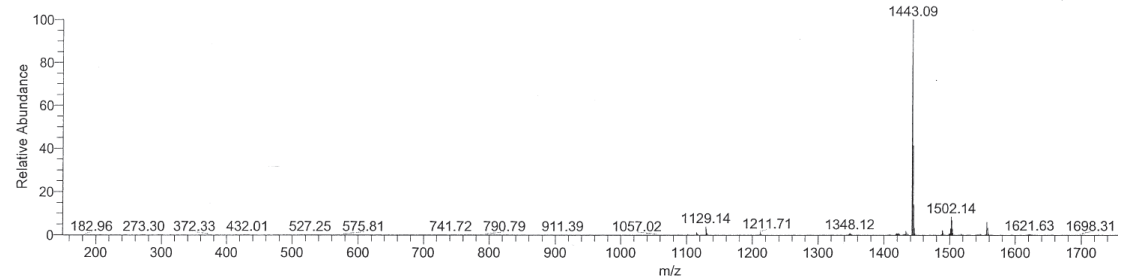

Figure 16. ESI-MS of **3-Y**. *m*/*z* = 1443 consistent with $[LYMn_3O_4(triam)]^+$.

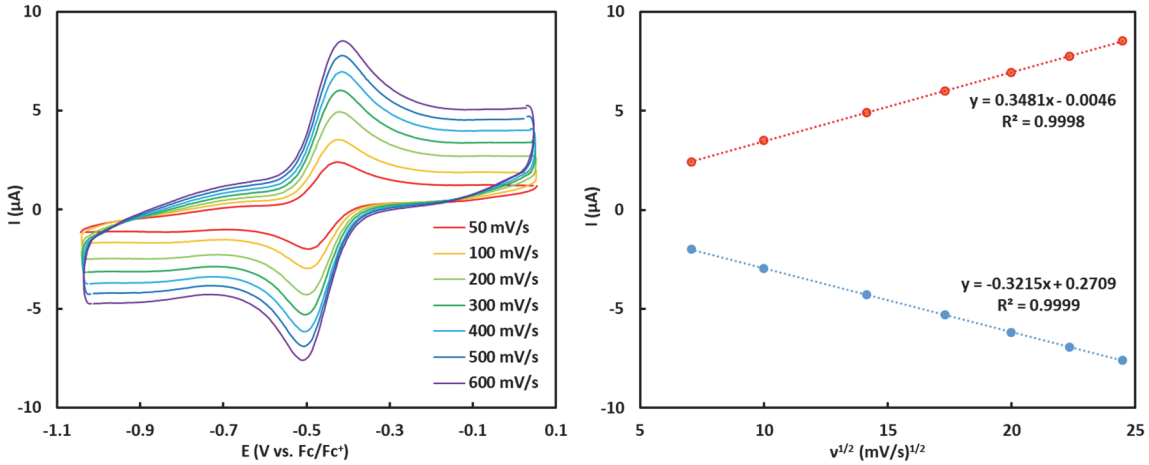

Figure 17. Cyclic voltammogram of **4-Mn** at various scan rates and plot of peak current vs. square root of scan rate.

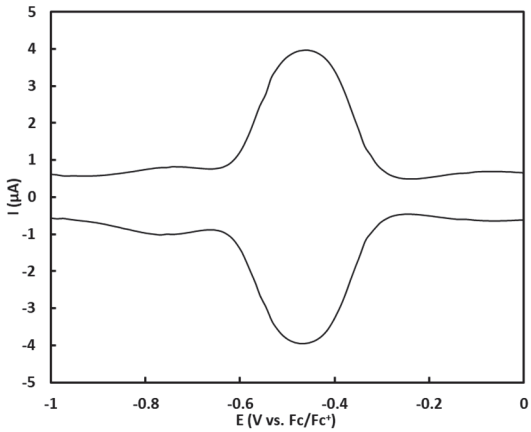

Figure 18. Square-wave voltammogram of **4-Mn**.

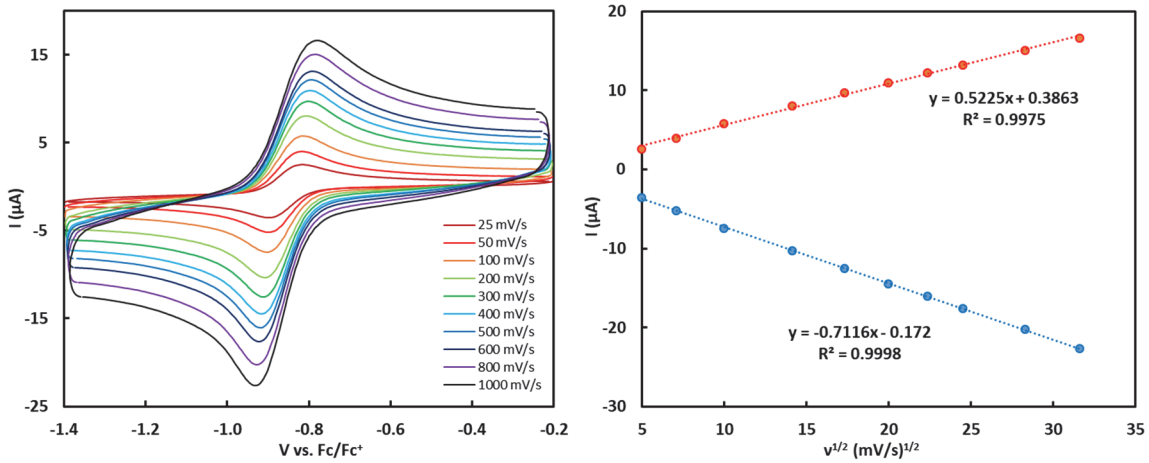

Figure 19. Cyclic voltammogram of **2-Y** at various scan rates and plot of peak current vs. square root of scan rate.

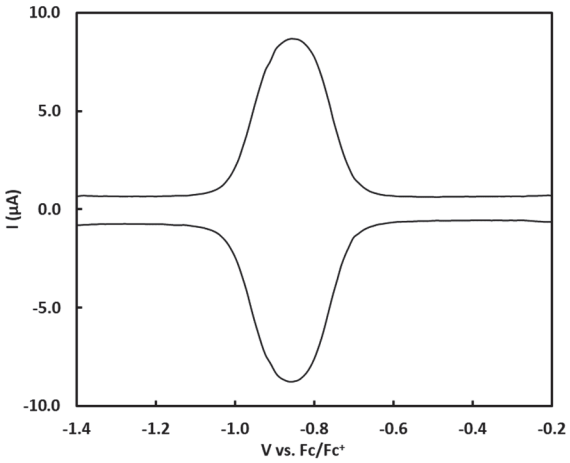

Figure 20. Square-wave voltammogram of **2-Y**.

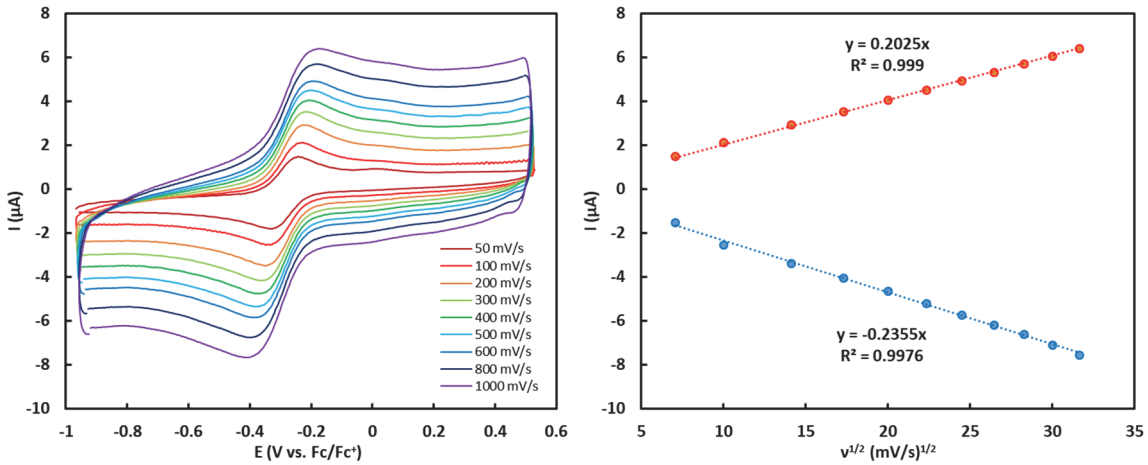

Figure 21. Cyclic voltammogram of **3-Y** at various scan rates and plot of peak current vs. square root of scan rate.

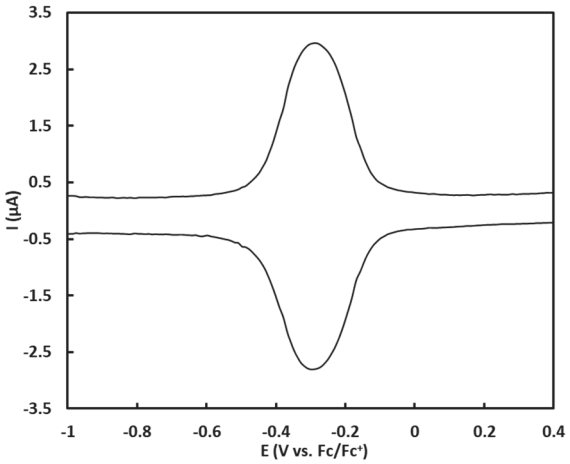

Figure 22. Square-wave voltammogram of **3-Y**.

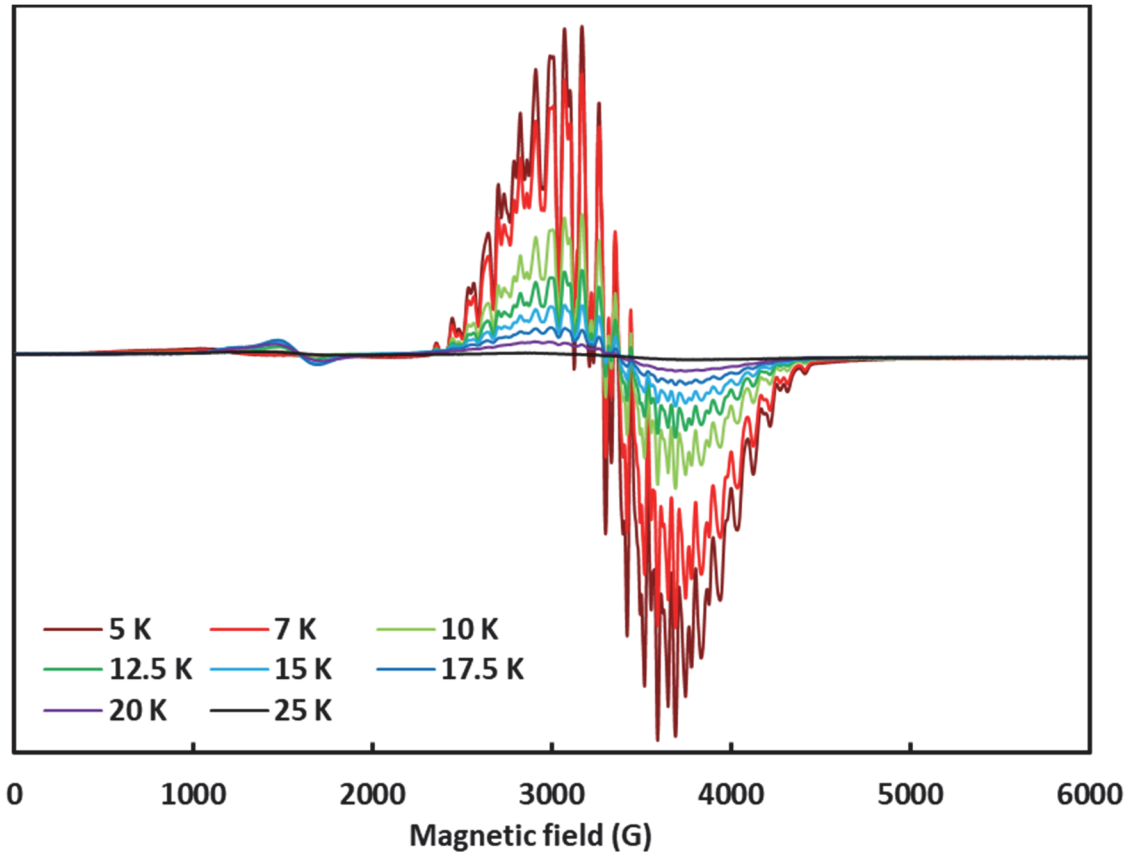

Figure 23. X-band CW-EPR of **4-Mn-ox**. Data acquisition parameters: frequency = 9.366 MHz, power = 2 mW, conversion time = 20.48 ms, modulation amplitude = 8 G. The variable-temperature behavior of **4-Mn-ox** is reminiscent of a reported complex $[LMn^{III}Mn_3^{IV}O_4(diamidate)(OAc)]^+$ (Chapter 3).

Table 3. Values of ligand pK_a in DMSO, effective basicity, and cluster redox potential.

Complex	Ligand 1	Ligand 2	pKa ligand 1	pKa ligand 2	Effective basicity	Redox potential (V vs. Fc/Fc^+)
1-Mn	Acetate		12.6	-	9.45	250
2-Mn	Acetamide	CF_3-benzoate	25.9		15.35	−15
3-Mn	Acetamide	Acetate	25.9	12.6	16.1	−150
4-Mn	Acetamide		25.9	-	19.42	−465
1-Y	Acetate		12.6	-	9.45	−430
2-Y	Acetoxime	Acetate	25.2	12.6	15.75	−860

4.5) References

(1) Gray, H. B.; Winkler, J. R., *Annu. Rev. Biochem.* **1996**, *65*, 537.
(2) Moser, C. C.; Keske, J. M.; Warncke, K.; Farid, R. S.; Dutton, P. L., *Nature* **1992**, *355*, 796.
(3) Solomon, E. I.; Heppner, D. E.; Johnston, E. M.; Ginsbach, J. W.; Cirera, J.; Qayyum, M.; Kieber-Emmons, M. T.; Kjaergaard, C. H.; Hadt, R. G.; Tian, L., *Chem. Rev.* **2014**, *114*, 3659.
(4) Liu, J.; Chakraborty, S.; Hosseinzadeh, P.; Yu, Y.; Tian, S.; Petrik, I.; Bhagi, A.; Lu, Y., *Chem. Rev.* **2014**, *114*, 4366.
(5) Dennison, C., *Coord. Chem. Rev.* **2005**, *249*, 3025.
(6) Dawson, J. H., *Science* **1988**, *240*, 433.
(7) Hosseinzadeh, P.; Lu, Y., *Biochim. Biophys. Acta - Bioenerg.* **2016**, *1857*, 557.
(8) Xiong, P.; Nocek, J. M.; Vura-Weis, J.; Lockard, J. V.; Wasielewski, M. R.; Hoffman, B. M., *Science* **2010**, *330*, 1075.
(9) Cowan, J. A.; Lui, S. M., Structure-Function Correlations in High-Potential Iron Proteins. In *Advances in Inorganic Chemistry*, Sykes, A. G., Ed. Academic Press: 1998; Vol. 45, pp 313.
(10) Dauter, Z.; Wilson, K. S.; Sieker, L. C.; Meyer, J.; Moulis, J.-M., *Biochemistry* **1997**, *36*, 16065.
(11) Langen, R.; Jensen, G. M.; Jacob, U.; Stephens, P. J.; Warshel, A., *J. Biol. Chem.* **1992**, *267*, 25625.
(12) Backes, G.; Mino, Y.; Loehr, T. M.; Meyer, T. E.; Cusanovich, M. A.; Sweeney, W. V.; Adman, E. T.; Sanders-Loehr, J., *J. Am. Chem. Soc.* **1991**, *113*, 2055.
(13) Garner, D. K.; Vaughan, M. D.; Hwang, H. J.; Savelieff, M. G.; Berry, S. M.; Honek, J. F.; Lu, Y., *J. Am. Chem. Soc.* **2006**, *128*, 15608.
(14) Hay, S.; Wydrzynski, T., *Biochemistry* **2005**, *44*, 431.
(15) Springs, S. L.; Bass, S. E.; McLendon, G. L., *Biochemistry* **2000**, *39*, 6075.
(16) Kowal, A. T.; Werth, M. T.; Manodori, A.; Cecchini, G.; Schroeder, I.; Gunsalus, R. P.; Johnson, M. K., *Biochemistry* **1995**, *34*, 12284.
(17) Werth, M. T.; Cecchini, G.; Manodori, A.; Ackrell, B. A.; Schröder, I.; Gunsalus, R. P.; Johnson, M. K., *Proc. Nat. Acad. Sci.* **1990**, *87*, 8965.
(18) Birrell, J. A.; Laurich, C.; Reijerse, E. J.; Ogata, H.; Lubitz, W., *Biochemistry* **2016**, *55*, 4344.
(19) Hadt, R. G.; Sun, N.; Marshall, N. M.; Hodgson, K. O.; Hedman, B.; Lu, Y.; Solomon, E. I., *J. Am. Chem. Soc.* **2012**, *134*, 16701.
(20) Dey, A.; Jenney, F. E.; Adams, M. W. W.; Babini, E.; Takahashi, Y.; Fukuyama, K.; Hodgson, K. O.; Hedman, B.; Solomon, E. I., *Science* **2007**, *318*, 1464.
(21) Low, D. W.; Hill, M. G., *J. Am. Chem. Soc.* **2000**, *122*, 11039.
(22) Tezcan, F. A.; Winkler, J. R.; Gray, H. B., *J. Am. Chem. Soc.* **1998**, *120*, 13383.
(23) Brinkert, K.; De Causmaecker, S.; Krieger-Liszkay, A.; Fantuzzi, A.; Rutherford, A. W., *Proc. Nat. Acad. Sci.* **2016**, *113*, 12144.
(24) Pantazis, D. A., *ACS Catal.* **2018**, 9477.
(25) Shen, J.-R., *Annu. Rev. Plant Biol.* **2015**, *66*, 23.
(26) Yano, J.; Yachandra, V., *Chem. Rev.* **2014**, *114*, 4175.
(27) Cox, N.; Pantazis, D. A.; Neese, F.; Lubitz, W., *Acc. Chem. Res.* **2013**, *46*, 1588.

(28) Cox, N.; Retegan, M.; Neese, F.; Pantazis, D. A.; Boussac, A.; Lubitz, W., *Science* **2014**, *345*, 804.
(29) Kulik, L. V.; Epel, B.; Lubitz, W.; Messinger, J., *J. Am. Chem. Soc.* **2007**, *129*, 13421.
(30) Lee, C.-I.; Lakshmi, K. V.; Brudvig, G. W., *Biochemistry* **2007**, *46*, 3211.
(31) Lohmiller, T.; Shelby, M. L.; Long, X.; Yachandra, V. K.; Yano, J., *J. Phys. Chem. B* **2015**, *119*, 13742.
(32) Miqyass, M.; Marosvölgyi, M. A.; Nagel, Z.; Yocum, C. F.; van Gorkom, H. J., *Biochemistry* **2008**, *47*, 7915.
(33) Pantazis, D. A.; Ames, W.; Cox, N.; Lubitz, W.; Neese, F., *Angew. Chem. Int. Ed.* **2012**, *51*, 9935.
(34) Peloquin, J. M.; Campbell, K. A.; Randall, D. W.; Evanchik, M. A.; Pecoraro, V. L.; Armstrong, W. H.; Britt, R. D., *J. Am. Chem. Soc.* **2000**, *122*, 10926.
(35) Vrettos, J. S.; Stone, D. A.; Brudvig, G. W., *Biochemistry* **2001**, *40*, 7937.
(36) Siegbahn, P. E. M., *Acc. Chem. Res.* **2009**, *42*, 1871.
(37) Siegbahn, P. E. M.; Crabtree, R. H., *J. Am. Chem. Soc.* **1999**, *121*, 117.
(38) Mukherjee, S.; Stull, J. A.; Yano, J.; Stamatatos, T. C.; Pringouri, K.; Stich, T. A.; Abboud, K. A.; Britt, R. D.; Yachandra, V. K.; Christou, G., *Proc. Nat. Acad. Sci.* **2012**, *109*, 2257.
(39) Tsui, E. Y.; Kanady, J. S.; Agapie, T., *Inorg. Chem.* **2013**, *52*, 13833.
(40) Zhang, C.; Chen, C.; Dong, H.; Shen, J.-R.; Dau, H.; Zhao, J., *Science* **2015**, *348*, 690.
(41) Ono, T.-a.; Rompel, A.; Mino, H.; Chiba, N., *Biophysical Journal* **2001**, *81*, 1831.
(42) Boussac, A.; Rutherford, A. W., *Biochemistry* **1988**, *27*, 3476.
(43) Herbert, D. E.; Lionetti, D.; Rittle, J.; Agapie, T., *J. Am. Chem. Soc.* **2013**, *135*, 19075.
(44) Kanady, J. S.; Tsui, E. Y.; Day, M. W.; Agapie, T., *Science* **2011**, *333*, 733.
(45) Lin, P.-H.; Takase, M. K.; Agapie, T., *Inorg. Chem.* **2015**, *54*, 59.
(46) Tsui, E. Y.; Agapie, T., *Proc. Nat. Acad. Sci.* **2013**, *110*, 10084.
(47) Tsui, E. Y.; Tran, R.; Yano, J.; Agapie, T., *Nat. Chem.* **2013**, *5*, 293.
(48) Krewald, V.; Neese, F.; Pantazis, D. A., *Phys. Chem. Chem. Phys.* **2016**, *18*, 10739.
(49) Bang, S.; Lee, Y.-M.; Hong, S.; Cho, K.-B.; Nishida, Y.; Seo, M. S.; Sarangi, R.; Fukuzumi, S.; Nam, W., *Nat. Chem.* **2014**, *6*, 934.
(50) Chantarojsiri, T.; Reath, A. H.; Yang, J. Y., *Angew. Chem. Int. Ed.* **2018**, *57*, 14037.
(51) Park, Y. J.; Ziller, J. W.; Borovik, A. S., *J. Am. Chem. Soc.* **2011**, *133*, 9258.
(52) Reath, A. H.; Ziller, J. W.; Tsay, C.; Ryan, A. J.; Yang, J. Y., *Inorg. Chem.* **2017**, *56*, 3713.
(53) Lee, H. B.; Shiau, A. A.; Oyala, P. H.; Marchiori, D. A.; Gul, S.; Chatterjee, R.; Yano, J.; Britt, R. D.; Agapie, T., *J. Am. Chem. Soc.* **2018**, *140*, 17175.
(54) Nguyen, A. I.; Wang, J.; Levine, D. S.; Ziegler, M. S.; Tilley, T. D., *Chem. Sci.* **2017**, *8*, 4274.
(55) Bordwell, F. G.; Algrim, D., *J. Org. Chem.* **1976**, *41*, 2507.
(56) Hansch, C.; Leo, A.; Taft, R. W., *Chem. Rev.* **1991**, *91*, 165.
(57) Kütt, A.; Leito, I.; Kaljurand, I.; Sooväli, L.; Vlasov, V. M.; Yagupolskii, L. M.; Koppel, I. A., *J. Org. Chem.* **2006**, *71*, 2829.
(58) Bordwell, F. G.; Harrelson, J. A.; Lynch, T. Y., *J. Org. Chem.* **1990**, *55*, 3337.
(59) Lin, P.-H.; Tsui, E. Y.; Habib, F.; Murugesu, M.; Agapie, T., *Inorg. Chem.* **2016**, *55*, 6095.

(60) Bordwell, F. G.; Ji, G. Z., *J. Org. Chem.* **1992**, *57*, 3019.
(61) Kanady, J. S.; Lin, P.-H.; Carsch, K. M.; Nielsen, R. J.; Takase, M. K.; Goddard, W. A.; Agapie, T., *J. Am. Chem. Soc.* **2014**, *136*, 14373.
(62) Davis, K. M.; Pushkar, Y. N., *J. Phys. Chem. B* **2015**, *119*, 3492.
(63) Koua, F. H. M.; Umena, Y.; Kawakami, K.; Shen, J.-R., *Proc. Nat. Acad. Sci.* **2013**, *110*, 3889.
(64) Boussac, A.; Ugur, I.; Marion, A.; Sugiura, M.; Kaila, V. R. I.; Rutherford, A. W., *Biochim. Biophys. Acta - Bioenerg.* **2018**, *1859*, 342.
(65) Qin, C.-J.; James, L.; Chartres, J. D.; Alcock, L. J.; Davis, K. J.; Willis, A. C.; Sargeson, A. M.; Bernhardt, P. V.; Ralph, S. F., *Inorg. Chem.* **2011**, *50*, 9131.

CHAPTER 5

$CaMn_3^{IV}O_4$ Cubane Models of the Biological Oxygen Evolving Complex: Desymmetrization and Oxo Protonation Lead to $S < 9/2$

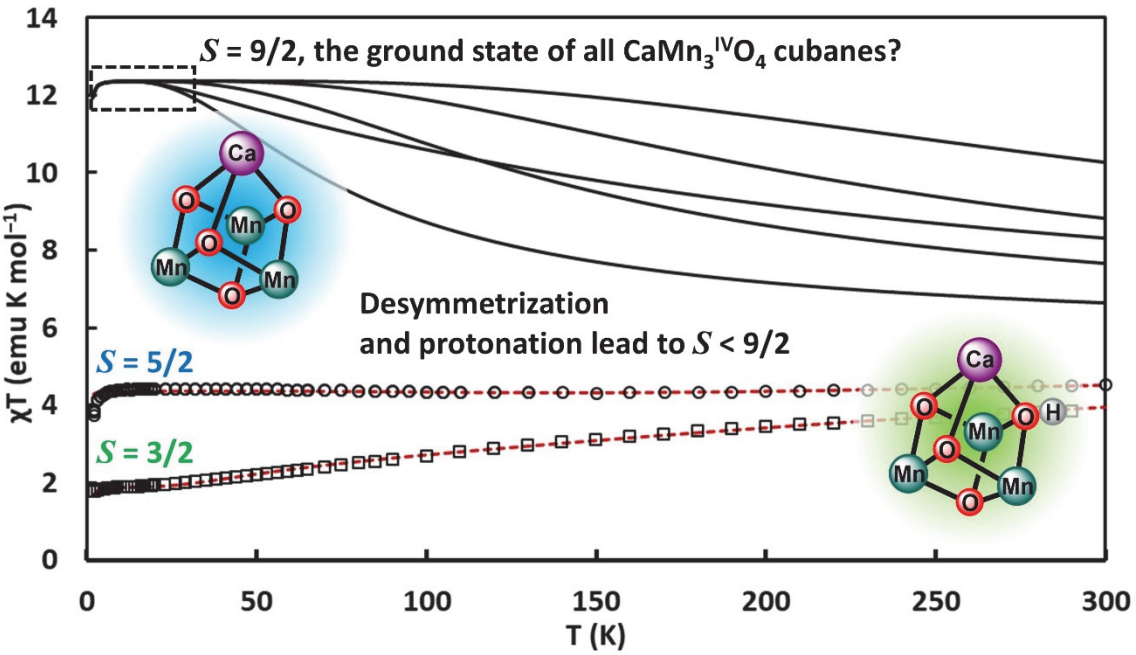

Abstract

Biological water oxidation is catalyzed at the oxygen evolving complex (OEC) of Photosystem II featuring a $CaMn_4O_5$ core. Mechanistic proposals are guided by spectroscopic characterization of intermediates such as the S_2 and S_3 states. On the basis of the spin ground state of such intermediates, a $CaMn_3^{IV}O_4$ cuboidal subunit of ferromagnetically coupled Mn^{IV} centers has been proposed. Herein, we report the synthesis, crystal structure, XAS, magnetic susceptibility, and multifrequency EPR data for a series of $MMn_3^{IV}O_4$ ($M = Ca^{II}$, Y^{III}) complexes as structural and spectroscopic models of the cuboidal subunit of the OEC. The effect of systematic changes in cluster geometry, heterometal identity, and bridging oxo protonation on cluster spin state structure was investigated. Importantly, the spin ground state of $CaMn_3^{IV}O_n(OH)_{(4-n)}$ (n = 0~4) complexes need not necessarily be $S = 9/2$ as previously reported. Desymmetrization and slight geometrical changes in the previously reported *pseudo*-C_3 symmetric $MMn_3^{IV}O_4$ complexes with an $S = 9/2$ ground state lead to a lower, $S = 5/2$ ground state. Protonation of a single bridging oxo moiety has a strong influence in attenuating the magnitude of the magnetic exchange coupling interactions, and an $S = 3/2$ ground state is observed in $CaMn_3^{IV}O_3(OH)$. Removal of the heterometal leads to a *pseudo*-C_3 symmetric $Mn_3^{IV}O_4$ complex with an $S = 3/2$ ground state, suggesting that geometric considerations are not sufficient for the deduction of the nature of magnetic exchange coupling interactions. Our model studies suggest that the magnetic properties of the OEC may also react very sensitively to small changes in structure; the protonation state of the bridging oxo moieties and the magnetic coupling scheme within the $CaMn_3^{IV}O_4$ cuboidal subunit in the OEC need to be carefully assessed.

5.1) Introduction

Biological water oxidation is catalyzed at the oxygen evolving complex (OEC) of Photosystem II (PSII).[1-3] The active site of the OEC has been characterized crystallographically, revealing a heterometallic $CaMn_3O_4$ cubane motif binding to a fourth Mn center via bridging oxo moieties.[4-7] Mechanistic studies have been performed within the context of the Joliot-Kok cycle of S_n (n = 0~4) states,[8-9] with the Mn oxidation states of the dark-stable S_1 state corresponding to $Mn_2^{III}Mn_2^{IV}$.[10] Light-induced one electron oxidation leads to the formation of the S_2 state, and numerous mechanistic studies have been performed to better understand the (electronic)structure of the S_2 state and the requirements needed to advance to the more oxidized S_3 state.[11-26] In the absence of direct and unambiguous structural data concerning the O–O bond forming S_4 intermediate,

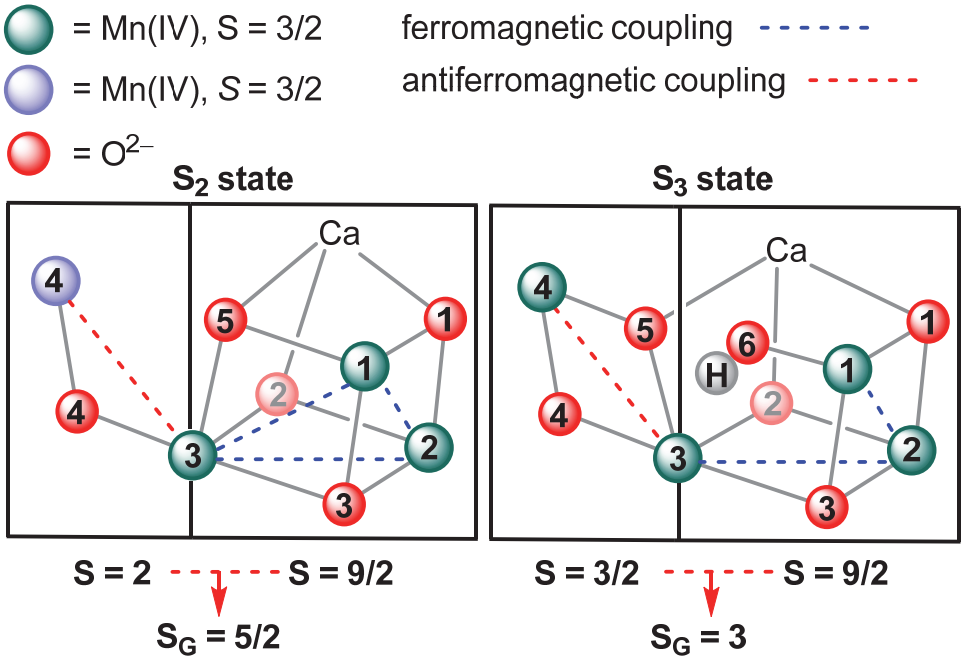

Figure 1. Proposed structures of the inorganic $CaMn_4O_5$ core of the OEC in the S_2 and S_3 states. Overall ferromagnetic coupling between the Mn centers within the $CaMn_3^{IV}O_4$ subsite has been proposed, leading to S = 9/2. Antiferromagnetic coupling to the dangling Mn leads to the observed spin ground states S_G = 5/2 and S_G = 3 for S_2 and S_3 respectively. Nature of the computed magnetic exchange coupling interactions shown in red (antiferromagnetic) and blue (ferromagnetic) dashed lines.

spectroscopic characterization of lower S_n state intermediates heavily influence mechanistic proposals for O−O bond formation.[27-30]

Connected to oxidation state changes and possible structural differences, each of the S_n state intermediates adopts a unique electronic structure with a characteristic spin ground state:[31] $S(S_0) = 1/2$,[19] $S(S_1) = 0$,[32] $S(S_2) = 1/2$ or $5/2$,[33-35] $S(S_3) = 3$.[16, 36] The interconversion between the $S = 1/2$ and $S = 5/2$ forms of the S_2 state (Mn oxidation states $Mn^{III}Mn_3^{IV}$) is particularly interesting:[34] supported with computed values of magnetic exchange coupling constants (J_{ij}) between adjacent Mn centers, structural differences have been proposed to lead to changes in the magnetic coupling interactions in the OEC, resulting in different spin ground states.[22] In the so-called "closed-cubane" structure with the $S = 5/2$ ground state, ferromagnetic coupling between Mn(1), Mn(2), and Mn(3) is proposed to lead to an $S = 9/2$ spin state for the $CaMn_3^{IV}O_4$ cuboidal subsite; antiferromagnetic coupling to the dangling Mn(4) would lead to the observed $S = 5/2$ ground state (Figure 1). In the "open-cubane" structure, an internal valence redistribution is proposed, with the $CaMn^{III}Mn_2^{IV}O_4$

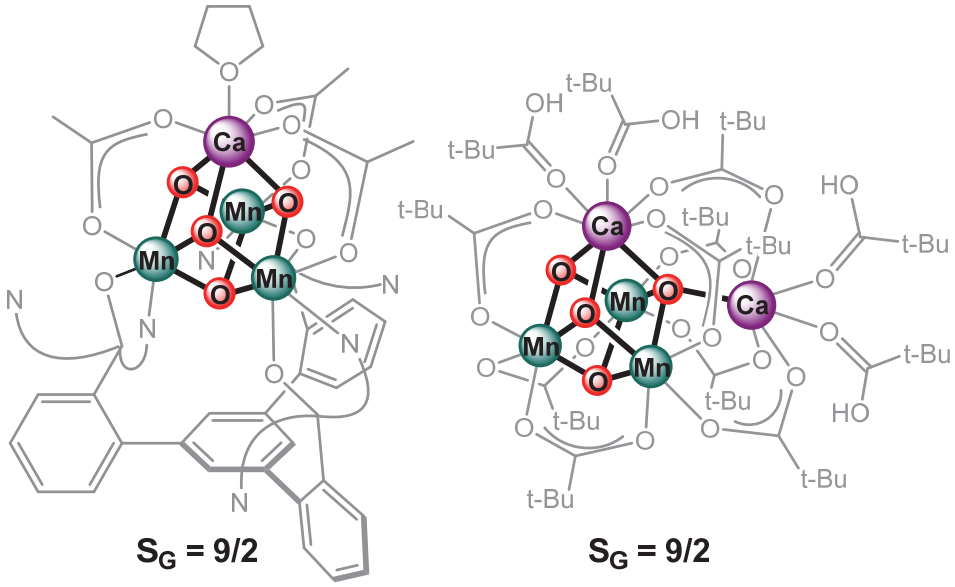

Figure 2. Previously reported complexes featuring a $CaMn_3O_4$ core with an $S = 9/2$ ground state.

subsite now proposed to have an S = 1 spin state; antiferromagnetic coupling to the dangling Mn(4) would lead to the observed S = 1/2 ground state.[22, 31] On the basis of two reported $CaMn_3^{IV}O_4$ complexes having an S = 9/2 ground state *vide infra*, the spin state equilibrium observed in the S_2 state has been attributed to the structural flexibility of the OEC core. Such a concept has been firmly established in the literature, strongly influencing current mechanistic proposals that focus on the incorporation of a sixth substrate oxygen O(6) in the cleft between Mn(1) and Mn(4) (Figure 1).[37] A similar magnetic coupling scheme has been advanced for the S_3 state, featuring a ferromagnetically coupled $CaMn_3^{IV}O_4$ subsite with an S = 9/2 spin state: antiferromagnetic coupling to Mn(4) would lead to the observed S = 3 ground state (Figure 1).[16] Since changes in the nature and magnitude of J_{ij} affect not only the spin ground state of the cluster but also other spectroscopic properties such as the sign and magnitude of the projected ^{55}Mn hyperfine coupling constants (A_i), a better understanding of the magnetic coupling interactions in the OEC is desirable.[38]

In contrast to the extensive studies performed on the OEC, structural, magnetic, and spectroscopic studies of heterometallic MMn_3O_4 complexes remain rare.[39] Relevant studies on $CaMn_3O_4$ complexes can be summarized as follows (Figure 2). On the basis of magnetic and EPR spectroscopic data, the spin ground state of a pivalate-bridged asymmetric $CaMn_3O_4$ model of the OEC has been assigned to S = 9/2.[40] On the basis of magnetic and computational data, the spin ground state of an acetate-bridged *pseudo*-C_3 symmetric $CaMn_3^{IV}O_4$ complex has been assigned to S = 9/2.[41-43] In general, studies on the effect of structural distortions, heterometal identity, and bridging oxo protonation on the electronic structure of heterometallic model complexes remain rare, in part due to the synthetic

difficulties in obtaining a series of compounds suitable for comparisons.[44-46] Despite significant efforts to prepare complexes that mimic the OEC in terms of structure and redox state, accurate models for benchmarking against the biological system are rare.[39, 47-52]

Herein, we report synthesis, crystal structure, magnetic susceptibility, and D-band pulsed EPR data for a series of cuboidal complexes featuring $CaMn_3^{IV}O_4$, $YMn_3^{IV}O_4$, and $CaMn_3^{IV}O_3(OH)$ cores. Additionally, the synthesis and characterization of an incomplete cubane with a $Mn_3^{IV}O_4$ core that mimics the Ca^{2+}-depleted cuboidal subsite of the OEC is reported. Similar to our previous studies on $Mn^{III}Mn_3^{IV}O_4$ complexes,[53] results show that the electronic structure of $CaMn_3^{IV}O_4$ complexes are highly sensitive not only to small geometrical changes promoted by the nature of the supporting ligands, but also to the

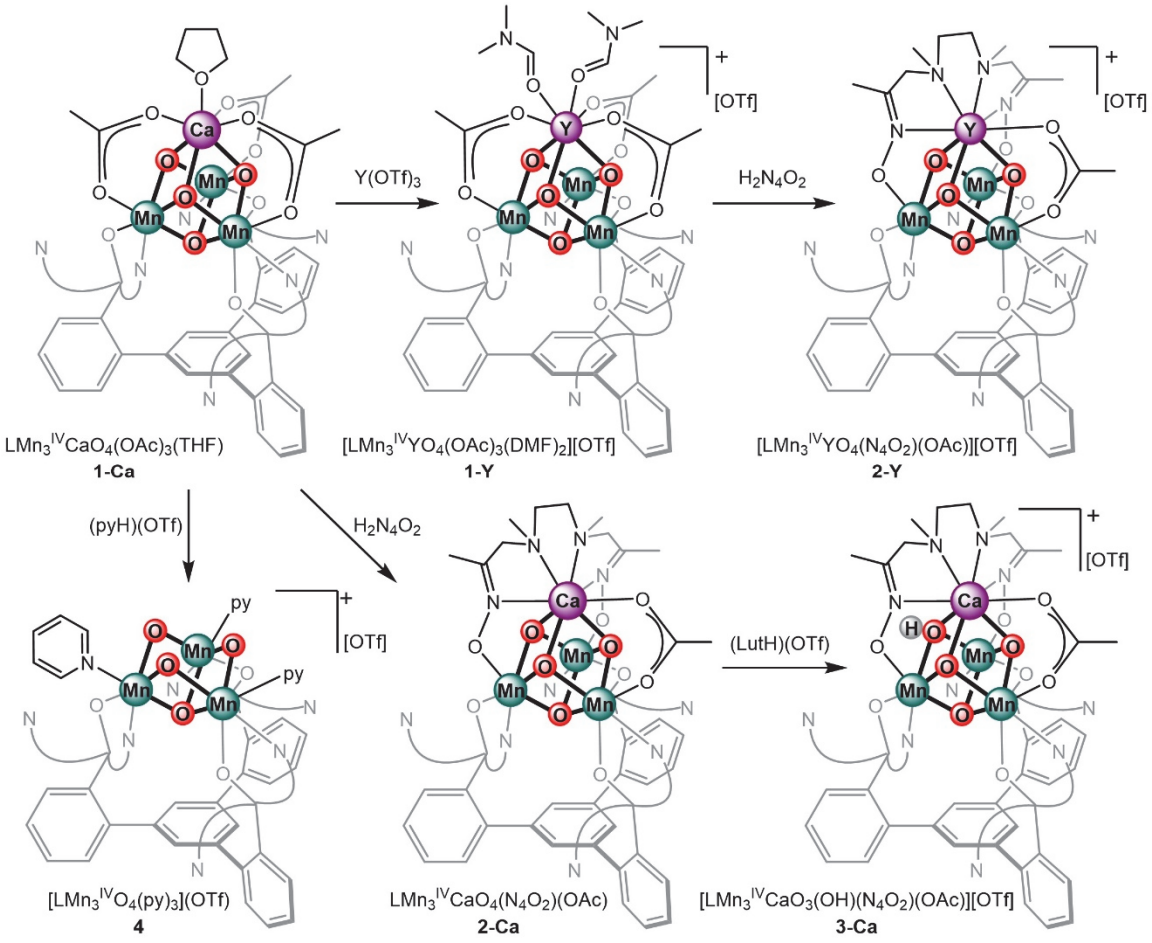

Figure 3. Synthesis of complexes studied in this work.

protonation state of the bridging oxo moieties. Our results contradict previous computational studies that predict an S = 9/2 ground state for all $CaMn_3^{IV}O_4$ complexes including analogues with protonated oxo moieties.[43] Results indicate that ground states such as S = 5/2 and S = 3/2 are possible in such complexes. Removal of the heterometal leads to a *pseudo*-C_3 symmetric $Mn_3^{IV}O_4$ complex with an S = 3/2 ground state, suggesting that geometric considerations are not sufficient for the deduction of the nature of magnetic exchange coupling interactions. The protonation state of the bridging oxo moieties and the magnetic coupling scheme within the $CaMn_3^{IV}O_4$ cuboidal subunit need to be carefully assessed.

5.2) Synthesis and crystal structure

We have previously reported the synthesis of $LCaMn_3^{IV}O_4(OAc)_3$ (**1-Ca**) (Figure 3).[42] Magnetic susceptibility and computational studies on **1-Ca** indicate an S = 9/2 ground state.[41, 43] Treatment of **1-Ca** with $Y(OTf)_3$ leads to the formation of $[LYMn_3O_4(OAc)_3]^+$ (**1-Y**).[52] Magnetic studies on **1-Y** also indicate an S = 9/2 ground state with no significant magnetic anisotropy, consistent with the Mn_3^{IV} oxidation state assignment.[54] Desymmetrization of the *pseudo*-C_3 symmetric complex **1-Ca** was achieved via substitution of two acetate moieties with a chelating bis-oximate ligand ($H_2N_4O_2$, Figure 3). Treatment of **1-Ca** with $H_2N_4O_2$ results in the formation of $LCaMn_3O_4(N_4O_2)(OAc)$ (**2-Ca**) via a protonolysis reaction.[55] Due to its limited solubility, a crystal structure of **2-Ca** has not been obtained to date. However, treatment of **2-Ca** with 1 equiv 2,6-lutidinium triflate (LutH)(OTf) results in the protonation of a unique oxo to afford $[LCaMn_3O_3(OH)(N_4O_2)(OAc)]^+$ (**3-Ca**), consistent with the desymmetrized, *pseudo*-C_s symmetric $CaMn_3O_4$ core in **2-Ca**. The crystal structure of **3-Ca** features Mn-(μ^3-OH)

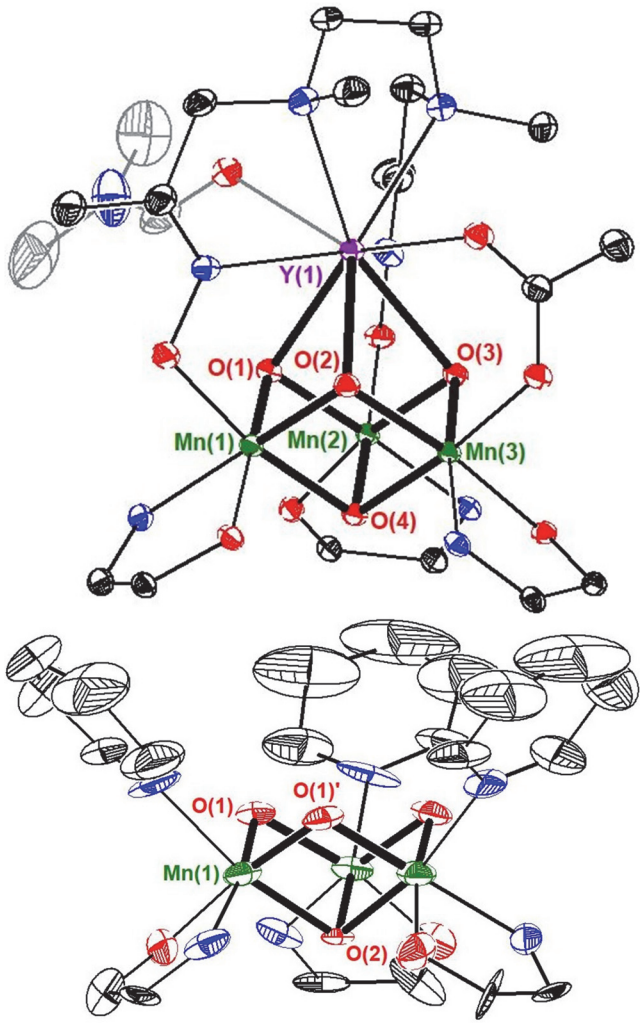

Figure 4. Truncated crystal structures of **2-Y** (top) and **4** (bottom). Mn (green), O (red), N (blue), C (black). Bolded bonds highlight metal-oxo bonds. Selected bond distances (Å): **2-Y**: Mn(1)−O(1) 1.863(3), Mn(1)−O(2) 1.882(2), Mn(1)−O(4) 1.941(3), Mn(2)−O(1) 1.875(3), Mn(2)−O(3) 1.849(2), Mn(2)−O(4) 1.949(3), Mn(3)−O(2) 1.836(3), Mn(3)−O(3) 1.869(3), Mn(3)−O(4) 1.906(2), Y(1)−O(1) 2.308(2), Y(1)−O(2) 2.396(2), Y(1)−O(3) 2.422(3), Mn(1)−Mn(2) 2.8817(8), Mn(1)−Mn(3) 2.8362(8), Mn(2)−Mn(3) 2.8400(8), Mn(1)−Y(1) 3.1810(6), Mn(2)−Y(1) 3.1934(6), Mn(3)−Y(1) 3.2950(6). **4**: Mn(1)−O(1) 1.839(9), Mn(1)−O(1)' 1.881(9), Mn(1)−O(2) 1.913(7), Mn−Mn 2.799(4).

distances that are slightly elongated by 0.09 Å in comparison to the corresponding Mn-(μ^3-O) distances in **1-Ca**. Ca-oxo/hydroxo distances in **3-Ca** are also slightly elongated by 0.05 Å in comparison to the Ca-oxo distances in **1-Ca**.[55] Such relatively small structural changes have a significant influence in the spin state structure of the $CaMn_3^{IV}O_4$ core *vide infra*.

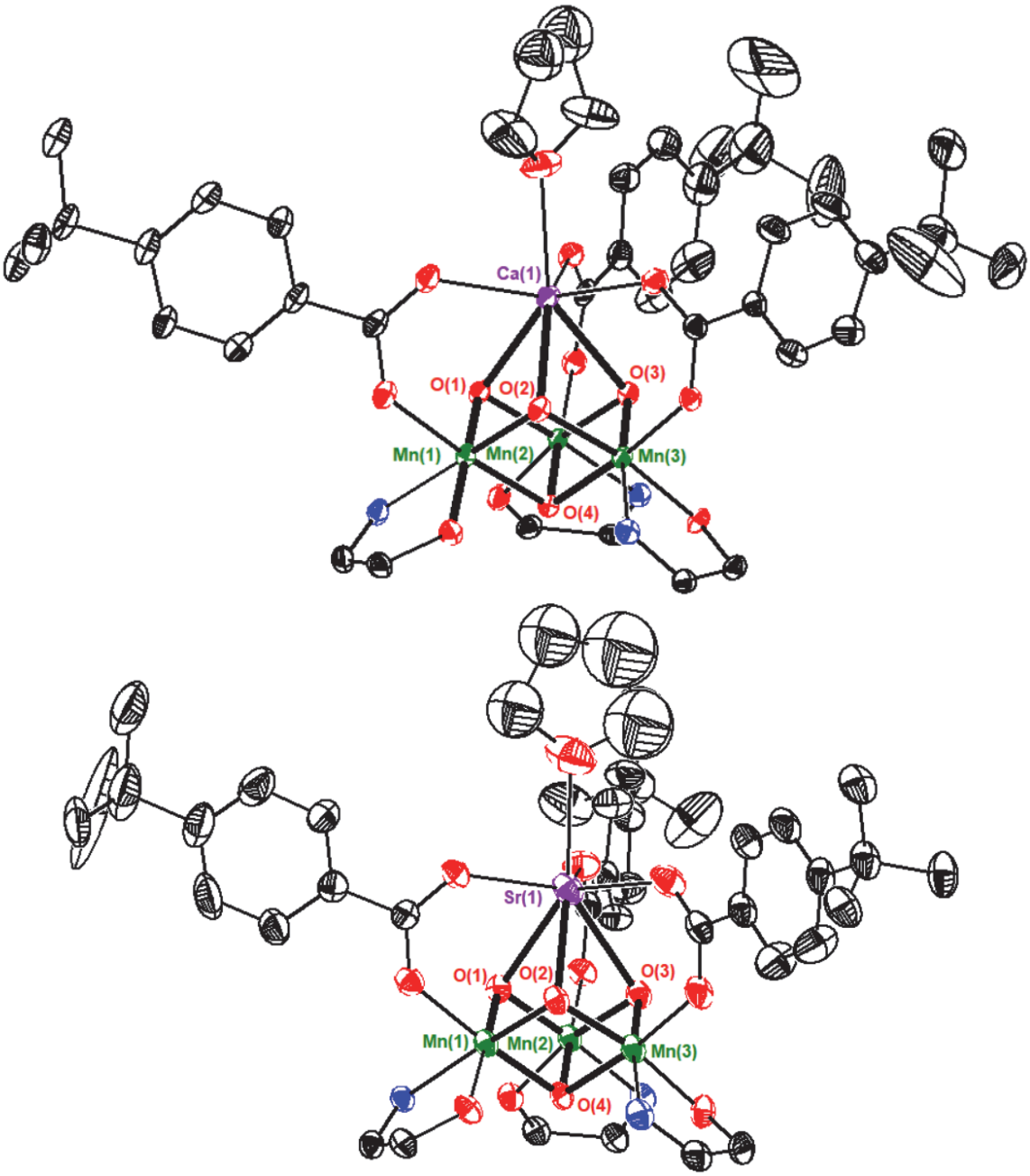

Figure 5. Truncated crystal structures of $LCaMn_3O_4(OBz)_3$ (top) and $LSrMn_3O_4(OBz)_3$ (bottom) synthesized from **4** via reconstitution of the cubane. Mn (green), O (red), N (blue), and C (black). Bolded bonds highlight metal-oxo bonds.

Toward expanding the series of desymmetrized cuboidal complexes featuring a closed-shell, redox inactive metal, the Y-analogue of **2-Ca** was targeted. Treatment of **1-Y** with $H_2N_4O_2$ results in the formation of **2-Y** via a protonolysis reaction. The ESI-MS peak at m/z = 1460 is consistent with the mass of $[LYMn_3O_4(N_4O_2)(OAc)]^+$. The X-ray crystal

structure of **2-Y** shows the *pseudo*-C_S symmetry of the YMn_3O_4 core, with the mirror plane containing the Y(1)−O(1) vector and bisecting the Mn(1)−Mn(2) vector (Figure 4). Accordingly, Y(1)−O(2) and Y(1)−O(3) distances are similar to each other and longer than the Y(1)−O(1) distance; Y(1)−Mn(1) and Y(1)−Mn(2) distances are similar to each other and shorter than the Y(1)−Mn(3) distance. A DMF solvent molecule completes the coordination sphere around Y(1). On the basis of the crystal structure of **2-Y**, a similar *pseudo*-C_S symmetric $CaMn_3O_4$ core is expected in **1-Ca**.

While no reaction is observed between **1-Ca** and (LutH)(OTf),[55] treatment of **1-Ca** with 3 equiv (pyH)(OTf) in the presence of added py results in the formation of **4** via a protonolysis reaction. The ESI-MS peaks at m/z = 1242 and 1321 are consistent with the masses of $[LMn_3O_4(py)_2]^+$ and $[LMn_3O_4(py)_3]^+$, respectively. Complex **4** crystallizes in the rhombohedral $R\bar{3}$ space group with the asymmetric unit containing a third of the molecule. The crystal structure of **4** is consistent with the *pseudo*-C_3 symmetry of the incomplete cubane Mn_3O_4 core lacking a fourth metal (Figure 4). The bond metrics in **4** are similar to that of **1-Ca**, with the Mn(1)−O(2) distance of 1.913(7) Å in **4** being comparable to the corresponding average distance of 1.917(2) Å in **1-Ca**; similar to the Mn(1)−O(1) 1.839(9) Å and Mn(1)−O(1)' 1.881(9) Å distances in **4**, a similar set of corresponding average distances 1.832(2) Å and 1.866(2) Å is observed in **1-Ca**. In the OEC, removal of Ca^{II} is found to have a minimal effect in the Mn-oxo core structure,[56] and spectroscopic properties of the Ca^{II}-depleted S_2 state do not differ significantly from the native S_2 state.[57-58] While such observations may suggest that the electronic structure of **1-Ca** and **4** should be similar, this is not the case *vide infra*. Reconstitution of the cubane core is possible via treatment of **4** with different metal-benzoate precursors $M^{II}(OBz)_2$, leading to the formation of

$LM^{II}Mn_3^{IV}O_4(OBz)_3$ complexes (Figure5). Crystal structures of examples with Ca(4-*tert*-Bu-benzoate)$_2$, Sr(4-*tert*-Bu-benzoate)$_2$, and Ca(2,6-diphenyl-benzoate)$_2$ are reported, underscoring the versatility of **4** as a precursor for the synthesis of heterometallic cuboidal complexes with different bridging ligands. Overall, **1-Ca(Y)**, **2-Ca(Y)**, **3-Ca**, and **4** represent a unique series of complexes mimicking the cuboidal substructure of the OEC in which cluster symmetry, heterometal identity, and oxo protonation state is systematically varied.

5.3) Magnetometry

To obtain insight into the magnetic exchange coupling interactions between adjacent Mn^{IV} centers, magnetic susceptibility studies were performed on powdered samples of **2-Ca**, **3-Ca**, and **4** in the temperature range 1.8−300 K at a non-saturating field of 0.2 T. For three uncoupled Mn^{IV} ($S = 3/2$) centers, a temperature independent χT value of 5.625 emu K mol^{-1} ($g = 2$) is expected; the temperature dependence of χT provides information about the nature and magnitude of the magnetic exchange coupling interactions. For *pseudo-C*$_S$ symmetric Mn_3^{IV} cores, an isotropic spin exchange Hamiltonian (equation 1) with two distinct magnetic interactions can be employed, with a unique $J' = J_{12}$ and $J = J_{13} = J_{23}$.[59] For Mn_3^{IV} systems with equivalent local spin $S_i = 3/2$, application of the vector coupling model $S' = S_1 + S_2$, $S_T = S' + S_3$ gives rise to a total of twelve (S_T, S') states, in which S' varies in integer increments from 0 to $2S_i$ (i.e. $S' = 0, 1, 2, 3$); for each value of S', S_T varies in integer increments from $|S' - S_i|$ to $S' + S_i$ (i.e. for $S' = 3$, $S_T = 3/2, 5/2, 7/2, 9/2$) (Table 1). The relative energies of the (S_T, S') states can be expressed as shown in equation 2. By incorporation of the energies of the twelve (S_T, S') states into the simplified Van Vleck equation (first order Zeeman only), an analytical solution for the magnetic susceptibility χ

can be obtained. Qualitatively, one can regard χ as being derived from the sum of the individual (S_T, S') states weighed by their Boltzmann populations: At sufficiently low temperatures where only the ground state is significantly populated, variable-temperature, variable-field (VT-VH) magnetization studies can be performed to obtain information about the spin ground state and magnetic anisotropy.

$$\hat{H} = -2J(S_1S_3 + S_2S_3) - 2J'S_1S_2 \qquad (1)$$

$$E(S_T, S') = -\mathrm{J}S_T(S_T + 1) - (J' - J)S'(S' + 1) \qquad (2)$$

Table 1. Twelve possible (S_T, S') states in an exchange coupled Mn_3^{IV} system.

S_T	S'
3/2	3
5/2	3
7/2	3
9/2	3
1/2	2
3/2	2
5/2	2
7/2	2
1/2	1
3/2	1
5/2	1
3/2	0

Complex **2-Ca** was studied by SQUID magnetometry (Figure 6). The χT value of 4.526 emu K mol^{-1} at 300 K decreases slowly to a local minimum χT value of 4.313 emu K mol^{-1} at 150 K. Upon further cooling, the χT value increases slowly to reach a plateau value of 4.405 emu K mol^{-1} at 15 K, in good agreement with the expected value of 4.375 emu K mol^{-1} for an S = 5/2 (g = 2) ground state. Further decrease in χT with temperature can be attributed to intermolecular antiferromagnetic interactions and/or magnetic anisotropy. The temperature dependence of χT observed in **2-Ca** is indicative of an irregular spin state structure where the first excited state is $S \leq 3/2$ and the second excited state is $S \geq 5/2$.

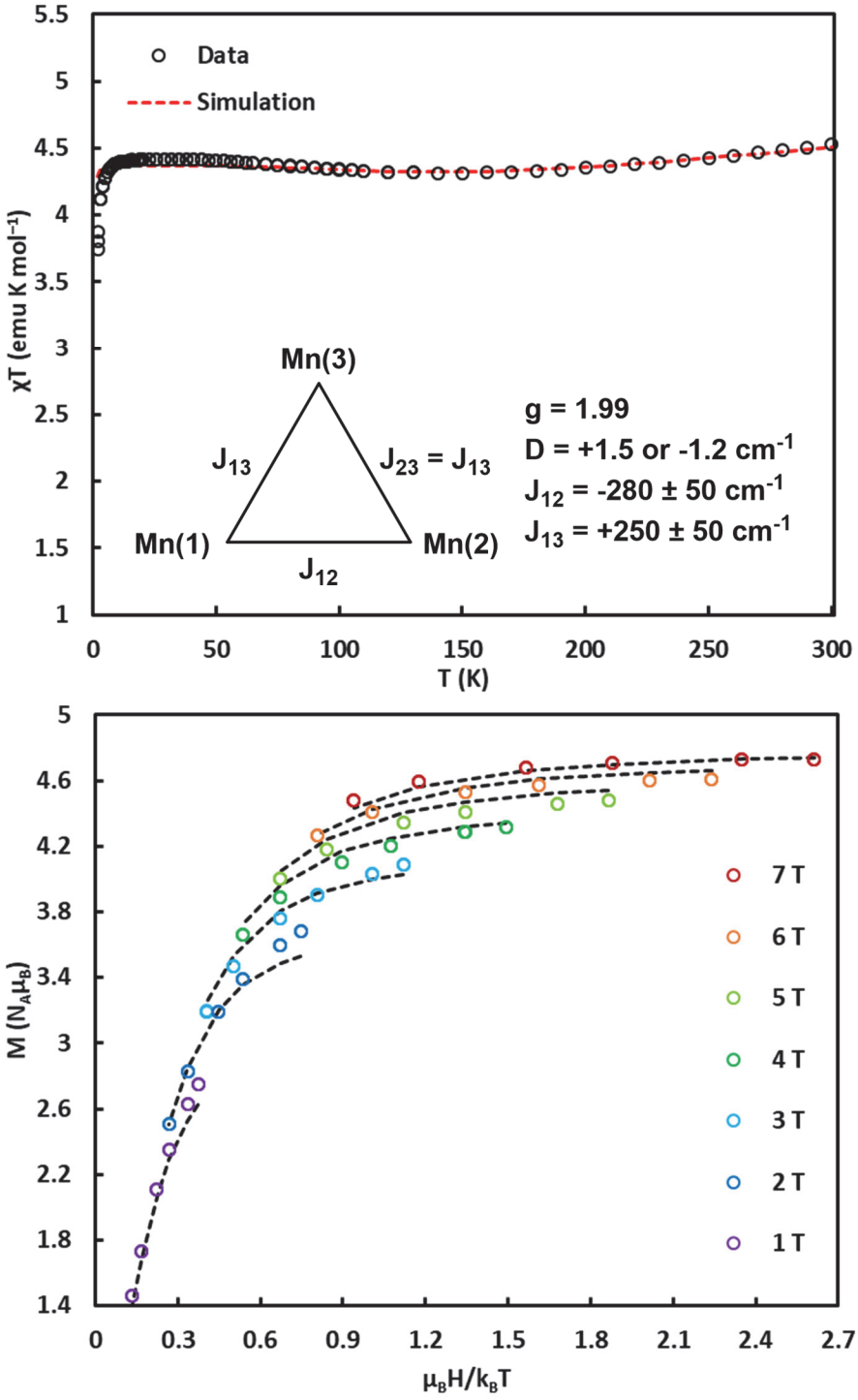

Figure 6. Exchange coupling model, fit parameters, χT vs T plot, and reduced magnetization plot of complex **2-Ca**.

Similar magnetic behavior has been observed in other trinuclear systems.[60-63] On the basis of the small curvature of the χT vs. T curve, the expected separation between the spin

ground state and the first excited state is in the order of hundreds of wavenumbers. To simulate the susceptibility data, an isotropic exchange coupling model consisting of an isosceles triangle was employed (Figure 6). The following parameters were used: $g = 1.99 \pm 0.01$, $J = J_{13} = J_{23} = +250 \pm 50$ cm^{-1}, $J' = J_{12} = -280 \pm 50$ cm^{-1}. Due to the small curvature of the χT vs. T curve, small changes in the diamagnetic correction lead to a relatively large variance in the fitted J values. The range in the J/J' ratio is narrower, between −0.90 and −0.93, and falls within the predicted region for an $S = 5/2$ ground state (Figure 7).[43] The $(S_T, S') = (5/2, 1)$ ground state is separated from the (3/2, 0) first excited state by 210 ± 50 cm^{-1} (equiv. temp. 302 ± 72 K) and from the (7/2, 2) second excited state by 350 ± 50 cm^{-1} (equiv. temp. 504 ± 72 K). Thermally well-isolated spin ground states have been observed in multinuclear complexes, with values of $|J|$ in the range of 160~900 cm^{-1}.[64-66] Such systems behave as pure Curie paramagnets, with no temperature dependence of χT. To further characterize the spin ground state in **2-Ca**, VT-VH magnetization studies were performed. The reduced magnetization isofield at 7 T reaches a value of 4.71 $N_A\mu_B$ at 1.8 K, consistent with the $S = 5/2$ ground state. Reduced magnetization isofields were simulated assuming a single value of $D = +1.46$ cm^{-1} or -1.17 cm^{-1}. In many cases, powder susceptibility data is insensitive to the sign of D.[67] D-band EPR studies on **2-Ca** are currently ongoing to determine a more precise value of D. Magnetic studies on **2-Ca** show that the ligand environment has a strong influence in the nature and magnitude of the magnetic coupling interactions; in the case of **2-Ca**, the relatively large values of $|J|$ can be attributed to the increased ligand basicity of the chelating oximates ($pK_a \approx 25$ in DMSO) compared to acetates ($pK_a = 12.6$ in DMSO).[53, 68-70] The electronic influence of the ligand framework is manifested in the increased oxo basicity of **2-Ca** compared to **1-Ca**: **1-Ca**

does not react with (Lut)(OTf) while **2-Ca** reacts readily to give the protonated analogue **3-Ca**. Even in the hypothetical case where J and J' are an order of magnitude smaller, at J = +25cm^{-1} and J' = −28 cm^{-1}, an S = 5/2 ground state would still be observed, albeit with a smaller energy separation from the same first and second excited states, at 19 and 37 cm^{-1} respectively. Overall, magnetic studies on **2-Ca** show that geometric considerations are not sufficient for the reliable deduction of magnetic coupling interactions. An intact $CaMn_3^{IV}O_4$ cubane moiety need not necessarily have an S = 9/2 ground state.

Complex **3-Ca** was studied by SQUID magnetometry (Figure 8). The χT value of 3.856 emu K mol^{-1} at 300 K decreases monotonically to reach a plateau value of 1.886 emu K mol^{-1} at 10 K, in good agreement with the expected value of 1.875 emu K mol^{-1} for an S = 3/2 (g = 2) ground state. To simulate the susceptibility data, the following parameters were used: g = 2.00, J = +11 cm^{-1}, and J' = −55 cm^{-1} (Figure 8). The J/J' ratio of −0.2 falls within the predicted region for an S = 3/2 ground state (Figure 7).[43] The (S_T, S') = (3/2, 0)

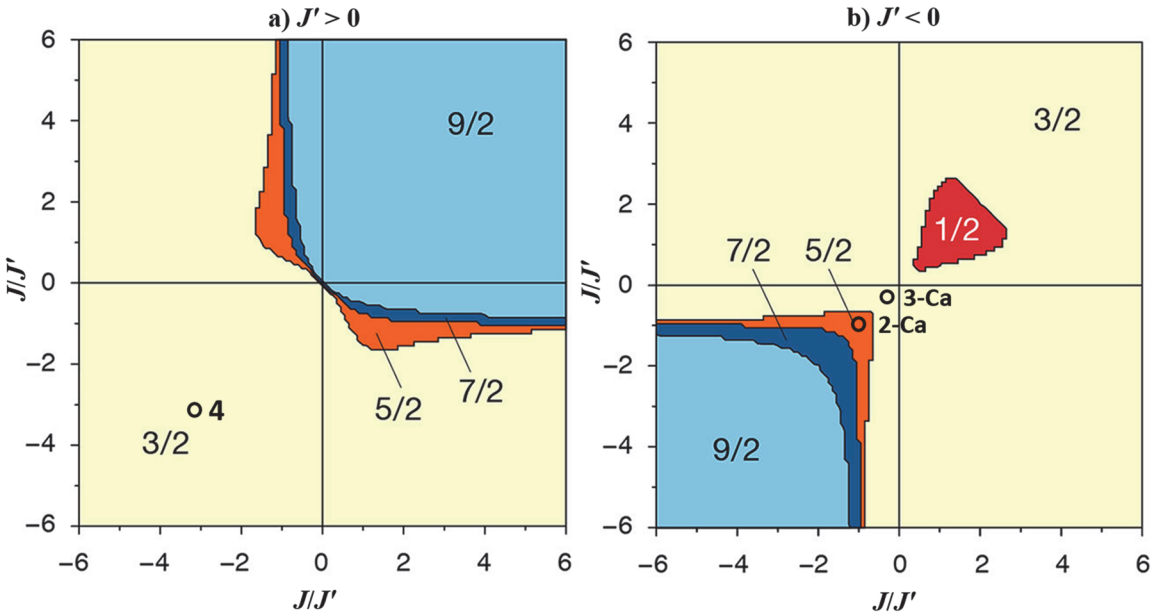

Figure 7. Dependence of the total spin ground state for three coupled S = 3/2 spin sites through an isosceles coupling model described in the text. Experimentally determined ratios for **2-Ca**, **3-Ca**, and **4**.

ground state is separated from the (5/2, 1) first excited state by 77 cm^{-1} (equiv. temp. 110 K) and from the (3/2, 1) second excited state by 132 cm^{-1} (equiv. temp. 190 K). VT-VH

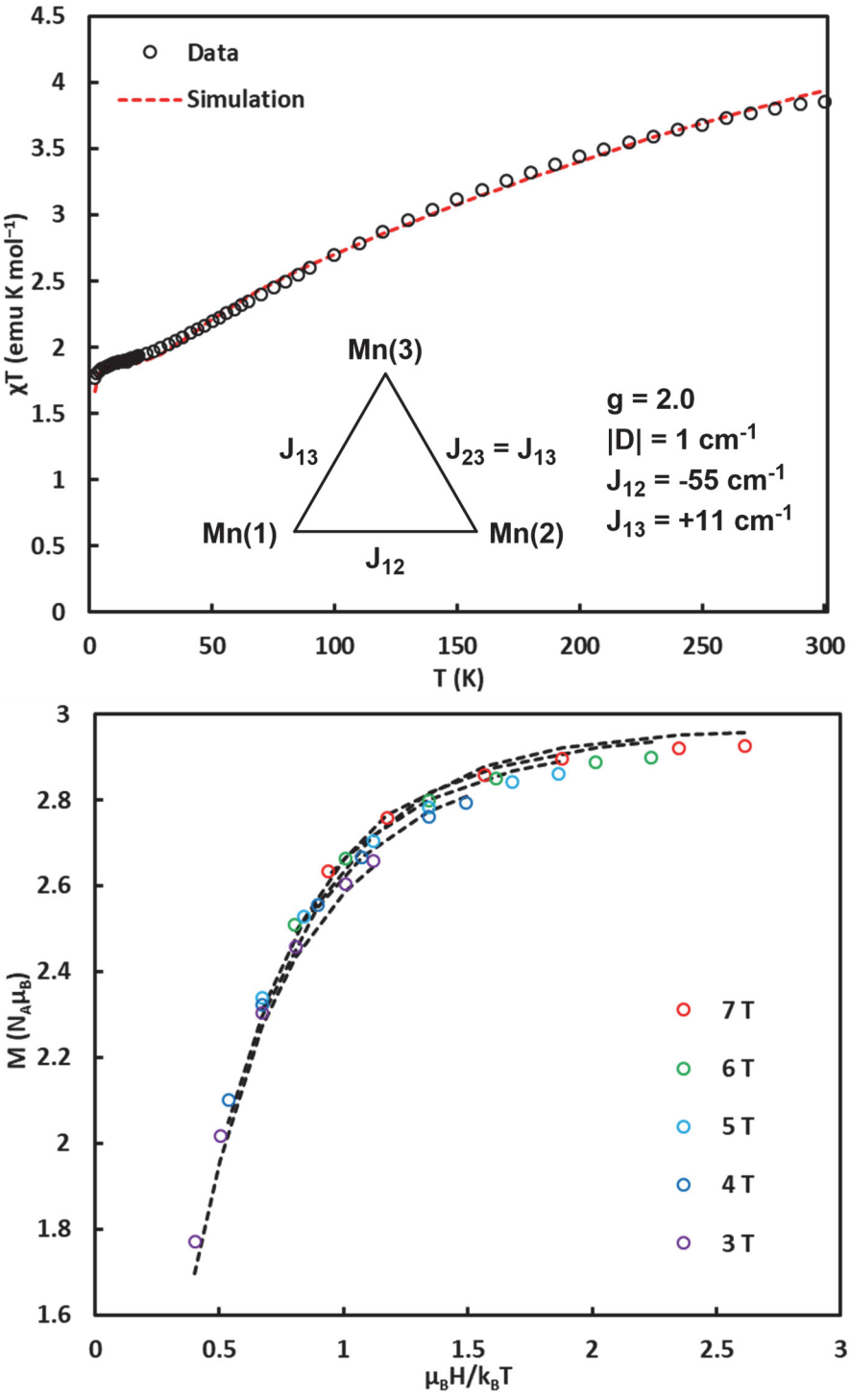

Figure 8. Exchange coupling model, fit parameters, χT vs T plot, and reduced magnetization plot of complex **3-Ca**.

magnetization studies were performed. The reduced magnetization isofield at 7 T reaches a value of 2.93 $N_A\mu_B$ at 1.8 K, consistent with the S = 3/2 ground state. Reduced magnetization isofields were simulated assuming a single value of $D = \pm 1.0$ cm^{-1}. For a more careful determination of the zero field splitting parameter in **3-Ca**, D-band (130 GHz) EPR studies are currently ongoing. Magnetic studies on **3-Ca** show that protonation of a single bridging oxo moiety has a strong influence in attenuating the magnitude of the magnetic coupling interactions.[71] In this case, protonation of **2-Ca** does not change the nature (sign) of the magnetic coupling interactions in **3-Ca**; in a different case, a complete reversal from ferromagnetic to antiferromagnetic interactions has been reported in a tetranuclear Mn_4 system.[72] Overall, magnetic studies on **3-Ca** show that the protonation state of the bridging oxos in an intact $CaMn_3^{IV}O_4$ cubane moiety may have a large effect in lowering the spin state of the cluster below the predicted S = 9/2 ground state.

Complex **4** was studied by SQUID magnetometry (Figure 9). The χT value of 4.73 emu K mol^{-1} at 300 K decreases monotonically with temperature, reaching a plateau value of 1.882 emu K mol^{-1} at 15 K, in good agreement with the expected χT value of 1.875 emu K mol^{-1} for an S = 3/2 (g = 2) ground state. Similar to the other complexes, the near-ideal Curie behavior observed between 1.8−15 K can be attributed to a well-isolated S = 3/2 ground state. To simulate the susceptibility data, the following parameters were used: g = 2.0, $J = -11.4$ cm^{-1}, and $J' = +3.9$ cm^{-1} (Figure 9). The J/J' ratio of −2.92 falls well within the predicted region for an S = 3/2 ground state (Figure 7).[43] The expected (S_T, S') = (3/2, 3) ground state is separated from two nearly isoenergetic excited states (5/2, 3) and (1/2, 2) by ~58 cm^{-1} (equiv. temp. ~83 K). The reduced magnetization isofield at 7 T reaches a value of 2.90 $N_A\mu_B$ at 1.8 K, consistent with the S = 3/2 ground state. Reduced

magnetization isofields were simulated assuming a single value of $D = \pm 1.7$ cm^{-1}. The increase in the magnitude of $|J|$ in **4** compared to **1-Ca** can be attributed to the absence of

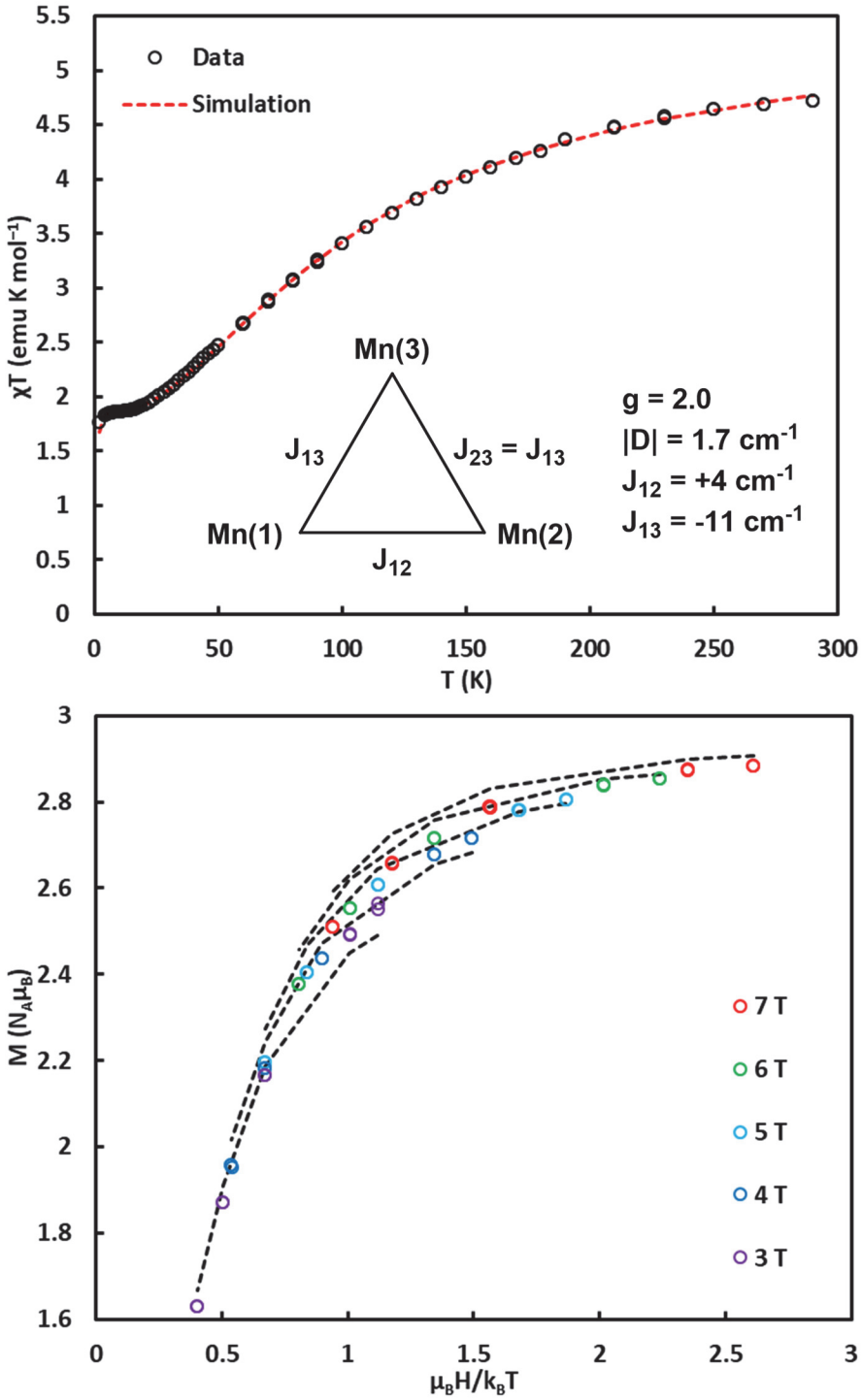

Figure 9. Exchange coupling model, fit parameters, χT vs T plot, and reduced magnetization plot of complex **3-Ca**.

a Lewis acidic Ca^{2+} metal center. Overall, magnetic studies on **4** further show that spin ground states do not translate between complexes of similar geometry and symmetry, urging a careful reevaluation of the $S = 9/2$ ground state assignment for the closed-cubane $CaMn_3^{IV}O_4$ subsite of the OEC.

5.4) EPR spectroscopy

Complex **2-Ca** was studied by continuous-wave X-band EPR spectroscopy (Figure 10). The spectrum of **2-Ca** at 5 K shows two broad signals centered at ~1200 G (g = 5.7) and ~1600 G (g = 4.3). Additionally, a weak signal near ~3300 G (g = 2) is observed. On the basis of the reduced magnetization data collected for **2-Ca**, the zero field splitting parameter is expected to be larger than the X-band EPR quanta ($D >> h\nu \approx 0.3$ cm^{-1} at X-band). In the case of half-integer spin systems with $D >> h\nu$, the $|\pm m_s\rangle$ states can be treated as Kramers doublets, and rhombograms that describe the position of the X-band EPR

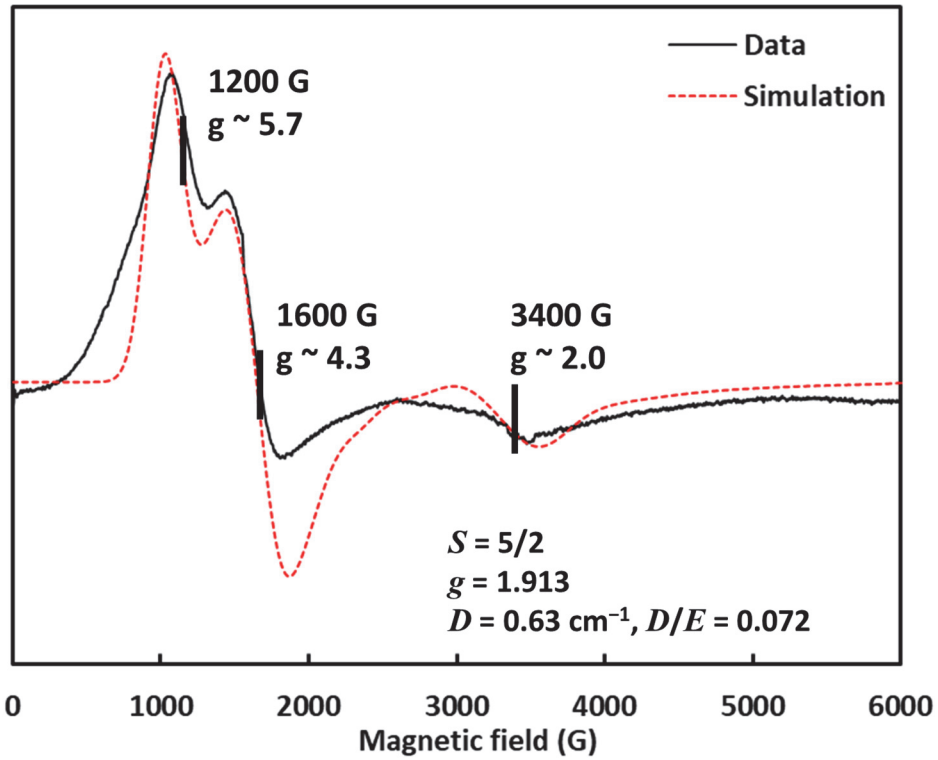

Figure 10. Continuous-wave X-band EPR spectrum of **2-Ca**.

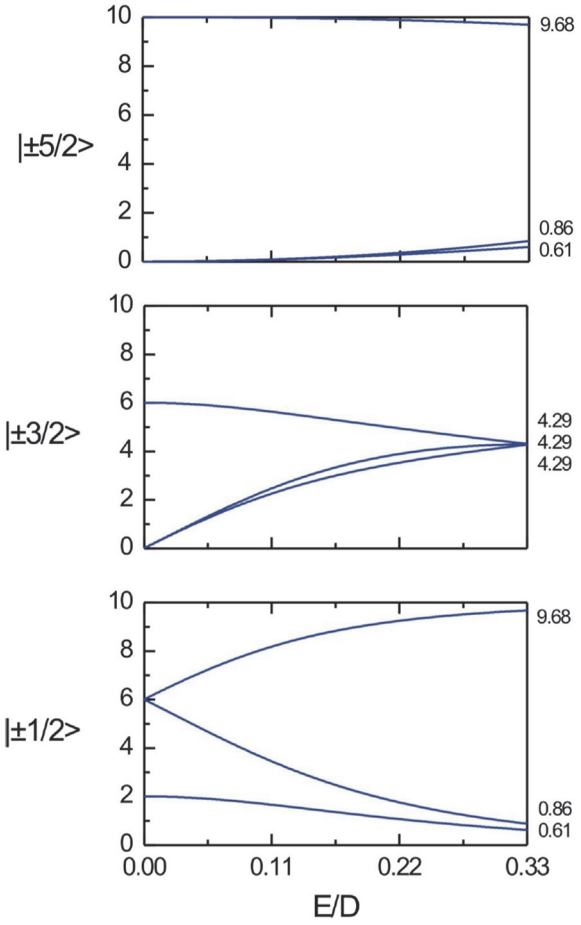

Figure 11. Rhombogram for $S = 5/2$.

transitions as a function of rhombicity are available (Figure 11). For a purely axial system with $g = 2$, a signal centered at ~1100 G ($g = 6$) and ~3400 G ($g = 2$) is expected from the $|\pm 1/2\rangle$ Kramers doublet; the signal from the $|\pm 3/2\rangle$ Kramers doublet overlaps at $g = 6$ (Figure 11). With a slight increase in rhombicity, at $E/D = 0.06$, three signals are expected from the $|\pm 1/2\rangle$ Kramers doublet, roughly at g ~ 7, 4.5, and 1.95. Two signals are expected from the $|\pm 3/2\rangle$ Kramers doublet roughly at g ~ 5.9, and 1.9. Taken together, these are the signals that are observed in the EPR spectrum of **2-Ca**, supporting the $S = 5/2$ spin ground state determined from magnetic susceptibility studies. The shoulder at 800 G can be assigned to the signal from the $|\pm 5/2\rangle$ Kramers doublet roughly at $g = 10$ (~700 G). The

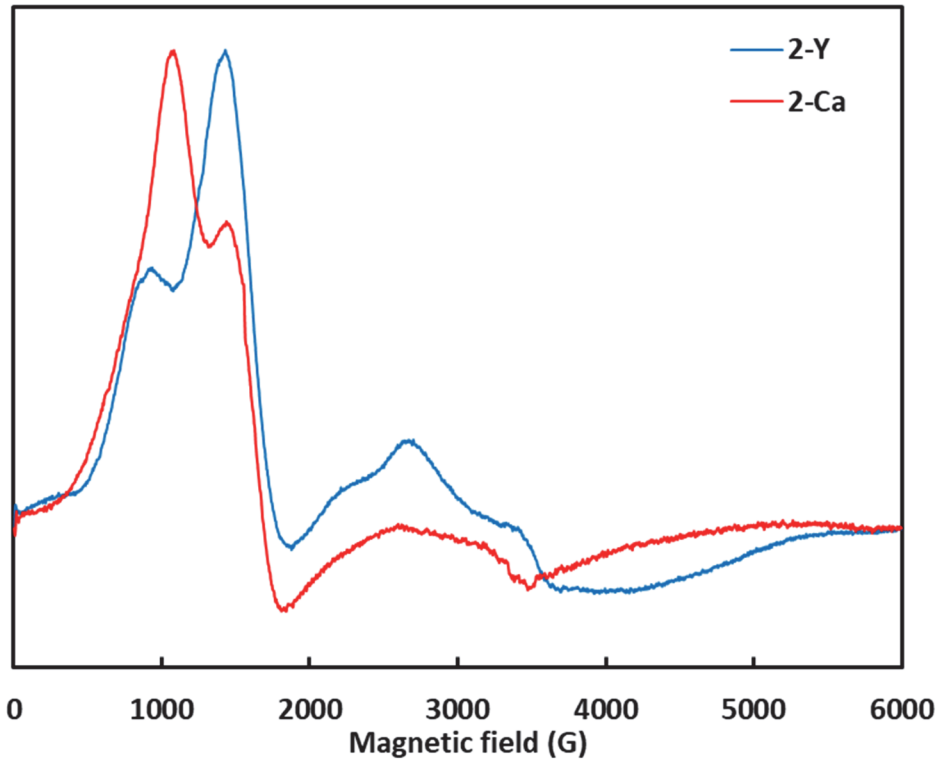

Figure 12. Continuous-wave X-band EPR spectrum of **2-Y**.

precise value of *D* cannot be determined reliably from X-band EPR spectrum alone, and D-band studies are currently ongoing.

Complex **2-Y** was studied by continuous-wave X-band EPR spectroscopy (Figure 12). Similar to the spectrum of **2-Ca**, the spectrum of **2-Y** at 5 K shows the same two broad signals centered at ~1200 G (g = 5.7) and ~1600 G (g = 4.3). The broad signal at ~4500 G (g = 1.5) corresponds to the high field edge of the $|\pm 3/2\rangle$ Kramers doublet signal that was too broad to observe in **2-Ca**. On the basis of the similar peak positions observed in the spectrum of **2-Y**, the ground state of **2-Y** is assigned as S = 5/2. The differences in the relative intensities of the two signals at 1200 G and 1600 G can be explained in terms of the relative Boltzmann populations of the $|\pm 1/2\rangle$ and the $|\pm 3/2\rangle$ Kramers doublets. In the case of **2-Y**, the intensity of the peak at 1000 G assigned to the $|\pm 3/2\rangle$ Kramers doublet is reduced in comparison to **2-Ca**; this is consistent with the thermal depopulation of the

|±3/2⟩ Kramers doublet for a system with positive zero field splitting. In effect, more intense EPR transitions within the lowest energy |±1/2⟩ Kramers doublet is observed, consistent with a larger positive zero field splitting in **2-Y** than in **2-Ca**. Accordingly, the larger signal at 1000 G in **2-Ca** is due to a higher population of the |±3/2⟩ Kramers doublet resulting from a smaller zero field splitting. Importantly, the spin ground state of both **2-Ca** and **2-Y** is $S = 5/2$, in agreement with magnetic susceptibility studies on **2-Ca**.

Complex **3-Ca** was studied by continuous-wave X-band EPR spectroscopy (Figure 13). The spectrum of **3-Ca** at 5 K shows a broad feature in the range 1000−2000 G. The lineshape of this transition suggests that two signals are overlapping in this region, one that is centered at around $g = 5.7$ and another that is centered at around $g = 4.2$. The spectrum also features several more transitions centered at $g = 2.45$, $g = 1.96$, and a very broad transition at $g = 1.4$. On the basis of the zero field splitting parameter determined from

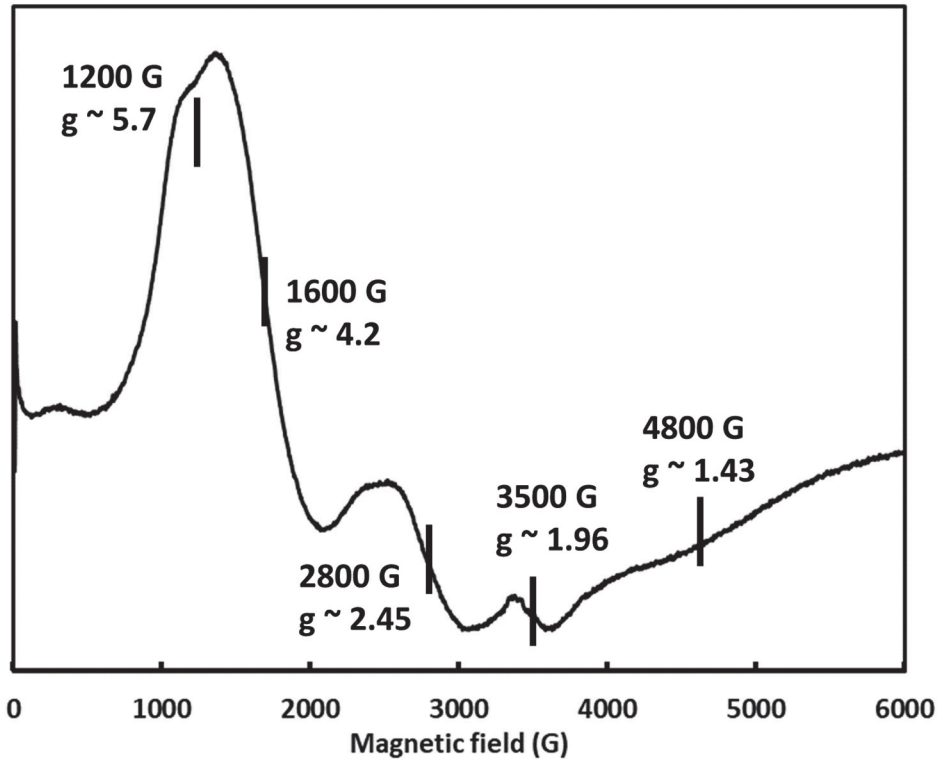

Figure 13. Continuous-wave X-band EPR spectrum of **3-Ca**.

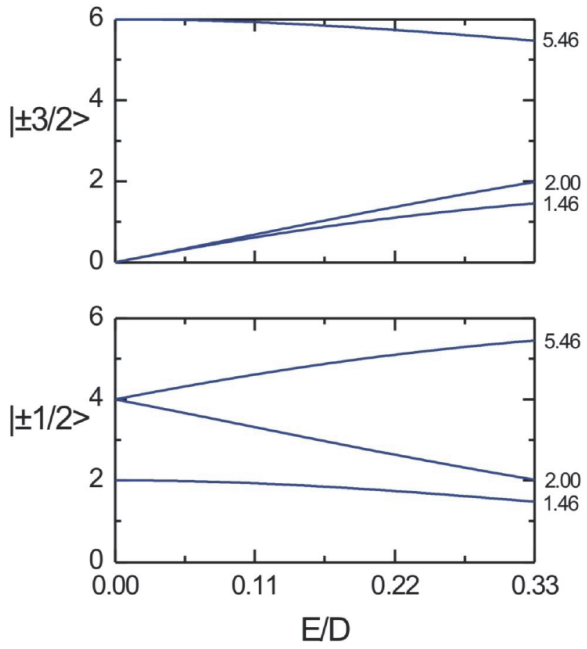

Figure 14. Rhombogram for $S = 3/2$.

reduced magnetization studies on **3-Ca**, the rhombograms for the $S = 3/2$ state were used to interpret the spectrum (Figure 14). For a purely axial system with $g = 2$, two signals centered at $g = 4$ and $g = 2$ are expected from the $|\pm 1/2\rangle$ Kramers doublet; a signal centered at $g = 6$ is expected from the $|\pm 3/2\rangle$ Kramers doublet (Figure 14). With a slight increase in rhombicity, the $g = 4$ signal diverges into two separate signals. The g = 2 and the g = 6 signal decrease slightly with the increase in rhombicity, and a new signal at the high field edge of the spectrum may be observed from the $|\pm 3/2\rangle$ Kramers doublet. Due to the broadness of the signals and the presence of multiple overlapping signals, satisfactory simulations have not been obtained thus far. D-band EPR studies are underway. However, the signals observed in the X-band EPR spectrum agree with the expected peaks predicted by using the rhombograms, and support the $S = 3/2$ spin ground state of **3-Ca** as determined from magnetic susceptibility studies.

Complex **4** was studied by continuous-wave X-band EPR spectroscopy (Figure 15). The spectrum of **4** at 5 K shows a broad feature in the range 1000−2000 G. The lineshape

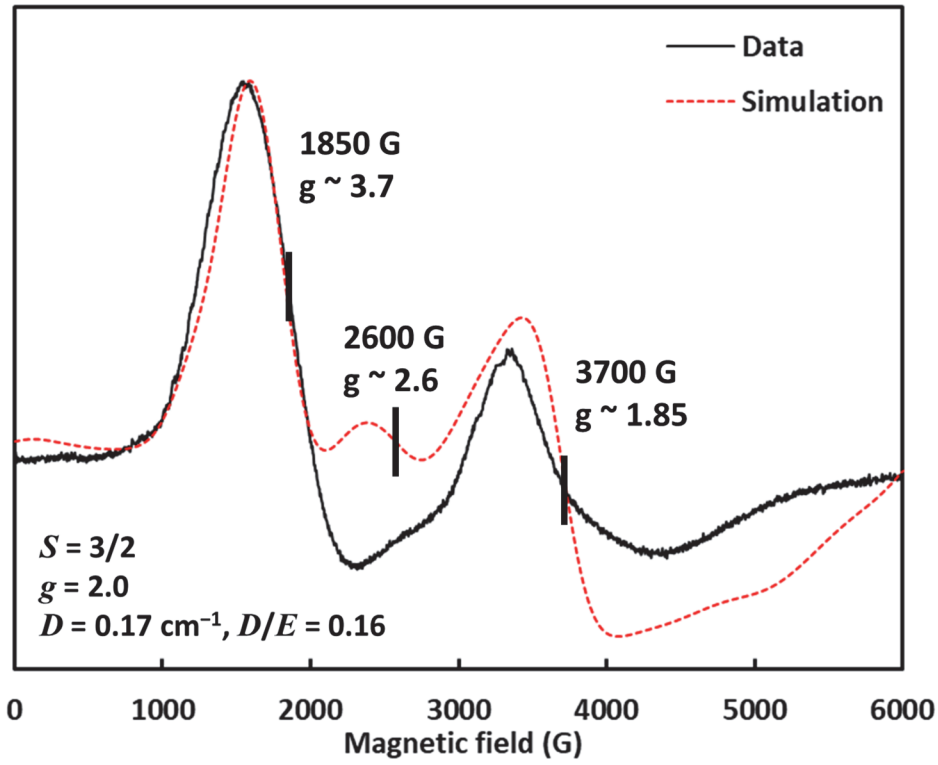

Figure 15. Continuous-wave X-band EPR spectrum of **4**.

of this transition suggests that two signals are overlapping in this region, one that is centered at around $g = 3.7$ and another that is centered at around $g = 2.6$. The spectrum also features another broad transition in the range 3000−5000 G. Similarly, the lineshape of this transition suggests that two signals are overlapping in this region. These features cannot be explained using the rhombograms for the $S = 3/2$ state, and suggests that the zero field splitting in **4** is smaller than the value obtained from magnetometry. Thus far, spin states other than $S = 3/2$ have not given satisfactory simulations. Using the parameters shown in Figure 15, the spin ground state of **4** is assigned as S = 3/2, with a small zero field splitting parameter of 0.17 cm^{-1}.

5.5) Discussion

A series of $MMn_3^{IV}O_4$ cuboidal complexes has been synthesized and characterized by XRD, SQUID magnetometry, and EPR spectroscopy. To our knowledge this is the first set

of experimental studies that directly addresses the effect of systematic changes in cluster geometry, heterometal identity, and bridging oxo protonation on the spin state structure of tetranuclear cubane models of the OEC. With implications in the interpretation of the OEC spectroscopic properties, our benchmarking results show that the electronic structure of the Mn_3^{IV} core is highly sensitive to small geometric changes, the nature of the bridging ligands, and the protonation state of the bridging oxos. Even in the absence of large oxo movements proposed to account for the high spin and low spin signals of the S_2 state of the OEC, we find that the spin ground states of essentially isostructural compounds can be S = 3/2, 5/2, or 9/2. Recent *p*H dependence studies show that deprotonation of the S = 1/2 form leads to the S = 5/2 form of the S_2 state. This phenomenon was interpreted in the context of the "open cubane"–"closed cubane" paradigm. An alternative interpretation based on deprotonation of a bridging hydroxo can be invoked. Interpretation of EPR signals and subsequent structural assignments based on an S = 9/2 spin state of the $CaMn_3O_4$ subsite of the OEC must be done very cautiously. The development of computational methods that reproduce experimentally observed spin ground states of exchange-coupled tetranuclear complexes will be of great interest.

5.6) Experimental section

Complexes **1-Ca**, **2-Ca**, and **3-Ca** were synthesized according to published procedure.[42, 55] Complex **2-Y** was synthesized according to the procedure described in Chapter 4.

Synthesis of **4**: Complex **4** can be synthesized from a variety of starting materials. Treatment of $LCaMn_3O_4(OAc)_3$, $LMn_4O_4(OAc)_3$, or $LMn_4O_4(diam)(OAc)$ with three equivalents of pyridinium triflate all lead to the formation of $LMn_3O_4(py)_3(OTf)$ (**4**). A

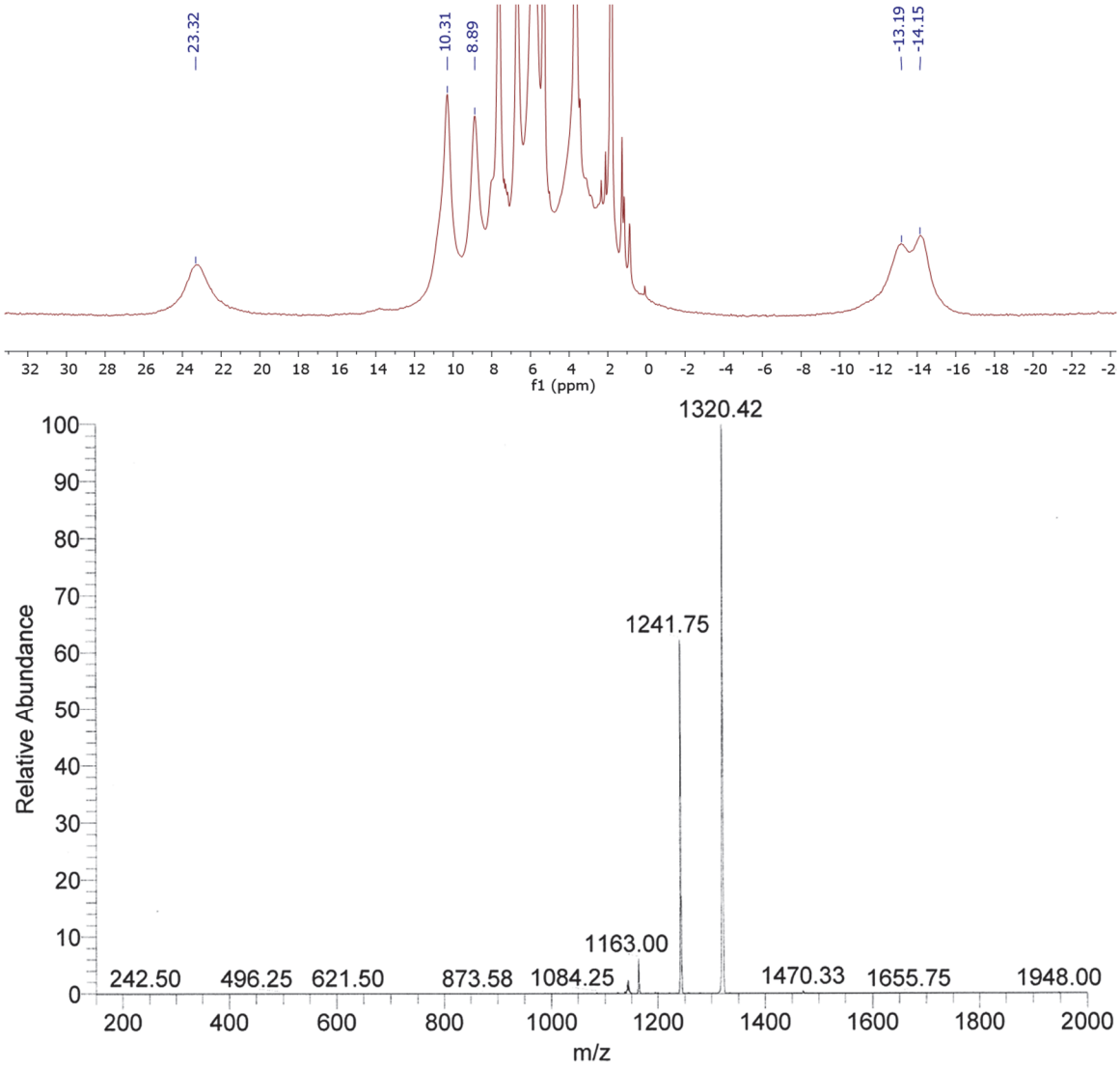

Figure 16. ^{1}H NMR spectrum in CD_2Cl_2 and ESI-MS of **4**. *m/z* = 1321 consistent with $[LMn_3O_4(py)_3]^+$. *m/z* = 1242 consistent with $[LMn_3O_4(py)_2]^+$.

representative procedure starting from $LCaMn_3O_4(OAc)_3$ is described below. A suspension of $LCaMn_3O_4(OAc)_3(THF)$ (1.66 g, 1.21 mmol, 1 equiv) in a 1:1 mixture of THF-pyridine (50 mL) is treated with a solution of pyridinium triflate (0.86 g, 3.75 mmol, 3.1 equiv) in pyridine (20 mL). The resulting mixture is stirred overnight at room temperature. All volatiles are removed, and the residue is washed with generous amounts of Et_2O and benzene. The residue is dissolved in CH_2Cl_2 and filtered through a pad of Celite. All volatiles are removed from the filtrate. The residue is treated with a small amount of THF

and stirred until a fine suspension is obtained. The precipitate is collected on a pad of Celite and rinsed with a small amount of THF and then with Et_2O. Complex **4** is isolated as a brown solid (0.86 g, 48 %). Crystals suitable for X-ray crystallography were obtained from slow vapor diffusion of Et_2O into a concentrated solution of **4** in CH_2Cl_2 with a drop of pyridine. ^1H NMR (300 MHz, CD_2Cl_2): δ 23.0, 10.3, 8.9, −13.2, −14.2 ppm. Analysis calculated for $[LMn_3O_4(py)_3](OTf)\cdot CH_2Cl_2$ $[C_{74}H_{56}Cl_2F_3Mn_3N_9O_{10}S]$: C 57.12, H 3.63, N 8.10; found: C 57.41, H 3.56, N 8.55.

5.7) References

(1) Yano, J.; Yachandra, V., *Chem. Rev.* **2014**, *114*, 4175.
(2) Shen, J.-R., *Annu. Rev. Plant Biol.* **2015**, *66*, 23.
(3) Pantazis, D. A., *ACS Catalysis* **2018**, *8*, 9477.
(4) Kern, J.; Alonso-Mori, R.; Tran, R.; Hattne, J.; Gildea, R. J.; Echols, N.; Glöckner, C.; Hellmich, J.; Laksmono, H.; Sierra, R. G.; Lassalle-Kaiser, B.; Koroidov, S.; Lampe, A.; Han, G.; Gul, S.; DiFiore, D.; Milathianaki, D.; Fry, A. R.; Miahnahri, A.; Schafer, D. W.; Messerschmidt, M.; Seibert, M. M.; Koglin, J. E.; Sokaras, D.; Weng, T.-C.; Sellberg, J.; Latimer, M. J.; Grosse-Kunstleve, R. W.; Zwart, P. H.; White, W. E.; Glatzel, P.; Adams, P. D.; Bogan, M. J.; Williams, G. J.; Boutet, S.; Messinger, J.; Zouni, A.; Sauter, N. K.; Yachandra, V. K.; Bergmann, U.; Yano, J., *Science* **2013**, *340*, 491.
(5) Suga, M.; Akita, F.; Hirata, K.; Ueno, G.; Murakami, H.; Nakajima, Y.; Shimizu, T.; Yamashita, K.; Yamamoto, M.; Ago, H.; Shen, J.-R., *Nature* **2014**, *517*, 99.
(6) Kern, J.; Chatterjee, R.; Young, I. D.; Fuller, F. D.; Lassalle, L.; Ibrahim, M.; Gul, S.; Fransson, T.; Brewster, A. S.; Alonso-Mori, R.; Hussein, R.; Zhang, M.; Douthit, L.; de Lichtenberg, C.; Cheah, M. H.; Shevela, D.; Wersig, J.; Seuffert, I.; Sokaras, D.; Pastor, E.; Weninger, C.; Kroll, T.; Sierra, R. G.; Aller, P.; Butryn, A.; Orville, A. M.; Liang, M.; Batyuk, A.; Koglin, J. E.; Carbajo, S.; Boutet, S.; Moriarty, N. W.; Holton, J. M.; Dobbek, H.; Adams, P. D.; Bergmann, U.; Sauter, N. K.; Zouni, A.; Messinger, J.; Yano, J.; Yachandra, V. K., *Nature* **2018**.
(7) Umena, Y.; Kawakami, K.; Shen, J.-R.; Kamiya, N., *Nature* **2011**, *473*, 55.
(8) Joliot, P., *Biochimica et Biophysica Acta (BBA) - Biophysics including Photosynthesis* **1965**, *102*, 116.
(9) Kok, B.; Forbush, B.; McGloin, M., *Photochemistry and Photobiology* **1970**, *11*, 457.
(10) Krewald, V.; Retegan, M.; Cox, N.; Messinger, J.; Lubitz, W.; DeBeer, S.; Neese, F.; Pantazis, D. A., *Chem. Sci.* **2015**, *6*, 1676.
(11) Ames, W.; Pantazis, D. A.; Krewald, V.; Cox, N.; Messinger, J.; Lubitz, W.; Neese, F., *J. Am. Chem. Soc.* **2011**, *133*, 19743.
(12) Bovi, D.; Narzi, D.; Guidoni, L., *Angew. Chem. Int. Ed.* **2013**, *52*, 11744.

(13) Britt, R. D.; Lorigan, G. A.; Sauer, K.; Klein, M. P.; Zimmermann, J.-L., *Biochim. Biophys. Acta - Bioenergetics* **1992**, *1140*, 95.
(14) Chatterjee, R.; Han, G.; Kern, J.; Gul, S.; Fuller, F. D.; Garachtchenko, A.; Young, I. D.; Weng, T.-C.; Nordlund, D.; Alonso-Mori, R.; Bergmann, U.; Sokaras, D.; Hatakeyama, M.; Yachandra, V. K.; Yano, J., *Chem. Sci.* **2016**, *7*, 5236.
(15) Cox, N.; Rapatskiy, L.; Su, J.-H.; Pantazis, D. A.; Sugiura, M.; Kulik, L.; Dorlet, P.; Rutherford, A. W.; Neese, F.; Boussac, A.; Lubitz, W.; Messinger, J., *J. Am. Chem. Soc.* **2011**, *133*, 3635.
(16) Cox, N.; Retegan, M.; Neese, F.; Pantazis, D. A.; Boussac, A.; Lubitz, W., *Science* **2014**, *345*, 804.
(17) DeRose, V. J.; Latimer, M. J.; Zimmermann, J.-L.; Mukerji, I.; Yachandra, V. K.; Sauer, K.; Klein, M. P., *Chem. Phys.* **1995**, *194*, 443.
(18) Kim, D. H.; Britt, R. D.; Klein, M. P.; Sauer, K., *Biochemistry* **1992**, *31*, 541.
(19) Kulik, L. V.; Epel, B.; Lubitz, W.; Messinger, J., *J. Am. Chem. Soc.* **2007**, *129*, 13421.
(20) Oyala, P. H.; Stich, T. A.; Debus, R. J.; Britt, R. D., *J. Am. Chem. Soc.* **2015**, *137*, 8829.
(21) Oyala, P. H.; Stich, T. A.; Stull, J. A.; Yu, F.; Pecoraro, V. L.; Britt, R. D., *Biochemistry* **2014**, *53*, 7914.
(22) Pantazis, D. A.; Ames, W.; Cox, N.; Lubitz, W.; Neese, F., *Angew. Chem. Int. Ed.* **2012**, *51*, 9935.
(23) Peloquin, J. M.; Campbell, K. A.; Randall, D. W.; Evanchik, M. A.; Pecoraro, V. L.; Armstrong, W. H.; Britt, R. D., *J. Am. Chem. Soc.* **2000**, *122*, 10926.
(24) Su, J.-H.; Cox, N.; Ames, W.; Pantazis, D. A.; Rapatskiy, L.; Lohmiller, T.; Kulik, L. V.; Dorlet, P.; Rutherford, A. W.; Neese, F.; Boussac, A.; Lubitz, W.; Messinger, J., *Biochim. Biophys. Acta - Bioenergetics* **2011**, *1807*, 829.
(25) Lohmiller, T.; Krewald, V.; Sedoud, A.; Rutherford, A. W.; Neese, F.; Lubitz, W.; Pantazis, D. A.; Cox, N., *J. Am. Chem. Soc.* **2017**, *139*, 14412.
(26) Rapatskiy, L.; Cox, N.; Savitsky, A.; Ames, W. M.; Sander, J.; Nowaczyk, M. M.; Rögner, M.; Boussac, A.; Neese, F.; Messinger, J.; Lubitz, W., *J. Am. Chem. Soc.* **2012**, *134*, 16619.
(27) Pérez Navarro, M.; Ames, W. M.; Nilsson, H.; Lohmiller, T.; Pantazis, D. A.; Rapatskiy, L.; Nowaczyk, M. M.; Neese, F.; Boussac, A.; Messinger, J.; Lubitz, W.; Cox, N., *Proc. Nat. Acad. Sci.* **2013**, *110*, 15561.
(28) Cox, N.; Pantazis, D. A.; Neese, F.; Lubitz, W., *Acc. Chem. Res.* **2013**, *46*, 1588.
(29) Siegbahn, P. E. M., *Acc. Chem. Res.* **2009**, *42*, 1871.
(30) Gupta, R.; Taguchi, T.; Lassalle-Kaiser, B.; Bominaar, E. L.; Yano, J.; Hendrich, M. P.; Borovik, A. S., *Proc. Nat. Acad. Sci.* **2015**, *112*, 5319.
(31) Krewald, V.; Retegan, M.; Neese, F.; Lubitz, W.; Pantazis, D. A.; Cox, N., *Inorg. Chem.* **2016**, *55*, 488.
(32) Yamauchi, T.; Mino, H.; Matsukawa, T.; Kawamori, A.; Ono, T.-a., *Biochemistry* **1997**, *36*, 7520.
(33) Boussac, A.; Rutherford, A. W., *Biochim. Biophys. Acta* **2000**, *1457*, 145.
(34) Boussac, A.; Un, S.; Horner, O.; Rutherford, A. W., *Biochemistry* **1998**, *37*, 4001.
(35) Haddy, A.; Lakshmi, K. V.; Brudvig, G. W.; Frank, H. A., *Biophys. J.* **2004**, *87*, 2885.
(36) Morton, J.; Chrysina, M.; Craig, V. S. J.; Akita, F.; Nakajima, Y.; Lubitz, W.; Cox, N.; Shen, J.-R.; Krausz, E., *Biochim. Biophys. Acta - Bioenergetics* **2018**, *1859*, 88.

(37) Suga, M.; Akita, F.; Sugahara, M.; Kubo, M.; Nakajima, Y.; Nakane, T.; Yamashita, K.; Umena, Y.; Nakabayashi, M.; Yamane, T.; Nakano, T.; Suzuki, M.; Masuda, T.; Inoue, S.; Kimura, T.; Nomura, T.; Yonekura, S.; Yu, L.-J.; Sakamoto, T.; Motomura, T.; Chen, J.-H.; Kato, Y.; Noguchi, T.; Tono, K.; Joti, Y.; Kameshima, T.; Hatsui, T.; Nango, E.; Tanaka, R.; Naitow, H.; Matsuura, Y.; Yamashita, A.; Yamamoto, M.; Nureki, O.; Yabashi, M.; Ishikawa, T.; Iwata, S.; Shen, J.-R., *Nature* **2017**, *543*, 131.

(38) Isobe, H.; Shoji, M.; Yamanaka, S.; Mino, H.; Umena, Y.; Kawakami, K.; Kamiya, N.; Shen, J. R.; Yamaguchi, K., *Phys. Chem. Chem. Phys.* **2014**, *16*, 11911.

(39) Tsui, E. Y.; Kanady, J. S.; Agapie, T., *Inorg. Chem.* **2013**, *52*, 13833.

(40) Mukherjee, S.; Stull, J. A.; Yano, J.; Stamatatos, T. C.; Pringouri, K.; Stich, T. A.; Abboud, K. A.; Britt, R. D.; Yachandra, V. K.; Christou, G., *Proc. Nat. Acad. Sci.* **2012**, *109*, 2257.

(41) Kanady, J. S.; Mendoza-Cortes, J. L.; Tsui, E. Y.; Nielsen, R. J.; Goddard, W. A.; Agapie, T., *J. Am. Chem. Soc.* **2013**, *135*, 1073.

(42) Kanady, J. S.; Tsui, E. Y.; Day, M. W.; Agapie, T., *Science* **2011**, *333*, 733.

(43) Krewald, V.; Neese, F.; Pantazis, D. A., *J. Am. Chem. Soc.* **2013**, *135*, 5726.

(44) Mukhopadhyay, S.; Mandal, S. K.; Bhaduri, S.; Armstrong, W. H., *Chem. Rev.* **2004**, *104*, 3981.

(45) Mullins, C. S.; Pecoraro, V. L., *Coord. Chem. Rev.* **2008**, *252*, 416.

(46) Paul, S.; Neese, F.; Pantazis, D. A., *Green Chem.* **2017**, *19*, 2309.

(47) Tsui, E. Y.; Tran, R.; Yano, J.; Agapie, T., *Nat. Chem.* **2013**, *5*, 293.

(48) Zhang, C.; Chen, C.; Dong, H.; Shen, J.-R.; Dau, H.; Zhao, J., *Science* **2015**, *348*, 690.

(49) Lee, H. B.; Tsui, E. Y.; Agapie, T., *Chem. Commun.* **2017**, *53*, 6832.

(50) Hewitt, I. J.; Tang, J.-K.; Madhu, N. T.; Clérac, R.; Buth, G.; Anson, C. E.; Powell, A. K., *Chem. Commun.* **2006**, 2650.

(51) Mishra, A.; Wernsdorfer, W.; Abboud, K. A.; Christou, G., *Chem. Commun.* **2005**, 54.

(52) Tsui, E. Y.; Agapie, T., *Proc. Nat. Acad. Sci.* **2013**, *110*, 10084.

(53) Lee, H. B.; Shiau, A. A.; Oyala, P. H.; Marchiori, D. A.; Gul, S.; Chatterjee, R.; Yano, J.; Britt, R. D.; Agapie, T., *J. Am. Chem. Soc.* **2018**, *140*, 17175.

(54) Lin, P.-H.; Tsui, E. Y.; Habib, F.; Murugesu, M.; Agapie, T., *Inorg. Chem.* **2016**, *55*, 6095.

(55) Kanady, J. S.; Lin, P.-H.; Carsch, K. M.; Nielsen, R. J.; Takase, M. K.; Goddard, W. A.; Agapie, T., *J. Am. Chem. Soc.* **2014**, *136*, 14373.

(56) Lohmiller, T.; Shelby, M. L.; Long, X.; Yachandra, V. K.; Yano, J., *J. Phys. Chem. B* **2015**, *119*, 13742.

(57) Ono, T.-a.; Rompel, A.; Mino, H.; Chiba, N., *Biophys. J.* **2001**, *81*, 1831.

(58) Kimura, Y.; Hasegawa, K.; Ono, T.-a., *Biochemistry* **2002**, *41*, 5844.

(59) Baffert, C.; Orio, M.; Pantazis, D. A.; Duboc, C.; Blackman, A. G.; Blondin, G.; Neese, F.; Deronzier, A.; Collomb, M.-N., *Inorg. Chem.* **2009**, *48*, 10281.

(60) Pei, Y.; Journaux, Y.; Kahn, O., *Inorg. Chem.* **1988**, *27*, 399.

(61) Gao, E.-Q.; Tang, J.-K.; Liao, D.-Z.; Jiang, Z.-H.; Yan, S.-P.; Wang, G.-L., *Inorg. Chem.* **2001**, *40*, 3134.

(62) Ribas, J.; Diaz, C.; Costa, R.; Journaux, Y.; Mathoniere, C.; Kahn, O.; Gleizes, A., *Inorg. Chem.* **1990**, *29*, 2042.

(63) Chaudhuri, P., *Coord. Chem. Rev.* **2003**, *243*, 143.
(64) DeGayner, J. A.; Jeon, I.-R.; Harris, T. D., *Chem. Sci.* **2015**, *6*, 6639.
(65) Jeon, I.-R.; Park, J. G.; Xiao, D. J.; Harris, T. D., *J. Am. Chem. Soc.* **2013**, *135*, 16845.
(66) Sánchez, R. H.; Betley, T. A., *J. Am. Chem. Soc.* **2018**, *140*, 16792.
(67) Boča, R., *Coord. Chem. Rev.* **2004**, *248*, 757.
(68) Kampert, E.; Janssen, F. F. B. J.; Boukhvalov, D. W.; Russcher, J. C.; Smits, J. M. M.; de Gelder, R.; de Bruin, B.; Christianen, P. C. M.; Zeitler, U.; Katsnelson, M. I.; Maan, J. C.; Rowan, A. E., *Inorg. Chem.* **2009**, *48*, 11903.
(69) Bordwell, F. G.; Ji, G. Z., *J. Org. Chem.* **1992**, *57*, 3019.
(70) Kütt, A.; Leito, I.; Kaljurand, I.; Sooväli, L.; Vlasov, V. M.; Yagupolskii, L. M.; Koppel, I. A., *J. Org. Chem.* **2006**, *71*, 2829.
(71) Baldwin, M. J.; Stemmler, T. L.; Riggs-Gelasco, P. J.; Kirk, M. L.; Penner-Hahn, J. E.; Pecoraro, V. L., *J. Am. Chem. Soc.* **1994**, *116*, 11349.
(72) Hagen, K. S.; Westmoreland, T. D.; Scott, M. J.; Armstrong, W. H., *J. Am. Chem. Soc.* **1989**, *111*, 1907.

APPENDIX 1

^{17}O-labeled [$Mn^{III}Mn_3^{IV}O_4$] and [$CaMn_3^{IV}O_4$] Complexes as Models of the Oxygen Evolving Complex in Photosystem II

Abstract

One of the most important questions about the mechanism of biological water oxidation at the oxygen evolving complex (OEC) of Photosystem II is the location of the substrate water molecules binding to the $CaMn_4$ core of the OEC. On the basis of previous FTIR spectroscopy, mass spectrometry, and W-band ^{17}O EPR studies on the S_2 state, three classes of fast, solvent exchangeable oxygen nuclei have been identified as potential substrate binding sites: terminal Ca-H_2O, terminal Mn-OH/H_2O, and a unique bridging μ^3-oxo. Beside dinuclear $Mn^{III}Mn^{IV}(\mu^2\text{-}O)_2$ complexes, relevant spectroscopic studies on ^{17}O labeled higher nuclearity complexes mimicking the structure of the OEC are absent in the literature. Herein, we report the synthesis and D-band pulsed EPR data for ^{17}O labeled $[MnMn_3^{IV}O_4]$ and $[CaMn_3^{IV}O_4]$ complexes as models of the OEC. Such complexes resemble aspects of structure, redox state, and spin state; characterization of μ^3-oxos in such complexes provide valuable benchmarking parameters for future mechanistic studies.

A1.1) Introduction

Despite extensive biochemical, spectroscopic, and computational studies, the mechanism of biological water oxidation by the oxygen evolving complex (OEC) of Photosystem II remains a subject of significant debate.[1-3] Recent studies employing femtosecond X-ray free electron laser (XFEL) techniques provide opportunities to observe time-resolved structural and spectroscopic changes in the OEC along the S-state catalytic cycle.[4-11] Thus far, the structure and spectroscopic properties of the O−O bond forming S_4 state remains elusive, and characterization of earlier S_0−S_3 intermediates heavily influence mechanistic proposals for O−O bond formation.[12-21] Importantly, the location of the substrate water binding to the $CaMn_4$ core of the OEC is debated.[22-23] On the basis of previous FTIR spectroscopy, mass spectrometry, and W-band ^{17}O EPR studies on the S_0 and S_2 states, three classes of fast, solvent exchangeable oxygen nuclei have been proposed as potential substrate binding sites: terminal Ca-H_2O, terminal Mn-OH/H_2O, and a unique bridging μ^3-oxo (Figure 1).[24-27] The ^{17}O hyperfine coupling constants for the exchangeable

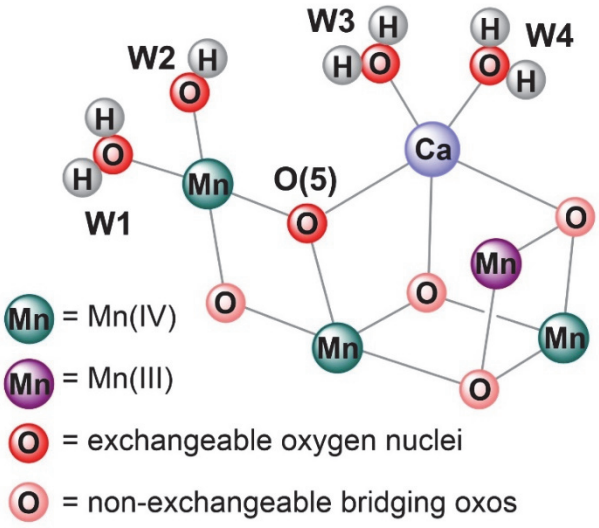

Figure 1. Proposed structure of the $CaMn_4$ core of the S_2 state of the OEC showing the proposed location of the fast, solvent exchangeable oxygen nuclei: terminal Mn(Ca)-bound aquo or hydroxo moieties W1~W4 and a unique, bridging μ^3-O(5).

oxygen nuclei at ~10 MHz, ~5 MHz, and <2 MHz have been assigned to bridging oxo, terminal Mn-aquo(hydroxo), and Ca-aquo, respectively.[22-23] A non-competitive inhibitor, ammonia, binds to the S_2 state via displacement of water at W1.[18, 20] While the precise mechanism of ammonia inhibition and the changes in ^{17}O spectral features upon ammonia binding are not fully understood, mechanistic proposals such as (1) formation of a terminal oxo at W2 and nucleophilic attack by W3 or (2) bridging oxo coupling involving O(5) remain viable.

To support the assignment of observed ^{17}O hyperfine interactions to specific moieties in the OEC, relevant synthetic and EPR spectroscopic studies on ^{17}O-labeled Mn model complexes need to be performed.[28] Such studies remain rare, and can be summarized as follows. Incorporation of ^{17}O label was achieved by incubation of the antiferromagnetically coupled (S = 1/2), dinuclear complex $[(bpy)_4Mn^{III}Mn^{IV}O_2][ClO_4]_3$ with ^{17}O water.[29] The $[Mn^{III}Mn^{IV}O_2(OAc)]^{2+}$ core of a related synthetic complex and the dimanganese catalase was also labeled through a similar incubation procedure.[28] The experimental ^{17}O isotropic hyperfine coupling constants were found to be similar in the three species mentioned above, varying from +5.2 to +6.4 MHz.[28] The insensitivity of the ^{17}O coupling to the exact geometry of the $[Mn^{III}Mn^{IV}O_2]$ core was used to suggest that μ-oxos in related systems may have similar isotropic coupling values. On the other hand, the ^{17}O hyperfine anisotropy is more sensitive to the overall geometry and electronic structure of the complex. In general, ^{17}O hyperfine tensors depend on the relative contribution of the different Mn centers to the overall effective spin state of the complex: the contribution from each metal center is described in terms of spin projection coefficients, which depend on the nature and magnitude of the magnetic exchange coupling interactions.[16, 23, 30] On the basis that

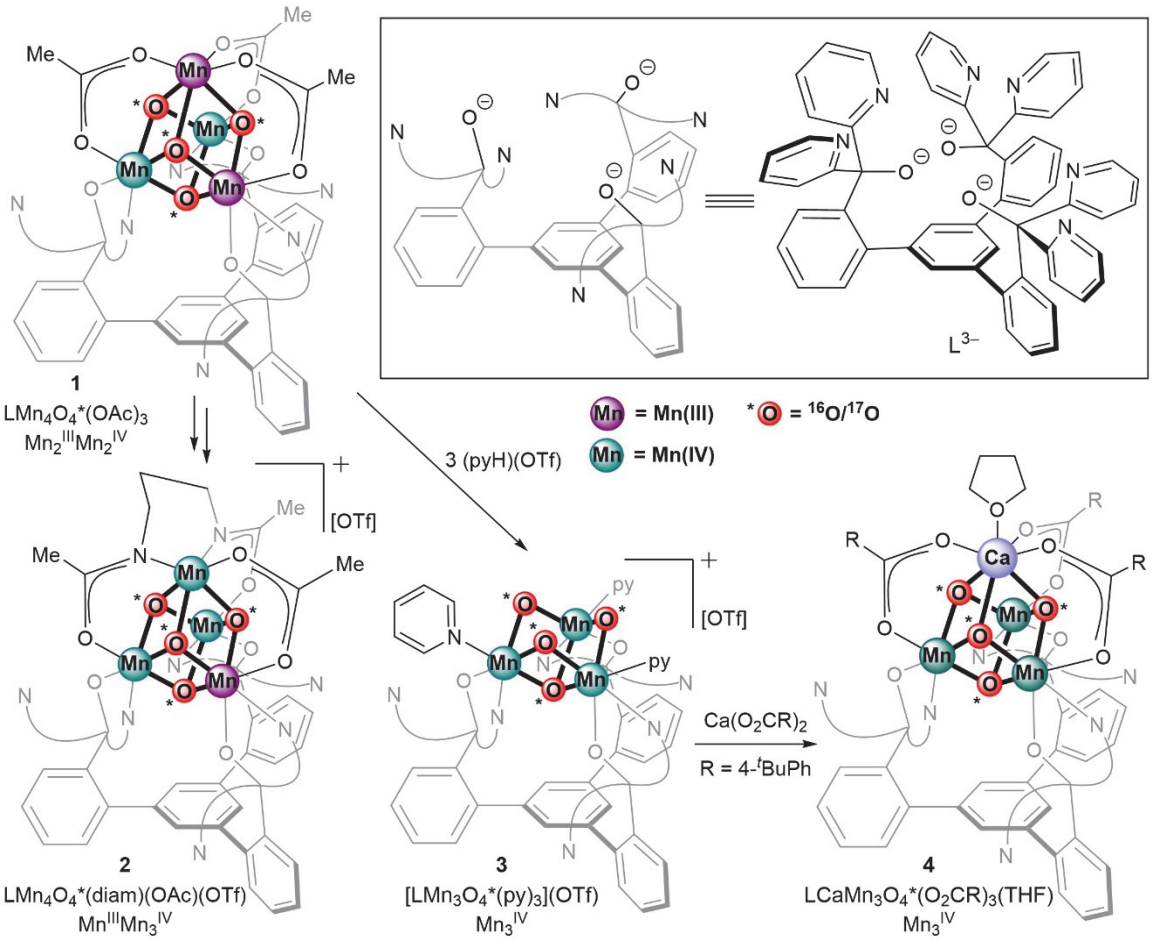

Figure 2. Synthesis of complexes **1**~**4**.

magnetic exchange coupling interactions in tetranuclear Mn complexes are sensitive to small structural changes,[31] spectroscopic studies on well-defined, ^{17}O labeled high-nuclearity complexes are crucial. Thus far, such studies on ^{17}O labeled tri- and tetranuclear Mn model complexes have not been reported.

Herein, we report the synthesis and high-field (D-band) pulsed EPR data for ^{17}O-labeled $[Mn^{III}Mn_3^{IV}O_4]$, $[Mn_3^{IV}O_4]$, and $[CaMn_3^{IV}O_4]$ complexes. This unique series of compounds resemble aspects of structure, redox state, and spin state. With an $S = 1/2$ ground state, the $[Mn^{III}Mn_3^{IV}O_4]$ complex resembles the spin state and spectroscopy of the S_2 state. With an $S = 9/2$ ground state, the $[Ca^{II}Mn_3^{IV}O_4]$ complex closely mimics the

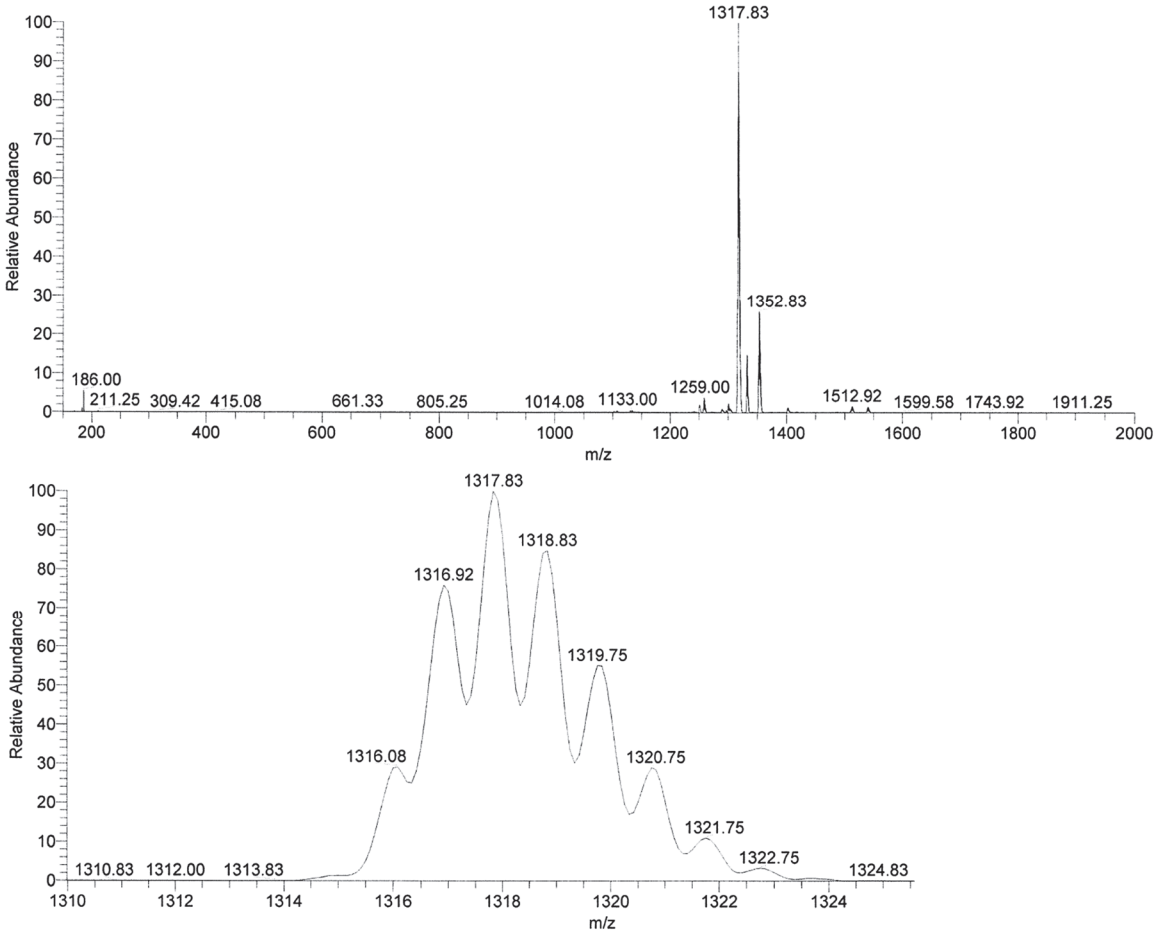

Figure 3. ESI-MS of ^{17}O labeled complex **1**. Mass of $LMn_4(^{16}O)_4(OAc)_3$ = 1316.

cuboidal subsite of the OEC. Characterization of μ^3-oxos in such complexes provide valuable benchmarking parameters for future mechanistic studies.

A1.2) Synthesis

Treatment of the previously reported $LMn_3^{II}(OAc)_3$ complex with $Mn(OTf)_2$ and KO_2 leads to the formation of $LMn_4^{III}O_3(OAc)_3$.[32] Oxidative incorporation of ^{18}O-water to the $[Mn_4^{III}O_3]$ species leads to a mixture of isotopologues $LMn_2^{III}Mn_2^{IV}(^{16}O)_n(^{18}O)_{(4-n)}(OAc)_3$ (n = 0~4), in which the ^{18}O label is scrambled in all four positions.[33] Incubation of the $[Mn_2^{III}Mn_2^{IV}(^{16}O)_4]$ species in ^{18}O water does not result in label incorporation. Analogously, treatment of $LMn_4^{III}O_3(OAc)_3$ with 30 equiv ^{17}O-water, 2 equiv Et_3N, and 4

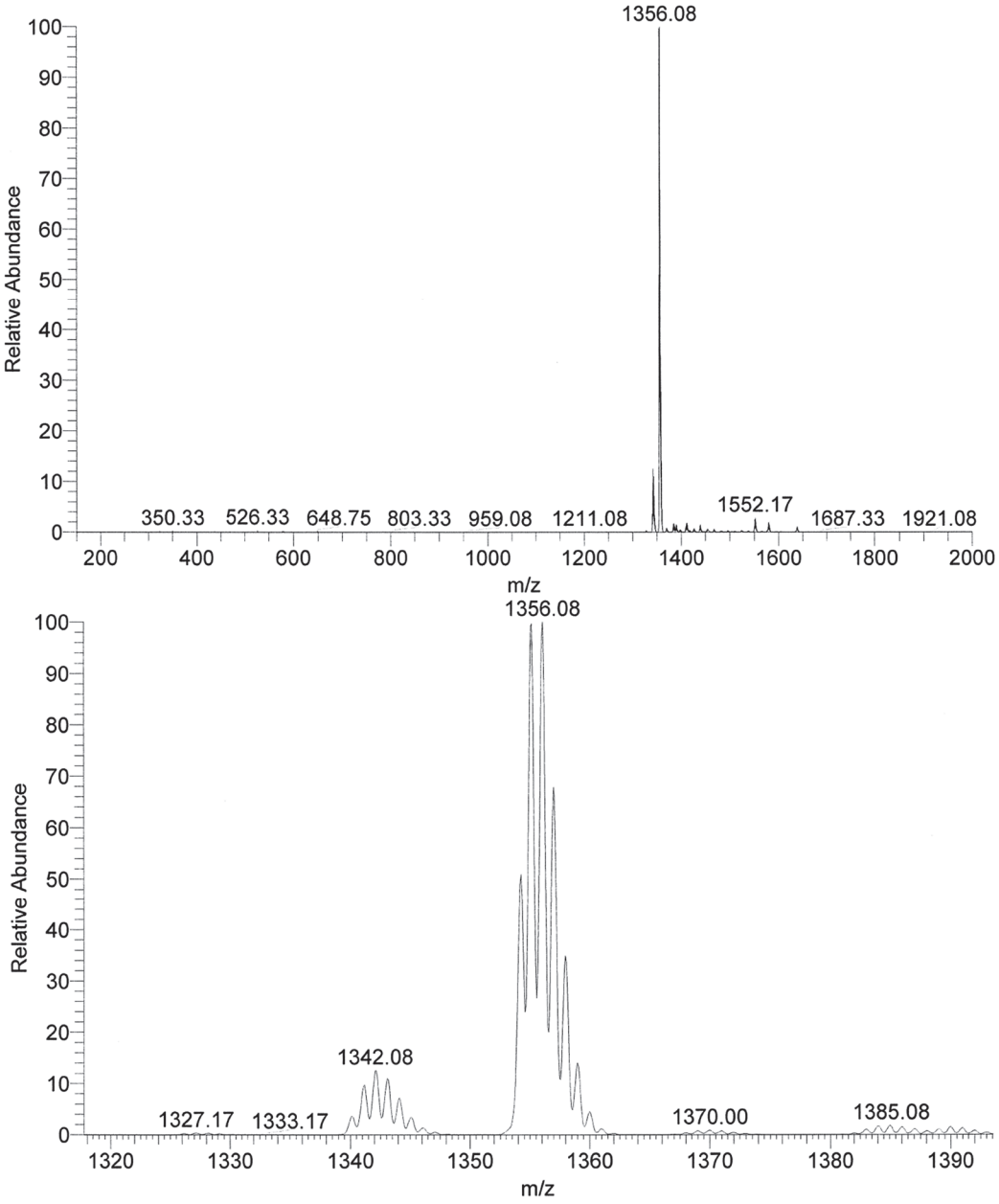

Figure 4. ESI-MS of ^{17}O labeled complex **2**. Mass of $LMn_4(^{16}O)_4(diam)(OAc) = 1354$.

equiv Fc(OTf) leads to a mixture of isotopologues $LMn_2^{III}Mn_2^{IV}(^{16}O)_n(^{17}O)_{(4-n)}(OAc)_3$ (n = 0~4): The distribution of ESI-MS peaks at *m*/*z* = 1317−1321 is consistent with this assignment (Figure 3). On the basis of the largest intensity observed for the peak at *m*/*z* = 1319, $[Mn_2^{III}Mn_2^{IV}(^{16}O)_2(^{17}O)_2]$ is assigned qualitatively as the major isotopologue. The use of $Fc(PF_6)$ instead of Fc(OTf) leads to the oxidative incorporation of fluoride, resulting

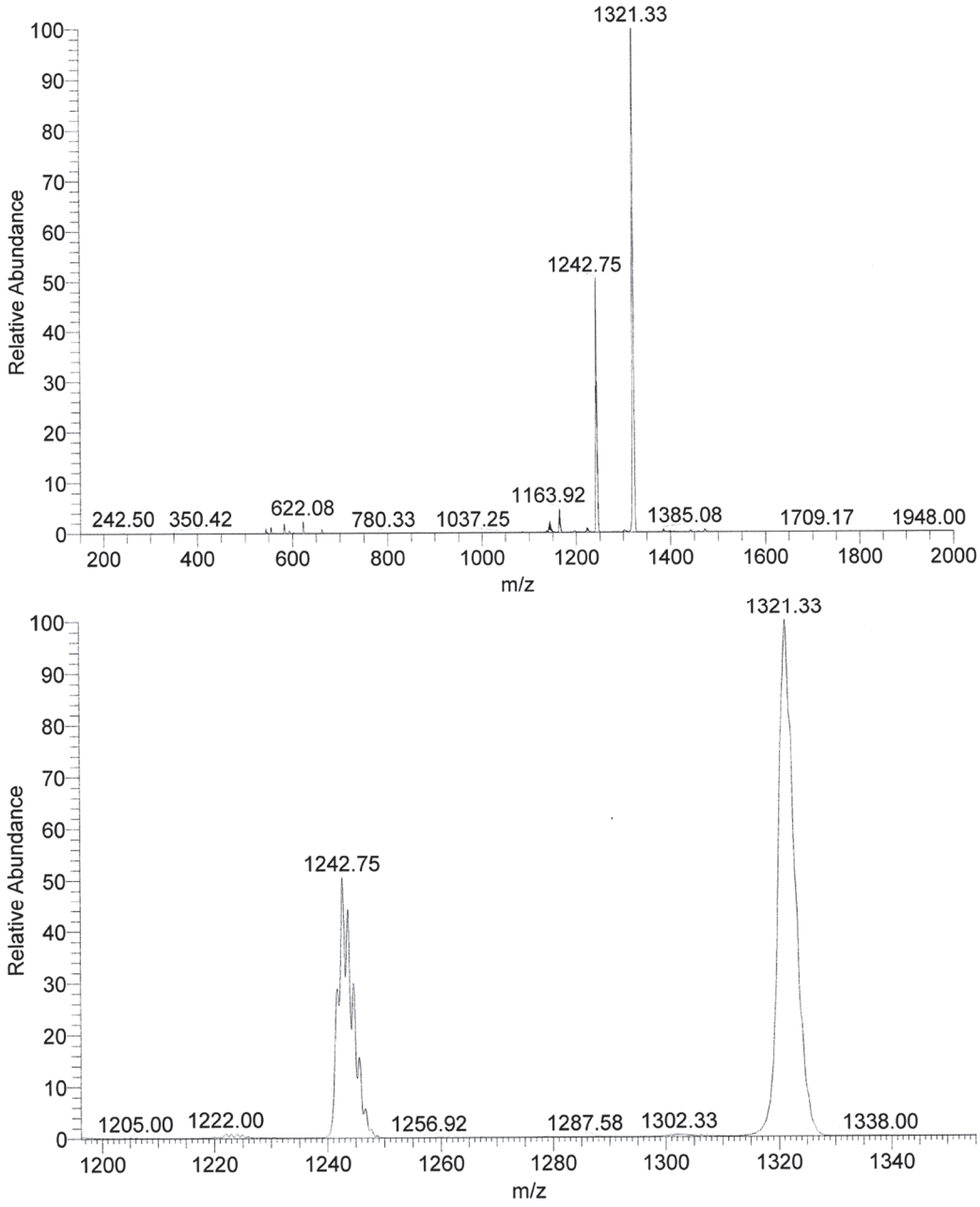

Figure 5. ESI-MS of ^{17}O labeled complex **3**. Mass of $LMn_4(^{16}O)_3(py)_2 = 1242$.

in the formation of $LMn_3^{III}Mn^{IV}O_3F(OAc)_3$ (Figure 8). For ease of notation, the mixture of $^{16}O/^{17}O$ will be shown as O^* (e.g. $LMn_2^{III}Mn_2^{IV}O^*_4(OAc)_3$) (**1**, Figure 2). Substitution of two acetate moieties in **1** with a tethered diamidate ligand ($diam^{2-}$) followed by one electron oxidation leads to the formation of $[LMn^{III}Mn_3^{IV}O^*_4(diam)(OAc)][OTf]$ (**2**): the distribution of ESI-MS peaks at $m/z = 1355\sim1359$ is consistent with this assignment (Figure

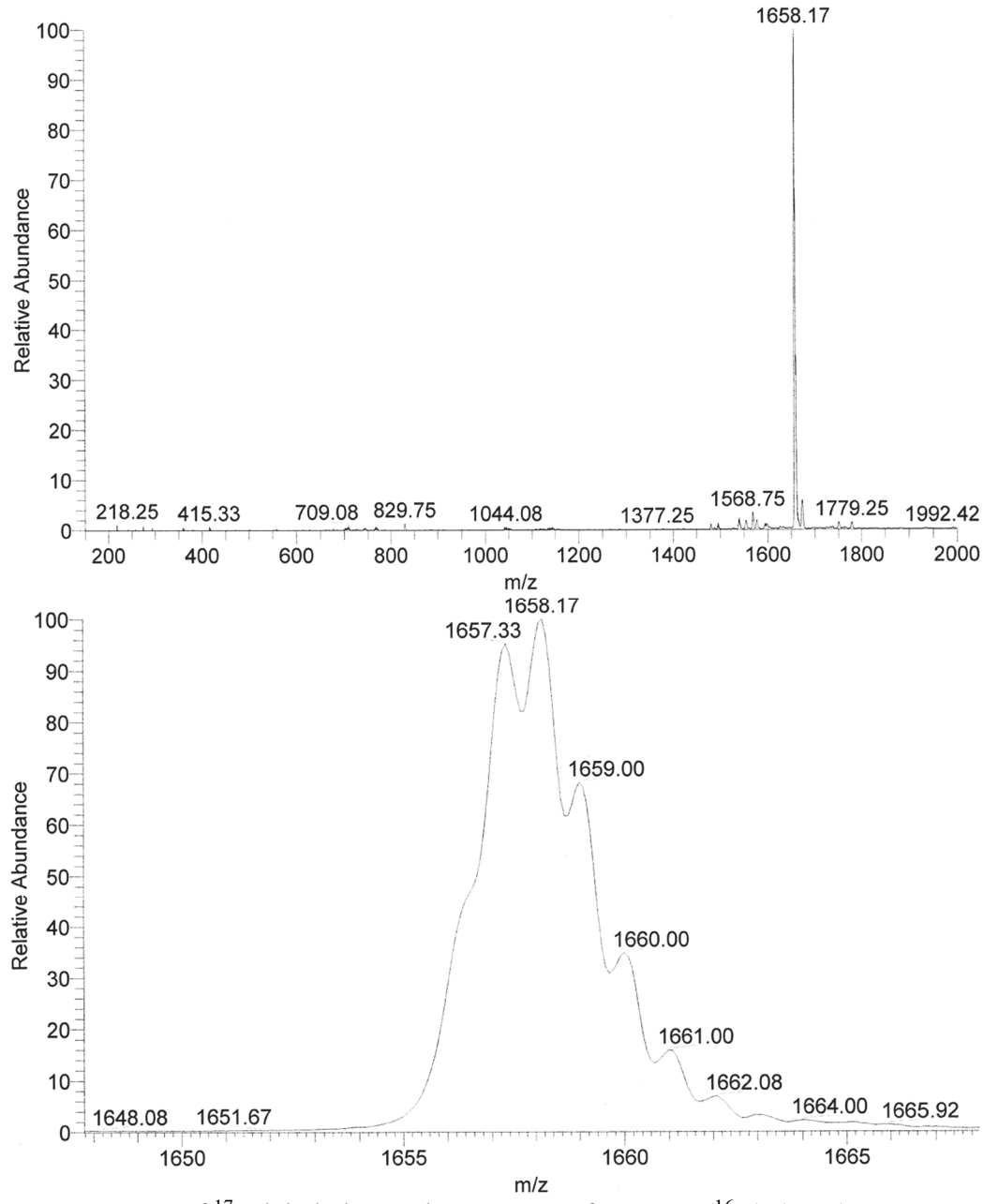

Figure 6. ESI-MS of ^{17}O labeled complex **4**. Mass of $LCaMn_3(^{16}O)_4(OBz)_3$ = 1655.

4).[31] With Mn oxidation states and EPR spectrum resembling the S_2 state, complex **2** is a valuable target for further spectroscopic studies involving ^{17}O (Chapter 3). Treatment of **1** or **2** with 3 equiv (pyH)(OTf) leads to the formation of $[LMn_3^{IV}O^*_4][OTf]$ (**3**), featuring an incomplete cubane core resembling a subsite of the Ca-depleted OEC (Chapter 5). The distribution of ESI-MS peaks at *m*/*z* = 1242~1246 and 1321~1324 is consistent with the

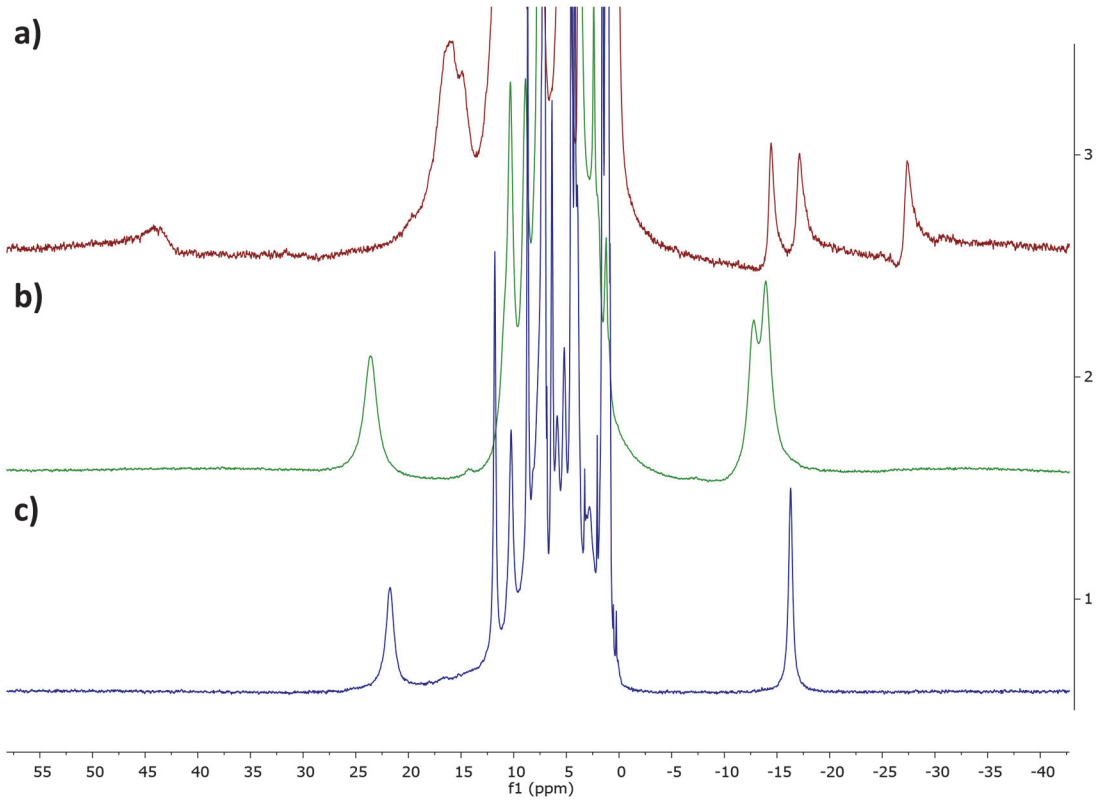

Figure 7. ^{1}H NMR spectra of ^{17}O labeled complexes a) **2**, b) **3**, and c) **4**.

mass of $[LMn_3^{IV}O_4^{*}(py)_2]^{+}$ and $[LMn_3^{IV}O_4^{*}(py)_3]^{+}$, respectively (Figure 5). Previous magnetic and spectroscopic studies indicate an S = 3/2 ground state for **3** (Chapter 5). Reconstitution of the cubane is possible by treating **3** with the choice of metal carboxylate or by addition of metal triflates and the choice of bridging ligands. Accordingly, treatment of **3** with Ca(4-^{t}Bu-benzoate)$_2$ leads to the formation of the highly soluble cuboidal complex $LCaMn_3^{IV}O^{*}_4(OBz)_3$ (**4**): the distribution of ESI-MS peaks at m/z = 1656~1660 is consistent with this assignment (Figure 6). With an S = 9/2 ground state, complex **4** closely resembles the $CaMn_3O_4$ subsite of the OEC (Chapter 5). The ^{1}H NMR of ^{17}O labeled complexes **2~4** are identical to their unlabeled counterparts (Figure 7). Overall, complexes **2~4** represent a unique series of ^{17}O labeled model complexes that mimic

aspects of structure, redox state, and spectroscopy in the OEC. D-band pulse EPR studies are ongoing.

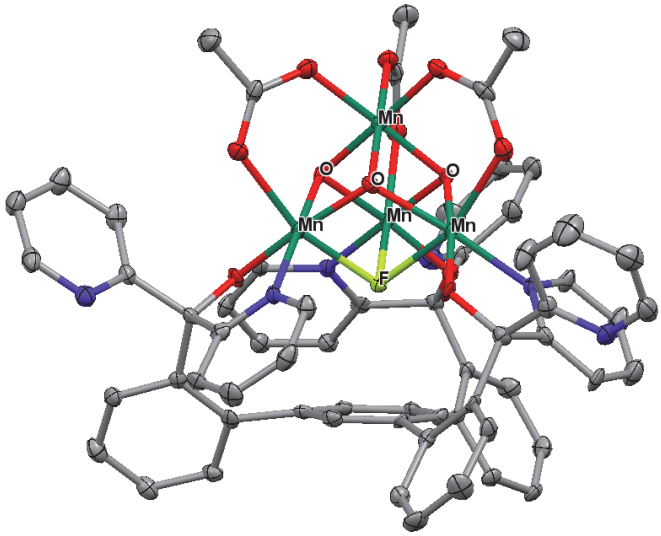

Figure 8. Structure of $LMn_3^{III}Mn^{IV}O_3F(OAc)_3$, obtained via oxidative fluoride incorporation at $LMn_4^{III}O_3(OAc)_3$ using $(Fc)(PF_6)$.

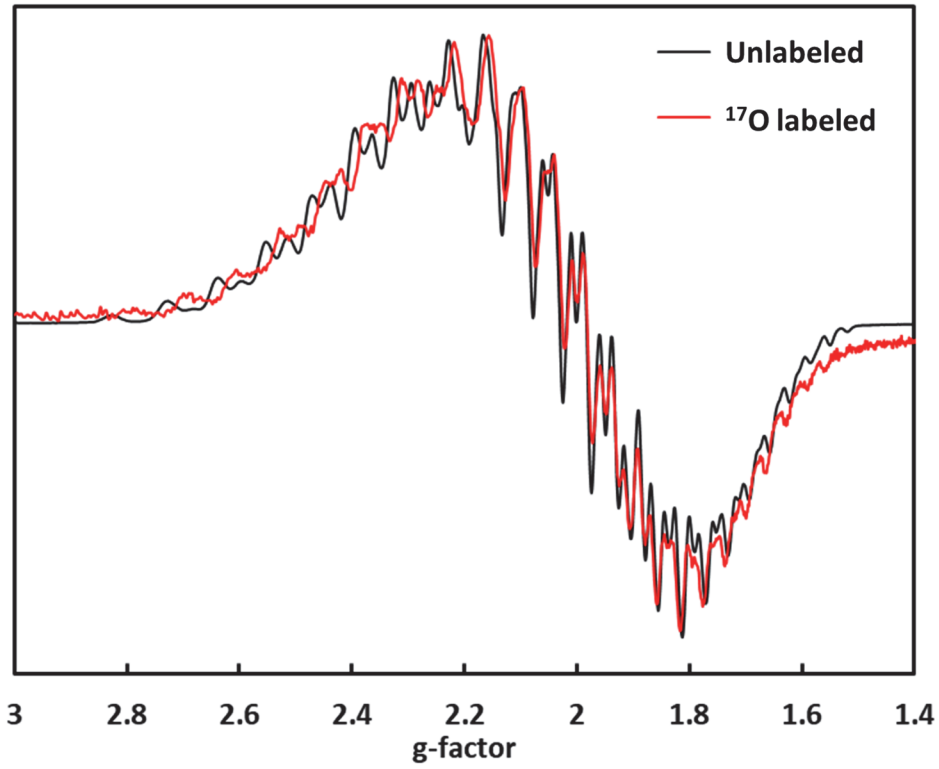

Figure 9. Comparison of the X-band EPR spectra of unlabeled and ^{17}O labeled **2**.

A1.3) References

(1) Cox, N.; Pantazis, D. A.; Neese, F.; Lubitz, W., *Acc. Chem. Res.* **2013**, *46*, 1588.
(2) Shen, J.-R., *Annu. Rev. Plant Biol.* **2015**, *66*, 23.
(3) Yano, J.; Yachandra, V., *Chem. Rev.* **2014**, *114*, 4175.
(4) Kern, J.; Alonso-Mori, R.; Tran, R.; Hattne, J.; Gildea, R. J.; Echols, N.; Glöckner, C.; Hellmich, J.; Laksmono, H.; Sierra, R. G.; Lassalle-Kaiser, B.; Koroidov, S.; Lampe, A.; Han, G.; Gul, S.; DiFiore, D.; Milathianaki, D.; Fry, A. R.; Miahnahri, A.; Schafer, D. W.; Messerschmidt, M.; Seibert, M. M.; Koglin, J. E.; Sokaras, D.; Weng, T.-C.; Sellberg, J.; Latimer, M. J.; Grosse-Kunstleve, R. W.; Zwart, P. H.; White, W. E.; Glatzel, P.; Adams, P. D.; Bogan, M. J.; Williams, G. J.; Boutet, S.; Messinger, J.; Zouni, A.; Sauter, N. K.; Yachandra, V. K.; Bergmann, U.; Yano, J., *Science* **2013**, *340*, 491.
(5) Kern, J.; Tran, R.; Alonso-Mori, R.; Koroidov, S.; Echols, N.; Hattne, J.; Ibrahim, M.; Gul, S.; Laksmono, H.; Sierra, R. G.; Gildea, R. J.; Han, G.; Hellmich, J.; Lassalle-Kaiser, B.; Chatterjee, R.; Brewster, A. S.; Stan, C. A.; Glöckner, C.; Lampe, A.; DiFiore, D.; Milathianaki, D.; Fry, A. R.; Seibert, M. M.; Koglin, J. E.; Gallo, E.; Uhlig, J.; Sokaras, D.; Weng, T.-C.; Zwart, P. H.; Skinner, D. E.; Bogan, M. J.; Messerschmidt, M.; Glatzel, P.; Williams, G. J.; Boutet, S.; Adams, P. D.; Zouni, A.; Messinger, J.; Sauter, N. K.; Bergmann, U.; Yano, J.; Yachandra, V. K., *Nat. Commun.* **2014**, *5*, 4371.
(6) Kupitz, C.; Basu, S.; Grotjohann, I.; Fromme, R.; Zatsepin, N. A.; Rendek, K. N.; Hunter, M. S.; Shoeman, R. L.; White, T. A.; Wang, D.; James, D.; Yang, J.-H.; Cobb, D. E.; Reeder, B.; Sierra, R. G.; Liu, H.; Barty, A.; Aquila, A. L.; Deponte, D.; Kirian, R. A.; Bari, S.; Bergkamp, J. J.; Beyerlein, K. R.; Bogan, M. J.; Caleman, C.; Chao, T.-C.; Conrad, C. E.; Davis, K. M.; Fleckenstein, H.; Galli, L.; Hau-Riege, S. P.; Kassemeyer, S.; Laksmono, H.; Liang, M.; Lomb, L.; Marchesini, S.; Martin, A. V.; Messerschmidt, M.; Milathianaki, D.; Nass, K.; Ros, A.; Roy-Chowdhury, S.; Schmidt, K.; Seibert, M.; Steinbrener, J.; Stellato, F.; Yan, L.; Yoon, C.; Moore, T. A.; Moore, A. L.; Pushkar, Y.; Williams, G. J.; Boutet, S.; Doak, R. B.; Weierstall, U.; Frank, M.; Chapman, H. N.; Spence, J. C. H.; Fromme, P., *Nature* **2014**, *513*, 261.
(7) Sauter, N. K.; Echols, N.; Adams, P. D.; Zwart, P. H.; Kern, J.; Brewster, A. S.; Koroidov, S.; Alonso-Mori, R.; Zouni, A.; Messinger, J.; Bergmann, U.; Yano, J.; Yachandra, V. K., *Nature* **2016**, *533*, E1.
(8) Suga, M.; Akita, F.; Hirata, K.; Ueno, G.; Murakami, H.; Nakajima, Y.; Shimizu, T.; Yamashita, K.; Yamamoto, M.; Ago, H.; Shen, J.-R., *Nature* **2014**, *517*, 99.
(9) Suga, M.; Akita, F.; Sugahara, M.; Kubo, M.; Nakajima, Y.; Nakane, T.; Yamashita, K.; Umena, Y.; Nakabayashi, M.; Yamane, T.; Nakano, T.; Suzuki, M.; Masuda, T.; Inoue, S.; Kimura, T.; Nomura, T.; Yonekura, S.; Yu, L.-J.; Sakamoto, T.; Motomura, T.; Chen, J.-H.; Kato, Y.; Noguchi, T.; Tono, K.; Joti, Y.; Kameshima, T.; Hatsui, T.; Nango, E.; Tanaka, R.; Naitow, H.; Matsuura, Y.; Yamashita, A.; Yamamoto, M.; Nureki, O.; Yabashi, M.; Ishikawa, T.; Iwata, S.; Shen, J.-R., *Nature* **2017**, *543*, 131.
(10) Young, I. D.; Ibrahim, M.; Chatterjee, R.; Gul, S.; Fuller, F. D.; Koroidov, S.; Brewster, A. S.; Tran, R.; Alonso-Mori, R.; Kroll, T.; Michels-Clark, T.; Laksmono, H.; Sierra, R. G.; Stan, C. A.; Hussein, R.; Zhang, M.; Douthit, L.; Kubin, M.; de Lichtenberg, C.; Vo Pham, L.; Nilsson, H.; Cheah, M. H.; Shevela, D.; Saracini, C.; Bean, M. A.; Seuffert, I.; Sokaras, D.; Weng, T.-C.; Pastor, E.; Weninger, C.; Fransson, T.; Lassalle, L.; Bräuer, P.; Aller, P.; Docker, P. T.; Andi, B.; Orville, A. M.; Glownia, J. M.; Nelson, S.;

Sikorski, M.; Zhu, D.; Hunter, M. S.; Lane, T. J.; Aquila, A.; Koglin, J. E.; Robinson, J.; Liang, M.; Boutet, S.; Lyubimov, A. Y.; Uervirojnangkoorn, M.; Moriarty, N. W.; Liebschner, D.; Afonine, P. V.; Waterman, D. G.; Evans, G.; Wernet, P.; Dobbek, H.; Weis, W. I.; Brunger, A. T.; Zwart, P. H.; Adams, P. D.; Zouni, A.; Messinger, J.; Bergmann, U.; Sauter, N. K.; Kern, J.; Yachandra, V. K.; Yano, J., *Nature* **2016**, *540*, 453.

(11) Kern, J.; Chatterjee, R.; Young, I. D.; Fuller, F. D.; Lassalle, L.; Ibrahim, M.; Gul, S.; Fransson, T.; Brewster, A. S.; Alonso-Mori, R.; Hussein, R.; Zhang, M.; Douthit, L.; de Lichtenberg, C.; Cheah, M. H.; Shevela, D.; Wersig, J.; Seuffert, I.; Sokaras, D.; Pastor, E.; Weninger, C.; Kroll, T.; Sierra, R. G.; Aller, P.; Butryn, A.; Orville, A. M.; Liang, M.; Batyuk, A.; Koglin, J. E.; Carbajo, S.; Boutet, S.; Moriarty, N. W.; Holton, J. M.; Dobbek, H.; Adams, P. D.; Bergmann, U.; Sauter, N. K.; Zouni, A.; Messinger, J.; Yano, J.; Yachandra, V. K., *Nature* **2018**, *563*, 421.

(12) Ames, W.; Pantazis, D. A.; Krewald, V.; Cox, N.; Messinger, J.; Lubitz, W.; Neese, F., *J. Am. Chem. Soc.* **2011**, *133*, 19743.

(13) Boussac, A.; Ugur, I.; Marion, A.; Sugiura, M.; Kaila, V. R. I.; Rutherford, A. W., *Biochim. Biophys. Acta - Bioenergetics* **2018**, *1859*, 342.

(14) Chatterjee, R.; Han, G.; Kern, J.; Gul, S.; Fuller, F. D.; Garachtchenko, A.; Young, I. D.; Weng, T.-C.; Nordlund, D.; Alonso-Mori, R.; Bergmann, U.; Sokaras, D.; Hatakeyama, M.; Yachandra, V. K.; Yano, J., *Chem. Sci.* **2016**, *7*, 5236.

(15) Cox, N.; Rapatskiy, L.; Su, J.-H.; Pantazis, D. A.; Sugiura, M.; Kulik, L.; Dorlet, P.; Rutherford, A. W.; Neese, F.; Boussac, A.; Lubitz, W.; Messinger, J., *J. Am. Chem. Soc.* **2011**, *133*, 3635.

(16) Cox, N.; Retegan, M.; Neese, F.; Pantazis, D. A.; Boussac, A.; Lubitz, W., *Science* **2014**, *345*, 804.

(17) Kulik, L. V.; Epel, B.; Lubitz, W.; Messinger, J., *J. Am. Chem. Soc.* **2007**, *129*, 13421.

(18) Oyala, P. H.; Stich, T. A.; Debus, R. J.; Britt, R. D., *J. Am. Chem. Soc.* **2015**, *137*, 8829.

(19) Pantazis, D. A.; Ames, W.; Cox, N.; Lubitz, W.; Neese, F., *Angew. Chem. Int. Ed.* **2012**, *51*, 9935.

(20) Pérez Navarro, M.; Ames, W. M.; Nilsson, H.; Lohmiller, T.; Pantazis, D. A.; Rapatskiy, L.; Nowaczyk, M. M.; Neese, F.; Boussac, A.; Messinger, J.; Lubitz, W.; Cox, N., *Proc. Nat. Acad. Sci.* **2013**, *110*, 15561.

(21) Su, J.-H.; Cox, N.; Ames, W.; Pantazis, D. A.; Rapatskiy, L.; Lohmiller, T.; Kulik, L. V.; Dorlet, P.; Rutherford, A. W.; Neese, F.; Boussac, A.; Lubitz, W.; Messinger, J., *Biochim. Biophys. Acta - Bioenergetics* **2011**, *1807*, 829.

(22) Lohmiller, T.; Krewald, V.; Sedoud, A.; Rutherford, A. W.; Neese, F.; Lubitz, W.; Pantazis, D. A.; Cox, N., *J. Am. Chem. Soc.* **2017**, *139*, 14412.

(23) Rapatskiy, L.; Cox, N.; Savitsky, A.; Ames, W. M.; Sander, J.; Nowaczyk, M. M.; Rögner, M.; Boussac, A.; Neese, F.; Messinger, J.; Lubitz, W., *J. Am. Chem. Soc.* **2012**, *134*, 16619.

(24) Hillier, W.; Wydrzynski, T., *Coord. Chem. Rev.* **2008**, *252*, 306.

(25) Nilsson, H.; Rappaport, F.; Boussac, A.; Messinger, J., *Nat. Commun.* **2014**, *5*, 4305.

(26) Noguchi, T., *Coord. Chem. Rev.* **2008**, *252*, 336.

(27) Noguchi, T.; Sugiura, M., *Biochemistry* **2002**, *41*, 15706.

(28) Rapatskiy, L.; Ames, W. M.; Pérez-Navarro, M.; Savitsky, A.; Griese, J. J.; Weyhermüller, T.; Shafaat, H. S.; Högbom, M.; Neese, F.; Pantazis, D. A.; Cox, N., *J. Phys. Chem. B* **2015**, *119*, 13904.
(29) Usov, O. M.; Grigoryants, V. M.; Tagore, R.; Brudvig, G. W.; Scholes, C. P., *J. Am. Chem. Soc.* **2007**, *129*, 11886.
(30) Isobe, H.; Shoji, M.; Yamanaka, S.; Mino, H.; Umena, Y.; Kawakami, K.; Kamiya, N.; Shen, J. R.; Yamaguchi, K., *Phys. Chem. Chem. Phys.* **2014**, *16*, 11911.
(31) Lee, H. B.; Shiau, A. A.; Oyala, P. H.; Marchiori, D. A.; Gul, S.; Chatterjee, R.; Yano, J.; Britt, R. D.; Agapie, T., *J. Am. Chem. Soc.* **2018**, *140*, 17175.
(32) Kanady, J. S.; Tran, R.; Stull, J. A.; Lu, L.; Stich, T. A.; Day, M. W.; Yano, J.; Britt, R. D.; Agapie, T., *Chem. Sci.* **2013**, *4*, 3986.
(33) Kanady, J. S.; Mendoza-Cortes, J. L.; Tsui, E. Y.; Nielsen, R. J.; Goddard, W. A.; Agapie, T., *J. Am. Chem. Soc.* **2013**, *135*, 1073.

APPENDIX 2

Tetranuclear [$Mn_4^{IV}O_4$] Complexes as Spectroscopic Models of the S_3 State of the Oxygen Evolving Complex in Photosystem II

Abstract

The S_3 state is the last observable intermediate prior to O−O bond formation at the oxygen evolving complex (OEC) of Photosystem II, and its electronic structure has been assigned to a homovalent Mn_4^{IV} core with an $S = 3$ ground state. While characterization of the further one electron oxidized S_4 state remains a challenge, valuable mechanistic insight can be obtained through synthetic and spectroscopic studies on complexes mirroring the redox and spin state of the S_3 state. Herein, we report our ongoing efforts on the synthesis, X-ray spectroscopy, and multifrequency EPR spectroscopy for unique tetranuclear $[Mn_4^{IV}O_4]$ complexes as models of S_3 state. Preliminary results show that the $[Mn_4^{IV}O_4]$ complex has an $S = 3$ ground state, resembling the electronic structure of the S_3 state. The $S = 3$ effective spin ground state may arise from an ααaβ spin topology arising from a trimer-monomer magnetic coupling model of pseudo-octahedral Mn^{IV} centers.

A2.1) Introduction

Mechanistic studies of biological water oxidation at the oxygen evolving complex (OEC) of Photosystem II (PSII) are performed in the context of the Joliot-Kok cycle of S_n (n = 0−4) states.[1-4] Starting from the dark stable S_1 state, sequential light-induced one electron oxidations lead to the progression to higher S_n states, resulting in the formation of the S_3 state, the last observable intermediate prior to dioxygen formation.[5-6] Involving a series of elementary steps that include H^+ transfer, substrate H_2O binding, and e^- transfer, the $S_2 \rightarrow S_3$ transition represents a critical step in the catalytic cycle of the OEC; despite being the subject of extensive biochemical, structural, spectroscopic, and computational studies, the S_3 state remains poorly understood, both in terms of its (electronic) structure and mechanism of formation.[7-24] To obtain a better understanding of the S_3 state and beyond, toward the elusive S_4 state, systematic structure-function (property) studies on relevant model complexes may be necessary. Despite significant efforts to prepare tetra- and pentanuclear complexes as models of the OEC, relevant complexes in terms of structure, redox state, spectroscopy, and reactivity are rare.[25-39]

On the basis of EPR, MCD, and X-ray spectroscopic studies, the electronic structure of the S_3 state has been assigned to a homovalent Mn_4^{IV} core with an $S = 3$ spin ground state.[5, 40-42] Two structural isomers S_3^A (dimer-of-dimers) and S_3^B (trimer-monomer) with the same $S = 3$ spin state have been proposed to account for the spectroscopic heterogeneity of the S_3 state (Figure 1a).[5, 43] A similar structural isomerism has been proposed for the S_2 state.[25, 44] Such proposed structural changes may lead to differences in the nature and magnitude of the magnetic exchange interactions (J_{ij}) between adjacent Mn centers, which in turn affect not only the spin ground state of the cluster but also the observed sign and

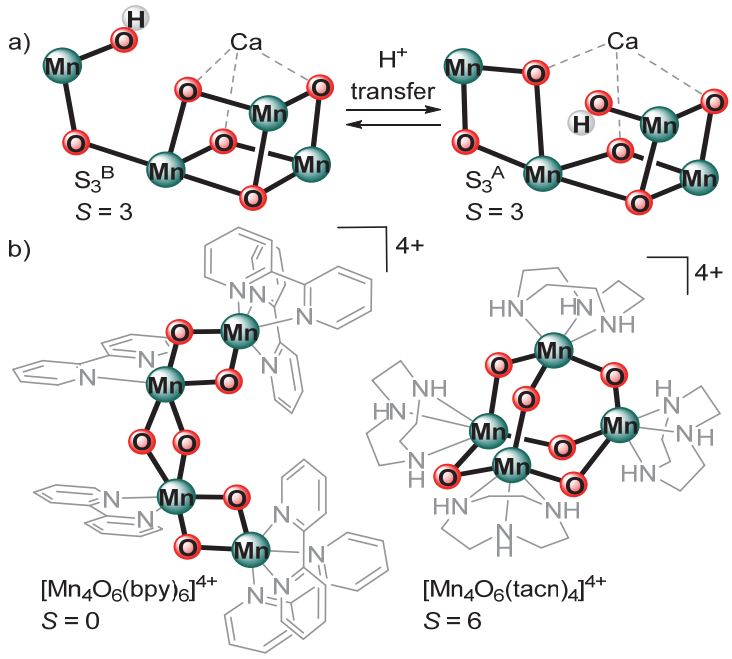

Figure 1. a) Proposed isomers S_3^A and S_3^B of the inorganic $CaMn_4O_5(OH)$ core of the S_3 state of the OEC. b) Representative examples of Mn_4^{IV} complexes and their corresponding spin ground states.

magnitude of the projected ^{55}Mn hyperfine coupling constants (A_i).[44-45] The observed A_i for the S_3 state has been accommodated with the calculated J_{ij} for the S_3^A structure.[5] Although high-resolution (2.04 Å), time-resolved structural data of the S_3 state obtained using femtosecond X-ray free electron laser (XFEL) techniques also support the S_3^A structure,[8] further improvements in resolution and possible contributions from lower oxidation state components need to be addressed, as evidenced from abnormally long Mn-oxo bond distances of ca. 2.2 Å.[8, 46]

In contrast to the extensive studies performed on the S_3 state, synthetic and spectroscopic studies on Mn_4^{IV} model complexes remain rare. Only two general classes of tetranuclear Mn_4^{IV} complexes have been described in the literature: linear and adamantane-shaped complexes, both featuring $[Mn_4^{IV}O_6]^{4+}$ cores (Figure 1b).[47-53] For the linear

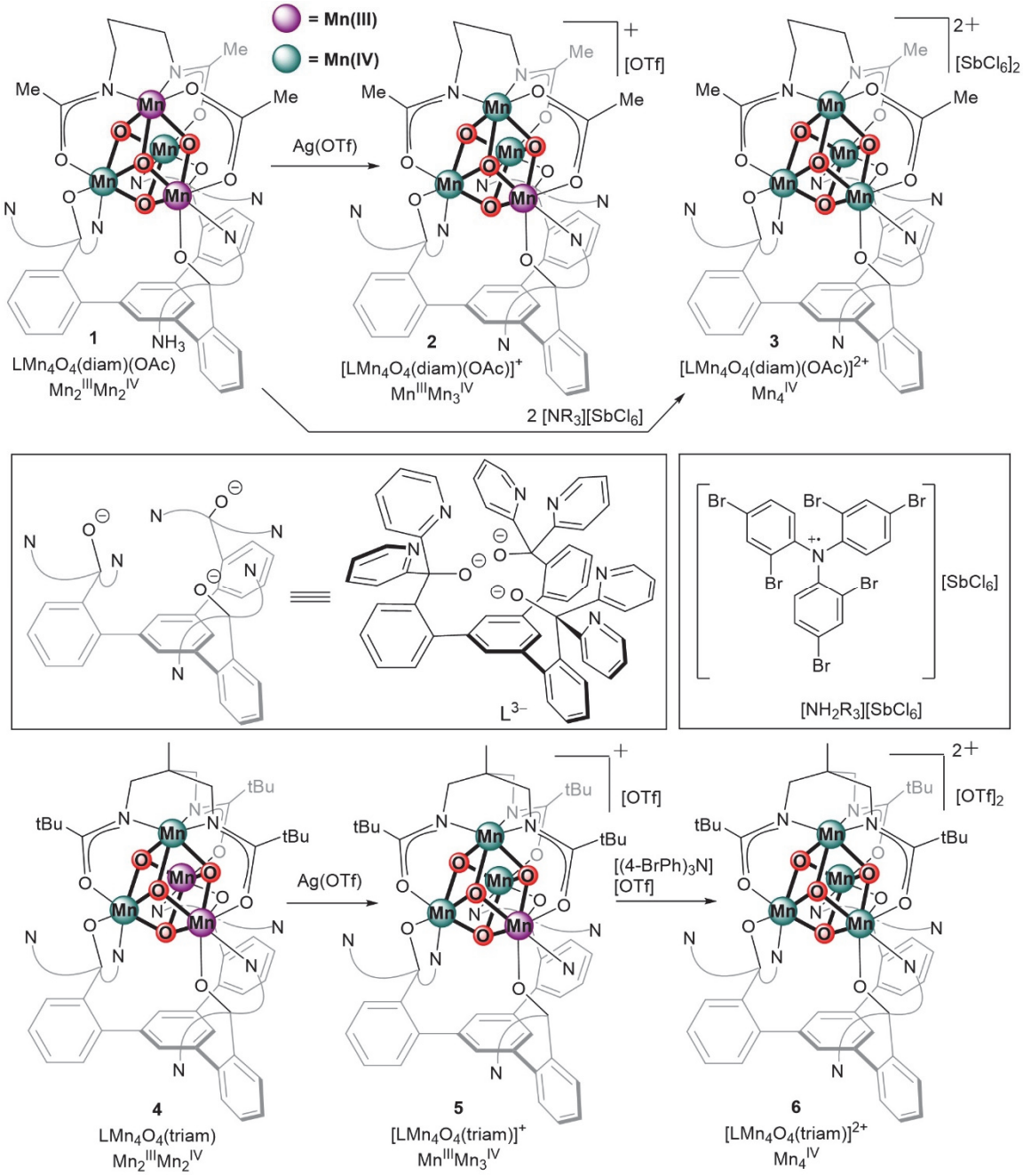

Figure 2. Synthesis of complexes **1~6** studied in this work.

complexes, strong pairwise antiferromagnetic interactions lead to a diamagnetic $S = 0$ ground state:[47] An EPR spectrum has been reported at 140 K from the population of thermally accessible spin excited states, but further characterization has not been provided.[52] Magnetic susceptibility studies on a series of adamantane-shaped $[Mn_4^{IV}O_6]^{4+}$

complexes indicate overall ferromagnetic interactions giving rise to an $S = 6$ ground state.[48] EPR studies for the adamantane-shaped complexes have not been reported. For the adamantane-shaped complexes, the $[Mn_4^{IV}]/[Mn_3^{IV}Mn^{V}]$ redox couple was observed upon substitution of the facially-coordinating triamine ligands with anionic, stronger donor ligands such as aminedicarboxylates.[48] Further spectroscopic properties of the $[Mn_3^{IV}Mn^{V}]$ species have not been reported. In general, detailed spectroscopic studies on Mn_4^{IV} and $Mn_3^{IV}Mn^{V}$ model complexes suitable for comparisons with the S_3 and S_4 states are absent in the literature.

Herein, we report our ongoing efforts on the synthesis, X-ray spectroscopy, and multifrequency EPR spectroscopy for unique tetranunclear $[Mn_4^{IV}O_4]$ complexes as models of S_3 state. Preliminary results show that the $[Mn_4^{IV}O_4]$ complex has an $S = 3$ ground state, resembling the electronic structure of the S_3 state. The $S = 3$ effective spin ground state may arise from an αααβ spin topology arising from a trimer-monomer magnetic coupling model of pseudo-octahedral Mn^{IV} centers.

A2.2) Synthesis

The tethered diamidate-bridged cuboidal complex $LMn_2^{III}Mn_2^{IV}O_4(diam)(OAc)$ (**1**) was used as the precursor for the targeted $[Mn_4^{IV}O_4]$ complex (**3**) (Figure 2).[25] In propylene carbonate, the cyclic voltammogram of **1** shows a reversible oxidation to the previously characterized one electron oxidized $[Mn^{III}Mn_3^{IV}O_4]$ complex (**2**) at −50 mV vs Fc/Fc^+.[25] A second quasi-reversible $[Mn^{III}Mn_3^{IV}]/[Mn_4^{IV}]$ couple is observed at +780 mV vs Fc/Fc^+ (Figure 3). Notably, formation of the $[Mn_4^{IV}]$ species is not observed for analogous tris-acetate or tris-phosphinate complexes, highlighting the ability of amidate ligands in supporting high oxidation state complexes.[54] Accordingly, treatment of **1** with two

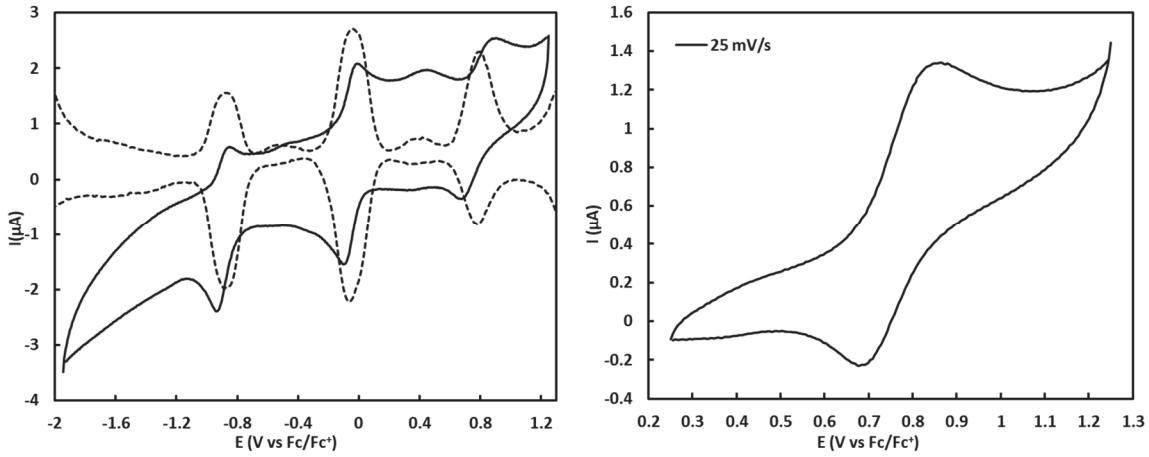

Figure 3. (Right) Overlay of the cyclic voltammogram and square wave voltammogram of **1** in propylene carbonate. (Left) Isolated $[Mn^{III}Mn_3^{IV}]/[Mn_4^{IV}]$ couple +780 mV vs Fc/Fc^+.

equivalents of tris(2,4-dibromophenyl)aminium hexachloroantimonate ($E_{1/2}$ = +1140 mV vs Fc/Fc^+ in MeCN)[55-56] in thawing MeCN leads to the formation of the two electron oxidized $[Mn_4^{IV}O_4]$ complex (**3**). Addition of fewer equivalents of the aminium oxidant leads to a mixture of **2** and **3** by ^{1}H NMR (Figure 4). While the ESI-MS of **2** shows a peak at *m*/*z* = 1354 consistent with the mass of $[LMn_4O_4(diam)(OAc)]^+$, the ESI-MS of **3** shows two additional peaks at *m*/*z* = 677 and 1687 consistent with $[LMn_4O_4(diam)(OAc)]^{2+}$ and $[LMn_4O_4(diam)(OAc)(SbCl_6)]^+$, respectively (Figure 5), supporting the formulation of **3** as $[LMn_4^{IV}O_4(diam)(OAc)][SbCl_6]_2$. EPR studies show that **3** has an *S* = 3 ground state *vide infra*.

The tethered triamidate-bridged cuboidal complex $LMn_2^{III}Mn_2^{IV}O_4(triam)$ (**4**) was also used as the precursor for an analogous $[Mn_4^{IV}O_4]$ complex (**6**) (Figure 2). While the cyclic voltammogram of **4** does not show a quasi-reversible $[Mn^{III}Mn_3^{IV}]/[Mn_4^{IV}]$ couple, the $[Mn_2^{III}Mn_2^{IV}]/[Mn^{III}Mn_3^{IV}]$ decreases by 300 mV relative to the corresponding **1**/**2** couple. Synthesis of the one electron oxidized complex **5** via treatment of **4** with Ag(OTf) has been previously reported (Chapter 4). Treatment of **5** with tris(4-bromophenyl)aminium triflate

($E_{1/2}$ = +670 mV vs Fc/Fc^+ in MeCN) leads to the $[Mn_4^{IV}O_4]$ complex (**6**). Addition of fewer equivalents of the above aminium oxidant leads to a mixture of **5** and **6** by ^{1}H NMR (Figure 6). While the ESI-MS of **5** shows a peak at *m*/*z* = 1505 consistent with the mass of $[LMn_4O_4(triam)]^+$, the ESI-MS of **6** shows an additional peak at *m*/*z* = 753 consistent with

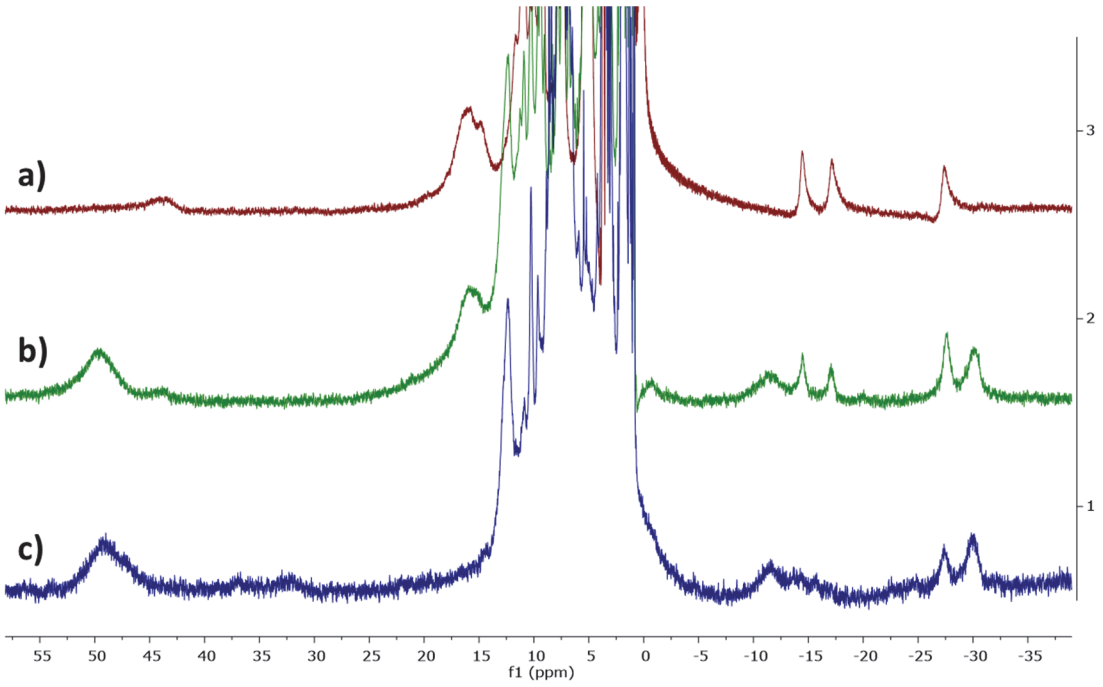

Figure 4. ^{1}H NMR spectra of a) **2**, b) mixture of **2** and **3**, and c) **3**.

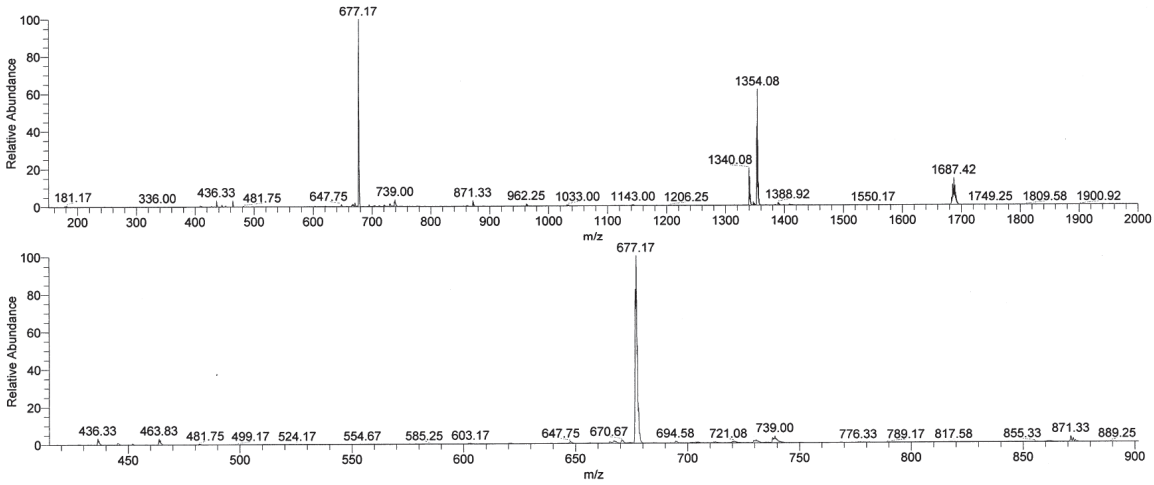

Figure 5. ESI-MS of **3**. Peak assignments: $[LMn_4O_4(diam)(OAc)]^{2+}$ (*m*/*z* = 677), $[LMn_4O_4(diam)(OAc)]^+$ (*m*/*z* = 1354), and $[LMn_4O_4(diam)(OAc)(SbCl_6)]^+$ (*m*/*z* = 1684).

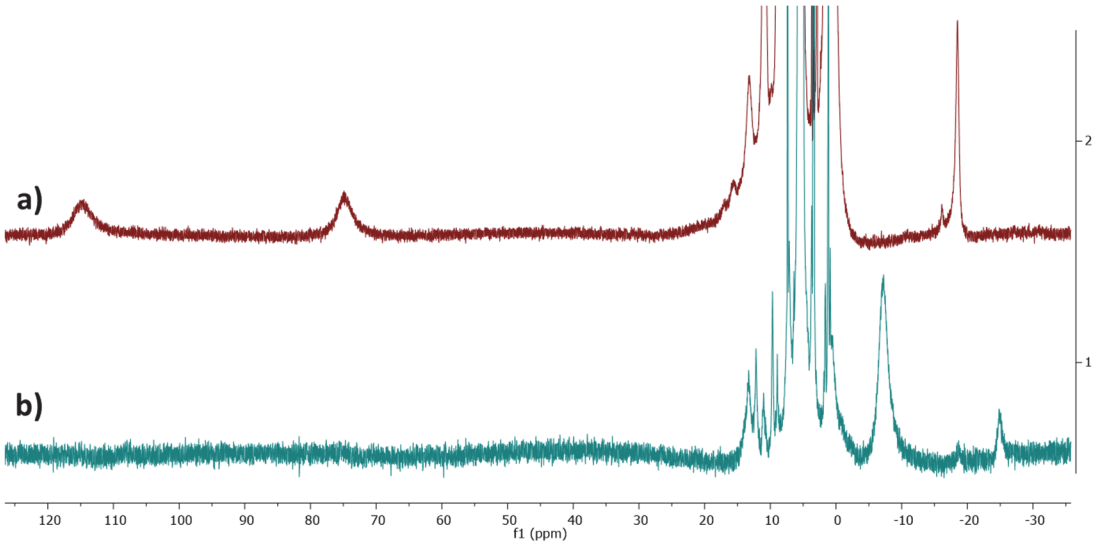

Figure 6. ^{1}H NMR spectra of a) **5** and b) **6**.

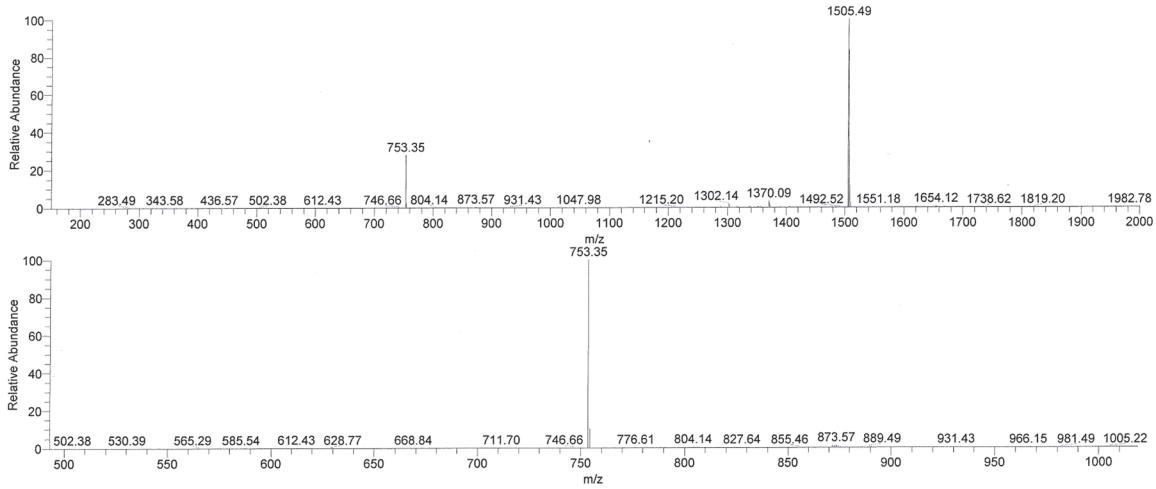

Figure 7. ESI-MS of **6**. Peak assignments: $[LMn_4O_4(triam)]^{2+}$ (m/z = 753), $[LMn_4O_4(triam)]^{+}$ (m/z = 1505).

$[LMn_4O_4(triam)]^{2+}$ (Figure 7), supporting the formulation of **6** as $[LMn_4^{IV}O_4(triam)][OTf]_2$. EPR studies show that the spin ground state of **6** is also an S = 3 *vide infra*. Due to the difficulties in working with **6**, subsequent XAS studies were performed only on **3**.

A2.3) X-ray spectroscopy

Frozen solution Mn K-edge X-ray absorption near-edge spectroscopy (XANES) and extended X-ray absorption fine structure (EXAFS) were used to further characterize metal

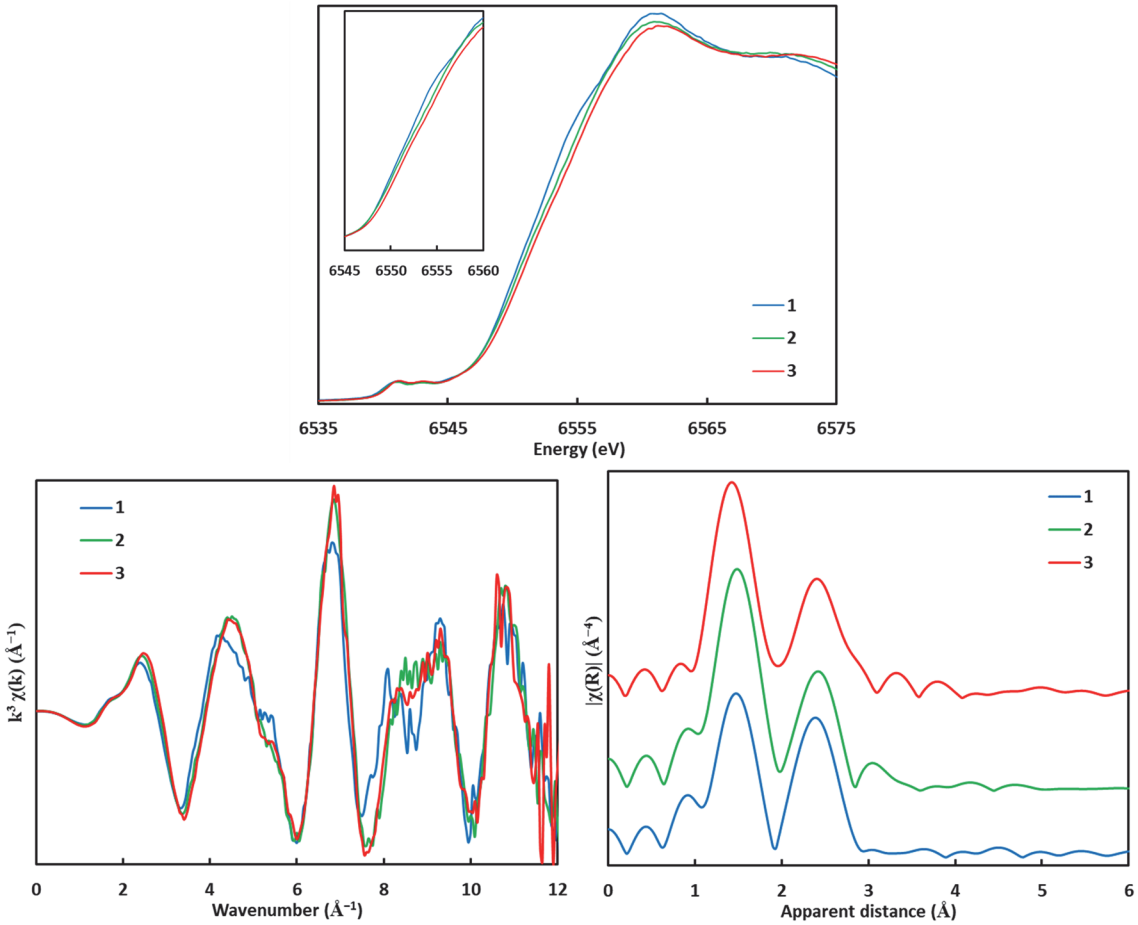

Figure 8. Comparison of the XANES and EXAFS spectrum of complexes **1**, **2**, and **3**.

oxidation states and provide evidence of structural similarity among the series **1**~**3** in solution (Figure 8). While the exact Mn edge energy depends on the structure of the Mn ion and the nature of the coordinated ligands, higher edge energies are generally expected as the oxidation state of Mn is increased. For a series of isostructural complexes **1**~**3**, the highest edge energy for **3** is expected. This is exactly what is observed in the XANES spectra of the three complexes. The EXAFS regions of the spectrum is sensitive to the coordination environment around Mn, and again, for the series of isostructural complexes **1**~**3**, similar EXAFS spectra are expected. The EXAFS spectra of the three complexes can be plotted in k-space or r-space; aside from small shifts in peak position presumably due

to small changes in Mn−Mn distances, significant changes are not observed, consistent with a conserved [Mn_4O_4] cuboidal core in all three complexes.

A2.4) EPR spectroscopy

Parallel mode EPR studies of **3** and **6** were conducted in frozen solution at X-band. The spectrum features a broad transition centered at g ~ 12 (Figure 9). This signal is reminiscent of the corresponding spectrum for the S_3 state.[5-6] The spectral lineshape is suggestive of an axial signal, and the spectrum can be approximated using the following parameters: $S = 3$, $g = 2.0$, $D = 0.114$ cm^{-1}, and $E/D = 0.134$. These fit values may change upon obtaining a

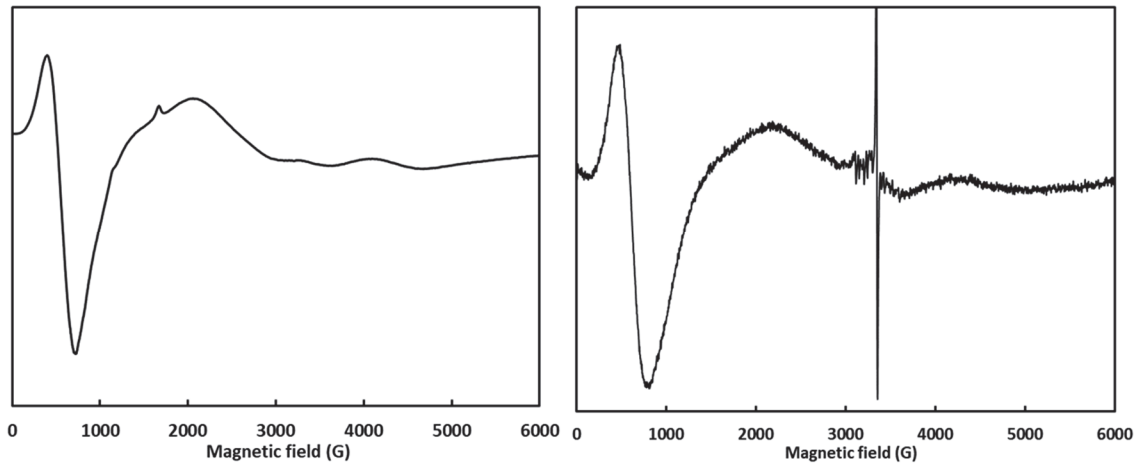

Figure 9. Comparison of the parallel mode X-band EPR of **3** (left) and **6** (right).

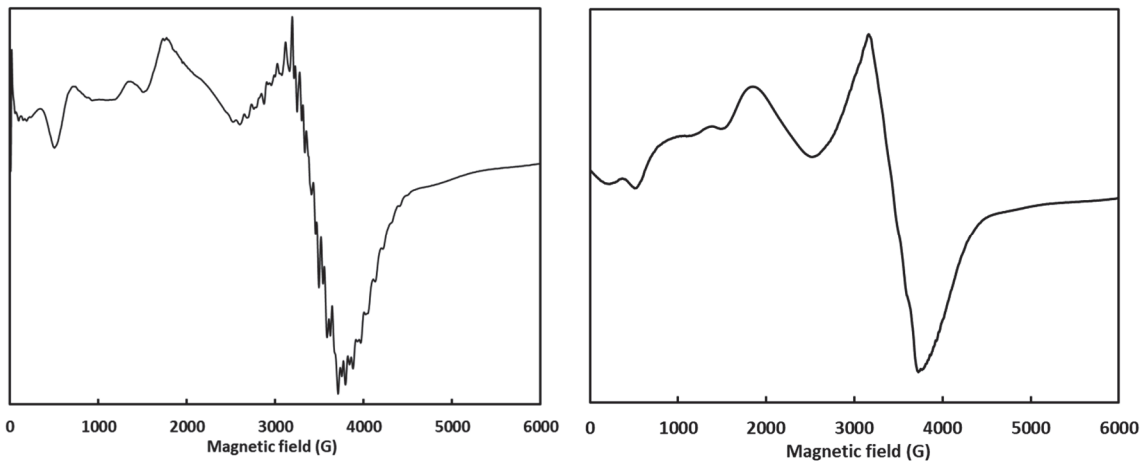

Figure 10. Perpendicular mode X-band EPR of **3**. (Left) Frozen solution in 2-methyl-THF. (Right) Frozen solution in MeCN.

higher frequency D-band EPR. A glimpse of the ^{55}Mn hyperfine interactions can be seen in the 750−1000 G region of the spectrum of **3**. The corresponding parallel mode X-band EPR of **6** also shows this signal at g ~ 12. The sharp signal and the multiline signal at g = 2 is from residual **5** and the excess aminium radical. Perpendicular mode EPR studies were performed on **3**. While satisfactory fits have not been obtained thus far, the spectrum indicates the presence of a small zero field splitting parameter, on the order of 0.2 cm^{-1}, as is observed for the S_3 state. Further D-band EPR studies are ongoing.

D-band EPR studies are ongoing, but aspects of spectral interpretation are mentioned here. On the basis of the electron-spin nutation experiment performed at the low-field or high-field edge of the spectrum, the spin ground state of **3** may be more definitively assigned. On the low- and high-field edges of the spectrum, contributions from the $|-3\rangle \rightarrow |-2\rangle$ transition (negative zero field splitting assumed) can be proved selectively. Relative to the EPR transition of an $S = 1/2$ species, the optimal π pulse length for each $|m_s\rangle \rightarrow |m_s+1\rangle$ transition in $S > 1/2$ spin states is always shorter by a factor ω described in equation 1. Relative to an organic $S = 1/2$ radical species, the optimal pulse length for the $|-3\rangle \rightarrow |-2\rangle$ transition in an $S = 3$ system is expected to be shorter by a factor of $\omega = \sqrt{6} \approx 2.45$.[5]

$$\omega = \sqrt{S(S+1) - m_s(m_s+1)} \qquad (1)$$

To be able to perform spin nutation experiments at an isolated $|m_s\rangle \rightarrow |m_s+1\rangle$ transition, well-isolated transition need to obtained. The breadth of EPR spectra depends largely on the axial zero field splitting (ZFS) parameter D, which removes the degeneracy of the $|m_s\rangle$ states. For an integer spin system $S = n$, m_s takes the values 0, …, ±(n−1), ±n. For $D < 0$, $|m_s\rangle = \pm n$ is the lowest in energy at zero field; for $D > 0$, $|m_s\rangle = 0$ is the lowest. Following

the electron Zeeman effect, the magnitude of D determines the magnetic field position of a given EPR transition; for isotropic systems with D = 0, all EPR transitions are coincidental at g_e. The relative amplitude of the allowed EPR transitions $|m_s\rangle \rightarrow |m_s+1\rangle$ follow the Boltzmann distribution of $|m_s\rangle$ states.

To gain a better understanding of the ^{55}Mn hyperfine interactions in **3**, electron-nuclear double resonance (ENDOR) and electron-electron double resonance detected NMR (EDNMR) spectra can be collected at selected field positions along the D-band ESE-EPR spectrum. In the strong coupling regime ($|A| > 2\nu_n$), ENDOR and EDNMR peaks appear about multiples of the hyperfine coupling constant separated by $2\nu_n$ (i.e. $n|A|\pm\nu_n$ where n represents the $|ms\rangle$ level being pumped). $\nu_n(^{55}Mn)$ varies linearly with magnetic field as 10.554 MHz/T. Qualitatively, the relative amplitude of the $n|A|\pm\nu_n$ peaks depend on the sign of A, with a larger amplitude of the $n|A|+\nu_n$ peak observed for $A > 0$ and a larger amplitude of the $n|A|-\nu_n$ peak observed for $A < 0$. For A > 0 in the weak coupling regime ($|A| < 2\nu_n$), peaks appear shifted by multiples of A about ν_n (i.e. $\nu_n \pm nA$). For A < 0 in the weak coupling regime, peak positions depend on the specific $|ms\rangle$ level being pumped: (1) If $n|A| > \nu_n$, the strong coupling pattern is observed (i.e. $n|A| \pm \nu_n$, $n|A| - \nu_n$ being more prominent). (2) If $n|A| < \nu_n$, the weak coupling pattern is observed (i.e. $\nu_n \pm n|A|$). Additionally, the sign of A can be determined from shifts in peak position with magnetic field: For A > 0, peak position increases with increasing field and for A < 0, peak position decreases with increasing field. Using this information, half-integer spin systems will feature peaks at $(1/2)|A|\pm\nu_n$, $(3/2)|A|\pm\nu_n$, $(5/2)|A|\pm\nu_n$, etc.; integer spin systems will feature peaks at uniformly spaced $(1)|A|\pm\nu_n$, $(2)|A|\pm\nu_n$, $(3)|A|\pm\nu_n$, etc., which can be used to further ascertain the spin state of the system. D-band studies are ongoing.

A2.5) Experimental section

Synthesis of **3**. A suspension of **1** (13 mg, 9.6 μmol, 1 equiv) in MeCN is frozen in the cold well. Separately, thawing MeCN (1 mL) is added to tris(2,4-dibromophenyl)aminium hexachloroantimonate (31 mg, 29.4 μmol, 3 equiv), resulting in a dark green-blue solution. The cold aminium solution is added to the thawing suspension of **1**. Upon complete thawing, a bright red solution is obtained, with the tris(2,4-dibromophenyl)amine byproduct precipitating out of solution. The mixture is stirred for 1 min after thawing and filtered quickly through a pad of Celite. The pad of Celite is rinsed with thawing MeCN and all volatiles are removed from the combined MeCN filtrate. The residue is then treated with thawing THF and quickly filtered to remove a white, insoluble byproduct. The bright red filtrate contains complex **3**. The purity of the material is checked by ^{1}H NMR and is shown in Figure 5c. Attempts to scale up the reaction result in a mixture of species. Attempts to crystallize the product result in decomposition. In particular, treatment of **3** with 2-methyltetrahydrofuran results in rapid decomposition, suggesting that **3** may engage in hydrogen atom transfer reactivity with weak C−H bonds. XAS and D-band EPR samples were prepared as a concentrated, frozen solution of **3** in MeCN.

A2.6) References

(1) Pantazis, D. A., *ACS Catalysis* **2018**, *8*, 9477.
(2) Shen, J.-R., *Annu. Rev. Plant Biol.* **2015**, *66*, 23.
(3) Yano, J.; Yachandra, V., *Chem. Rev.* **2014**, *114*, 4175.
(4) Cox, N.; Pantazis, D. A.; Neese, F.; Lubitz, W., *Acc. Chem. Res.* **2013**, *46*, 1588.
(5) Cox, N.; Retegan, M.; Neese, F.; Pantazis, D. A.; Boussac, A.; Lubitz, W., *Science* **2014**, *345*, 804.
(6) Boussac, A.; Sugiura, M.; Rutherford, A. W.; Dorlet, P., *J. Am. Chem. Soc.* **2009**, *131*, 5050.
(7) Beal, N. J.; Corry, T. A.; O'Malley, P. J., *J. Phys. Chem. B* **2018**, *122*, 1394.
(8) Kern, J.; Chatterjee, R.; Young, I. D.; Fuller, F. D.; Lassalle, L.; Ibrahim, M.; Gul, S.; Fransson, T.; Brewster, A. S.; Alonso-Mori, R.; Hussein, R.; Zhang, M.; Douthit, L.; de Lichtenberg, C.; Cheah, M. H.; Shevela, D.; Wersig, J.; Seuffert, I.; Sokaras, D.; Pastor, E.;

Weninger, C.; Kroll, T.; Sierra, R. G.; Aller, P.; Butryn, A.; Orville, A. M.; Liang, M.; Batyuk, A.; Koglin, J. E.; Carbajo, S.; Boutet, S.; Moriarty, N. W.; Holton, J. M.; Dobbek, H.; Adams, P. D.; Bergmann, U.; Sauter, N. K.; Zouni, A.; Messinger, J.; Yano, J.; Yachandra, V. K., *Nature* **2018**.

(9) Isobe, H.; Shoji, M.; Shen, J.-R.; Yamaguchi, K., *Inorg. Chem.* **2016**, *55*, 502.

(10) Askerka, M.; Wang, J.; Vinyard, D. J.; Brudvig, G. W.; Batista, V. S., *Biochemistry* **2016**, *55*, 981.

(11) Retegan, M.; Krewald, V.; Mamedov, F.; Neese, F.; Lubitz, W.; Cox, N.; Pantazis, D. A., *Chem. Sci.* **2016**, *7*, 72.

(12) Oyala, P. H.; Stich, T. A.; Debus, R. J.; Britt, R. D., *J. Am. Chem. Soc.* **2015**, *137*, 8829.

(13) Weng, T.-C.; Hsieh, W.-Y.; Uffelman, E. S.; Gordon-Wylie, S. W.; Collins, T. J.; Pecoraro, V. L.; Penner-Hahn, J. E., *J. Am. Chem. Soc.* **2004**, *126*, 8070.

(14) Ioannidis, N.; Nugent, J. H. A.; Petrouleas, V., *Biochemistry* **2002**, *41*, 9589.

(15) Ioannidis, N.; Petrouleas, V., *Biochemistry* **2002**, *41*, 9580.

(16) Geijer, P.; Morvaridi, F.; Styring, S., *Biochemistry* **2001**, *40*, 10881.

(17) Ioannidis, N.; Petrouleas, V., *Biochemistry* **2000**, *39*, 5246.

(18) Liang, W.; Roelofs, T. A.; Cinco, R. M.; Rompel, A.; Latimer, M. J.; Yu, W. O.; Sauer, K.; Klein, M. P.; Yachandra, V. K., *J. Am. Chem. Soc.* **2000**, *122*, 3399.

(19) Matsukawa, T.; Mino, H.; Yoneda, D.; Kawamori, A., *Biochemistry* **1999**, *38*, 4072.

(20) Wincencjusz, H.; van Gorkom, H. J.; Yocum, C. F., *Biochemistry* **1997**, *36*, 3663.

(21) Messinger, J.; Badger, M.; Wydrzynski, T., *Proc. Nat. Acad. Sci.* **1995**, *92*, 3209.

(22) DeRose, V. J.; Latimer, M. J.; Zimmermann, J.-L.; Mukerji, I.; Yachandra, V. K.; Sauer, K.; Klein, M. P., *Chem. Phys.* **1995**, *194*, 443.

(23) MacLachlan, D. J.; Nugent, J. H. A.; Evans, M. C. W., *Biochim. Biophys. Acta - Bioenergetics* **1994**, *1185*, 103.

(24) Boussac, A.; Zimmermann, J. L.; Rutherford, A. W., *Biochemistry* **1989**, *28*, 8984.

(25) Lee, H. B.; Shiau, A. A.; Oyala, P. H.; Marchiori, D. A.; Gul, S.; Chatterjee, R.; Yano, J.; Britt, R. D.; Agapie, T., *J. Am. Chem. Soc.* **2018**, *140*, 17175.

(26) Reed, C. J.; Agapie, T., *J. Am. Chem. Soc.* **2018**, *140*, 10900.

(27) Paul, S.; Neese, F.; Pantazis, D. A., *Green Chem.* **2017**, *19*, 2309.

(28) Han, Z.; Horak, K. T.; Lee, H. B.; Agapie, T., *J. Am. Chem. Soc.* **2017**, *139*, 9108.

(29) Lee, H. B.; Tsui, E. Y.; Agapie, T., *Chem. Commun.* **2017**, *53*, 6832.

(30) Zhang, C.; Chen, C.; Dong, H.; Shen, J.-R.; Dau, H.; Zhao, J., *Science* **2015**, *348*, 690.

(31) Kanady, J. S.; Lin, P.-H.; Carsch, K. M.; Nielsen, R. J.; Takase, M. K.; Goddard, W. A.; Agapie, T., *J. Am. Chem. Soc.* **2014**, *136*, 14373.

(32) Kanady, J. S.; Mendoza-Cortes, J. L.; Tsui, E. Y.; Nielsen, R. J.; Goddard, W. A.; Agapie, T., *J. Am. Chem. Soc.* **2013**, *135*, 1073.

(33) Kanady, J. S.; Tran, R.; Stull, J. A.; Lu, L.; Stich, T. A.; Day, M. W.; Yano, J.; Britt, R. D.; Agapie, T., *Chem. Sci.* **2013**, *4*, 3986.

(34) Tsui, E. Y.; Agapie, T., *Proc. Nat. Acad. Sci.* **2013**, *110*, 10084.

(35) Tsui, E. Y.; Kanady, J. S.; Agapie, T., *Inorg. Chem.* **2013**, *52*, 13833.

(36) Tsui, E. Y.; Tran, R.; Yano, J.; Agapie, T., *Nat. Chem.* **2013**, *5*, 293.

(37) Mukherjee, S.; Stull, J. A.; Yano, J.; Stamatatos, T. C.; Pringouri, K.; Stich, T. A.; Abboud, K. A.; Britt, R. D.; Yachandra, V. K.; Christou, G., *Proc. Nat. Acad. Sci.* **2012**, *109*, 2257.
(38) Kanady, J. S.; Tsui, E. Y.; Day, M. W.; Agapie, T., *Science* **2011**, *333*, 733.
(39) Mukhopadhyay, S.; Mandal, S. K.; Bhaduri, S.; Armstrong, W. H., *Chem. Rev.* **2004**, *104*, 3981.
(40) Morton, J.; Chrysina, M.; Craig, V. S. J.; Akita, F.; Nakajima, Y.; Lubitz, W.; Cox, N.; Shen, J.-R.; Krausz, E., *Biochim. Biophys. Acta - Bioenergetics* **2018**, *1859*, 88.
(41) Schuth, N.; Zaharieva, I.; Chernev, P.; Berggren, G.; Anderlund, M.; Styring, S.; Dau, H.; Haumann, M., *Inorg. Chem.* **2018**, *57*, 10424.
(42) Krewald, V.; Retegan, M.; Cox, N.; Messinger, J.; Lubitz, W.; DeBeer, S.; Neese, F.; Pantazis, D. A., *Chem. Sci.* **2015**, *6*, 1676.
(43) Boussac, A.; Rutherford, A. W.; Sugiura, M., *Biochim. Biophys. Acta - Bioenergetics* **2015**, *1847*, 576.
(44) Pantazis, D. A.; Ames, W.; Cox, N.; Lubitz, W.; Neese, F., *Angew. Chem. Int. Ed.* **2012**, *51*, 9935.
(45) Isobe, H.; Shoji, M.; Yamanaka, S.; Mino, H.; Umena, Y.; Kawakami, K.; Kamiya, N.; Shen, J. R.; Yamaguchi, K., *Phys. Chem. Chem. Phys.* **2014**, *16*, 11911.
(46) Suga, M.; Akita, F.; Sugahara, M.; Kubo, M.; Nakajima, Y.; Nakane, T.; Yamashita, K.; Umena, Y.; Nakabayashi, M.; Yamane, T.; Nakano, T.; Suzuki, M.; Masuda, T.; Inoue, S.; Kimura, T.; Nomura, T.; Yonekura, S.; Yu, L.-J.; Sakamoto, T.; Motomura, T.; Chen, J.-H.; Kato, Y.; Noguchi, T.; Tono, K.; Joti, Y.; Kameshima, T.; Hatsui, T.; Nango, E.; Tanaka, R.; Naitow, H.; Matsuura, Y.; Yamashita, A.; Yamamoto, M.; Nureki, O.; Yabashi, M.; Ishikawa, T.; Iwata, S.; Shen, J.-R., *Nature* **2017**, *543*, 131.
(47) Chen; Collomb, M.-N.; Duboc, C.; Blondin, G.; Rivière, E.; Faller, J. W.; Crabtree, R. H.; Brudvig, G. W., *Inorg. Chem.* **2005**, *44*, 9567.
(48) Dubé, C. E.; Mukhopadhyay, S.; Bonitatebus, P. J.; Staples, R. J.; Armstrong, W. H., *Inorg. Chem.* **2005**, *44*, 5161.
(49) Chen, H.; Faller, J. W.; Crabtree, R. H.; Brudvig, G. W., *J. Am. Chem. Soc.* **2004**, *126*, 7345.
(50) Mukhopadhyay, S.; Staples, R. J.; Armstrong, W. H., *Chem. Commun.* **2002**, 864.
(51) Dubé, C. E.; Wright, D. W.; Pal, S.; Bonitatebus, P. J.; Armstrong, W. H., *J. Am. Chem. Soc.* **1998**, *120*, 3704.
(52) Philouze, C.; Blondin, G.; Girerd, J.-J.; Guilhem, J.; Pascard, C.; Lexa, D., *J. Am. Chem. Soc.* **1994**, *116*, 8557.
(53) Hagen, K. S.; Westmoreland, T. D.; Scott, M. J.; Armstrong, W. H., *J. Am. Chem. Soc.* **1989**, *111*, 1907.
(54) Gupta, R.; Taguchi, T.; Lassalle-Kaiser, B.; Bominaar, E. L.; Yano, J.; Hendrich, M. P.; Borovik, A. S., *Proc. Nat. Acad. Sci.* **2015**, *112*, 5319.
(55) Steckhan, E., *Angew. Chem. Int. Ed.* **1986**, *25*, 683.
(56) Yueh, W.; Bauld, N. L., *J. Am. Chem. Soc.* **1995**, *117*, 5671.

APPENDIX 3

Synthesis and characterization of tetranuclear $MCo_3(\mu^4\text{-}O)$ complexes supported by benzoate and pyrazolate bridging ligands.

Abstract

Starting from a trimetallic cobalt complex, synthetic efforts have been extended toward the synthesis of benzoate bridged heterometallic cobalt μ^4–oxido clusters of the form $[Co_3M'O]$ and $[Co_3M'O(OH)]$, featuring redox-inactive metals M'. Systematic electrochemical studies could provide important insights into the role of redox-inactive metals in the redox chemistry of cobalt oxo species. Previous effort in this area has resulted in the isolation of tetrametallic $[Mn_3M'O_4]$, $[Mn_3M'O(OH)]$, and $[Fe_3M'O(OH)]$ clusters. So far, isolation of cobalt clusters with higher oxido content has been challenging. Using pyrazolates as bridging ligands, the synthesis of lower oxidation state, tetrametallic clusters has been demonstrated.

A3.1) Introduction

In both biological and synthetic systems, Lewis acidic, redox-inactive metals play an important role in tuning redox reactions. In particular, participation of Lewis acids has been implicated in the chemistry of metal-oxygen species. The Ca^{2+} ion is vital for the function of the oxygen-evolving complex in Photosystem II.[1] In synthetic systems, binding of Ca^{2+} or Sr^{+2} to an iron peroxo moiety facilitates the release of dioxygen upon oxidation, whereas other, more acidic metals preclude this process.[2] The oxygen evolution activity of $LnBaCo_2O_{5+x}$ double-perovskite materials depend on the identity of the lanthanide ion.[3] Based on previous studies performed in our group, the redox potentials of metal-oxo complexes are correlated to the Lewis acidity of the redox-inactive metal (Figure 1).[4] To further understand the role of Lewis acids in the redox chemistry of metal-oxo species, heterometallic cobalt oxo cluster complexes were targeted.[5]

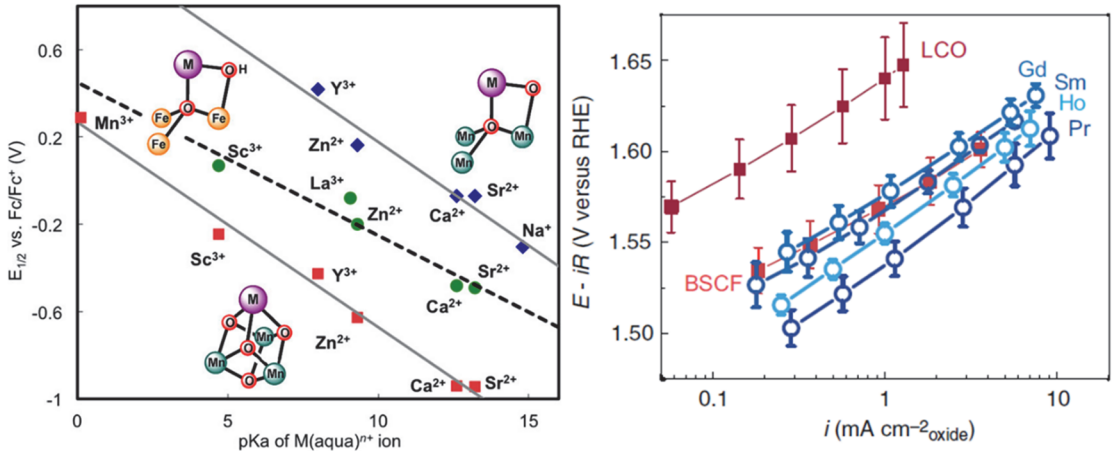

Figure 1. Effect of Lewis acids in the redox potential of Mn[4a, 4b] and Fe[4c] oxo clusters (left), and oxygen evolution activity of $LnBaCo_2O_{5+x}$ double-perovskite materials[3] (right).

A3.2) Results

Following a modified literature procedure[6], the trimetallic cobalt benzoate complex was synthesized via a protonolysis reaction. Under ambient conditions, treatment of a

suspension of cobalt bis(4-*tert*-butylbenzoate) with **H_3L** in dichloromethane results in the formation of a violet species (Figure 2). After removal of all volatiles, the residue is washed with copious amounts of diethyl ether to remove the benzoic acid byproduct. Violet crystals of **1a** are obtained by slow vapor diffusion of diethyl ether to a concentrated DCM solution. Analogous tricobalt acetate cluster **1b** can be synthesized according to literature[6]. The crystal structure of **1a** shows that each alkoxide moiety from the ligand bridges between two adjacent cobalt centers, to which each pyridyl moiety is bound. The tricobalt trialkoxide core is reminiscent of the cyclohexane chair conformation. The coordination sphere around each cobalt center is completed by three benzoate ligands, featuring both monodentate and bidentate binding modes (Figure 3). Additionally, the benzoate ligands are labile and react with electrophiles such as methyl triflate (Figure 2). Reaction of **1a** with 3 equivalents of MeOTf results in the selective removal of two benzoate moieties, giving rise to complex **2a**. Similar reactivity is observed with **1b**. The structure of **2a** and **2b** was confirmed by x-ray crystallography (Figure 4).

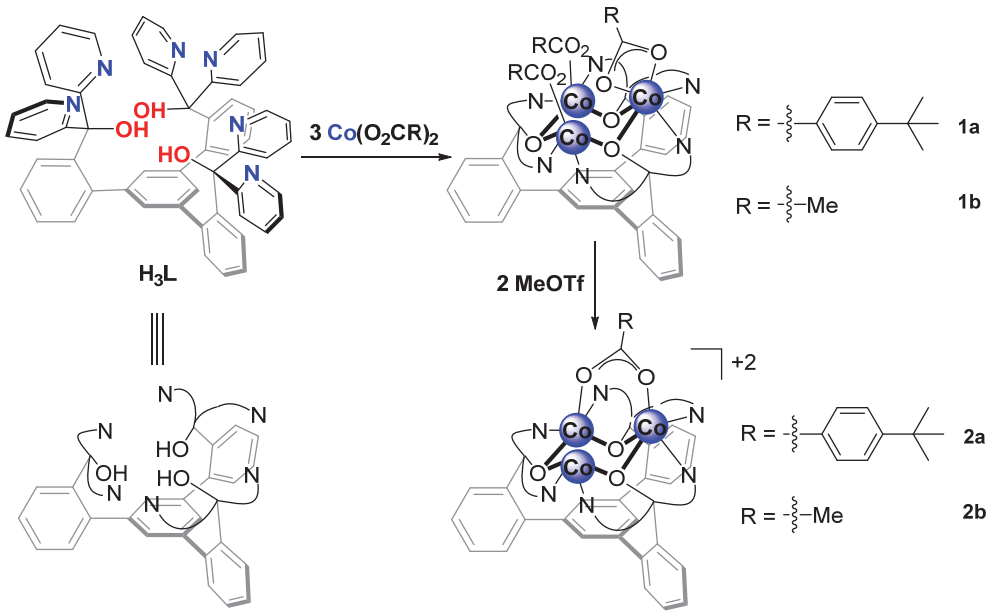

Figure 2. Synthesis of tricobalt tricarboxylate (**1a**, **1b**) and monocarboxylate (**2a**, **2b**) complexes.

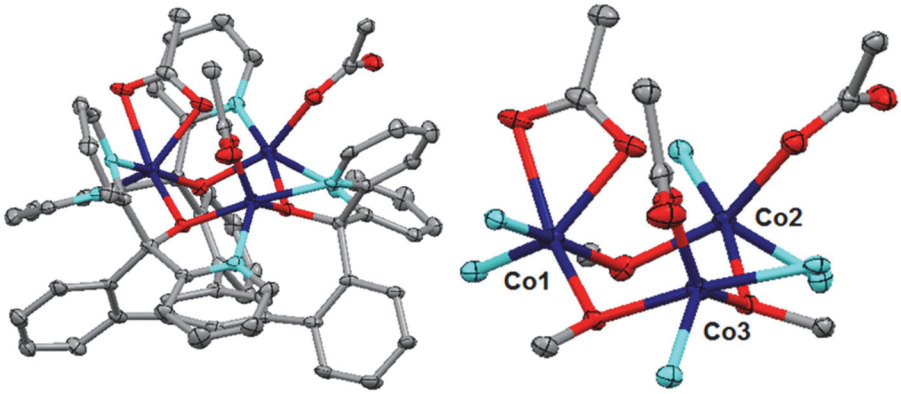

Figure 3. Crystal structure of **1a**, and truncated structure of **1a** highlighting the tricobalt core.

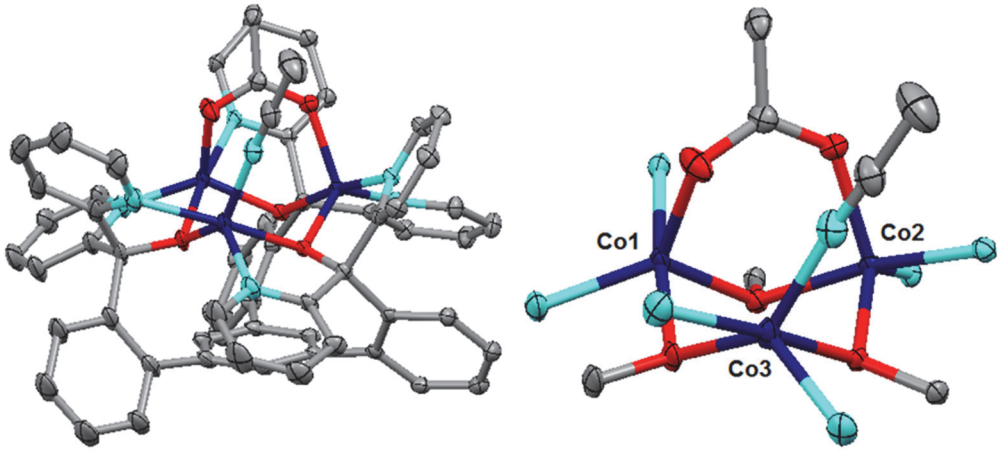

Figure 4. Crystal structure of **2a**, and truncated structure of **2a** highlighting the tricobalt core. Two triflate anions were omitted for clarity.

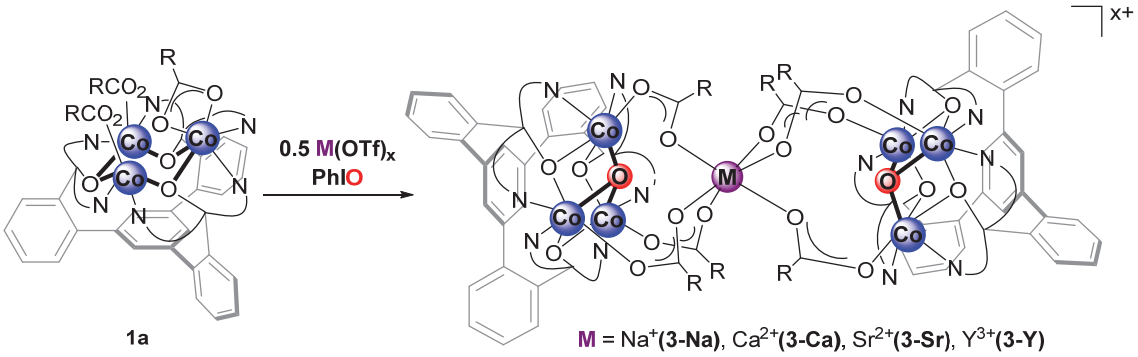

Figure 5. Synthesis of carboxylate bridged hexacobalt oxo complexes **3-Na**, **3-Ca**, **3-Sr**, and **3-Y**.

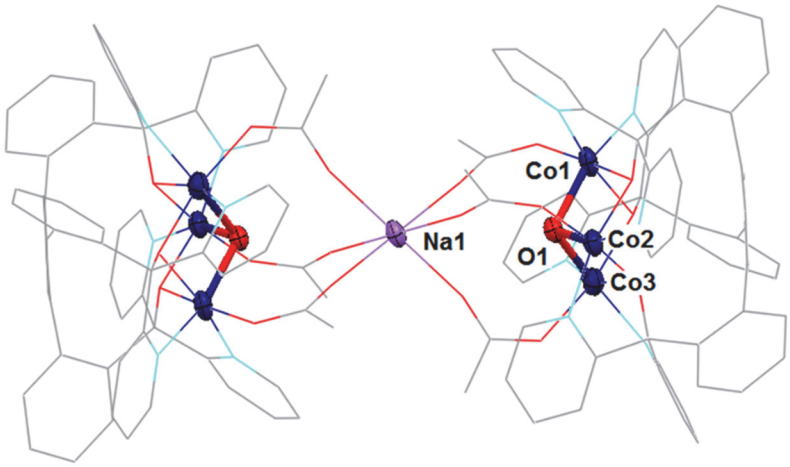

Figure 6. Crystal structure of **3-Na**. Notable bond distances (Å): Co1−O1 1.967(4), Co2−O1 1.950(4), Co3−O1 2.034(5), Na1−O1 3.895.

Following synthetic protocols developed for tetrametallic manganese[4a] [$Mn_3M'O(OH)$] and iron[4c] [$Fe_3M'O(OH)$] clusters incorporating redox-inactive metals M', similar heterometallic cobalt oxo clusters were targeted. Treatment of a suspension of **1a** in THF with metal triflate salts and iodosobenzene (PhIO) or H_2O_2 as oxygen atom transfer reagents results in the formation of carboxylate bridged, hexacobalt bis(μ^3−oxo) clusters **3-M** (Figure 5). Reactions performed with sodium (**3-Na**), calcium (**3-Ca**), strontium (**3-Sr**), and yttrium (**3-Y**) triflate salts all give similar results. Recrystallization from DCM/Et_2O gives analytically pure samples. All four clusters were characterized crystallographically. The crystal structure of **3-Na** shows slight differences in Co−oxo bond distances (Figure 6): the two shorter Co−O bond distances at ~1.95 Å are assigned to Co^{III} centers and a longer Co−O bond ~2.03 Å is assigned to a Co^{II} center. A long Na−oxo distance ~3.90 Å indicates that there is negligible interaction between the redox-inactive metal and the [Co_3O] core. Changing the stoichiometry of the added metal triflate salt, and/or adding macrocyclic crown ethers to prevent dimerization does not change the outcome of the reaction. Switching to a bulky 2-phenylbenzoate results in the incorporation of a μ^3−oxo only (similar to Figure 7).

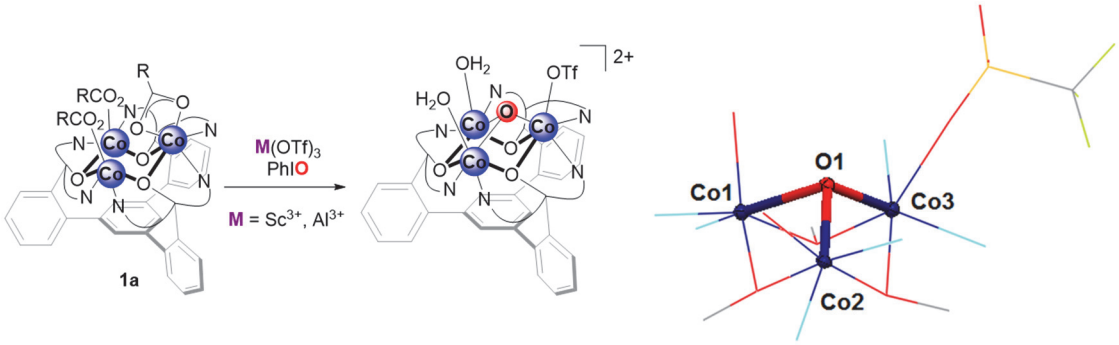

Figure 7. Synthesis and crystal structure of benzoate free, tricobalt oxo complex. Notable bond distances (Å): Co1−O1 2.247(2), Co2−O1 1.907(2), Co3−O1 2.027(2).

Following a periodic trend, the oxo moiety of the [Co_3O] core would be less Lewis basic as compared to both the [Mn_3O] and the [Fe_3O] analogs. We hypothesized that reduction of the cluster may lead to the formation of tetrametallic μ^4−oxido clusters by increasing the basicity at the oxo moiety. Electrochemical studies of **3-M** reveal broad cathodic peaks followed by irreversible anodic peaks. These results suggest that cluster decomposition is likely occurring upon reduction. Consistent with the electrochemical experiments, a complex mixture of products is obtained upon chemical reduction of these complexes with $CoCp_2$. An isolable product is **1a**. We next hypothesized that using a more Lewis acidic metal triflate salt may result in the formation of μ^4−oxido clusters. Treatment of **1a** with scandium or aluminum triflate and PhIO results in the formation of a carboxylate free tricobalt oxo complex (Figure 7). The crystal structure of the product indicate that all three benzoate ligands have been exchanged with triflates with incorporation of a μ^3−oxo coming from PhIO. Presumably, formation of the homoleptic Sc or Al tris-carboxylate is favored over formation of the tetrametallic cluster. Even more Lewis acidic Bi and Ga triflate salts react in a similar fashion.

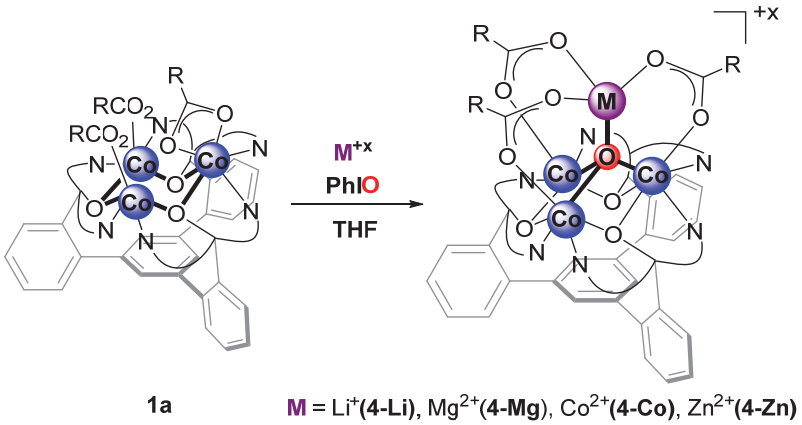

Figure 8. Synthesis of μ^4 oxo complexes.

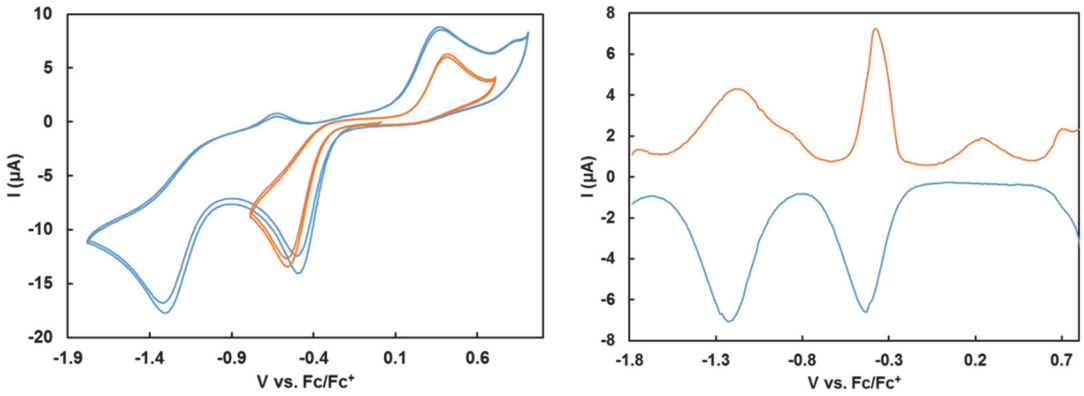

Figure 9. Cyclic voltammogram and differential pulse voltammogram of **4-Zn**.

At the fine balance between ionic radii and Lewis acidity, Treatment of a suspension of **1a** in THF with zinc tetrafluoroborate and PhIO results in the formation of the desired μ^4–oxido cluster **4-Zn**. An isostructural tetracobalt complex **4-Co** can be obtained when **1a** is treated with cobalt(II) tetrafluoroborate (Figure 8). Conveniently, both **4-Zn** and **4-Co** precipitate from the reaction mixture as green solids, and recrystallization from DCM/Et_2O affords single crystals amenable for x-ray diffraction. The triflate salts give rise to hexagonal crystals and due to problems with twinning, structure solution is complicated. The tetrafluoroborate salts are therefore preferred. The brown, THF soluble material from the synthesis of **4-Zn** or **4-Co** has later been shown to contain one electron reduced, monocationic zinc and cobalt complexes, correspondingly. Syntheses of lithium (**4-Li**) or

magnesium (**4-Mg**) analogs can also be achieved, but substitutional disorder with cobalt at the apical metal site complicates isolation.

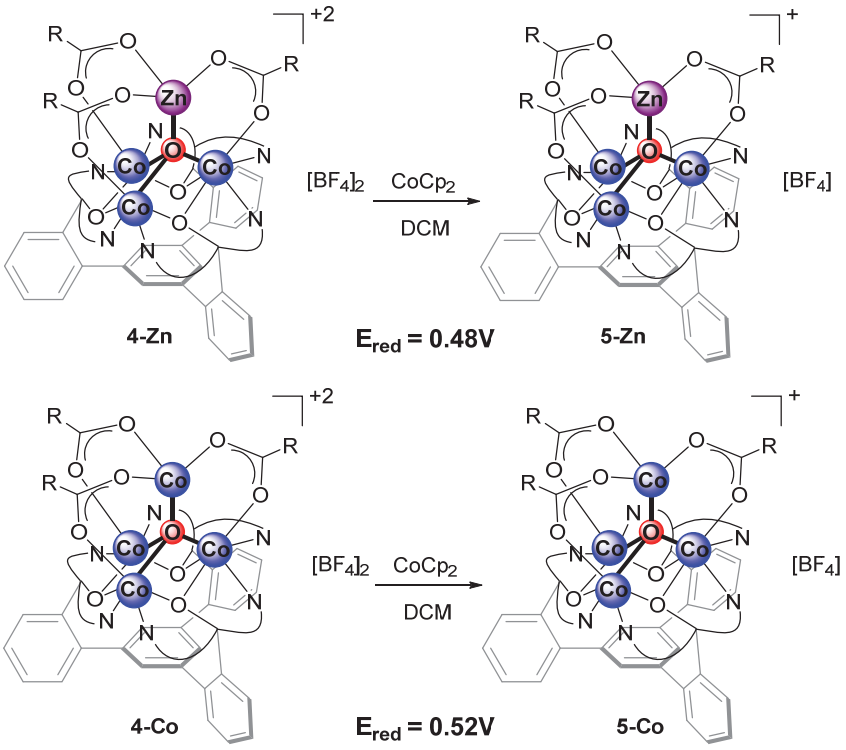

Figure 10. Chemical reduction of **4-Zn**/**4-Co** to afford reduced compounds **5-Zn**/**5-Co**.

Electrochemical experiments were performed to study the redox properties of **4-Zn** and **4-Co** (Figure 9). After testing a number of different conditions, it was found that a 3:1 mixture of MeCN:DCM was optimal for electrochemical measurements. Data was recorded in a conventional glassy carbon, platinum wire, silver wire three-electrode setup using [^{n}Bu$_4$N][PF$_6$] as the supporting electrolyte and ferrocene (Fc) as an internal standard. The cyclic voltammogram (CV) of **4-Zn** features an electrochemically irreversible reduction at ca. −0.5V vs. Fc/Fc$^+$. Together with the corresponding oxidation, isolation of this first redox couple can be achieved (Figure 9, left). The large separation between the cathodic and the anodic peak in the CV is likely due to slow electron transfer kinetics. In this case, the $E_{1/2}$ of the redox process can be more reliably assigned from the differential

pulse voltammogram (Figure 9, right). A second, chemically irreversible reduction at ca. −1.3V vs. Fc/Fc^{+} is also observed. The near absence of the returning oxidation wave suggests that the complex is unstable upon a second reduction.

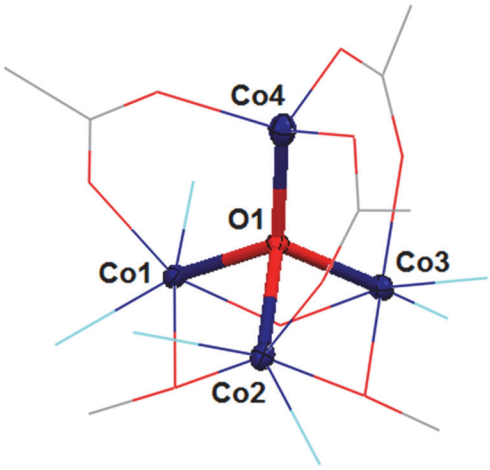

	4-Co $Co^{II}_2Co^{III}_3$	5-Co $Co^{II}_3Co^{III}$
Co4-O1	1.899(6)	1.889(2)
Co1-O1 Co2-O1 Co3-O1	1.894(8) 1.916(7) 2.078(7)	2.031(2) 2.079(2) 2.102(2)

Figure 11. Truncated crystal structure of **4/5-Co** and comparison of notable bond distances (Å).

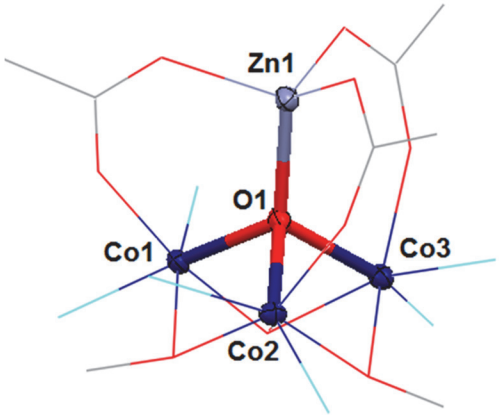

	4-Zn $Zn^{II}Co^{II}Co^{III}_2$	5-Zn $Zn^{II}Co^{II}_2Co^{III}$
Zn1-O1	1.911(3)	1.890(2)
Co1-O1 Co2-O1 Co3-O1	1.908(3) 1.889(3) 2.056(3)	1.931(2) 1.963(2) 2.051(2)

Figure 12. Truncated crystal structure of **4/5-Zn** and comparison of notable bond distances (Å).

Based upon the electrochemical data, chemical reductions of both **4-Zn** and **4-Co** were performed. Treatment of a solution of **4-Zn** in DCM with a dilute solution of cobaltocene in DCM results in the immediate change in color from green to brown. The reaction is nearly quantitative in 30 min, affording the reduced, monocationic complex **5-Zn** (Figure 10). A similar procedure with **4-Co** affords **5-Co**. Crystallographic studies indicate that the μ^4−oxo core is intact. Basal cobalt−oxo distances are elongated in both reduced species,

but apical metal−oxo distance is decreased. Both of these observations are consistent with a more reduced cluster. Consistent with the electrochemical data, further reduction with 2 equivalents of sodium acenaphthylene results in a complex mixture of products. An isolable product is **1a**.

Complex **4-Co** has been characterized using SQUID. The magnetization data shows no presence of ferromagnetic impurities and behaves as a paramagnet, giving rise to a linear plot. From the susceptibility measurement, the experimental room temperature χT value of 4.33 emu is close to a spin-only value of 3.75 emu for two 3/2 centers. The higher experimental χT value is likely due to unquenched orbital angular momentum. Complex **4-Co** behaves as a perfect paramagnet down to 100K. At lower temperatures, antiferromagnetic interactions dominate. Data is consistent with S=0 Co^{III} and S=3/2 Co^{II}.

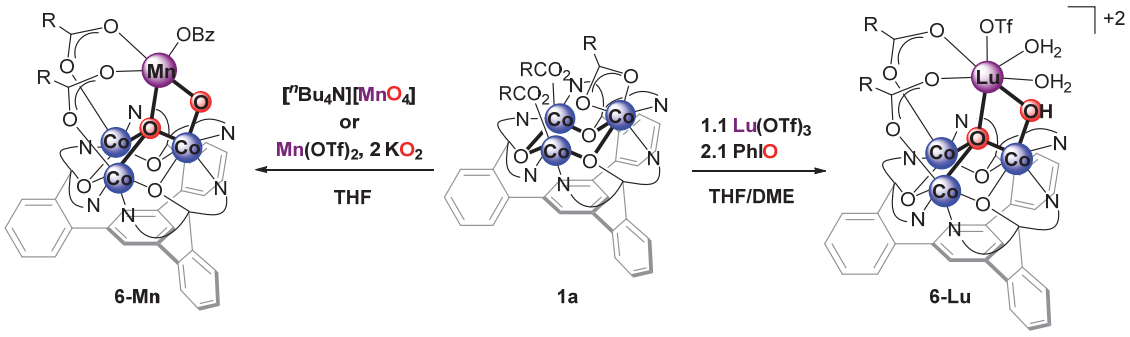

Figure 13. Synthesis of a lutetium μ^4−oxo, μ^2−hydroxo complex **6-Lu**.

To increase the scope of Lewis acids that can be incorporated into the cluster, synthesis of μ^4−oxo, μ^2−hydroxo complexes [$Co_3M'O(OH)$] were targeted. From electrochemical data, further oxidation of the $Co^{II}Co_2^{III}$ core does not seem to be accessible within the solvent window. Addition of excess PhIO, ^{t}BuOOH, or H_2O_2 to **4-Co** does not result in addition of oxo moieties. Reaction of **5-Co** with similar reagents results in one electron oxidation back to **4-Co**. Treatment of **1a** with permanganate results in the formation of a neutral, μ^4,μ^2−dioxo complex **6-Mn** (Figure 13, left). Similar results can be obtained with

Mn(II) triflate and KO_2. Recrystallization from benzene affords crystals amenable for diffraction studies (Figure 15). The crystal structure features a 5-coordinate trigonal bipyramidal Mn center with a very short Mn−oxo distance at ~1.78 Å, suggesting that the Mn center is in the +3 oxidation state. Treatment of **1a** with Lu(III) triflate and PhIO results in the formation of μ^4−oxo, μ^2−hydroxo Lu complex **6-Lu** (Figure 13, right). A carboxylate is lost during the reaction, likely during protonolysis with a water molecule. The crystal structure reveals a 7 coordinate Lu center with 2 water molecules bound terminally (Figure 14). Two outer-sphere triflate anions are poised toward hydrogen bonding with the terminal water molecules and the bridging hydroxide moiety. This is a rare example of a heterometallic cobalt-lanthanide oxo/hydroxo complex. Based on Co−oxo bond distances, Co1 and Co2 are assigned in the +3 oxidation state (Figure 14). Taking advantage of differences in Lewis acidity, isostructural Sc and Al complexes might be accessible via transmetallation.

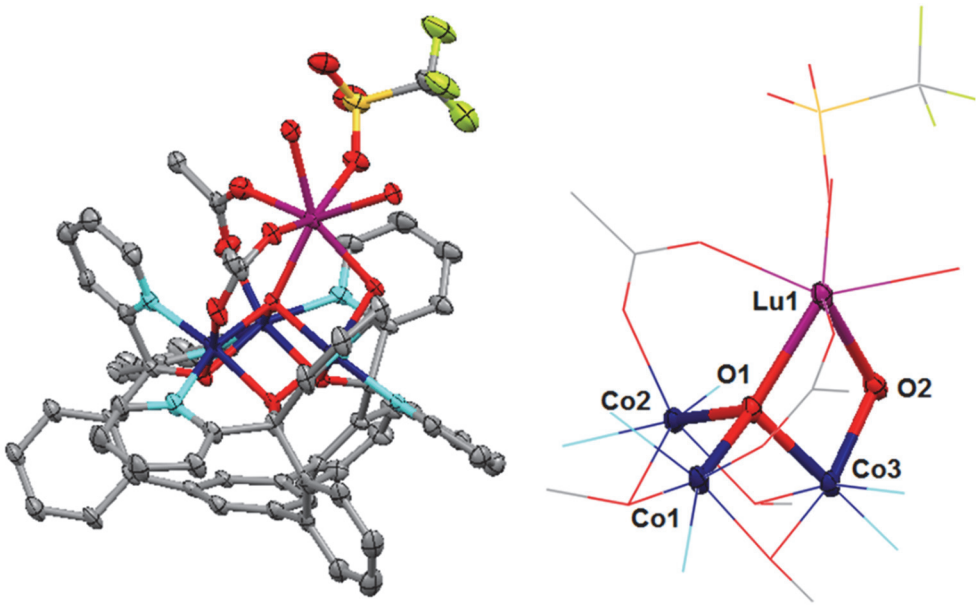

Figure 14. Truncated crystal structure of **6-Lu**. Notable bond distances (Å): Co1−O1 1.899(6), Co2−O1 2.088(6), Co3−O1 1.914(6), Co3−O2 1.902(6), Lu1−O1 2.234(6), Lu1−O2 2.231(6).

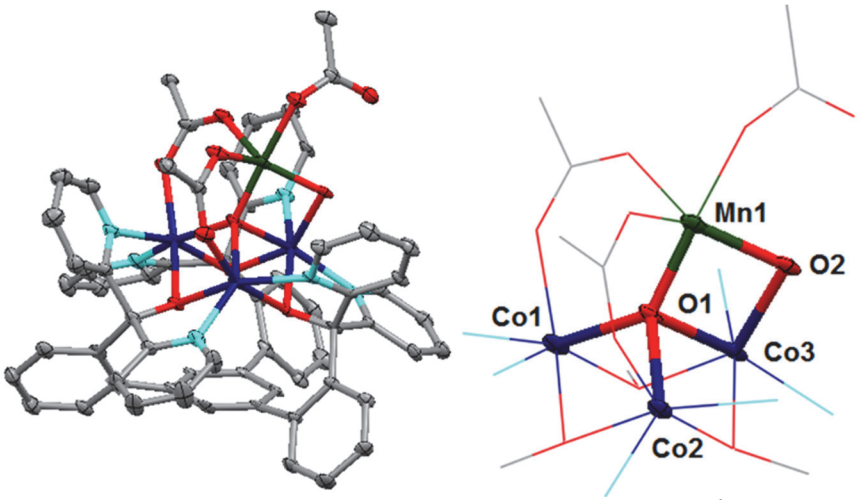

Figure 15. Crystal structure of **6-Mn**. Notable bond distances (Å): Co1−O1 2.047(5), Co2−O1 2.016(5), Co3−O1 2.149(5), Co3−O2 2.047(6), Mn1−O1 1.775(6), Mn1−O2 1.926(5).

Recently, the chemistry of tetrametallic Fe complexes using pyrazolates as bridging ligands has been explored in our group (isostructural to Figure 16). Reversible redox events were observed from [Fe_4^{II}] to [$Fe^{II}Fe_3^{III}$], and reactivity of small molecules such as NO and NH_3 at the apical Fe center is currently being studied. Intramolecular C−H bond hydroxylation has been demonstrated, suggesting possible formation of a transient, terminal Fe=O. To move beyond structure-property studies with cobalt cluster complexes, similar tetrametallic cobalt pyrazolate complexes were pursued. Taking advantage of the established [$Co_2^{II}Co^{III}M'$]/[$Co^{II}Co_2^{III}M'$] redox couple and any other redox processes available in the fourth metal center M', multi-electron redox processes can be envisioned[7]. Introduction of pyrazolate moieties can be achieved by a metathesis reaction between **2b** and alkali-pyrazolate salts. The product of this reaction is not isolated. Upon treatment of this intermediate with $Co_2(CO)_8$ and PhIO, a neutral [$Co_4^{II}O$] complex **7-Co** can be obtained (Figure 15, left). The structure of **7-Co** confirms the formation of the tetracobalt complex. The apical cobalt center is 4 coordinate, poised for substrate binding in the axial position. The synthesis of heterometallic Mn and Fe complexes is underway. Preliminary

ESI-MS data support the formation of a heterometallic [Co_3MnO_2] and [Co_3FeO] clusters. Furthermore, using low valent metal precursors, incorporation of μ^4–nitrido moieties can also be envisioned by reduction of azides[8]. The effect of the interstitial atom in bonding and the resulting reactivity of the cluster is actively being pursued in our lab.

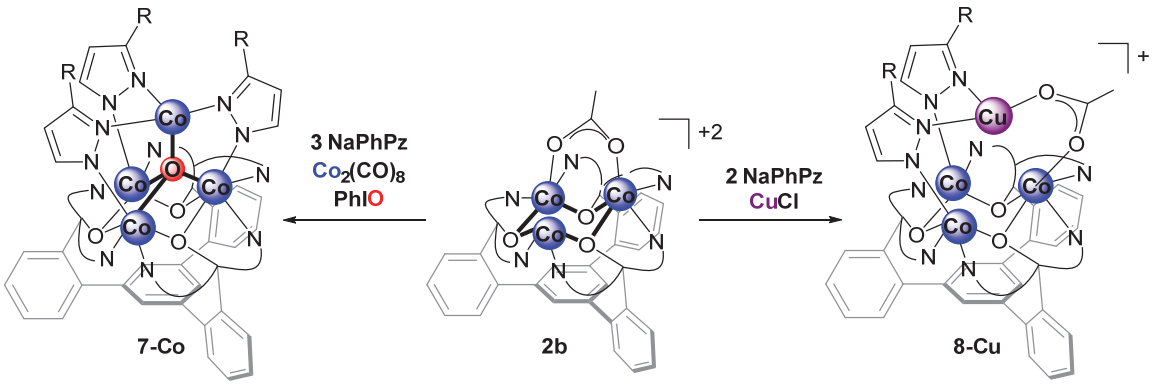

Figure 15. Synthesis of low ox. state tetrametallic clusters **7-Co** and **8-Cu** supported by pyrazolates.

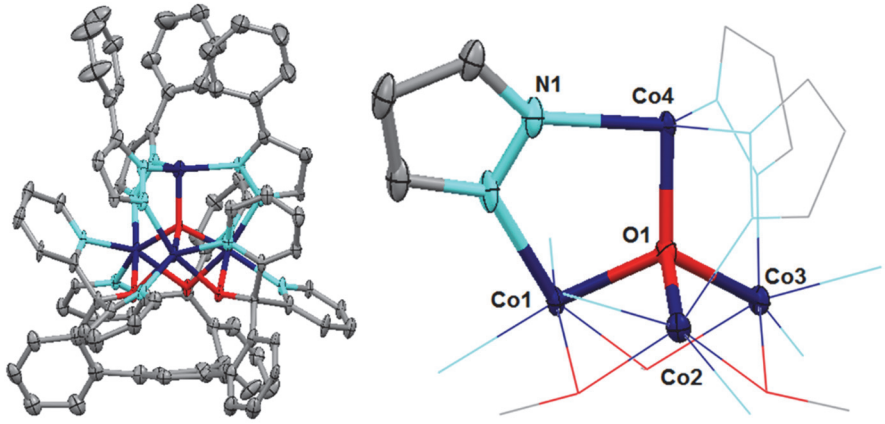

Figure 16. Crystal structure of **7-Co**. Notable bond distances (Å): Co1−O1 1.940(7), Co2−O1 1.947(5), Co3−O1 1.954(7), Co4−O1 1.898(5), Co4−N1 1.999(6).

Treatment of **2b** with 2 equivalents of sodium pyrazolate and copper(I) chloride results in the formation of **8-Cu** (Figure 15, right). The crystal structure reveals the presence of an acetate and two pyrazolate moieties and a three coordinate copper(I) center. A single acetate moiety bridges across three metal centers. Removal of this acetate moiety may lead to a reactive species able to reduce small molecules such as O_2, and NO_2^-, substrates for

copper metalloenzymes. A heterobimetallic CoMg cluster has been shown to reduce NO_2^- selectively to N_2O.[9] Given the propensity with which the tricobalt core incorporates oxo moieties in the interstitial μ^3 position, other element−oxygen bonds may be functionalized. Unlike carboxylate bridges, pyrazolate bridges provide an opportunity to incorporate reduced metal centers. The synthesis of heterometallic Mn and Fe complexes is underway.

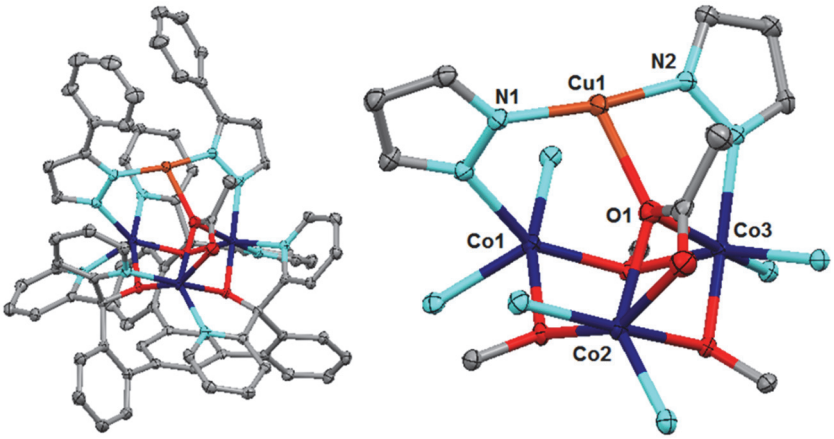

Figure 17. Crystal structure of **8-Cu**. Notable bond distances (Å): Co2−O1 2.188(2), Co3−O1 2.308(2), Cu1−O1 2.234(2), Cu1−N1 1.873(2), Cu1−N2 1.875(2).

A3.3) Summary and future studies

Toward understanding the role of Lewis acids in the redox chemistry of cobalt-oxo species, a trimetallic cobalt complex has been used for the synthesis of benzoate(acetate) bridged heterometallic complexes. The underlying, fundamental coordination chemistry of cobalt μ^3−oxo complexes has been established. Incorporation of Zn, Co, and Lu gives rise to tetrametallic μ^4−oxo complexes. Future studies can be directed toward expanding the series of μ^4−oxo μ^2−hydroxo complexes incorporating other Lewis acids such as Ca^{+2}. The effect of redox inactive metals in modulating redox potential can be studied by electrochemical methods.

The versatility of pyrazolates as bridging ligands has been demonstrated. Tetrametallic cobalt clusters incorporating lower oxidation state metal centers will be pursued for multi-

electron activation of small molecules such as O_2 and NO_2^-. Multimetal catalysis can be explored from such reduced clusters.[10]

A3.4) References

(1) Yocum, C. F., *Coord. Chem. Rev.*, **2008,** *252* (3–4), 296-305.
(2) Bang, S.; Lee, Y.-M.; Hong, S.; Cho, K.-B.; Nishida, Y.; Seo, M. S.; Sarangi, R.; Fukuzumi, S.; Nam, W., *Nat. Chem.*, **2014,** *6* (10), 934-940.
(3) Grimaud, A.; May, K. J.; Carlton, C. E.; Lee, Y.-L.; Risch, M.; Hong, W. T.; Zhou, J.; Shao-Horn, Y., *Nat. Commun.,* **2013,** *4*, 2439.
(4) (a) Tsui, E. Y.; Tran, R.; Yano, J.; Agapie, T., *Nat. Chem.,* **2013,** *5* (4), 293-9; (b) Tsui, E. Y.; Agapie, T., *Proc. Nat. Acad. Sci.,* **2013,** *110* (25), 10084-10088; (c) Herbert, D. E.; Lionetti, D.; Rittle, J.; Agapie, T., *J. Am. Chem. Soc.,* **2013,** *135* (51), 19075-19078.
(5) Pfaff, F. F.; Kundu, S.; Risch, M.; Pandian, S.; Heims, F.; Pryjomska-Ray, I.; Haack, P.; Metzinger, R.; Bill, E.; Dau, H.; Comba, P.; Ray, K., *Angew. Chem. Int. Ed.,* **2011,** *50* (7), 1711-1715.
(6) Tsui, E. Y.; Kanady, J. S.; Day, M. W.; Agapie, T., *Chem. Comm.,* **2011,** *47* (14), 4189-4191.
(7) Powers, T. M.; Betley, T. A., *J. Am. Chem. Soc.,* **2013,** *135* (33), 12289-12296.
(8) Scepaniak, J. J.; Vogel, C. S.; Khusniyarov, M. M.; Heinemann, F. W.; Meyer, K.; Smith, J. M., *Science,* **2011,** *331* (6020), 1049-1052.
(9) Uyeda, C.; Peters, J. C., *J. Am. Chem. Soc.*, **2013,** *135* (32), 12023-12031.
(10) Buchwalter, P.; Rose, J.; Braunstein, P., *Chem. Rev.*, **2015**, *115 (1)*, 28-126.

APPENDIX 4

Miscellaneous Mn, Fe, and Co structures

A4.1) Miscellaneous iron structures

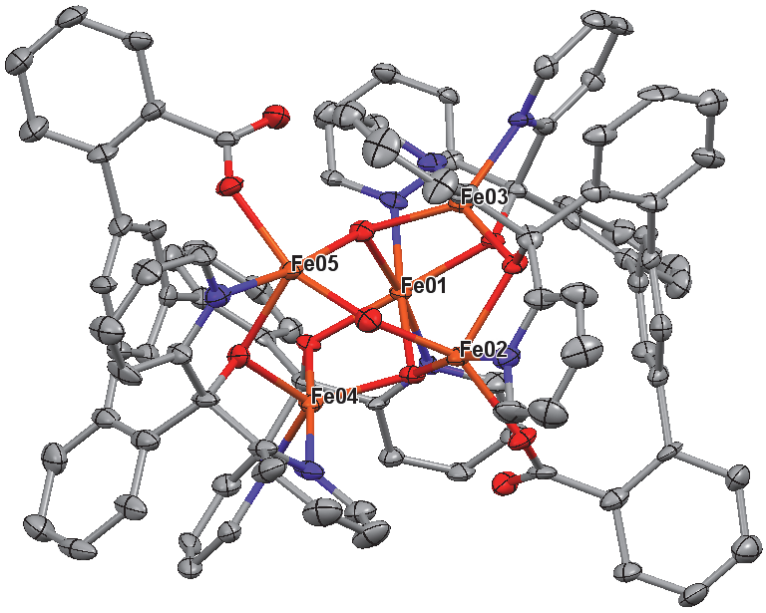

Figure 1. Structure of $[L'_2Fe_5O(OH)_2][OTf]$. Byproduct in the attempted metalation of H_3L' with $Fe^{II}(OTf)_2$ with exposure to air. All alkoxide moieties are bridging. A unique μ^2-oxo bridges Fe(2) and Fe(5). Two μ^3-hydroxos (based on bond distances) bridge Fe(1)-Fe(3)-Fe(5) and Fe(1)-Fe(2)-Fe(4). Tentative oxidation state assignment is $Fe_4^{II}Fe^{III}$.

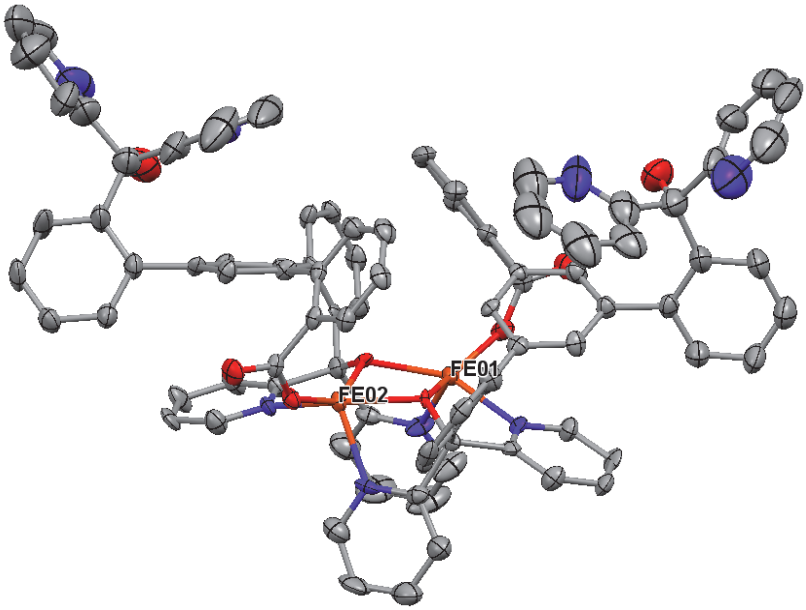

Figure 2. Structure of $(HL')_2Fe_2^{II}$. Byproduct in the attempted metalation of H_3L' with $Fe^{II}(OTf)_2$. One alkoxide arm from each ligand is bridging; one arm seems to be protonated and does not bind to the metals.

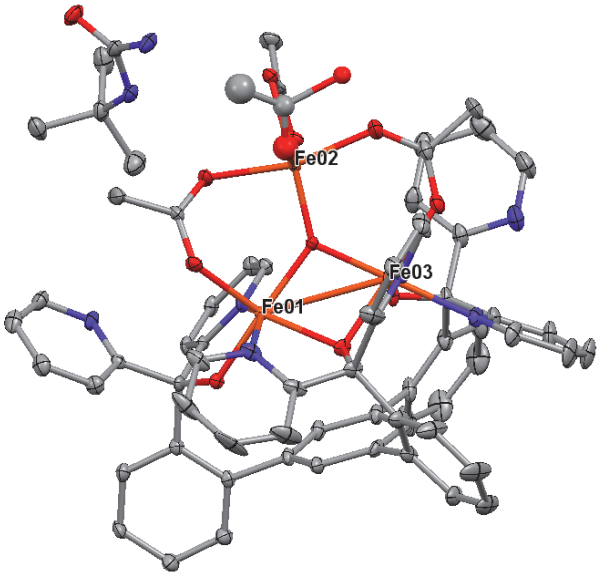

Figure 3. Structure of $LFe_3O(OAc)_{3/4}$. *N*-hydroxylureas were explored as potential two atom bridging ligands. Treatment of $LFe_3(OAc)_3$ with *N*-*t*Bu-*N*'-hydroxyurea results in the formation of a new species characterized crystallographically as $LFe_3O(OAc)_4$. Oxygen atom transfer is observed, leading to an acetate-bridged, planar $Fe_3(\mu^3\text{-}O)$ core. Two alkoxide arms are terminal; one alkoxide arm is bridging.

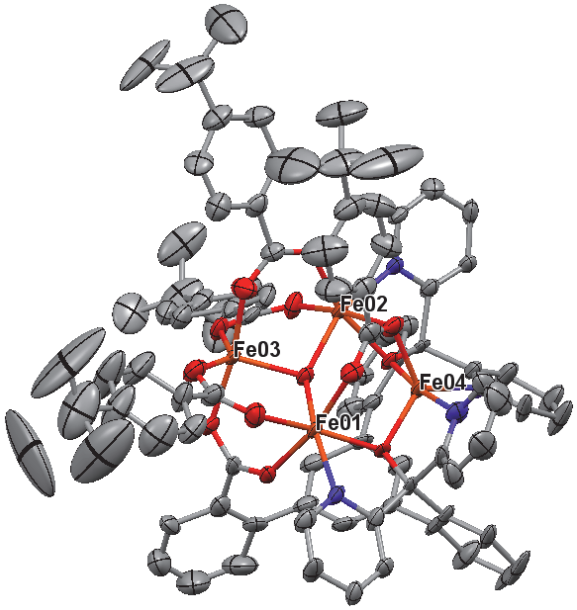

Figure 4. Structure of $L'Fe_4(OH)(p\text{-}t\text{Bu-OBz})_4$. Diamond Thomas, a visiting summer student, synthesized $Fe(p\text{-}t\text{Bu-OBz})_2$ via $FeCl_2$ and $Na(p\text{-}t\text{Bu-OBz})$. Treatment of $Fe(p\text{-}t\text{Bu-OBz})_2$ with H_3L' in wet THF leads to the formation of the desired tetrairon complex $L'Fe_4^{II}(OH)(p\text{-}t\text{Bu-OBz})_4$ which is highly analogous to the published complex **1-Fe** (Chapter 2).

A4.2) Miscellaneous cobalt structures

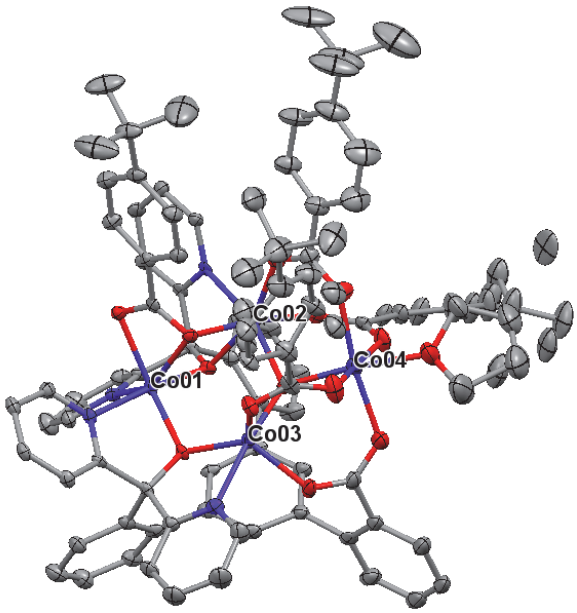

Figure 5. Structure of L'Co_4(OH)(*p*-*t*Bu-OBz)$_4$(THF). Co(*p*-*t*Bu-OBz)$_2$ is synthesized via $CoCl_2$ and Na(*p*-*t*Bu-OBz). Treatment of Co(*p*-*t*Bu-OBz)$_2$ with H_3L' in wet THF leads to the formation of the desired tetracobalt complex L'Co_4^{II}(OH)(*p*-*t*Bu-OBz)$_4$(THF) which is highly analogous to the published complex **1-Co** (Chapter 2).

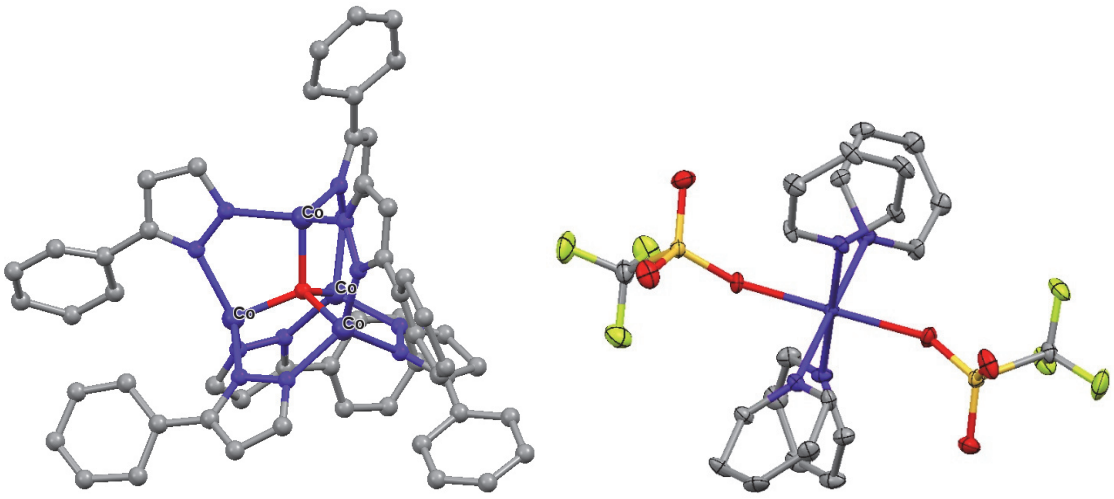

Figure 6. Structure of $Co_4(\mu^4\text{-}O)(PhPz)_6$ and $Co(py)_4(OTf)_2$.

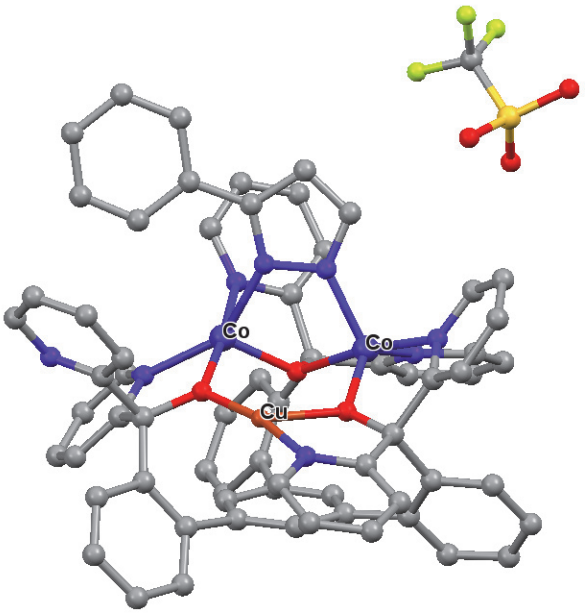

Figure 8. Structure of $[LCo_2^{II}Cu^{I}(PhPz)][OTf]$.

A4.3) Miscellaneous manganese structures

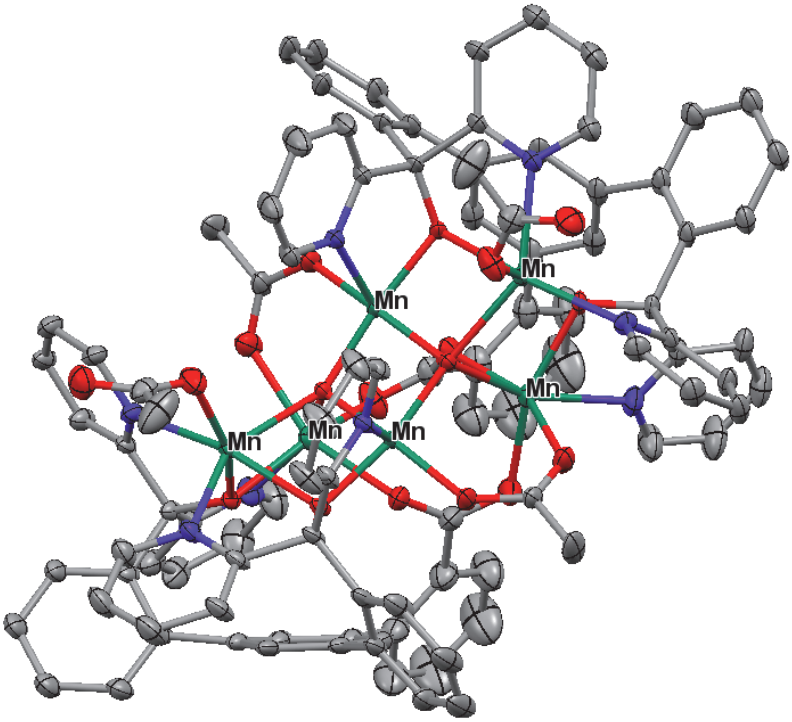

Figure 9. Structure of $[L'Mn_2^{II}Mn^{III}O(OAc)_2]_2$. Initial attempts to metallate H_3L' with $Mn(OAc)_2$ and NaO^tBu under anhydrous conditions led to a partially oxidized product.

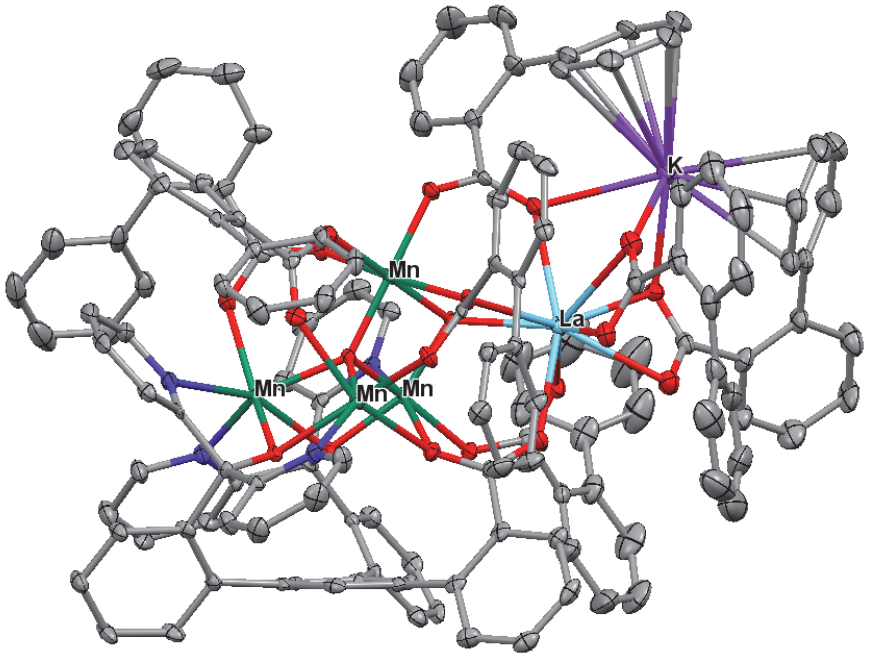

Figure 10. Structure of K[L'Mn_4LaO_2(2-Ph-OBz)$_7$]. Crystals formed in the reaction of L'Mn_4(OH)(2-Ph-OBz)$_4$ with La(OTf)$_2$, KO_2, and 2-phenyl-benzoic acid.

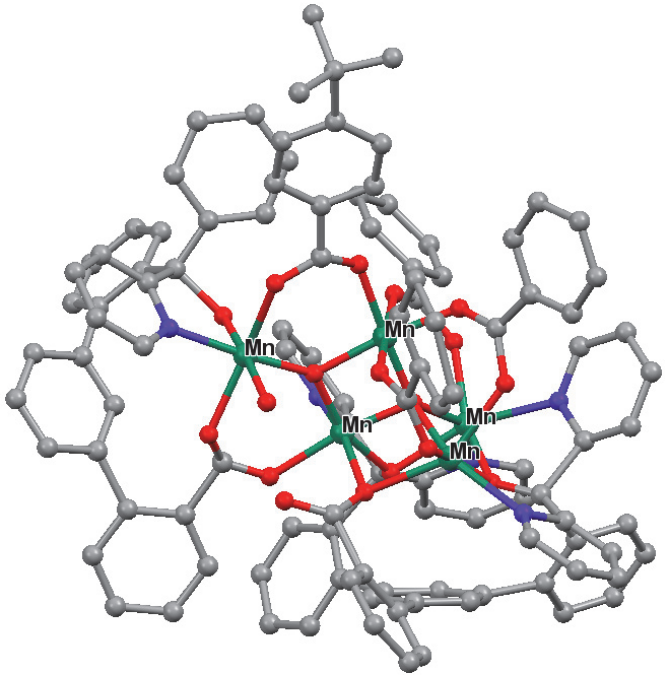

Figure 11. Structure of L'$_2Mn_5O_2$(4-*t*Bu-OBz)$_4$. Decomposition product of L'Mn_5O_2(4-*t*Bu-OBz)$_5$ upon attempted oxidation to a cluster with higher oxo content.

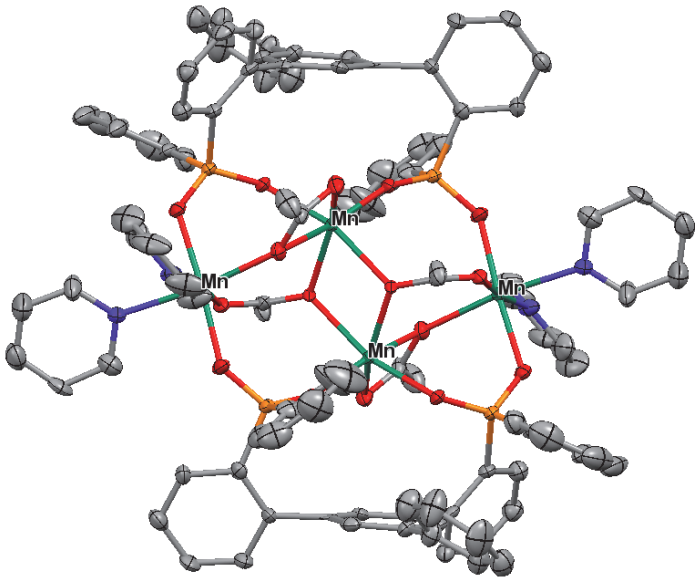

Figure 12. Structure of (bis-phosphinate)$_2$Mn$_4^{II}$(OAc)$_4$(py)$_4$. Treatment of 1,3,5-tris(2-lithiophenyl)-benzene with 3 equiv PhPH(O)(OEt) results in the formation of the bis-phosphinate ligand, presumable via deprotonation of the P−H bond. Product formed upon subsequent metalation with Mn(OAc)$_2$ in pyridine.

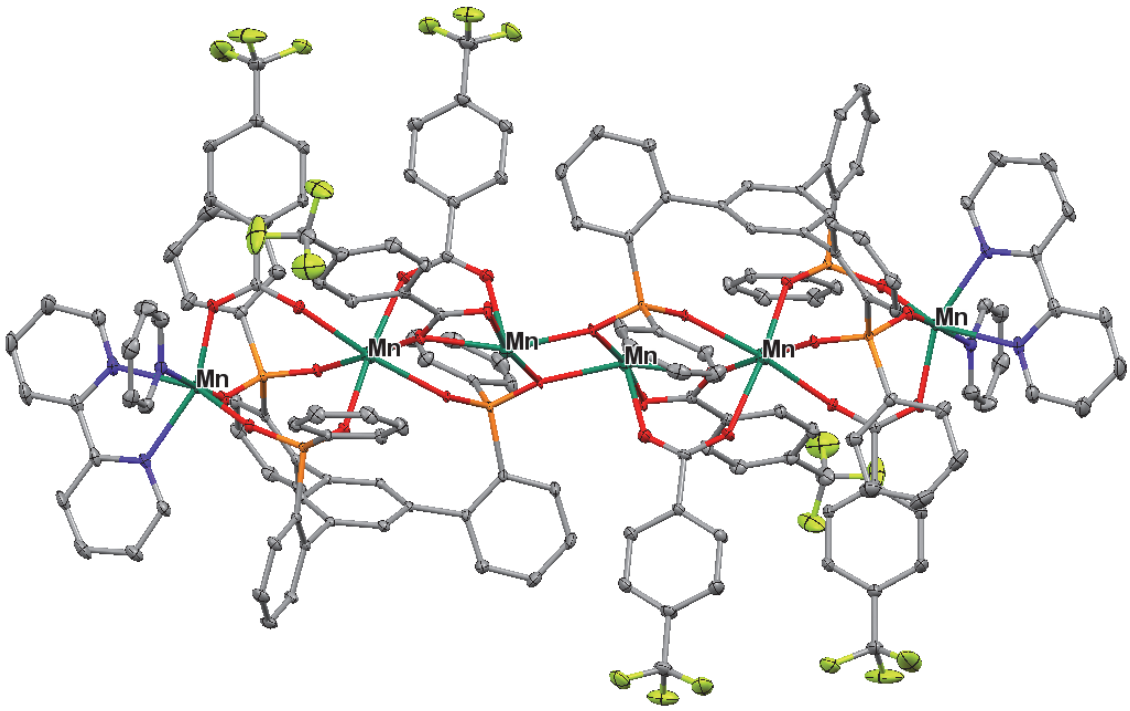

Figure 13. Structure of (tris-phosphinate)$_2$Mn$_6^{II}$(*p*-CF$_3$-OBz)$_6$(bpy)$_2$(py)$_4$. Tris-phosphinate ligand obtained via treatment of 1,3,5-tris(2-lithiophenyl)-benzene with 3 equiv PhPCl$_2$ and subsequent oxidative workup. Metalation with Mn(OBz)$_2$ with bpy and py.

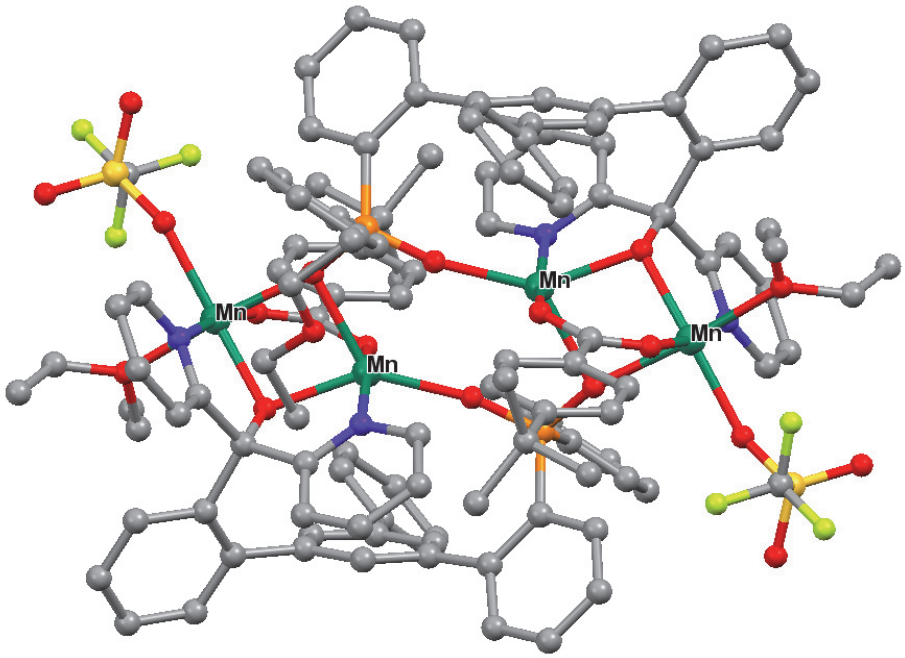

Figure 14. Structure of $(L^{P})_2Mn_4^{II}(p\text{-}t\text{Bu-OBz})_2(OTf)_2(Et_2O)_2$. Product of unsuccessful attempts to metalate H_2LiL^{P} with $Mn(OBz)_2/Mn(OTf)_2$.

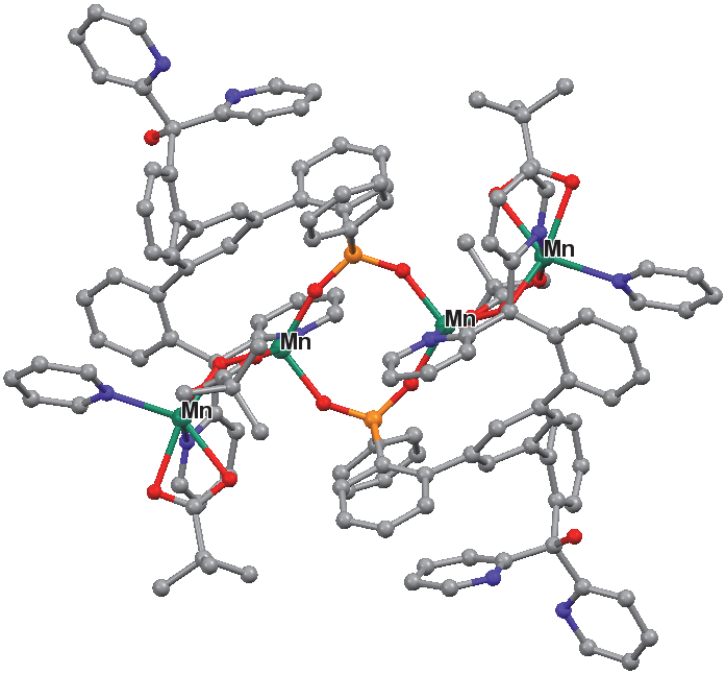

Figure 15. Structure of $(HL^{P})_2Mn_4^{II}(OPiv)_4(py)_2$. Product of unsuccessful attempts to metalate H_2LiL^{P} with $Mn(OPiv)_2/Mn(OTf)_2$.

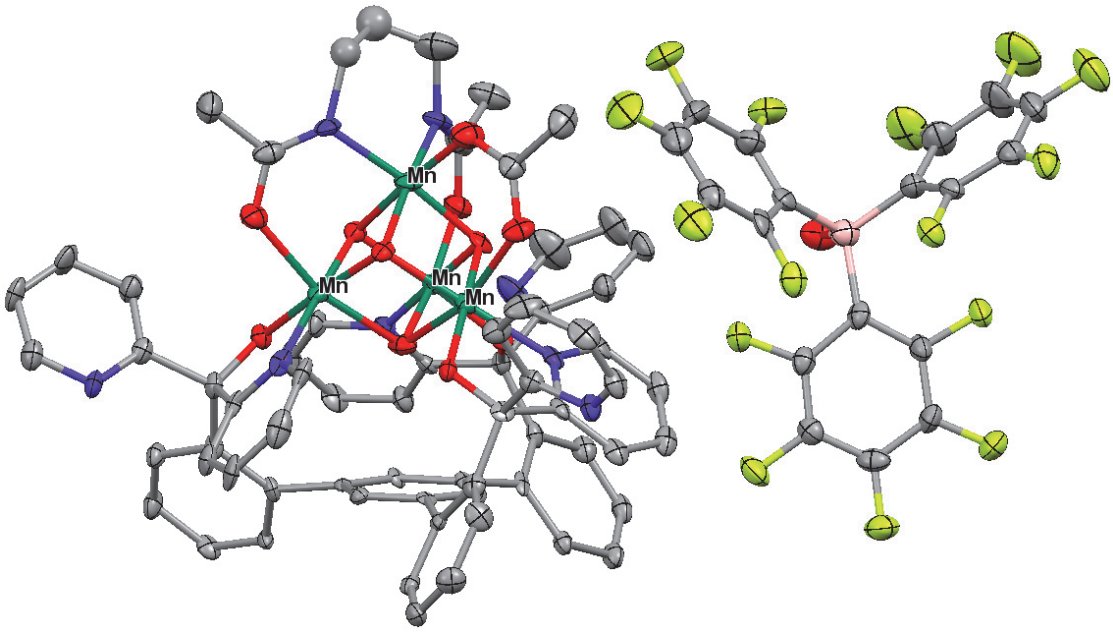

Figure 16. Structure of $[LMn^{III}Mn_3{}^{IV}O_4(diam)(OAc)][(C_6F_5)_3B(OH)]$. Treatment of $[LMn_2{}^{III}Mn_2{}^{IV}O_4(diam)(OAc)]$ with $B(C_6F_5)_3$ under not strictly anhydrous conditions leads to oxidation of the cluster instead of removal of the acetate moiety. Thus far, attempts to synthesize diamidate complexes that do not incorporate a bridging carboxylate have not been successful.

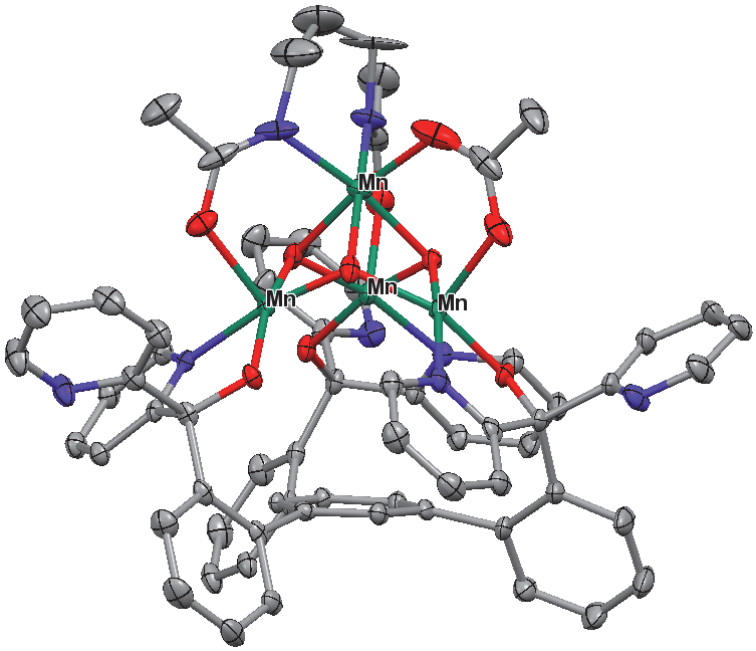

Figure 17. Structure of $LMn_4{}^{III}O_3(diam)(OAc)$. With the goal of removing the acetate moiety, treatment of $[LMn_2{}^{III}Mn_2{}^{IV}O_4(diam)(OAc)]$ with $B(C_6F_5)_3$ under reducing conditions ($CoCp_2$) leads to the trioxo complex. Presumably, $[CoCp_2]_2[(C_6F_5)_3BOB(C_6F_5)_3]$ is formed as a byproduct.

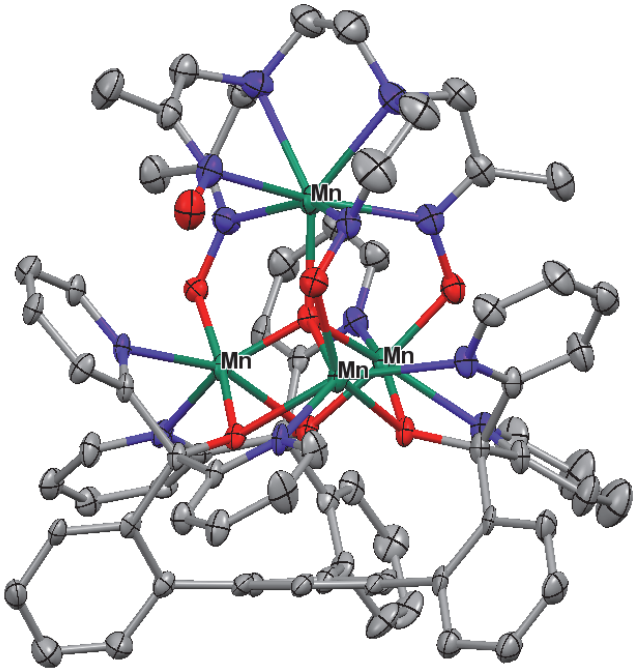

Figure 18. Structure of $LMn_2^{II}Mn_2^{III}O(tetraoxime)(OTf)_2$. Treatment of $LCaMn_3O_4(OAc)_3$ with the tetraoxime ligand results in decomposition of the cluster. Triflate from impure Ca cubane.

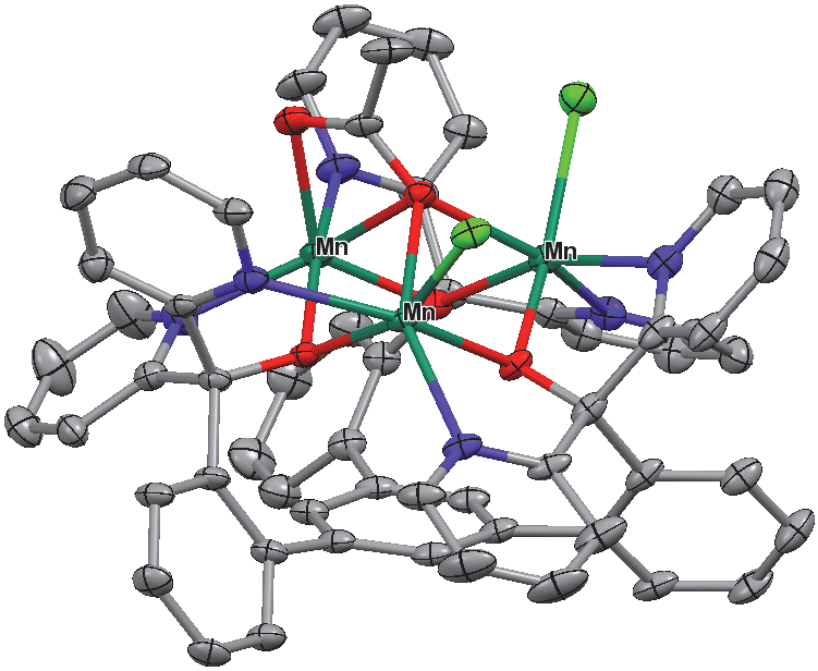

Figure 19. Structure of $LMn_3^{II}(OAc)(Cl)_2$.

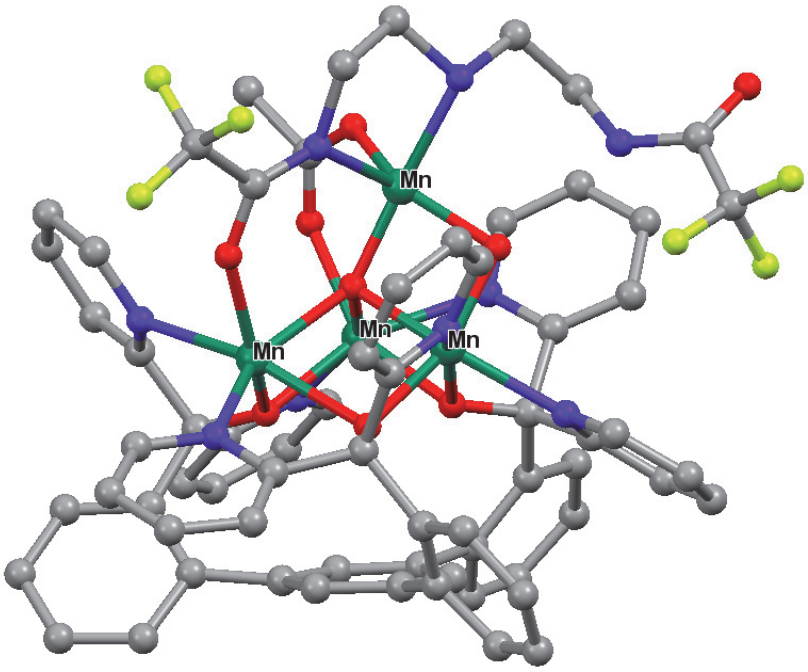

Figure 20. Structure of $LMn_2^{II}Mn_2^{III}O_2(CF_3\text{-diamidate})(OAc)(OTf)$.

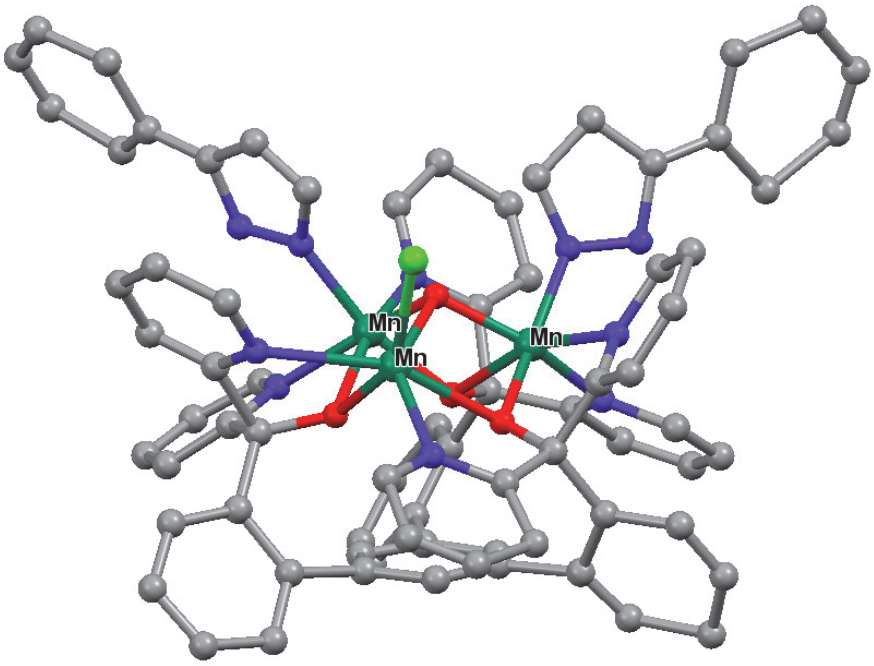

Figure 21. Structure of $LMn^{II}Mn_2^{III}O(PhPz)_2Cl$.

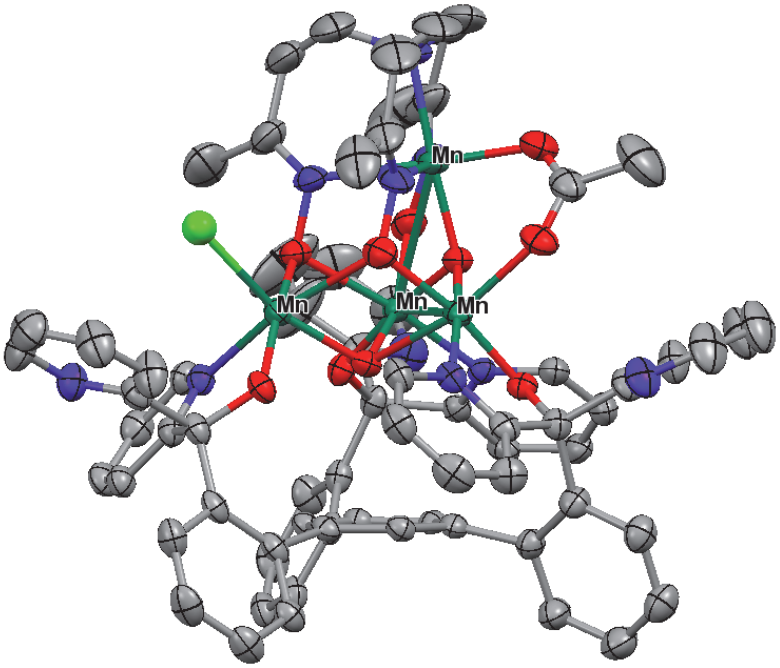

Figure 22. Structure of $[LMn_3^{III}Mn^{IV}O_2(trioxime)(OAc)Cl][BF_4]$.

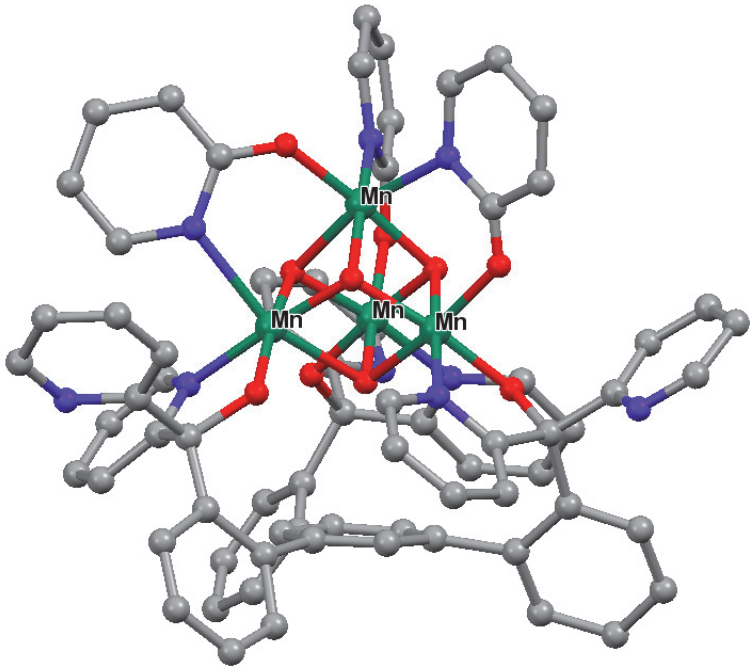

Figure 23. Structure of $LMn_2^{III}Mn_2^{IV}O_4(2\text{-pyridonate})_3$. Treatment of $[LMn_2^{III}Mn_2^{IV}O_4(OAc)_3]$ with deprotonated 2-hydroxypyridine leads to the formation of the tris-pyridonate complex.

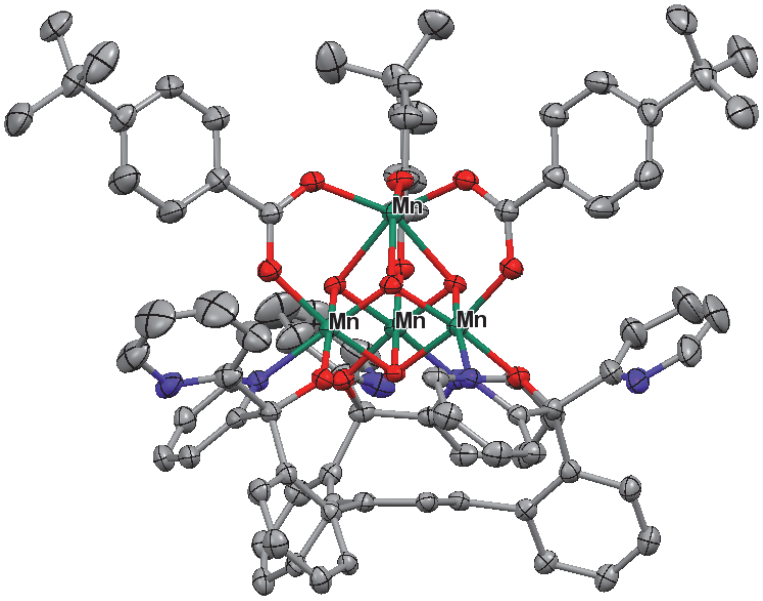

Figure 24. Structure of $LMn_2^{III}Mn_2^{IV}O_4$(*p*-*t*Bu-benzoate)$_3$. Treatment of [$LMn_2^{III}Mn_2^{IV}O_4$(diam)(OAc)] with excess benzoic acid leads to the formation of the tris-benzoate complex.

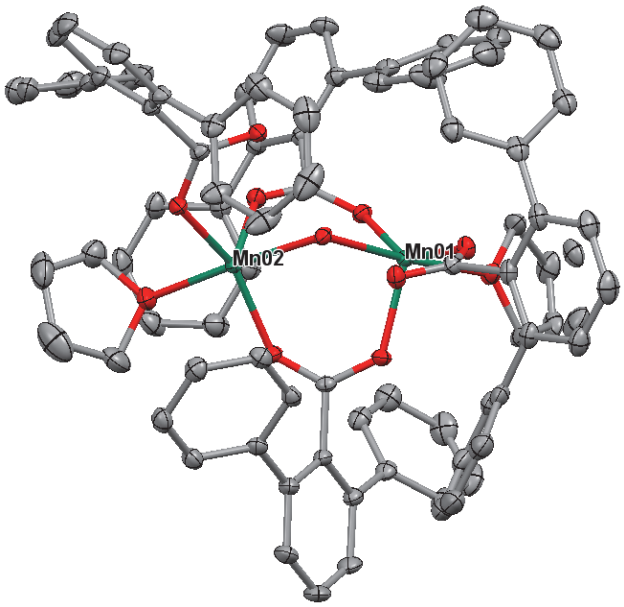

Figure 25. Structure of Mn_2^{II}(2,6-diphenyl-benzoate)$_4$(H_2O)(THF)$_2$. Crystals obtained upon treatment of $MnCl_2$ with Na(2,6-diphenyl-benzoate) in MeOH followed by THF workup.

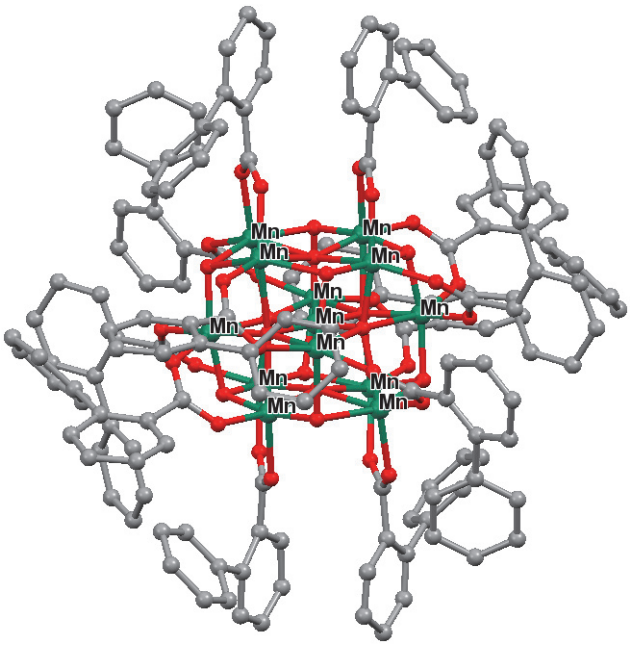

Figure 25. Structure of $Mn_{12}^{III}Mn^{IV}O_{14}$(2-phenylbenzoate)$_{12}$.

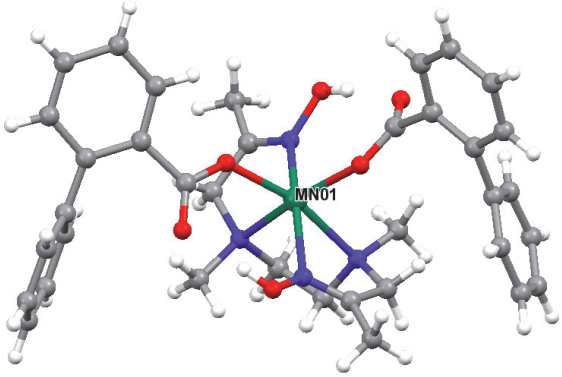

Figure 26. Structure of $Mn^{II}(H_2N_4O_2)$(2-PhOBz)$_2$.

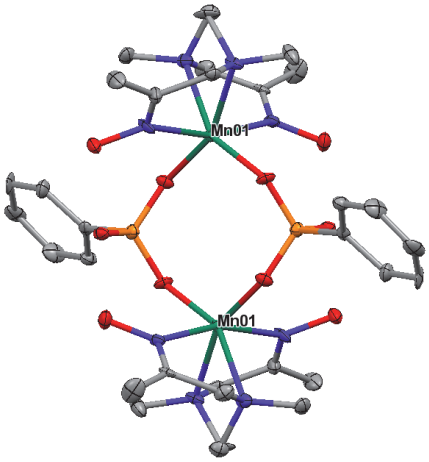

Figure 27. Structure of $Mn_2^{II}(H_2N_4O_2)_2(PhPO_3)_2$.

ABOUT THE AUTHOR

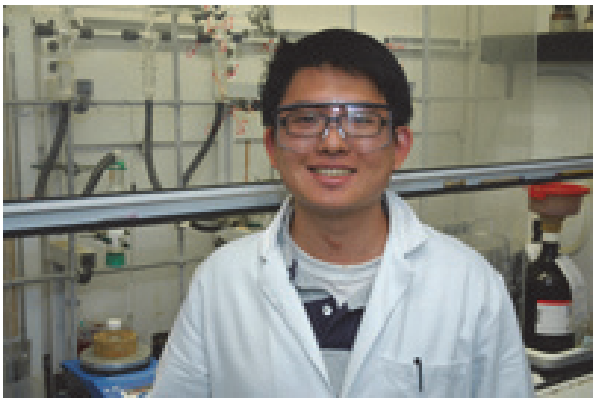

Heui Beom Lee is a passionate inorganic chemist specializing in the synthesis and characterization of transition metal and lanthanide coordination complexes. He is currently appointed as a postdoctoral scholar in the laboratories of Prof. Jonathan Rittle at the University of California, Berkeley. One day, he aspires to become a professor and educate the next generation of scientists and engineers.

Heui Beom had an interesting childhood. Born in South Korea, Heui Beom immigrated with his parents to Mexico at the age of seven. After three years in Mexico, he returned to Korea only to immigrate two years later to Guatemala, where he finished high school and developed a keen interest in the physical sciences. Against all odds during the financial crisis of 2009, he was fortunate to receive a generous financial aid package from the University of Pennsylvania, where he majored in chemical engineering and chemistry. At UPenn, he developed a taste for running reactions on a large scale (1 kg for an academic lab is huge), and the term “HB-scale” was coined by his peers.

Aside from running HB-scale reactions, Heui Beom enjoys playing soccer, playing the piano, grilling (or going to an all-you-can-eat Korean BBQ), and binge-watching TV shows.

HEUI BEOM LEE

hlee3@caltech.edu (heuibeomlee@gmail.com)

EDUCATION

California Institute of Technology, Pasadena, CA, U.S.A. **2019**
Degree program: Ph.D. in Chemistry, Inorganic

University of Pennsylvania, Philadelphia, PA, U.S.A. **2013**
Degree: Bachelor of Science in Engineering, Summa cum Laude
Majors: Chemical and Biomolecular Engineering • Chemistry

PUBLICATIONS

1. **Lee, H. B.**, Shiau, A. A., Oyala, P. H., Marchiori, D., Gul, S., Ruchira, C., Yano, J., Britt, R. D., Agapie, T. "Tetranuclear [$Mn^{III}Mn^{IV}_3O_4$] Complexes as Spectroscopic Models of the S_2 State of the Oxygen Evolving Complex in Photosystem II" *J. Am. Chem. Soc.*, **2018**, *140*, 17175-17187.
2. **Lee, H. B.**, Tsui, E. Y., Agapie, T. "$CaMn_4O_2$ model of the biological oxygen evolving complex: synthesis by cluster expansion on low symmetry ligand" *Chem. Commun.*, **2017**, *53*, 6832-6835.
3. Han, Z., Horak, K. T., **Lee, H. B.**, Agapie, T. "Tetranuclear Manganese Models of the OEC Displaying Hydrogen Bonding Interactions: Application to Electrocatalytic Water Oxidation to Hydrogen Peroxide" *J. Am. Chem. Soc.*, **2017**, *139*, 9108-9111.
4. Lifschitz, A. M., Hirscher, N. A., **Lee, H. B.**, Buss, J. A., Agapie, T. "Ethylene Tetramerization Catalysis: Effects of Aluminum-Induced Isomerization of PNP to PPN Ligands" *Organometallics*, **2017**, *36*, 1640-1648.
5. Bogart, J. A., Lewis, A. J., Boreen, M. A., **Lee, H. B.**, Medling, S. A., Carroll, P. J., Booth, C. H., Schelter, E. J. "A Ligand Field Series for the 4f-Block from Experimental and DFT Computed Ce(IV/III) Electrochemical Potentials" *Inorg. Chem.*, **2015**, *54*, 2830-2837.
6. **Lee, H. B.**, Bogart, J. A., Carroll, P. J., Schelter, E. J. "Synthesis and Characterization of a Cerium(IV) Hydroxamate Complex: Implications for the Beneficiation of Light Rare Earth Ores" *Chem. Commun.*, **2014**, *50*, 5361-5363.
7. Bogart, J. A., **Lee, H. B.**, Boreen, M. A., Jun, M., Schelter, E. J. "Fine-tuning the Oxidative Ability of Persistent Radicals: Electrochemical and Computational Studies of Substituted 2-Pyridyl Hydroxylamines" *J. Org. Chem.*, **2013**, *78*, 6344-6349.

RESEARCH EXPERIENCE

California Institute of Technology

- Tetranuclear [$Mn^{III}Mn^{IV}_3O_4$] and [$Mn^{IV}_4O_4$] cuboidal complexes and study of their electronic structure by EPR spectroscopy and SQUID magnetometry: The Mn oxidation states in these complexes correspond to those in the S_2 and S_3 intermediates in the catalytic cycle of biological water oxidation. Structure determination and spectroscopic characterization of intermediates in the S-state catalytic cycle heavily

influence mechanistic proposals for O−O bond formation. Electronic structure studies of structurally well-defined, biologically-relevant complexes remain rare. Results show that the electronic structure of tetranuclear Mn complexes are highly sensitive to small geometric changes and the nature of the bridging ligands.

- Effect of oxo protonation in the electronic structure of $[CaMn_3^{IV}O_4]$ cuboidal complexes: Growing experimental data support that conversion from the low-spin (LS) form of the S_2 state to its high-spin (HS) form is an intermediate step in the $S_2 \rightarrow S_3$ transition. pH dependence studies indicate that deprotonation of the LS form leads to the HS form. Protonation of well-defined, desymmetrized $[CaMn_3^{IV}O_4]$ cuboidal complexes lead to the corresponding $[CaMn_3^{IV}O_3(OH)]$ complexes. EPR and SQUID magnetometry studies indicate a change from ferromagnetic to antiferromagnetic interaction between the Mn centers upon protonation.
- Structure-property studies probing the effect of redox-inactive metals and the influence of ligands in modulating the oxidation potential of Mn oxido cluster complexes: Ca is a crucial metal for the function of the OEC, yet its role remains unclear. Amidate-supported $[M'Mn_3O_4]$ complexes where M' is a redox inactive metal were synthesized and studied by electrochemical methods. Results show that the geometric effect of a rigid chelating ligand framework may have a more significant impact in tuning the electronic properties of the cluster than the precise nature of the bridging ligands.
- Pentanuclear $[CaMn_4O_2]$ model of the biological oxygen evolving complex (OEC): Synthesis of Mn-oxido clusters containing heterometals such as Ca remain a challenge. A low symmetry multinucleating scaffold allowed the synthesis of tetranuclear Mn complexes to which heterometals could be added to afford pentanuclear clusters, providing a design strategy for the synthesis of accurate structural models of the OEC.

University of Pennsylvania

- Electrochemical study of a series of substituted pyridyl nitroxides: Nitroxides are a class of compounds that find diverse use in catalytic, medicinal, and materials chemistry. Substituent effects were used to fine-tune nitroxide redox potentials. Computational studies agree with the electrochemical studies and provide a toolset for the predictive design of nitroxides.
- A ligand field series for Ce: A systematic variation of ligand field and its effect in the electronic properties of Ce was investigated. Ce hydroxamate and hydroxylamine complexes were synthesized and characterized via spectroscopic, electrochemical, and computation methods. Results reveal that a broad range of Ce(III/IV) redox potentials correlate to ligand field strength, establishing a semi-empirical, predictive model for Ce redox thermodynamics.

TEACHING EXPERIENCE

California Institute of Technology
Ch112, Inorganic Chemistry − Fall **2017** and Fall **2015**.
Ch102, Introduction to Inorganic Chemistry – Spring **2014** and Spring **2017**
Ch5b, Advanced Techniques of Synthesis and Analysis – Fall **2013**
Ch4a, Synthesis and Analysis of Organic Compounds – Winter **2014**
Ch1a, General Chemistry I – Fall **2014**

POSTERS AND PRESENTATIONS

1. 2nd Socal BioInorganic Meeting – Caltech, CA, December **2018**. Short presentation and poster: "Structural and spectroscopic models of the oxygen evolving complex in Photosystem II"
2. 1st Socal BioInorganic Meeting – UC Irvine, CA, December **2017**. Poster: "Amidate-supported high oxidation state [Mn_4O_4] cubane complexes as spectroscopic models of the Oxygen Evolving Complex in Photosystem II"
3. 251st ACS National Meeting – San Diego, CA, March **2016**. Presentation: "Tetranuclear complexes as precursors for the rational design of pentanuclear oxido clusters reminiscent of the oxygen evolving complex in Photosystem II"
4. 14th Socal Organometallics Meeting – California Institute of Technology, Feb **2016**. Poster: "Heterometallic effects on redox potential of metal-oxo clusters and efforts toward an accurate structural and functional model of the Oxygen Evolving Complex in Photosystem II"
5. 248th ACS National Meeting – San Francisco, CA August **2014**. Presentation: "Synthesis and reactivity of heteromultimetallic cobalt-oxido cluster complexes relevant to water oxidation"

Honors and Awards

ACS Award Dept. of Chemistry Univ. of Pennsylvania	2013
ACS Inorganic Chemistry Award Dept. of Chemistry Univ. of Pennsylvania	2013
ACS Award Dept. of Chem. Eng. Univ. of Pennsylvania	2013
Philadelphia Section ACS Scholastic Achievement Award	2013
Josephine DeKarman Fellowship	2012
Korean American Scientists and Engineers Association Scholarship	2011
Korean Honors Scholarship from the Korean Embassy	2010
Korean American Scholarship Foundation	2009